

PHASE-SENSITIVE OPTICAL COHERENCE
TOMOGRAPHY FOR DYNAMIC PHOTOTHERMAL
DETECTION AND IMAGING OF GOLD NANO-RODS
IN SCATTERING MEDIA AND BIOLOGICAL TISSUE

A THESIS SUBMITTED TO
THE UNIVERSITY OF KENT

IN THE SUBJECT OF PHYSICS

FOR THE DEGREE
OF DOCTOR OF PHILOSOPHY

Yong Hu

December 2017

Abstract

Gold nanoparticles are particularly attractive agents in medical imaging and laser therapy due to their unique optical properties. This study seeks to propose and analyse solutions aimed at imaging the distribution of gold nanoparticles in scattering media and biological tissue using a photothermal modulation technique combined with phase sensitive Optical Coherence Tomography (OCT). In this thesis, a spectrometer based phase sensitive OCT system and a swept source based phase sensitive OCT system are developed separately to fulfil this goal. In each OCT system, a Ti:Sa laser beam is coaxially combined with the OCT probing beam. The photothermal detection of gold nano-rods in multiple layer of the sample is completed by fixing the combined beam on a single lateral position on the sample and modulating the frequency of the Ti:Sa beam to the sample. The photothermal imaging of gold nano-rods in multiple layers of the sample is achieved by raster scanning the combined beams over the sample, modulating the Ti:Sa beam to the sample and then generating high contrast *en-face* images displaying the phase values retrieved from the OCT signal.

Using the recently developed Complex Master/Slave interferometry technique, *en-face* images can be acquired in real time. In this thesis, application of this technique to a swept source based OCT system is presented. A system is specifically developed to produce *en-face* phase images of multiple layers of the studied sample. By doing this, the phase sensitive function of the Complex Master/Slave interferometry technique is demonstrated for the first time.

Acknowledgements

Completing this PhD was one of the things I have dedicated to do and would not have been possible without the supports of some intelligent people. I would first like to thank Dr George Dobre for his invaluable mentorship during the time. He is a fount of knowledge, or a walking encyclopaedia if I am modest to say so, to his students. His constant upbeat mood and considerate care often take me out of the stressful work. I really could not have asked for a better supervisor.

I would like to express my appreciation to my co-supervisor Professor Adrian Podoleanu who offered a ton of insights into the process of the project. He is a model of total commitment, and his hard working attitude inspires his collaborators all around.

Special thanks to my colleagues Dr Jingyu Wang and Dr Christopher Costa who shared their experiences in LabVIEW programming when I started to learn this skill without which I could not develop these OCT systems in such a short time.

When things got tough I was able to receive help from my colleagues of the Applied Optics Group, who were always there to provide supports. They are Dr Manuel Marques, Dr Ramona Cernat and Dr Adrian Bradu.

I would like to state and acknowledge that the data acquisition units in the LabVIEW codes used in Chapter 4, Chapter 5 and Chapter 6 were contributed by Dr Adrian Bradu. Thanks to Adrian for sharing his LabVIEW codes. Copying these units from his LabVIEW codes saved plenty of my time on coding, and the modified LabVIEW programmes operated stably.

All the work would not have been possible without the support of the University of Kent.

Lastly I would like to thank my family. Though they probably never fully understood my research, they have been unconditionally investing most in me. They provide me with the most important reason to keep going. It is to them that this work is dedicated.

Contents

Abstract	i
Acknowledgements	ii
Contents	iii
List of Acronyms	vi
Chapter 1	1
1.1 Introduction	1
1.2 Phase retrieval in monochromatic interferometry	5
<i>1.2.1 Interferometric phase to optical path difference</i>	6
<i>1.2.2 Interferometric phase to refractive index</i>	8
<i>1.2.3 Interferometric phase to Doppler shift</i>	9
1.3 Review of monochromatic interferometric techniques	11
<i>1.3.1 Monochromatic phase interferometry in cell volume measurement</i>	11
<i>1.3.2 Monochromatic phase interferometry in cell dynamics</i>	16
<i>1.3.3 Monochromatic phase interferometry in nerve fibre morphology</i>	19
1.4 Discussion and conclusion	22
Chapter 2	25
2.1 Introduction	25
2.2 Phase retrieval in FD-OCT	27
2.3 Depth resolved phase measurement in FD-OCT	28
2.4 Review of phase sensitive FD-OCT techniques	31
<i>2.4.1 Phase sensitive SD-OCT in imaging tissue motion</i>	32
<i>2.4.2 Phase sensitive SS-OCT in imaging and quantifying of microbubbles</i>	35
2.5 Discussion and conclusion	39
Chapter 3	40
3.1 Introduction	40
3.2 Optical properties of gold nanoparticles	40
3.3 Biomedical applications of gold nanoparticles	42

3.3.1 Drug delivery	42
3.3.2 Cancer diagnostic agents	43
3.3.3 Cancer treatment.....	43
3.4 Photothermal property and TPL emission of GNRs.....	44
3.5 Review of techniques in detecting and imaging gold nanoparticles	47
3.5.1 Photothermal trapping and TPL imaging of GNRs	47
3.5.2 Photothermal detection of GNRs using phase sensitive SS-OCT	52
3.6 Discussion and conclusion.....	55
Chapter 4	58
4.1 Introduction	58
4.2 Measuring micro vibration using phase sensitive OCT	60
4.3 System configuration.....	62
4.4 Methodology and Results.....	65
4.4.1 Output traces	66
4.4.2 Calibration.....	74
4.4.3 Characterization of displacement sensitivity.....	75
4.4.4 Improved displacement sensitivity	78
4.4.5 Degradation of displacement sensitivity to defocus	80
4.4.6 Photothermal response of GNRs to Ti:Sa modulation frequency	82
4.4.7 Photothermal response of GNRs to Ti:Sa power.....	86
4.4.8 Photothermal imaging of GNRs in clear media	88
4.4.9 Photothermal detection of GNRs in biological tissue.....	93
4.4.10 Photothermal imaging of GNRs in biological tissue	96
4.5 Discussion and Conclusion	98
Chapter 5	102
5.1 Introduction	102
5.2 System configuration.....	103
5.3 Methodology and Results.....	105
5.3.1 Phase measurement in A-scan	105
5.3.2 Phase measurement in B-scan	111

5.3.3 <i>Phase map generation & en-face phase image generation</i>	115
5.3.4 <i>System noise of SD-OCT and SS-OCT</i>	119
5.3.5 <i>Photothermal detection of GNRs in clear media</i>	122
5.3.6 <i>Photothermal imaging of GNRs in clear media</i>	124
5.3.7 <i>Photothermal imaging of GNRs in scattering media</i>	127
5.4 Discussion and Conclusion	129
Chapter 6	132
6.1 Introduction	132
6.2 Principles of MSI	134
6.3 Principles of CMSI	138
6.4 System configuration	141
6.5 Methodology and Results	142
6.5.1 <i>En-face OCT image and phase map generation in CMS-OCT</i>	142
6.5.2 <i>Phase measurements in CMS-OCT and SS-OCT</i>	146
6.6 Discussion and conclusion	149
Chapter 7	151
7.1 Summary	151
7.2 Achievements	152
7.3 Evaluation	154
7.4 Future work	155
References	156
Appendix	164

List of Acronyms

OCT	Optical Coherence Tomography
FD-OCT	Fourier Domain Optical Coherence Tomography
FWHM	Full Width Half Maximum
OPD	Optical Path Difference
OPL	Optical Path Length
SNR	Signal to Noise Ratio
SS-OCT	Swept Source Optical Coherence Tomography
SD-OCT	Spectra Domain Optical Coherence Tomography
SPR	Surface Plasmon Resonance
FFT	Fourier Transform
MSI	Master-Slave Interferometry
MS-OCT	Master-Slave Optical Coherence Tomography
CMSI	Complex Master-Slave Interferometry
SI	Slave Interferometer master interferometer
MI	Master Interferometer
GNRs	Gold Nano-rods

Chapter 1

Phase measurement in monochromatic interferometric techniques

1.1 Introduction

The human eye has evolved to produce images on the retina based on sensing the light generated or reflected by surrounding objects. To a great extent, photography evolved in the same way, mimicking the eye's ability to detect light and produce images of objects on a film or digital substrate. In a manner dependent on properties of the objects, interaction between the light and objects causes changes in the amplitude, wavelength and phase of the original lightwave. Changes in the amplitude arise from the transmission, absorption and scattering properties of objects, which on the whole give rise to the brightness change in the produced image. Changes in the transmitted spectrum cause a colour variation of the observed image. Although changes in the phase often carry important information, the human eye and conventional photographic equipment are not sensitive to them without special arrangements.

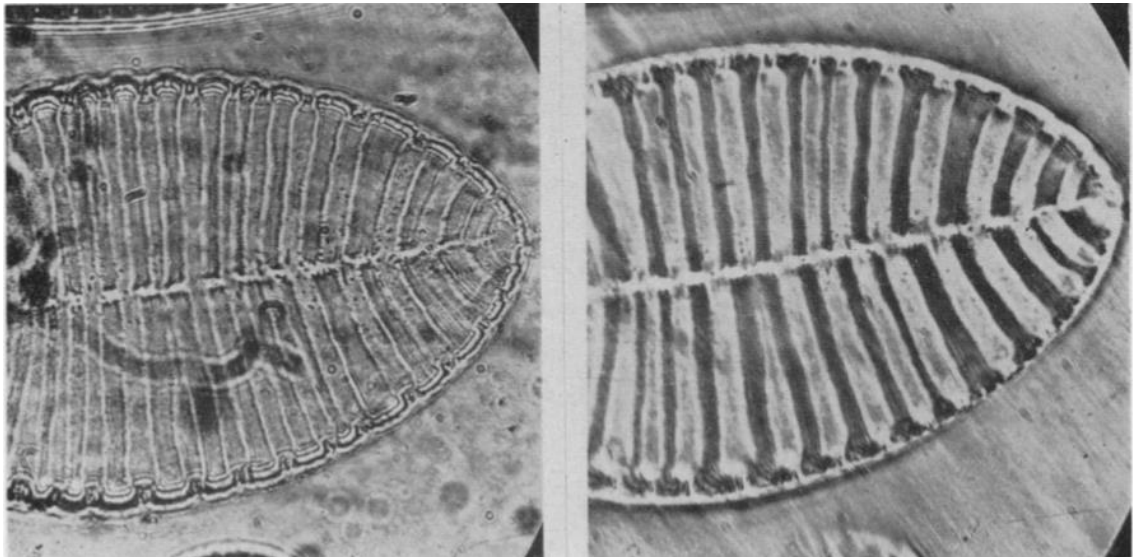


Fig. 1.1. Oldest phase contrast photomicrographs from Frits Zernike, taken in 1932. (Left): bright field image of a diatom. (Right): phase contrast image of the same diatom. (Reproduced from Zernike [1] by permission of the Science)

Phase contrast microscopy is an early optical microscopy technique that converts the phase shifts in light passing through a transparent specimen to brightness changes that can be seen by the eye or can be imaged by an instrument [1]. The technique is particularly important in biology. It enhances subcellular contrast and reveals many cellular structures that are either invisible with a bright field microscope or visible with a bright field microscope but only with additional efforts such as sample staining, which may kill cells. With the help of the phase contrast microscope, biologists are able to study living cells in their natural state without previously being killed, fixed, and stained. As a result, the dynamics of ongoing biological processes, depending on specimen, can be observed in high contrast [2].

Frits Zernike was awarded the Nobel Prize for Physics in 1953 for inventing the first phase contrast microscope. He added a phase plate [1] into a standard compound microscope to interfere the diffracted light passing through the specimen and the undiffracted background light. The degree of interference is manifest in the amplitude of the produced images, as shown in Fig. 1.1 and Fig. 1.2.

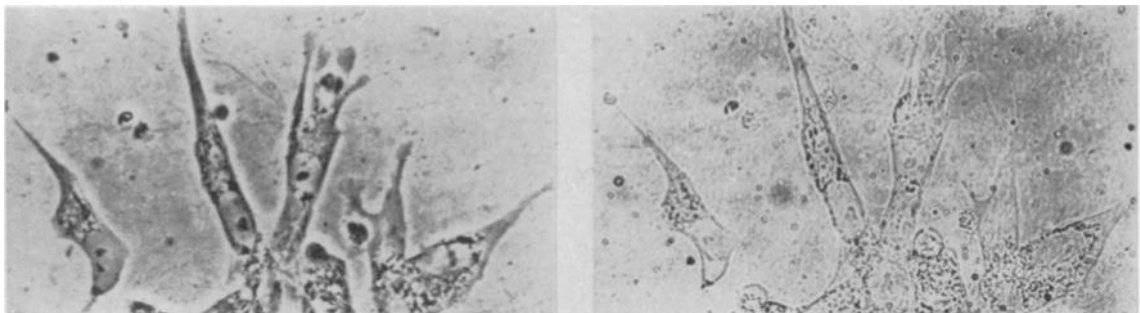


Fig. 1.2. (Left): living tissue culture with phase contrast. (Right): brightfield image of the same tissue culture. (Reproduced from Zernike [1] by permission of the Science)

The success of phase contrast microscope led to a number of phase imaging techniques, especially those employing interferometry. Interferometry is a powerful, although by no means the only technique [3] to retrieve the phase of coherent light wavefields. In an interferometer, the light beam is split into a reference beam and an object/sample beam. The object beam is scattered by the detected sample which then alters the amplitude, wavelength and phase of the object lightwave in a manner depending on the properties of the sample. The paths of the reference beam and the object beam are separate, but these two beams are coherent. When two beams are recombined, they interfere with each other, generating an interference signal that includes the sample information. The interference signal is recorded as an interferogram

at the output of the interferometer. Thus, the properties of the detected sample are encoded in the interferogram. Specifically, the amplitude variation of the object lightwave is related to the reflectivity of the detected sample, which is encoded in the interferometric amplitude of the interferogram. The wavelength and phase variation of the object lightwave is related to the movement status of the detected sample, which is encoded in the interferometric phase of the interferogram.

The interferometry employed to extract the interferometric phase variation is known as phase sensitive interferometry. The phase sensitive interferometry can be roughly grouped into two categories: monochromatic phase sensitive interferometry and broadband phase sensitive interferometry. Monochromatic interferometric techniques are able to reliably and quantitatively measure certain movements and the refractive index changes of the sample by detecting phase variations in the interference signal [4]. However, monochromatic techniques are not able to perform depth sectioning to distinguish phase content at different layers along the optical axis in the detected sample. In comparison, broadband interferometric techniques employ a broadband light source and the principles of optical coherence tomography (OCT), which are able to section and retrieve the phase, as well as the amplitude, from axial locations of interest and reject signals from other regions in the sample [4].

With an emphasis on the monochromatic phase sensitive interferometry, this chapter seeks to discuss the theory, with relevant mathematics, of a) retrieving the interferometric phase from the interferometric signal; and b) converting this phase variation into intensity variation which is a measurable parameter at the output (interferogram) of the interferometer.

In this chapter, the variation of the interferometric phase is discussed through three contributing factors: 1) the phase variation contributed by the optical path difference (OPD) between the detected sample and a reference mirror/reflector; 2) the phase variation contributed by changes in the optical index of the detected sample; and 3) the phase variation contributed by the Doppler shift induced by a moving sample. In addition, to show the significance of retrieving interferometric phase in the monochromatic interferometry, three monochromatic interferometric techniques and their applications in biological imaging are reviewed in this chapter.

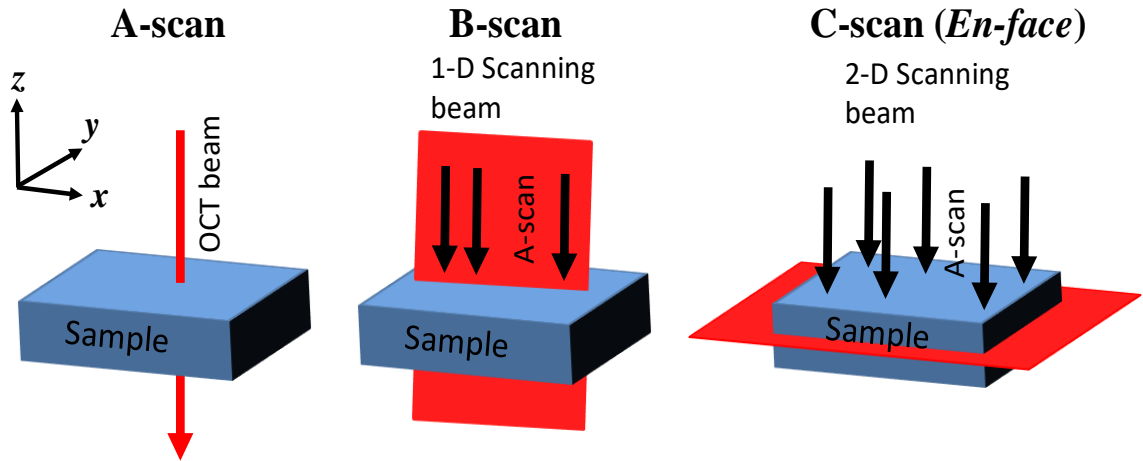


Fig. 1.3. Diagram showing three scanning schemes in OCT: A-scan, B-scan and *en-face* imaging.

As demonstrated in Fig. 1.3, in terms of the motion of the OCT beam, the detection and imaging in OCT can be classified into three types:

A-scan: An A-scan (also known as axial scan) provides axial reflectivity information along the direction of the OCT probing beam in the detected sample. In the **A-scan mode**, the OCT beam is fixed at a single lateral (x,y) location on the sample. The reflectivity of scatterers along z in the sample is measured simultaneously in an A-scan, resulting in an **A-scan profile** (1-D data array) showing as “reflectivity intensity against axial position” (such an example is the one in Fig. 6.3). The data acquisition rate in the A-scan mode is fast. For instance, the SS-OCT demonstrated in Chapter 5 completes the data acquisition in $4.1 \mu\text{s}$ for each A-scan.

B-scan: B-scan refers to cross-sectional imaging of the detected sample, in a plane containing the z axis. The B-scan is typically completed by employing a galvo-scanner mirror in the OCT setup. The scanner mirror sweeps the OCT beam across the detected sample. In this way, multiple A-scans are acquired transversally, generating a series of A-scan profiles (2-D data array). Mapping the 2-D array into grayscale values, a **B-scan image** is obtained. This B-scan image shows the reflectivity information of scatterers in the cross-sectional plane through the tissue.

C-scan (*en-face*): *en-face* images show the information from a particular layer in the sample perpendicular to the z axis. *En-face* imaging is typically carried out by employing a pair of galvo-scanner mirrors in the OCT setup. Using two scanners, the OCT beam is raster scanned in two dimensions across the

detected sample whilst acquiring A-scans. The data acquisition results in a 3-D data array representing a 3-D image of the detected sample. Then, the ***en-face* image** showing the reflectivity information of scatterers in the layer of interest in the sample can be sliced out from the 3-D image. In this thesis, ***en-face* OCT image** refers to *en-face* images mapped from amplitude values, and ***en-face* phase image** refers to *en-face* images mapped from phase values.

1.2 Phase retrieval in monochromatic interferometry

When discussing interference between monochromatic wavefields, it is usually convenient to represent the individual wavefield as a complex function:

$$E(\mathbf{r}, t) = \sqrt{I(\mathbf{r}, t)} \exp(-j2\pi vt) \exp(j\varphi(\mathbf{r})) \quad (1.1)$$

where \mathbf{r} is a vector representing the field location, t represents time, $I(\mathbf{r}, t)$ is the intensity, v is the frequency, and $\varphi(\mathbf{r})$ is the phase of the field. Represented in this way, a surface of constant $\varphi(\mathbf{r})$ describes the wavefront of the wavefield, while $\nabla\varphi(\mathbf{r})$ represents the propagation direction of the wavefield. This representation decouples the temporal variation $\exp(-j2\pi vt)$ and the spatial variation $\exp(j\varphi(\mathbf{r}))$ in the wavefield [4]. When two monochromatic waves of complex amplitudes:

$$E_R(\mathbf{r}, t) = \sqrt{I_R(\mathbf{r}, t)} \exp(-j2\pi vt) \exp(j\varphi_R(\mathbf{r})) \quad (1.2)$$

$$E_S(\mathbf{r}, t) = \sqrt{I_S(\mathbf{r}, t)} \exp(-j2\pi vt) \exp(j\varphi_S(\mathbf{r})) \quad (1.3)$$

are superposed, the interference results in a monochromatic wave with the same v and a complex amplitude E given by:

$$E(\mathbf{r}, t) = E_R(\mathbf{r}, t) + E_S(\mathbf{r}, t) \quad (1.4)$$

Monochromatic interferometric techniques employ a laser source to provide the monochromatic beam and an interferometer to split the beam into the reference beam $E_R(\mathbf{r}, t)$ and the sample beam $E_S(\mathbf{r}, t)$. Then, the detected intensity of the superposed signal can be expressed as:

$$I(\mathbf{r}, t) = |E(\mathbf{r}, t)|^2 = |E_R(\mathbf{r}, t) + E_S(\mathbf{r}, t)|^2$$

$$= I_R + I_S + \overline{E_R(\mathbf{r}, t)}E_S(\mathbf{r}, t) + E_R(\mathbf{r}, t)\overline{E_S(\mathbf{r}, t)} \quad (1.5)$$

where $I_R = |E_R(\mathbf{r}, t)|^2$ and $I_S = |E_S(\mathbf{r}, t)|^2$ are DC terms. The sample information is coded in $E_S(\mathbf{r}, t)$ in the AC terms:

$$\overline{E_R(\mathbf{r}, t)}E_S(\mathbf{r}, t) + E_R(\mathbf{r}, t)\overline{E_S(\mathbf{r}, t)} = 2\sqrt{I_R(\mathbf{r}, t)}\sqrt{I_S(\mathbf{r}, t)}\exp(j(\varphi_S(\mathbf{r}) - \varphi_R(\mathbf{r}))) \quad (1.6)$$

The interferometer detects Eq. (1.6) as:

$$I_{AC}(\mathbf{r}, t) = 2\sqrt{I_R(\mathbf{r}, t)}\sqrt{I_S(\mathbf{r}, t)}\cos(\varphi_S(\mathbf{r}) - \varphi_R(\mathbf{r})) \quad (1.7)$$

As seen in Eq. (1.7), using the interferometric technique, the variation of interferometric phase $\Delta\varphi = \varphi_S(\mathbf{r}) - \varphi_R(\mathbf{r})$ is converted into the intensity variation $I_{AC}(\mathbf{r}, t)$. The variation of the interferometric phase $\Delta\varphi$ can be caused by changes in the optical path length (OPL) of the detected sample, changes in the optical index of the sample material, and changes in the sample movements, as respectively discussed below.

1.2.1 Interferometric phase to optical path difference

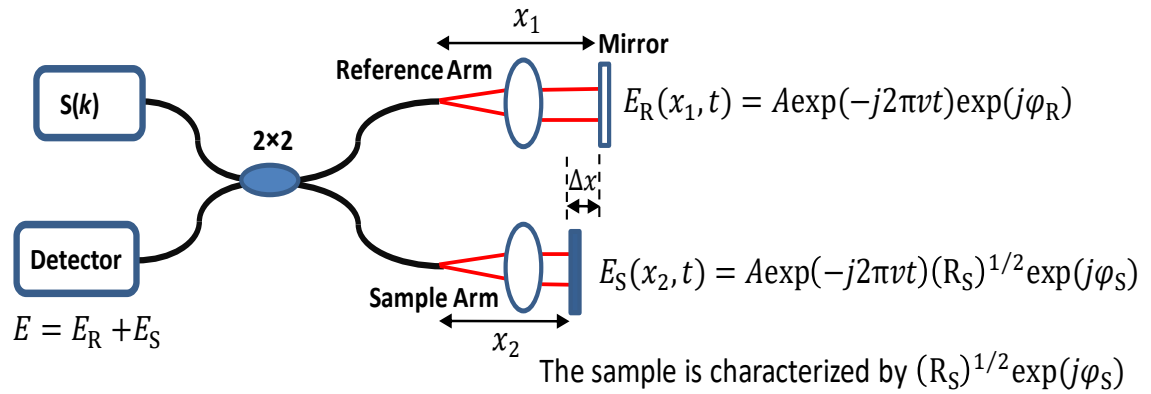


Fig. 1.4. 2x2 (50:50) Michelson Schematic. $S(k)$: a monochromatic laser source. $\Delta x = x_1 - x_2$: the OPD between the reference arm and the sample arm. v : optical frequency of the laser source. E_R and E_S : wavefields on surfaces of the reference mirror and the sample. φ_R : the phase on the reference mirror surface. φ_S : the phase on the sample surface. The sample surface is characterized by $(R_S)^{1/2} \exp(j\varphi_S)$.

The setup of a simplified Michelson interferometer used for studying the sample surface is illustrated in Fig. 1.4. As seen, the monochromatic light beam from the source $S(k)$ passes through a fibre based Michelson interferometer that splits the source beam into the reference arm and the sample arm.

It is assumed that beams in the reference arm and in the sample arm in Fig. 1.4 are propagating only in the direction of x in a medium with an uniform index of $n = 1$. The reference and sample arms have free space optical lengths of x_1 and x_2 respectively, and the OPD between two arms is $\Delta x = x_1 - x_2$. The field $E_R(x_1, t)$ at the detector from the reference arm is expressed as:

$$E_R(x_1, t) = A \exp(-j2\pi\nu t) \exp(j\varphi_R) \quad (1.8)$$

where A is the intensity of the beam on the mirror surface, ν is the optical frequency of the monochromatic beam, and φ_R is the phase on the mirror surface. As the fibre splitter has a ratio of 50:50, the field $E_S(x_2, t)$ at the detector from the sample arm is expressed as:

$$E_S(x_2, t) = A \exp(-j2\pi\nu t) (R_S)^{1/2} \exp(j\varphi_S) \quad (1.9)$$

where R_S is the reflectivity of the sample, and φ_S is the phase on the sample surface.

If the OPD (Δx) between two arms in Fig. 1.4 is the only factor influencing the interferometric phase, the phase difference $\Delta\varphi(x)$ between two wavefields reduces to:

$$\Delta\varphi(x) = \varphi_R - \varphi_S = 2k(x_1 - x_2) = 2k\Delta x \quad (1.10)$$

where k is the wavenumber ($k = 2\pi/\lambda$, and λ is the wavelength of the light in free space). Given by Eq. (1.7), the reflected light from both arms interfere at the detector, and the detected intensity of the AC signal I_{AC} in Eq. (1.7) is related to Δx :

$$I_{AC} \sim 2A^2 (R_S)^{1/2} \cos(\Delta\varphi(x)) = (R_S)^{1/2} \cos(2k\Delta x) \quad (1.11)$$

Given by Eq. (1.11), the interferometric intensity is related to the phase difference between two arms through the function $\cos(\Delta\varphi(x))$, which is then related to the OPD between two arms through the function $\cos(2k\Delta x)$. Thus, one insight that can be drawn from Eq. (1.11) is that the variation of the OPL value x_2 of the sample arm can be monitored by holding the length x_1 of the reference arm fixed, measuring the variation of the interferometric intensity I_{AC} , and then retrieving the interferometric phase $\Delta\varphi(x)$. In the end, the OPD variation (Δx) between the two arms can be calculated by dividing $\Delta\varphi(x)$ by $2k$, based on Eq. (1.10).

1.2.2 Interferometric phase to refractive index

The interferometric phase is also affected by the change in the optical index of the detected sample material. As shown in the setup configuration in Fig. 1.5, the free space path lengths of the reference arm and the sample arm are identical, but in the sample arm one can identify two distinct regions: the length of free space x , and the thickness of the sample x_n measured in free space. The samples imaged with low coherence techniques often consist of layers with different optical indices of refraction. In this case, the OPL of the reference arm is $x + x_n$, whereas the OPL of the sample arm is $x + n \cdot x_n$. The OPD between the two arms is:

$$\Delta x = x_n(n - 1) \quad (1.12)$$

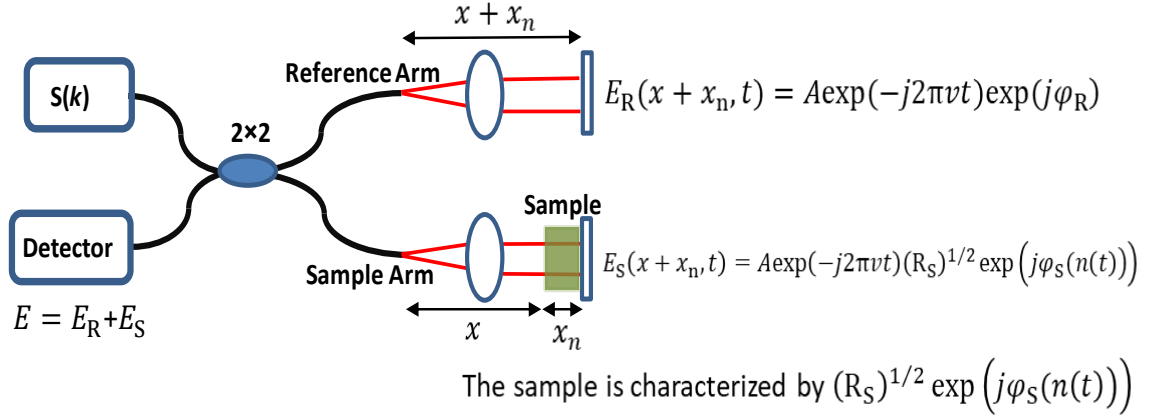


Fig. 1.5. 2×2 (50:50) Michelson Schematic. $S(k)$: a monochromatic source. The free space path lengths of the two arms are also assumed identical. The sample arm has two compartments: free space length x ; free space length x_n of the sample with a time-varying refractive index $n(t)$. v : optical frequency. E_R : wavefield reflected from the reference mirror surface. E_S : wavefield passed through the detected sample. The sample is characterized by the reflectivity R_S and the optical path induced phase function $\exp(j2k[x + x_n n(t)])$.

The wavefield arriving at the reference mirror surface and the wavefield that propagates once through the sample and arrives at the distal reflector surface (see Fig. 1.5) are expressed as:

$$E_R(x + x_n, t) = A \exp(-j2\pi vt) \exp(j\varphi_R) \quad (1.13)$$

$$E_S(x + x_n, t) = A \exp(-j2\pi vt) (R_S)^{1/2} \exp(j\varphi_S(n(t))) \quad (1.14)$$

Because of the return paths through the interferometer, the calculation of the phase difference between the two wavefields at the detector requires a doubling of OPD Δx in

Eq. (1.12). Hence the phase difference $\Delta\varphi$ is related to the refractive index n of the sample in the following way:

$$\Delta\varphi(n(t)) = \varphi_S(n(t)) - \varphi_R = 2kx_n(n(t) - 1) \quad (1.15)$$

Given by Eq. (1.7), reflected light from the two arms interfering at the detector gives rise to an AC signal of intensity I_{AC} , which is related to n :

$$I_{AC} \sim 2A^2(R_S)^{1/2} \cos(\Delta\varphi(n(t))) = (R_S)^{1/2} \cos(2kx_n[n - 1]) \quad (1.16)$$

As seen in Eq. (1.16), the refractive index variation $n(t)$ can be measured by retrieving the interferometric phase $\Delta\varphi(n(t))$ from the interferogram.

1.2.3 Interferometric phase to Doppler shift

Just as changes of the OPL and the optical index can be measured by retrieving the interferometric phase in the interferometric signal, sample motion of the order of sub-wavelength can likewise be measured by retrieving the interferometric phase.

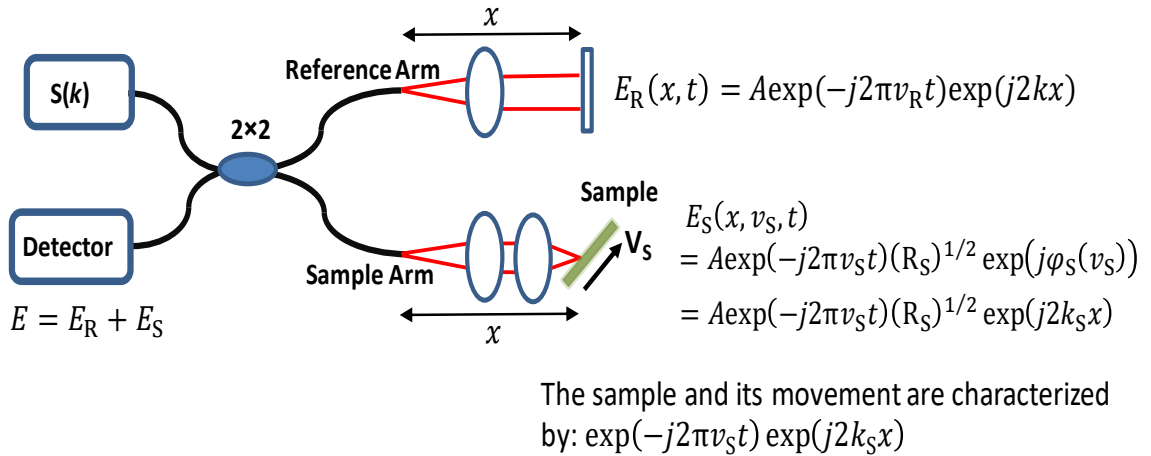


Fig. 1.6 2×2 (50:50) Michelson Schematic. $S(k)$: a monochromatic source. The free space path length of both arms are identical. The moving sample has a velocity of V_S . The field frequency ν_R and the wavenumber k on the reference mirror surface is constant, whereas the field frequency ν_S and the wavenumber k_S on the sample surface are changed by the sample movement. E_R and E_S : wavefields on surfaces of the reference mirror and the detected sample. The sample and its motion are characterized by the reflectivity R_S and the motion induced phase variation $\exp(-j2\pi v_S t) \exp(j2k_S x)$.

As shown in Fig. 1.6, when the monochromatic beam is incident on a sample moving with a velocity of V_S , the wavefield frequency of the light returned from the

sample is varied by the motion of the sample. The motion creates a Doppler shift that leads to a varying wavefield frequency ν_S and a varying wavenumber k_S . As the reference mirror in Fig. 1.6 is stationary, the field frequency ν_R and the wavenumber k reflected from the reference mirror surface are constant along the beam. Both arms have the identical optical lengths of x , the fields at the detector from the reference arm and from the sample arm can be expressed as:

$$E_R(x, t) = A \exp(-j2\pi\nu_R t) \exp(j\phi_R) = A \exp(-j2\pi\nu_R t) \exp(j2kx) \quad (1.17)$$

$$\begin{aligned} E_S(x, \nu_S, t) &= A \exp(-j2\pi\nu_S t) (R_S)^{1/2} \exp(j\phi_S(\nu_S)) \\ &= A \exp(-j2\pi\nu_S t) (R_S)^{1/2} \exp[j(k + k_S)x] \end{aligned} \quad (1.18)$$

Given by Eq. (1.7), the reflected lights from both arms interfere at the detector, and the detected intensity of AC signal I_{AC} is related to ν_S and k_S :

$$I_{AC} \sim (R_S)^{1/2} \cos(2\Delta k - 2\pi\Delta\nu) \quad (1.19)$$

where $\Delta k = k_S - k$ is the wavenumber difference, and $\Delta\nu = \nu_S - \nu_R$ is the optical frequency difference between the wavefields respectively reflected from the stationary reference mirror and the moving sample.

As seen in Eq. (1.18) and Eq. (1.19), the Doppler shift which the moving sample gives rise to can be measured by retrieving the interferometric phase from the interferometric intensity I_{AC} . It should be noted that the effects of OPD variation, changing optical index and Doppler shifting are inseparable in a phase sensitive interferometry system. For instance, when measuring photothermal response of gold nano-particles, changes in the refractive index can happen as a result of localised heating which also induces variations of the OPD. Both factors contribute to the variation of the interferometric phase, but it is impossible to distinguish the relative contribution of each factor.

Based on the theory covered in this section, phase sensitive interferometric techniques employing a monochromatic light source can be used to study the morphology, refractive index and motion of the detected sample. Unlike interferometric techniques that employ broadband light sources, monochromatic interferometric techniques are not able to perform depth sectioning and coherence gating along the

probing beam in the sample. Nonetheless, their capabilities to measure cell volumes and cell dynamics have achieved constructive results [5-10], as discussed below.

1.3 Review of monochromatic interferometric techniques

Although phase contrast microscopy provides high contrast intensity images (Fig. 1.2) of transparent biological structures without previous sample preparation, the phase information provided is qualitative. As discussed in section 1.2, monochromatic interferometry is capable of performing quantitative phase measurements. This section reviews applications of monochromatic interferometry in biological investigations of morphology and dynamics of transparent biological samples. The reviewed techniques include a monochromatic Mach-Zehnder interferometer based system demonstrated by Farinas and Verkman in 1996 for studying the volume of epithelial cells [5]; and a Hilbert phase microscope system demonstrated by M.S. Feld and colleagues in 2005 for investigating fast dynamics of epithelial cells [6],[7].

In addition, this section reviews a laser interference microscopy technique providing qualitative phase measurements [11]-[13]. Although this technique is not able to perform quantitative or dynamic phase measurements, the unique method it employed to simulate the phase measurement is able to provide morphological information of the studied sample.

1.3.1 Monochromatic phase interferometry in cell volume measurement

Transport of water through cell membranes is often done through a class of proteins called “aquaporins” or “water channels”. They are important and widely expressed in epithelial and endothelial tissues that participate in directional fluid transport. For instance, human kidney tissue has the aquaporin-2 water channel, whose lack of function is associated with nephrogenic diabetes insipidus [8]. The transporting properties of water channel proteins to water and other solutes can be analysed by measuring the water permeability P_f of the cell plasma membrane. P_f is determined by measuring the relative cell volume in response to osmotic gradients [9]. A semi-quantitative approach using light scattering has been used to infer cell volume changes in suspended cells [14][15]. However, this approach is suitable for certain cell types in which the intensity of the scattered light is sensitive to the cell volume. Another method, based on measuring the concentration of cytoplasmic fluorophores, has been developed to measure P_f of adherent cells [15]. By measuring the concentration of fluorophores,

the relative cell volume of these cells can be inferred from the inverse of the fluorophore concentration. In this method [15], the fluorophore concentration is estimated by using a confocal microscope to sample the fluorescence signal from a restricted volume. Another approach detecting the fluorophore concentration is based on total internal reflection (TIR) microfluorimetry that generates steady-state fluorescence signal [16]. Although the TIR method is quantitative, it is capable of measuring relative cell volume only of cells immobilized on a homogeneous transparent substrate. The measurements in non-adherent cell sheets is not achievable by the TIR method [5].

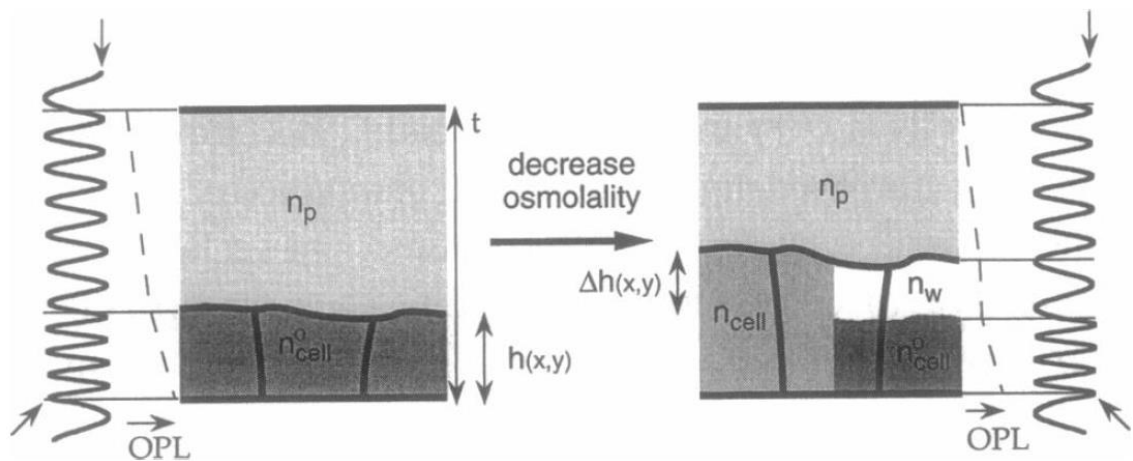


Fig. 1.6 Schematic layers of the perfusate and the cell. Images are showing that the OPL depends on the cell volume. Left: before the cell swelling. Right: after the cell swelling. n_p : refractive index of the perfusate. n_{cell}^0 : refractive index of the cell. n_w : refractive index of the water. $\Delta h(x,y)$: an increase in cell height. The difference in OPL created by the cell swelling results in a difference in the phase of the wavefield passing through the sample. (Reproduced from Farinas and Verkman [5] by permission of the Biophysical Journal)

In 1996, Javier Farinas and Alan Verkman applied interferometry to quantify the cell shape and the water permeability P_f in both adherent and non-adherent cell sheets [5]. The principle of the method is illustrated in Fig. 1.6 which shows the lightwave passing through the perfusate with the refractive index of n_p and then through the cell layer with the refractive index of n_{cell}^0 . As discussed in section 1.2.2, the wavefield passing through the sample experiences a phase shift. The amount of the shift is determined by the sum of the OPL in each medium in the sample. Thus, a cell volume change creates a change in the geometric length of each medium and thus a change in the cell refractive index n_{cell}^0 , resulting in a change in the total OPL.

From left to right in Fig. 1.6, a swollen cell creates a water channel with a refractive index of n_w . The difference in OPL between before (left) and after (right) the

cell swelling is the sum of the relative geometric length difference of each layer. Thus, the phase of the light passing through the sample is related to the cell volume, and the change in phase is a measure of the change in the cell volume.

Farinas and Verkman performed full-field monochromatic Mach-Zehnder interferometry on a single layer of epithelial cells. As illustrated in Fig. 1.7, a 5 mW diode laser emitting at 676 nm is employed as the monochromatic source. The cell layer is positioned in a flow chamber in the sample beam path, and a stack of glass microscope slides that match the OPL of the flow chamber are placed in the reference beam path. The OPL difference between two paths can be adjusted by tilting two plates in two paths. The two plates are also used to adjust the width between interference fringes in Fig. 1.7.A. A CCD camera is used to record the interference pattern.

To test the operating performance of the Mach-Zehnder interferometry microscope, measurements were firstly made on a test sample which was a glass slide sample consisting of a trapezoidal trough. Images in 1.7.A and Fig. 1.7.B present the interference pattern obtained from the testing sample. Images in Fig. 1.7.C and Fig. 1.7.D display the OPL map of the test sample.

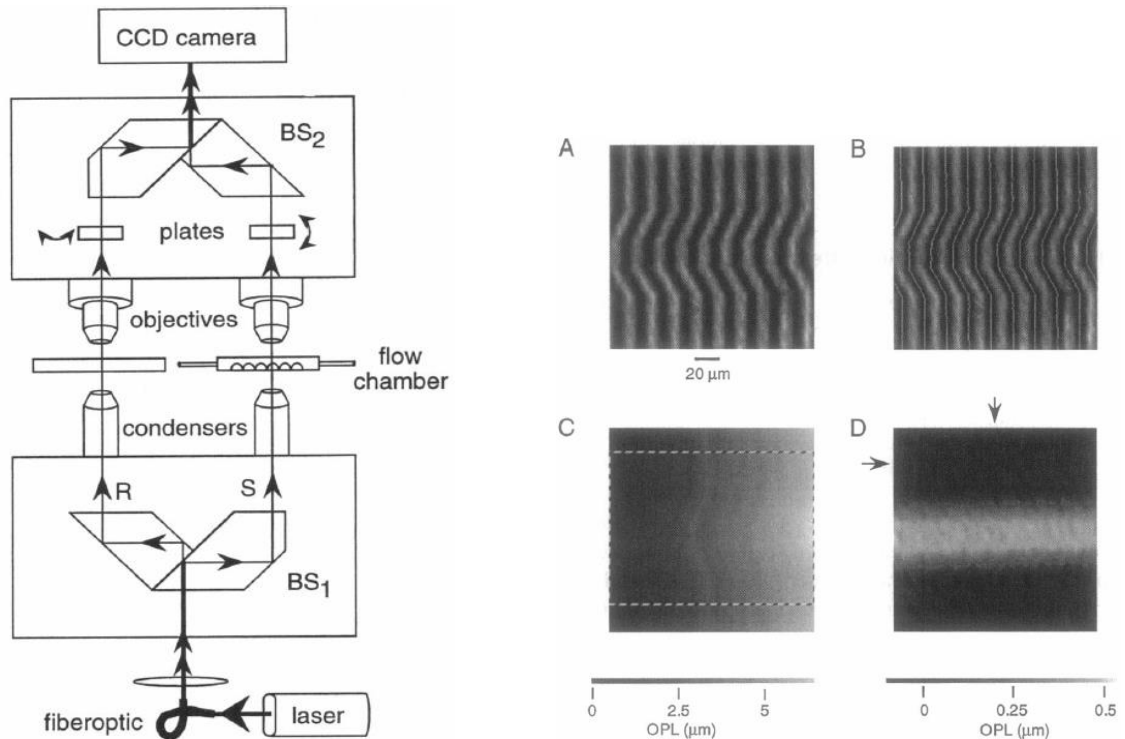


Fig. 1.7. Schematic of the full field Mach-Zehnder interferometry microscope developed by Farinas and Verkman. The parallel plates in two beam paths are used to adjust the width of interference fringes in (A) and (B). (A-D) were obtained from a test glass sample consisting of a trapezoidal trough. (A): interference fringes of the test sample. The image processing (B-C) is performed by seeking and identifying the minimum intensity between adjacent interference fringes. The regions with minimum intensity were indicated as the thin white lines in (B). Then, the local normalization between these white lines were performed. (C): the region (outside the dashed box) with no sample feature is selected as a common-mode background to be subtracted from the whole image of (C), resulting in the image (D) of the studied sample. (D): OPL map of the testing trapezoidal trough sample. (Reproduced from Farinas and Verkman [5] by permission of the Biophysical Journal)

The drawback of this technique is the complex procedure to quantitatively measure the interferometric phase. Firstly, because of the lack of a reference phase for removing the 2π ambiguity, a local normalization operation was performed between successive interference fringes in Fig. 1.7.A. To this end, a designed image analysis algorithm identified the lines of minimum intensity (shown as white lines in Fig. 1.7.B) and then performed the local normalization operation between these white lines. The obtained OPL map in Fig. 1.7.C presents the OPL information of the test trapezoidal trough sample. Secondly, to remove the effect from a non-uniform illumination, the region with no sample feature in the OPL map had to be identified (in Fig. 1.7.C, this region corresponds to the area outside the dashed box). This area was treated as a common-mode background which was then subtracted from the OPL map in Fig. 1.7.C. The OPL

map obtained through this algorithm is presented in Fig. 1.7.D, displaying the height features of the trapezoidal trough sample under test.

Another drawback of this technique is that the monochromatic interferometer was unable to coherently gate the phase information at the perfusate/cell interface from other layers. Thus, only the cell layer on the surface can be studied using the full field Mach-Zehnder interferometry microscope.

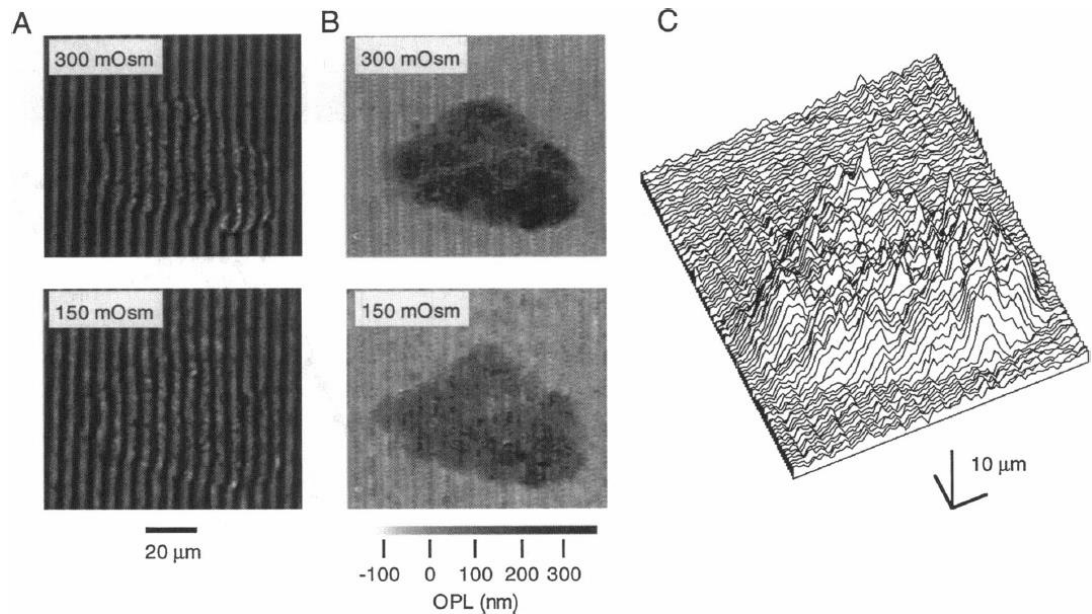


Fig. 1.8 Results taken from a flow chamber sample. (A): interference images of Madin Darby Canine Kidney (MDCK) cells perfused with 300 and 500 mOsm solutions. (B): OPL maps calculated from (A). (C): cell height profile calculated from the OPL map of the 300 mOsm solution. (Reproduced from Farinas and Verkman [5] by permission of the Biophysical Journal)

After the full field Mach-Zehnder interferometry microscope was tested by performing phase measurements on the test trapezoidal trough sample, the flow chamber sample was placed back in the sample path in Fig. 1.7. Cell volumes were measured on cells bathed in 300 mOsm and 150 mOsm perfusates. Interference images and OPL maps obtained in the way described above are presented in Fig. 1.8.A and Fig. 1.8.B respectively.

As demonstrated in Fig. 1.6, a swollen cell created a water channel around it. The variation of the cell volume, caused by the swelling, was measured by the deviations of the interference fringes in Fig. 1.8.A which was then used to calculate the OPL maps in Fig. 1.8.B. The height profile in Fig. 1.8.C was calculated from the 300 mOsm OPL map in Fig. 1.8.B.

The results presented in this section indicate that by quantitatively retrieving the interferometric phase, the cell volume change could be measured in the full-field monochromatic Mach-Zehnder interferometer. However, due to the camera acquisition rate and the time consuming processes of image processing, the operating speed of this setup is as slow as 1 Hz [5]. Consequently, for this technique to be suitable for measuring fast dynamics of cells, a faster operating speed is required.

The imaging speed of the monochromatic interferometry was improved by employing high-speed CCD cameras to record interference images and by employing Hilbert transformation to retrieve the interferometric phase. The technique is discussed below.

1.3.2 Monochromatic phase interferometry in cell dynamics

In 2005, Gabriel Popescu et.al. developed a Hilbert phase microscopy (HPM) technique which permits acquisition of full field quantitative phase images at hundreds Hz frame rates [6],[7].

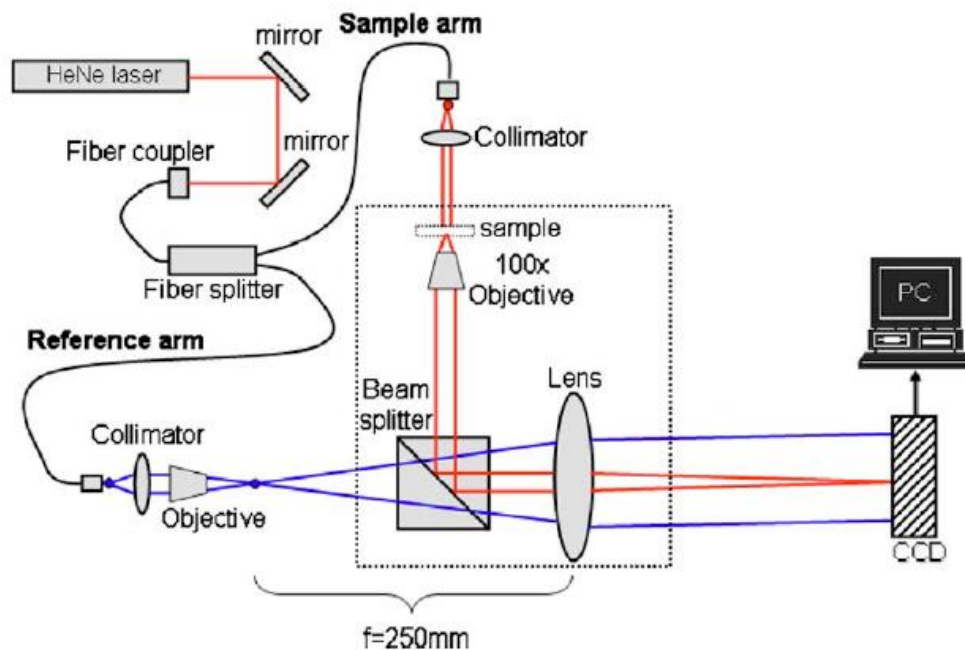


Fig. 1.9 Setup configuration of the HPM. HeNe laser centred at 633 nm is coupled into a single mode fibre coupler that launches collimated beams from both outputs. The reference beam is slightly tilted with respect to the sample beam. The interference pattern is recorded by the CCD camera. (Reproduced from Popescu et al. [7] by permission of Prof Popescu and the International Society for Optics and Photonics)

The experimental setup is illustrated in Fig. 1.9. In contrast with the setup in Fig. 1.7, the two parallel plates in Fig. 1.7 are removed (Fig. 1.9), and the width of

interference fringes in HPM was adjusted by tilting angle between the reference beam and sample beam. To guarantee the overlap of two beams, the reference beam was expanded by an objective in the reference arm. A CCD camera was positioned in the Fourier plane of the final lens to record the interference pattern. Since the phase imaging rate is limited only by the CCD, a fast acquisition rate enables HPM to quantify cell dynamic processes on a millisecond scale. HPM employed the Hilbert transform to extend the recorded interference pattern into a complex plane containing the phase information.

To test the operating performance of the HPM system, quantitative phase measurements were firstly made to display the height of an optical fibre in a cross section perpendicular to its axis. To generate the phase image, the following steps are conducted. Firstly, the interference pattern (acquired by the CCD camera) was Fourier transformed and high-pass filtered. Then, inverse Fourier transform was performed to the remaining frequency components, generating the sinusoidal fringes. Secondly, the Hilbert transform was performed to the sinusoidal fringes, obtaining a complex two-dimensional pattern containing the unique phase information of the tested fibre. Then, the phase information was retrieved followed by a phase unwrapping process. Unlike the method used in section 1.3.1 to remove the background common-mode phase, where a region with no subject feature was manually selected and subtracted from the whole image, the linear phase components obtained from the phase unwrapping process were subtracted from the unwrapped phase, resulting a phase image showing the features of the studied fibre sample [6].

After the system was tested, quantitative phase measurements were made to red blood cells from a blood smear sample. Steps demonstrated above were duplicated. In the produced image, each individual cell (6-8 μm in diameter) and the agglomeration of cells are identifiable.

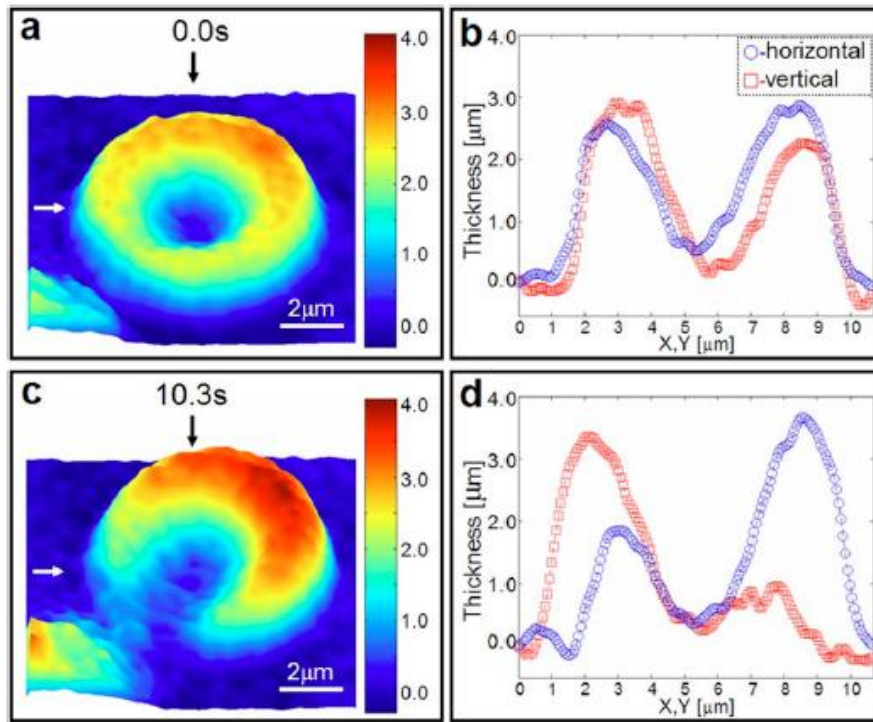


Fig. 1.10 Quantitative phase measurements of the shape transformation of a single blood cell at a time interval of 10.3 s, with an imaging rate of 10.3 ms / image. (b) and (d): transverse profiles indicated by the arrows in (a) and (c) (Reproduced from Popescu et al. [7] by permission of Prof Popescu and the International Society for Optics and Photonics)

HPM took 10.3 ms to generate a phase image. The high operating speed of the HPM system made it capable of studying fast dynamics of blood cells [7]. Fig. 1.10 presents the significant dynamic shape transformation of a single blood cell after a time interval of 10.3 s. The images were acquired 10.3 ms apart, generating 1000 images in 10.3 s. Fig. 1.10.a and Fig. 1.10.c represent the first and the last frames in the 1000-frame image set. With a nanometre accuracy, Fig. 1.10.b and Fig. 1.10.d show the thickness profiles indicated by the arrows in Fig. 1.10.a and Fig. 1.10.c. As seen, a rapid asymmetric shape change is easily quantified by the HPM measurement.

The results presented in this section indicate that the HPM technique has the ability to obtain quantitative phase images of cells, showing their shapes, volumes, and the mostly importantly, dynamics. Compared with the technique developed by Farinas and Verkman (section 1.3.1), the HPM technique employed a faster CCD camera for interference pattern recording. Hence, it consumed significantly less time on quantitative phase retrieval, which fulfilled the requirement of dynamic imaging. Since HPM simplified the setup and required fewer procedures in the manual adjustment, it achieved better accuracy than the technique developed by Farinas and Verkman.

However, the monochromatic laser source in HPM did not allow depth resolved phase measurement below the surface of the sample.

1.3.3 Monochromatic phase interferometry in nerve fibre morphology

On the basis of Eq. (1.8) and the principles of phase measurements in the interferometry discussed in section 1.2, phase profiles of the studied sample reconstructed from the interference patterns were described in sections 1.3.1 and 1.3.2. Two techniques employed different algorithms on the interference patterns to retrieve the interferometric phase. The retrieved phase from these methods was doubtful at some positions on the studied sample, especially when the measured intensity was below the system noise level. On such positions, the obtained information was inaccurate [11],[12].

To address this drawback, Amphora Laboratories developed a phase-modulation laser interference microscope (MIM) that employed a pixel-wise (one pixel at a time) phase profile reconstruction algorithm to obtain the phase information of each pixel on the detector independently [11],[12]. Although the MIM technique was not able to perform the quantitative phase measurement, it reconstructed the morphological profile of the studied sample by a method that simulated the phase measurement.

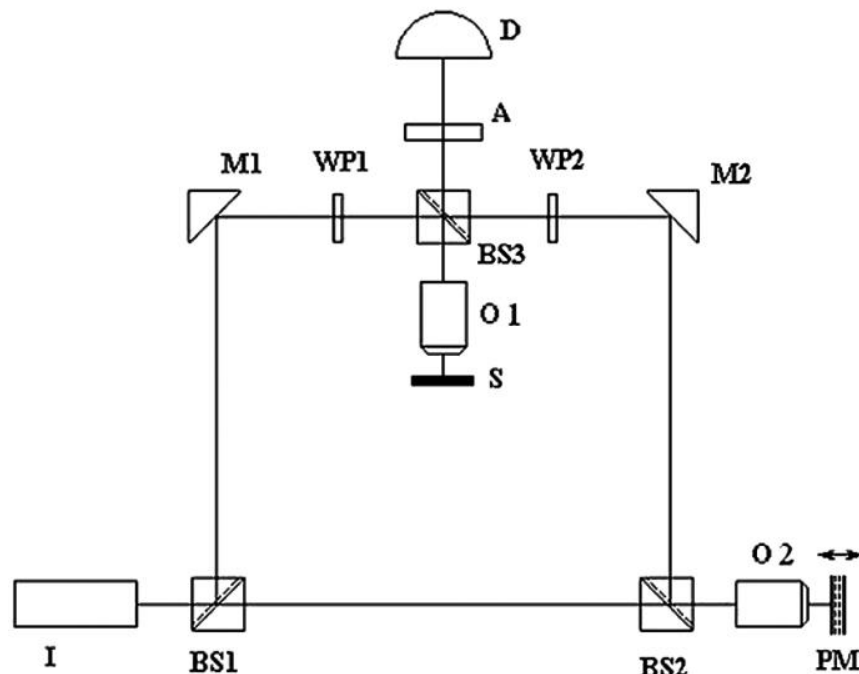


Fig. 1.11 Configuration of the phase-modulation laser interference microscope (MIM). Light source (I). Polarizing beam splitter (BS1, BS2). Detector (D). Phase plates (WP1, WP2). Analyzer (A). Beam splitters (BS1, BS2). Mirrors (M1, M2). Objective (O1, O2). Phase modulation mirror (PM). Sample (S). (Reproduced from Andreev et al. [12] by permission of the Springer Nature)

As illustrated in Fig. 1.11, the MIM setup is a modified Mach-Zehnder interferometer. The HeNe laser beam (I) is divided by the beam splitter (PBS) into two beams. In the reference arm, the beam is reflected from the reference phase modulation mirror (PM). The position of the phase modulation mirror (PM) is precisely controlled by a piezoelectric crystal. The phase status of two beams can be adjusted independently by two phase plates (WP1) and (WP2). The interference image is recorded by the CMOS photo-sensor plate (D) that consists of 1024×1024 pixels.

The PM modulated the phase of the reference beam by creating tiny displacements in the reference arm. At the same time, the interferometric phase varied on the CMOS detector. As discussed in 1.2, the interferometric phase $\Delta\varphi = \varphi_S(\mathbf{r}) - \varphi_R(\mathbf{r})$ in Eq. (1.8) can be obtained by measuring the intensity of the AC signal in the interference pattern which is normally by the CCD camera in the interferometer. Without using this approach, the MIM measured the phase of the object beam separately on every pixel. Specifically, the intensity of the interference signal on each pixel of the CMOS detector was measured as a function of the position of the PM. The intensity on each pixel varied with the moving PM. The PM position was chosen and fixed when the variation rate of the intensity reached the maximum. Parking the PM at this position, the OPL value of the reference arm was used to reconstruct the image displaying the height of a position on the sample at the corresponding pixel of the CMOS. This procedure was made separately for each pixel of the camera (1024×1024 pixels). One of the pixels was chosen as a reference, the height of which was set to zero, and the heights of the rest pixels were compared with that of the reference pixel. As a result, the reconstructed 2D image displayed a distribution of heights that simulating the OPL maps associated with the geometrical profile of the studied sample. Since the PM needed 20 ms to execute the movement and settle for each pixel, it took 20 s to reconstruct an image of 100×100 pixels. Thus, the MIM is not suitable for dynamic measurement.

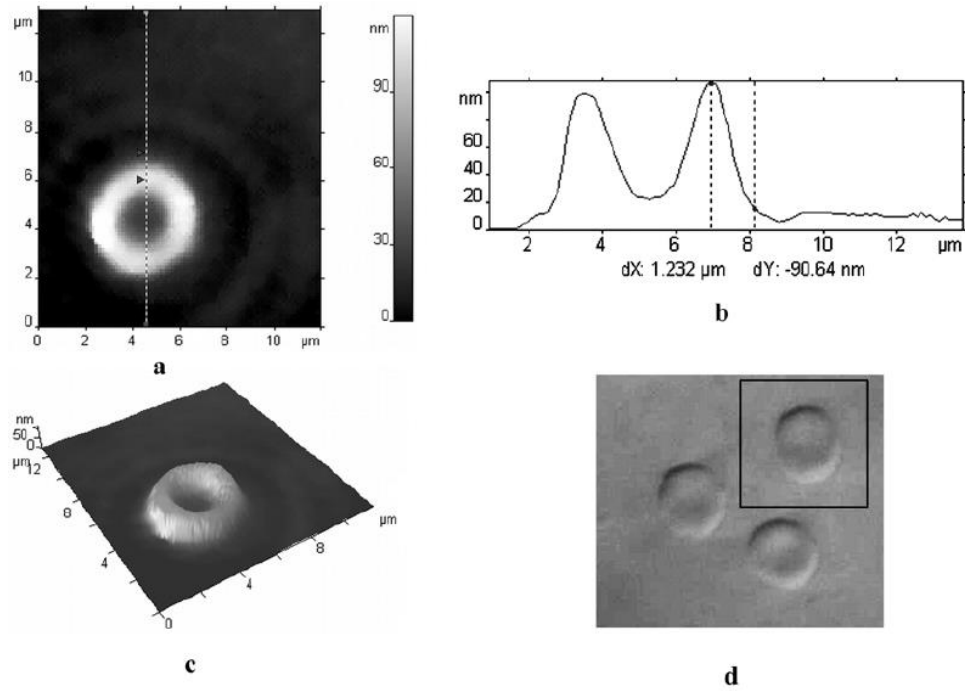


Fig. 1.12 A human erythrocyte cell. (a): Constructed image using MIM. (b): Transverse profile indicated by the dot line in (a). (c): 3D representation. (d) snapshot in white light. (Reproduced from Andreev et al. [12] by permission of the Springer Nature)

Since the MIM simulates the phase measurement instead of directly measuring the phase, it allows one to reveal general morphology information of the studied sample but does not provide strict quantitative information. An example of the MIM application in imaging the human erythrocyte cell is presented in Fig. 1.12. As seen in Fig. 1.12.b, the measured thickness of the erythrocyte cell is 80-110 nm which is far from the typical value of 2 - 2.5 μm. Nevertheless, the constructed image in Fig. 1.12.a reveals the morphology of the erythrocyte cell, and the measured disk diameter matches the actual value of 6.2-8.2 μm.

In another MIM configuration [13], the beam splitter (BS1) is replaced by a half-wave plate and a polarizing beam splitter. Compared with the setup in Fig. 1.12 and the techniques discussed in sections 1.3.1 and 1.3.2, the existence of the half wave plate and polarizing beam splitter gives the MIM technique the capability to control the ratio of beam intensities in the two arms. As discussed above, the measurement of the MIM is qualitative as it avoids direct and actual phase measurements. Although it doesn't provide quantitative phase measurements as the other two techniques do, its unique operating mechanism realizes the simulation of phase measurements, which can be used to study the morphology of the detected sample.

1.4 Discussion and conclusion

Besides the techniques discussed in section 1.3, some other techniques are being widely used nowadays performing phase detection and imaging. Common-path diffraction optical tomography (cDOT) is a monochromatic interferometric technique capable of quantitative phase imaging. It has been used for imaging both 3D structures and dynamics of biological cells [99]. cDOT is a combination of common-path laser interferometric microscopy and optical diffraction tomography. The laser interferometric microscopy is able to measure the 2D dynamic phase images of the studied sample. The common-path configuration minimizes the influence to the phase signal given by the environment disturbance, such as air flow. The 3D optical diffraction tomography image is structured by combining multiple 2D phase images with various illumination angles. The varying angle is achieved by scanning the laser beam in the laser interferometric microscope over the studied sample, and then the sample diffracted light is de-scanned before being detected by the detector.

Compared with the techniques discussed in section 1.3, cDOT is able to perform 3D phase imaging which is then can be used to produce axial cross-section (tomography) image of the studied sample. However, the image depth (tens of micrometres) of cDOT is much smaller than that of phase sensitive OCT (a few millimetres), as will be discussed in the following chapter. This is because the penetration depth of near-infrared light, in tissue, used in OCT in tissue is deeper than that of the visible light used in cDOT. Nevertheless, the lateral resolution of cDOT is better than that of OCT due to the shorter wavelength.

Transmission optical coherence tomography (transmission OCT) is a broadband interferometric technique. It has been used for measure optical material properties, including refractive index dispersion and attenuation coefficients, of turbid media (glasses, demineralised water, glucose solutions and silica particle suspensions) [100]. OCT has the nature to record the interference signal in frequency domain, and the interference signal can also be converted into time domain. To measure the refractive index dispersion, Transmission OCT employs Hilbert transform to the interferogram to retrieve the interferometric phase in frequency domain. Whereas the attenuation coefficients are measured by performing FFT to the interferogram to convert the signal into time domain, and then retrieving the phase information.

Although Transmission OCT is proved to be able to measure optical material properties [100], employing the light (1050 nm) in the therapeutic window (650 nm to 1350 nm) is not the best choice to study the transparent material since a longer wavelength results in a worse resolution. Thus, to improve the resolution and the sensitivity of Transmission OCT, a light source in the visible range should be used. Nevertheless, Transmission OCT is cost saving as it performs interferometric phase analysis in different domain (time domain and frequency domain) to measure different optical properties of material. Compared with it, since OCT has the nature to perform depth resolved measurements in biological tissue, the phase sensitive OCT has a great potential in biomedical applications rather than measuring optical material, as will be discussed in the following chapter.

This chapter provides a brief description of the significance of phase resolved measurements. When lightwaves travel through media, the interaction between the light and the media causes the wave amplitude, the optical frequency and the phase to change in a manner dependent on the properties of the medium. Although phase variations often carry important information, the photographic equipment and the human eye are not sensitive to the phase variation without special arrangements.

Zernike's early phase contrast microscope was an initial attempt at retrieving phase information of microscope samples by qualitatively enhancing subcellular details in unstained cells. However, due to the limitations of the time, the phase contrast microscope is not able to retrieve quantitative phase values.

Monochromatic phase interferometry is a technology for quantitative phase measurements. It encodes the fine information of the morphology of the detected sample into the interferometric signal by interfering the sample beam with a separate reference beam. The beams are mutually coherent. Since the generated interferogram is complex in nature, the interferometric phase value can be retrieved. In addition to enhancing the image contrast, phase sensitive monochromatic interferometry can also be used to measure the OPL variation, the refractive index variation and the nano-motion of the studied object. Details of the mathematical basis are given in this chapter to demonstrate how these variations can be coded in the interferometric phase, and how the interferometric phase variation can be converted to the interference intensity variation that can be detected and measured at the output of the interferometer.

Due to their high measurement sensitivity, techniques employing monochromatic phase interferometry have gained momentum in biological applications. This chapter reviews the applications of the phase sensitive monochromatic interferometry in the quantitative imaging of cellular morphology and dynamics. In order to perform real time imaging, a high speed CCD camera should be employed to perform the measurement. Moreover, sophisticated data processing procedures are needed to remove the background noise and to convert the phase values into images especially when the retrieved phase values are wrapped within 2π . Furthermore, although the phase measurement can be simulated, without performing the direct phase measurement, the obtained phase values can only be used to generate qualitative morphology images, without providing a quantitative outcome.

Monochromatic phase interferometry is not able to perform depth resolved phase measurements. Thus, the technique is not suitable for multi-layered samples since only the surface of the sample can be detected. For multi-layer samples, variations in the wave properties resulting from reflection both at the surface of the sample and at the layer boundaries inside the sample are recorded in the same interference signal, resulting in an overlap of phase information from all layers. The mixed information can be resolved by phase sensitive Optical Coherence Tomography technology that employs broadband and low coherent light sources to perform coherence gating and depth resolved phase measurements.

Chapter 2

Phase measurement in frequency domain optical coherence tomography

2.1 Introduction

The development of high resolution optical imaging of biological tissue received a considerable boost with the advent of Optical Coherence Tomography (OCT), which for the first time allowed unambiguous measurement of layer depths and thicknesses *in vivo*. Low coherence interferometry (essentially one-dimensional OCT) was initially applied to ophthalmology for *in vivo* measurement of eye axial length in 1988 [17]. Three years later, with the addition of lateral scanning capabilities, *in vivo* optical cross sectional images of the human retina and optic disk were obtained [18]. The depth slicing capability of the new technique, now capable of imaging whole layers within tissue, justified the use of “tomography” and so Optical Coherence Tomography emerged. OCT is fundamentally low coherence interferometry employing light with low temporal coherence but high spatial coherence (i.e., a broad range of optical frequencies), such as superluminescent diodes, ultrashort pulsed lasers and supercontinuum lasers. Unlike the monochromatic interferometry discussed in Chapter 1, the use of broad bandwidth light sources allows OCT to perform depth-resolved measurement along the optical axis in the sample for reasons that will be covered in this chapter.

The first OCT approach demonstrated historically is referred to as time-domain OCT (TD-OCT). It encodes backscattering signals directly in the time domain by axial scanning a reference mirror in the reference arm of the interferometer. Due to the movement of the reference mirror, the TD-OCT technique inherently suffers from a high noise level and a limited data acquisition speed which is determined by the scanning speed of the reference mirror [19].

The more advanced OCT approach is referred to as frequency-domain OCT (FD-OCT). It encodes signals in the frequency domain without the need for moving the reference mirror. FD-OCT can be implemented in two ways: spectral-domain OCT (SD-OCT) employing a broadband light source and a spectrometer; and swept-source

OCT (SS-OCT) employing a swept laser source and a photodetector. Since swept sources in SS-OCT that are commercially available today tend to be mostly in the wavelength range ($\lambda = 1 - 1.3 \mu\text{m}$), SS-OCT systems on the whole have lower axial resolution but deeper imaging depth compared with SD-OCT [19]-[21].

Both SS-OCT and SD-OCT record the interference signal and generate the interferogram in the frequency domain. A complex Fourier-transform (FFT) is performed on the interferogram, obtaining a one dimensional depth reflectivity profile (A-scan) of the sample along the probe beam. Because the elements in the reflectivity profile are complex in nature, at any particular depth of interest in the studied sample, both the amplitude information and the phase information can be retrieved from the gathered profile data. Volume imaging of reflectivity is usually achieved by grouping the amplitude information together and discarding the phase information.

Most OCT systems are concerned with retrieving the amplitude signal from a reflection event in the sample, whereas a phase sensitive OCT system outputs the retrieved phase as the signal. The phase sensitive OCT exhibits better measurement sensitivity than conventional OCT. For instance, phase sensitive SS-OCT has been reported to be capable of nanometre scale measurement sensitivity [22], and the phase sensitive SD-OCT reaches even sub-nanometre scale measurement sensitivity [23],[24].

The measurements of tiny optical index changes, micro OPD variations and sample movements using the phase sensitive monochromatic interferometry discussed in Chapter 1 can also be performed by the phase sensitive OCT. However, unlike phase sensitive monochromatic interferometry which can perform phase measurements on only the surface of the detected sample, phase sensitive OCT is able to perform depth-resolved phase measurements in the sample from multiple layers.

This chapter reviews the principles of phase retrieval and depth sectioning in FD-OCT. It then reviews the application of a phase sensitive SD-OCT system in imaging the tissue motion within the organ of Corti [25]; and the application of a phase sensitive SS-OCT system in imaging and quantifying microbubbles in clear and scattering media [26]. The configurations of the SD-OCT system and the SS-OCT system are explained in each corresponding section. The performance of the SD-OCT and that of SS-OCT are compared in the end of the chapter.

2.2 Phase retrieval in FD-OCT

Fig. 2.1 shows a schematic diagram of a simplified OCT system, with no scanning and focusing units, employing a fibre based Michelson interferometer. The OPL of the reference arm and that of the sample arm are l_R and l_S respectively.

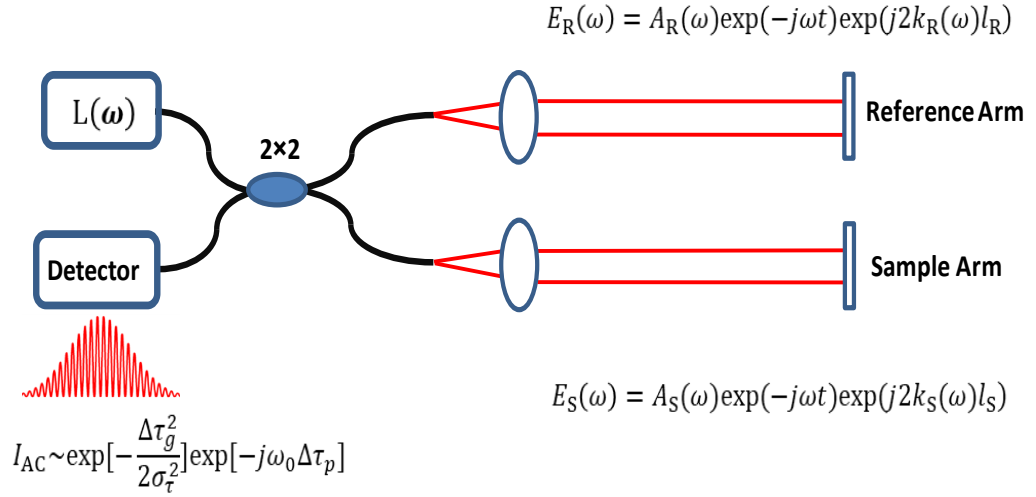


Fig. 2.1. 2x2 fibre coupler (50:50) Michelson interferometer based OCT system. $L(\omega)$: low coherent light source with a frequency bandwidth $\Delta\omega$. ω : optical frequency of the laser source. $E_R(\omega)$ and $E_S(\omega)$: wavefields on the reference mirror surface and on the sample surface.

Compared with the monochromatic interferometer schematically demonstrated in Fig. 1.4, the configuration in Fig. 2.1 employs a low coherent light source $L(\omega)$ with a finite bandwidth $\Delta\omega$ of optical frequencies rather than just a single frequency. At the detector (in Fig. 2.1) where the interference being detected, the field $E_R(\omega)$ from the reference arm and the field $E_S(\omega)$ from the sample arm can be expressed as:

$$E_R(\omega) = A_R(\omega)\exp(-j\omega t)\exp(j2k_R(\omega)l_R) \quad (2.1)$$

$$E_S(\omega) = A_S(\omega)\exp(-j\omega t)\exp(j2k_S(\omega)l_S) \quad (2.2)$$

where $A_R(\omega)$ and $A_S(\omega)$ are field amplitudes of the reference beam and the sample beam, ω is the optical frequency of the light source, $k_R(\omega)$ and $k_S(\omega)$ are the propagation constants of two beams. In free space, $k_R(\omega) = k_S(\omega)$.

Unlike the monochromatic beam that exhibits long coherence length, OCT low coherence light has micrometer scale coherence length Δd . Therefore, the interference

between the reference beam and the sample beam happens only when the OPLs of the two arms match each other within Δd . When this coherence condition between the two arms is fulfilled, the generated interference signal is the sum of interference signals at each optical frequency component (ω) across the optical frequency bandwidth $\Delta\omega$ of the light source. Assuming sample reflectivity is constant with ω , at coherence, therefore, the interferometric intensity I_{AC} can be expressed as:

$$I_{AC} \sim \text{Re} \left[\int_{-\infty}^{\infty} E_S(\omega) E_R(\omega)^* \frac{d\omega}{2\pi} \right] = \text{Re} \left[\int_{-\infty}^{\infty} S(\omega) \exp[-j\Delta\varphi(\omega)] \frac{d\omega}{2\pi} \right] \quad (2.3)$$

where
$$S(\omega) = A_S(\omega) A_R(\omega)^* \quad (2.4)$$

and
$$\Delta\varphi(\omega) = 2k_S(\omega)l_S - 2k_R(\omega)l_R \quad (2.5)$$

$S(\omega)$ is the power spectrum of the light source. $A_S(\omega)^*$ is the conjugate of $A_S(\omega)$. For each optical frequency component ω , $\Delta\varphi(\omega)$ is the interferometric phase, created by the interferometer OPD.

It is clear from Eq. (2.3) and Eq. (2.4) that the variation of interferometric phase $\Delta\varphi(\omega)$ is converted into a change of the interferometric intensity I_{AC} in FD-OCT. In the same way as the monochromatic interferometry, the interferometric phase in FD-OCT is sensitive to changes in OPD, optical index of sample material and sample movements. Nevertheless, since FD-OCT employs a light source with low coherence length, it is able to perform depth sectioning and coherence gating phase measurements along the optical axis in the sample, as demonstrated in the following section.

2.3 Depth resolved phase measurement in FD-OCT

Consider the case where the sample arm and the reference arm are in the same and nondispersive medium, and the spectrum of the low coherent light source $S(\omega - \omega_0)$ is centered at ω_0 . Assuming the refractive index is same in both arms, the propagation constant of the beam in each arm can be expressed as a first-order Taylor expansion around ω_0 :

$$k_R(\omega) = k_S(\omega) = k(\omega_0) + k'(\omega - \omega_0) \quad (2.6)$$

The phase mismatch $\Delta\varphi(\omega)$ in Eq. (2.5) is only determined by the optical path difference OPD with the value of Δl , which is equal to the OPL mismatch $\Delta l = l_S - l_R$ between the two arms:

$$\Delta\varphi(\omega) = k(\omega_0)(2\Delta l) + k'(\omega - \omega_0)(2\Delta l) \quad (2.7)$$

Eq. (2.3) then becomes:

$$I_{AC} \sim \text{Re} \left[\exp[-j\omega_0\Delta\tau_p] \int_{-\infty}^{\infty} S(\omega - \omega_0) \exp[-j(\omega - \omega_0)\Delta\tau_g] \frac{d(\omega - \omega_0)}{2\pi} \right] \quad (2.8)$$

where the phase delay mismatch $\Delta\tau_p$ and the group delay mismatch $\Delta\tau_g$ are defined as:

$$\Delta\tau_p = \frac{k(\omega_0)}{\omega_0} (2\Delta l) = \frac{2\Delta l}{v_p} \quad (2.9)$$

$$\Delta\tau_g = k'(\omega_0)(2\Delta l) = \frac{2\Delta l}{v_g} \quad (2.10)$$

where $v_p = \omega_0/k(\omega_0)$ corresponds to the phase velocity of ω_0 , and $v_g = 1/k'(\omega_0)$ is the group velocity. Given by Eq. (2.8) - Eq. (2.10), the generated interferogram consists of a carrier and an envelope, as shown in Eq. (2.12) and in Fig. 2.2. The envelope, which is the inverse Fourier transform of the source power spectrum $S(\omega - \omega_0)$, determines the axial point spread function and the axial resolution of the OCT system. The light source is assumed to have a Gaussian spectrum, which is expressed as:

$$S(\omega - \omega_0) = \left(\frac{2\pi}{\sigma_\omega^2}\right)^{1/2} \exp\left(-\frac{(\omega - \omega_0)^2}{2\sigma_\omega^2}\right) \quad (2.11)$$

which has been normalized to unit power $\int_0^\infty S(\omega) \frac{d\omega}{2\pi} = 1$. In Eq. (2.11), σ_ω is the standard deviation of the power spectrum bandwidth. Substituting Eq. (2.11) into Eq. (2.8) gives:

$$I_{AC} \sim \exp\left[-\frac{\Delta\tau_g^2}{2\sigma_\tau^2}\right] \exp[-j\omega_0\Delta\tau_p] \quad (2.12)$$

As seen in Fig. 2.2, I_{AC} contains a Gaussian envelope $\exp\left(-\frac{\Delta\tau_g^2}{2\sigma_\tau^2}\right)$ with a characteristic temporal width σ_τ which is inversely proportional to the power spectrum bandwidth σ_ω . It can be shown that:

$$2\sigma_\tau = \frac{2}{\sigma_\omega} \quad (2.13)$$

Thus, Eq. (2.12) explains the function of depth sectioning and coherence gating measurements in OCT. Interference happens only if the temporal mismatch between the reference and sample beams falls within the temporal Gaussian envelope, which has a full width σ_τ at width at $1/e^{0.5}$.

As indicated by Eq. (2.12), the Gaussian envelope falls off quickly with increased group delay mismatch $\Delta\tau_g$. Eq. (2.8) to Eq. (2.12) also indicate how, within the Gaussian envelope, interference fringes oscillate faster with increased phase delay mismatch $\Delta\tau_p$. Given by Eq. (2.10) and Eq. (2.13), the width Δl_{SD} of the point spread function (i.e. the $\pm\sigma_\tau$ width of the Gaussian envelope) is:

$$\Delta l_{SD} = \frac{v_g}{\sigma_\omega} \quad (2.14)$$

Eq. (2.14) indicates that the axial resolution of OCT is inversely proportional to the spectrum bandwidth σ_ω of the light source. In free space, $v_g = v_p = c$, where c is the speed of light, and then Eq. (2.14) becomes:

$$\Delta l_{SD} = \frac{c}{\sigma_\omega} \quad (2.15)$$

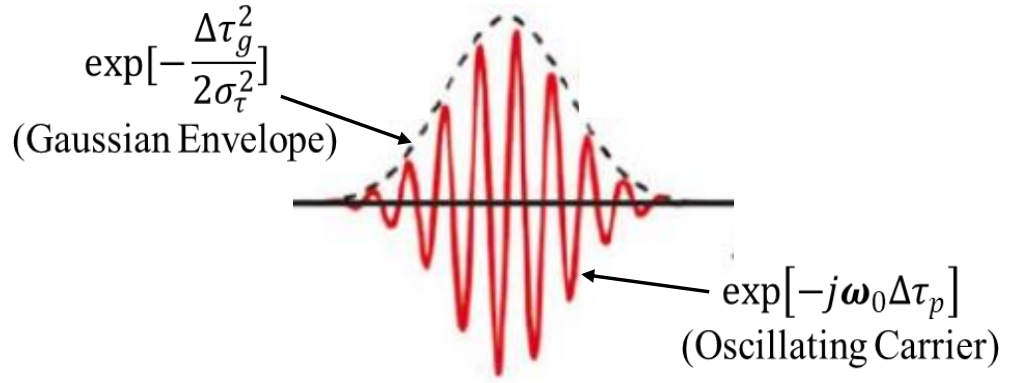


Fig. 2.2 Detected interferogram $I_{AC} \sim \exp[-\frac{\Delta\tau_g^2}{2\sigma_\tau^2}] \exp[-j\omega_0\Delta\tau_p]$. It is a Gaussian envelope $\exp[-\frac{\Delta\tau_g^2}{2\sigma_\tau^2}]$ modulated by an oscillating carrier $\exp[-j\omega_0\Delta\tau_p]$.

For convenience, the full-width at half-maximum (FWHM) is more often used than the standard deviation in the measurement of the OCT axial resolution. For a Gaussian spectrum with a standard deviation σ , the FWHM equals $2\sigma\sqrt{2\ln 2}$. Thus, for an OCT system employing a Gaussian spectrum source (centred at λ_0) in free space, the FWHM axial resolution Δl_{FWHM} is related to the FWHM wavelength bandwidth $\Delta\lambda$ by:

$$\Delta l_{FWHM} = \frac{2\ln 2}{\pi} \left(\frac{\lambda_0^2}{\Delta\lambda} \right) \quad (2.16)$$

As seen from Eq. (2.3), Eq. (2.5) and Eq. (2.16), OCT is able to perform the phase measurement within a region as short as its axial resolution, leaving out the phase information out of the axial resolution, whereas this depth resolving function does not exist in the monochromatic interferometry, whose transfer function lacks the Gaussian modulation and is therefore inherently ambiguous.

2.4 Review of phase sensitive FD-OCT techniques

Given the principles discussed above, depth resolved phase measurements are possible using techniques employing FD-OCT. This section reviews a spectrometer based phase sensitive OCT system for imaging the tissue motion within the organ of Corti in the inner ear [25], and a swept source based phase sensitive OCT system for imaging and quantifying of microbubbles in clear and scattering media [26].

2.4.1 Phase sensitive SD-OCT in imaging tissue motion

To study how the organ of Corti (OC) responds to sound, Wang and Nuttall presented the use of a spectrometer based phase sensitive OCT system with a sub-nanometre scale displacement sensitivity to characterize the motion and displacement of cellular compartments within the OC [25].

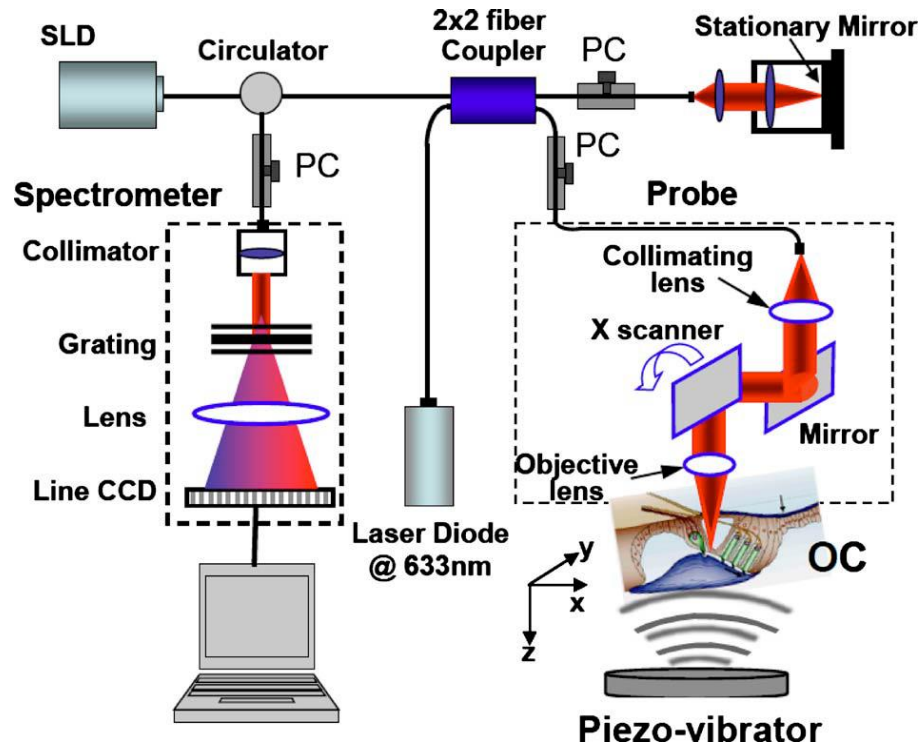


Fig. 2.3 Schematic of the phase sensitive SD-OCT system in measuring the nano-motion within the OC. Polarization controller (PC). The laser diode centred at 633 nm is for aiming purposes in the imaging process. (Reproduced from Wang and Nuttall [25] by permission of Prof Wang and the International Society for Optics and Photonics)

The system is schematically presented in Fig. 2.3. The superluminescent diode has a central wavelength of 1310 nm and a spectral bandwidth of 56 nm. Assuming a sample refractive index of 1.42, the light source provides an axial resolution of 9 μm in the OC sample. Passing through an optical circulator, the light beam is coupled into a 2 \times 2 fibre-based Michelson interferometer. In the reference arm of the interferometer, the beam is reflected by a stationary reference mirror. In the sample arm, the OCT beam is reflected by the OC sample mounted on a calibrated piezo-stack which is driven by a signal generator. The interference between the reference beam and the sample beam is detected by a spectrometer with a high-speed, 14-bit, 1024-pixels InGaAs line scan camera serving as a linear detector. The SD-OCT system has a theoretical spectral resolution of 0.141 nm and a measured imaging depth of 3.0 mm. Working in the phase

sensitive mode, the SD-OCT system has a displacement sensitivity of 0.2 nm, with a signal to noise ratio (SNR) of 56.

Fig. 2.4 shows the results obtained from the OC sample with the piezo-stack vibrating at 17 kHz with a magnitude of 0.2 nm. The physiological features of the OC sample can be seen in the B-scan OCT image in the top left corner of Fig. 2.4. The measurement of the frequency responses of the OC sample to the nano-motion at different positions labelled in the OCT image are presented in Fig. 2.4.a to Fig. 2.4.c respectively. Since the OCT has the advantage of depth sectioning, the phase measurement can be performed at different locations in the sample, as shown in the diagram.

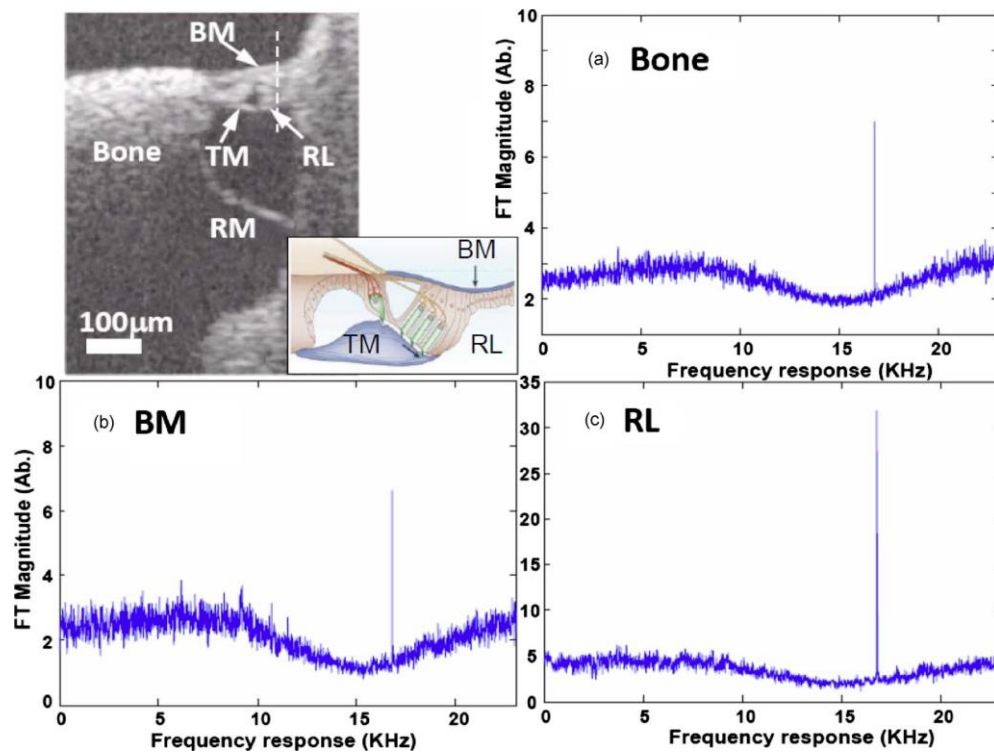


Fig. 2.4 Measured frequency responses of the OC sample to the nano-vibration, at 17 kHz with a magnitude of 0.2 nm, created by the piezo-stack. Results obtained from (a): bone, (b): basilar membrane (BM), and (c): reticular lamina (RL). Top left corner: B-scan OCT image showing labelled physiological features of the OC sample, along with a histological drawing of the OC. (Reproduced from Wang and Nuttall [25] by permission of Prof Wang and the International Society for Optics and Photonics)

To generate the traces in Fig. 2.4.a to Fig. 2.4.c, the complex Fourier transform was performed to the detected interferogram, generating depth-resolved A-scan profiles containing the sample information in both amplitude and phase. Then, the phase values at the depth of interest were retrieved from successive A-scans. Fourier analysis of the

phase variation with time are presented as the traces in Fig. 2.4.a to Fig. 2.4.c, which illustrate the frequency responses of various parts of the OC sample to the nano-motion.

As indicated by the height of the peaks in Fig. 2.4.a and Fig. 2.4.b, the vibration magnitude of the basilar membrane (BM) is comparable to that of the bone. However, the vibration magnitude of the reticular lamina (RL) is 8 times higher than those of the bone and the BM (Fig. 2.4.c). These results are consistent with the known mass and elastic properties of the OC sample, in which the cellular structure may vibrate differently than the BM.

Wang and Nuttall also employed the phase sensitive SD-OCT system to produce vibration maps over the cross section of the OC sample. In order to do that, the piezo-stack was driven at 14 kHz with a 0.4 nm amplitude and then at 20 kHz with a 0.1 nm amplitude. Obtained vibration maps are presented in Fig. 2.5.b and Fig. 2.5.c respectively. As seen, these pseudo-colour intensity maps show a complexity of the motion. For instance, maximum motions (red) are located at different regions in Fig. 2.5.b and Fig. 2.5.c, indicating that the technique can be used to search the resonance frequencies of different locations in the OC. The vibration maps indicate that by performing phase measurements using a SD-OCT system with a sub-nanometre-scale displacement sensitivity, it is possible to provide depth-resolved information related to the vibration amplitude in different parts of the OC sample and to present it in relative terms. However, the technique is not able to quantify in absolute terms the vibrating amplitude of the OC sample.

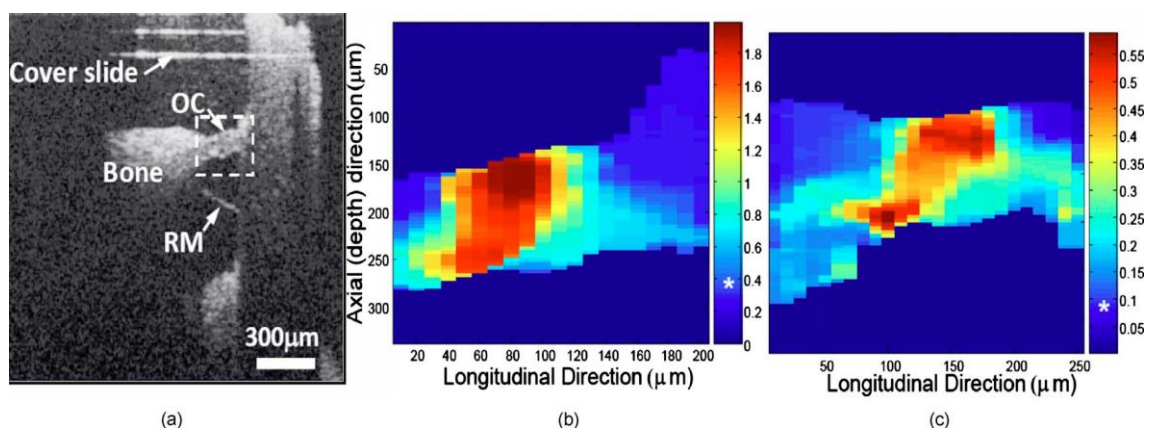


Fig. 2.5. (a) B-scan OCT image of the OC. (b): Vibration map within the dashed square in (a), from the 14 kHz, 0.4 nm vibration. (c): Vibration map within the dashed square in (a), from the 20 kHz, 0.1 nm vibration. The scale bars have a unit of nanometre. (Reproduced from Wang and Nuttall [25] by permission of Prof Wang and the International Society for Optics and Photonics)

2.4.2 Phase sensitive SS-OCT in imaging and quantifying of microbubbles

As discussed in section 2.2, since charge-coupled device (CCD) or CMOS detectors generally employed by SD-OCT systems are sensitive to wavelength up to 1 μm , the imaging and detection depth of the SD-OCT is highly limited. In contrast, SS-OCT systems employ a point photodetector that allows the application of longer wavelengths (1-1.3 μm), and therefore SS-OCT extends the imaging and detection depth of FD-OCT.

Microbubbles in blood and tissues account for serious and even life threatening disorders, such as decompression sickness, localized pain, and arterial and venous gas embroils [29]. Hence, non-invasive functional imaging and quantifying of microbubbles in blood and tissues is important for effective therapy and early stage diagnosis. A few imaging techniques have been applied to the purpose, including Doppler sonography [30], magnetic resonance imaging [31] and computer tomography [32]. Although Doppler sonography is the most popular technology among them, employing ultrasound limits the achievable resolution of the technology. In practice, Doppler sonography is only capable of detecting moving intravascular bubbles with diameters around 50 μm [26][30]. To enhance the resolution in imaging and quantifying microbubbles, Manapuram, Manne, and Larin applied a variant of the phase sensitive SS-OCT technique [26].

Using a basic SS-OCT setup to perform phase measurements has two major drawbacks [26]. The first one comes from the nonlinearity in the frequency sweep of the swept source, which results in broadened A-scan peaks, hence worse resolution, after the FFT is applied to the interferogram. The second drawback is the jitter present during the repeated sweeping action across the spectrum, which causes the interferogram to drift between successive A-scans. The drift creates mismatch in successive fringes, resulting in phase jumps up to π radians. To overcome these two drawbacks, Manapuram et al. implemented phase stabilization units in a basic SS-OCT system. As shown in Fig. 2.6, the system consists of a swept source (SLS), data acquisition electronics, a Mach-Zehnder interferometer (MZI) unit for sample detection, a MZI-clock unit generating a k -clock, and a trigger unit generating the TTL signal.

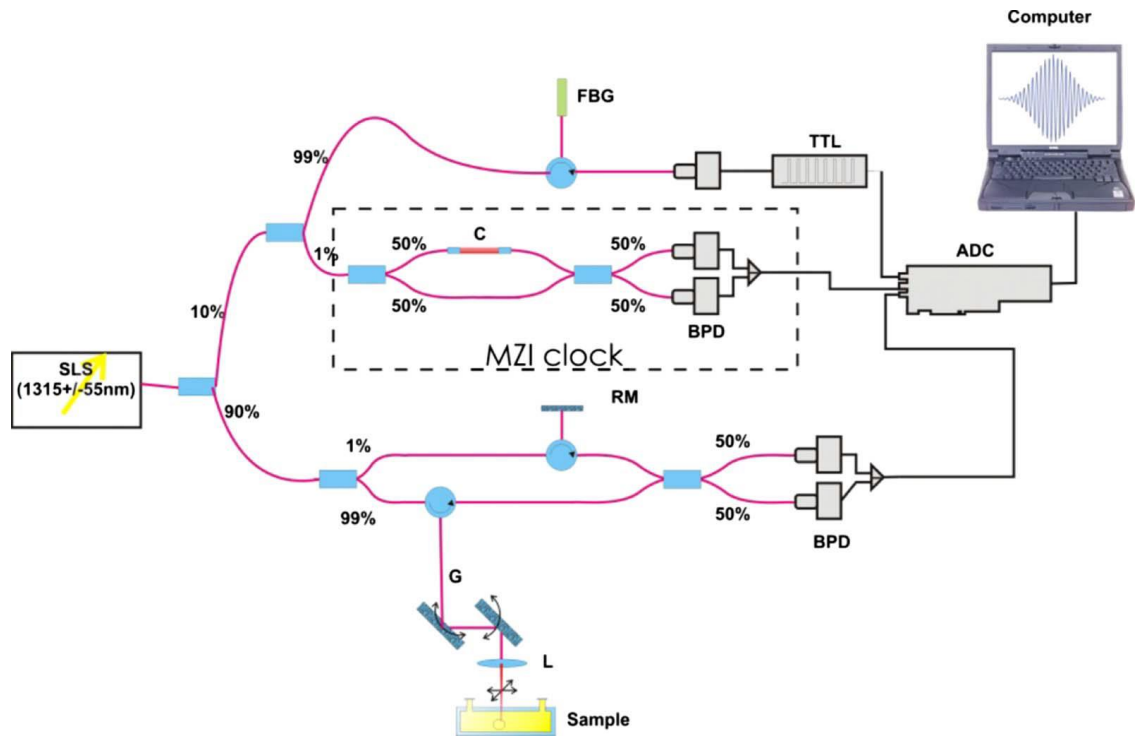


Fig. 2.6. Schematic of the phase sensitive SS-OCT system with phase stabilization units. Swept-laser source (SLS). Analog to digital converter (ADC). Balance photodetector (BPD). Collimators (C). The free space between two collimators can be used to adjust the optical path length of this arm. Fibre Bragg grating (FBG). Galvanometer scanner (G). Lens (L). Reflective mirror (RM). (Reproduced from Manapuram et al. [26] by permission of the Journal of Applied Physics)

As demonstrated in Fig. 2.6, 90% of the light from the source goes into the MZI unit, where the interference signal containing the sample information is detected by a balanced photodetector (BPD). Then, the interferogram encoded voltage signal is digitized by an analogue to digital converter (ADC) installed in the computer. Due to the nonlinear frequency sweep of the swept source, the digitized interferogram is chirped in frequency. The MZI-clock unit in Fig. 2.6 provides a k -clock for recalibration. The k -clock corrects the frequency chirp in the interferogram by applying to the interferogram a suitable nonlinear stretch such that fringes as a function of sweep time in the calibrated interferogram are equally spaced [77].

To remove the jitter induced phase jump, a synchronization between the frequency sweep of the swept source and the data acquisition of the ADC is required. The trigger unit in Fig. 2.6 is inserted between the swept source and the ADC. The trigger unit dynamically triggers the data acquisition of ADC by a TTL signal generated from a narrow band (0.1 nm) fibre Bragg grating (FBG). The FBG is connected with the swept source. Every time the frequency sweep crosses the wavelength of 1315 nm, the FBG

generates an optical pulse which is then converted to the TTL signal. Thus, the TTL signal has the same repetition frequency as the frequency sweep.

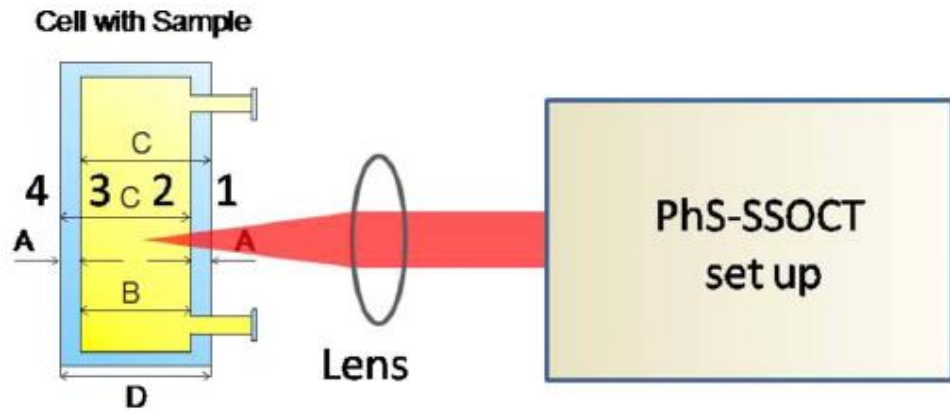


Fig. 2.7. Orientation of the 500 μm cuvette (filled with water containing microbubbles). 1, 2, 3, 4 are used to label the surfaces of the glass cuvette. (Reproduced from Manapuram et al. [26] by permission of the Journal of Applied Physics)

Fig. 2.7 demonstrates how the phase sensitive SS-OCT system is used for the microbubble imaging. The 500 μm cuvette is filled with water, and the air bubbles inside were created by blowing air into the cuvette. When the beam passes through an air bubble in the water medium, it experiences a refractive index change which introduces a phase shift. The diameter l of the bubble from the phase shift $d\phi$ can be calculated from:

$$dn = \frac{1}{l} \frac{\lambda}{4\pi} d\phi \quad (2.18)$$

where dn is the refractive index change introduced by the bubble. $dn = 0.33$, taking the refractive index of water as 1.33 and the refractive index of air as 1. Thus, if the retrieved phase from the SS-OCT system is wrapped within 2π , a 2π phase shift is created by an air bubble with the diameter of 2 μm . Since the resolution of the built SS-OCT system is 10 μm when it works in the conventional mode with no phase sensitive function, a bubble smaller than 10 μm cannot be resolved in the B-scan image.

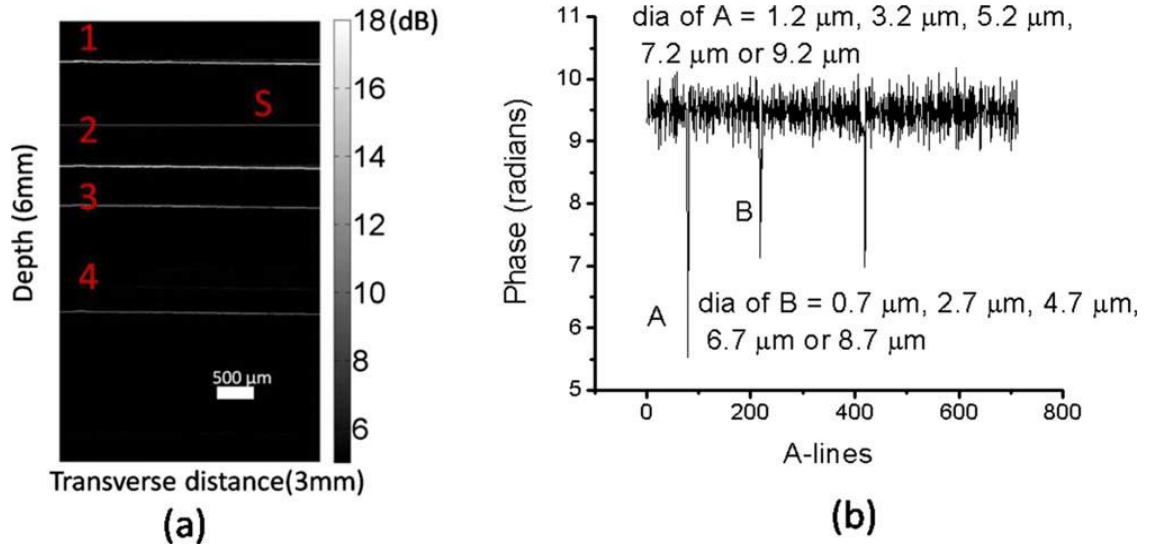


Fig. 2.8. (a): B-scan image of a 500 μm cuvette filled with water. Colour lines (1-4) are corresponding interfaces of the cuvette in Fig. 2.7. The colour line (S) is the self-interference image of interfaces 1 and 2 in Fig. 2.7. Air bubbles in the water medium are smaller than 10 μm since they cannot be resolved from the B-scan image in (a). (b): Temporal phase difference between the interface-2 and the interface-1 in (a). (Reproduced from Manapuram et al. [26] by permission of the Journal of Applied Physics)

The experimental results are presented in Fig. 2.8. Fig. 2.8.a shows a B-scan image of the 500 μm cuvette sample. Since no air bubble is visible in the B-scan image, the air bubbles in the water inside the cuvette are smaller than 10 μm . The bright lines (labelled by numbers 1, 2, 3, 4) in Fig. 2.8.a correspond to the interfaces of the cuvette showing in Fig. 2.7. Fig. 2.8.b shows a measure of phase differences between the cuvette interface-2 and the interface-1. The phase value retrieved from the interface-1 is treated as a reference phase, and the phase value retrieved from the interface-2 is the signal phase. By subtracting the reference phase from the signal phase, the extra OPD created by the action of beam scanning can be removed. The amplitude of the peak in Fig. 2.8.b. is used to estimate the diameter of the microbubble. Due to the lack of an effective phase unwrapping algorithm, the 2π ambiguity contributes errors of an integer multiple of 2 μm to the obtained results of the air bubble diameter. For instance, the diameter of the microbubble corresponding to peak B in Fig. 2.8.b. could be 0.7 μm , 2.7 μm , 4.7 μm , 6.7 μm or 8.7 μm . It is less likely to be 10.7 μm or bigger since the microbubble is not resolved in the B-scan image (Fig. 2.8.a).

The results of their study indicate that by implementing the k -clock and removing the jitter noise, the phase sensitive SS-OCT could be an effective device for imaging and quantifying microbubbles ($\leq 10 \mu\text{m}$) with diameters significantly smaller than the

imaging capability the employed OCT system in the conventional mode. However, the 2π ambiguity is an unsolved issue for the technique due to the lack of a phase unwrapping algorithm.

2.5 Discussion and conclusion

Interferometric phase techniques are roughly grouped into two categories: monochromatic phase sensitive interferometric techniques and broadband phase sensitive interferometric techniques. Both of them can be used to perform quantitative phase measurements. However, as discussed in Chapter 1, the monochromatic light source employed in the monochromatic interferometry does not allow the technology to perform depth-selective isolated phase measurements within the sample. In contrast, in broadband phase sensitive interferometry, the phase measurements can be performed on a particular layer of interest within the sample. This chapter provided a detailed mathematical explanation of how the depth resolved phase information is converted to the interference intensity which can be detected by the interferometer.

This chapter introduced the technique of FD-OCT that developed from the broadband interferometry. Depending on the setup configuration, FD-OCT is grouped into SS-OCT and SD-OCT. Both sub-categories are able to perform depth-resolved phase measurements. Nevertheless, the FD-OCT generates stable output phase by using a basic setup, whereas sophisticated implements need to be added into the SS-OCT setup to stabilize the output phase. On the other hand, SD-OCT has an upper illumination wavelength limit of $1\ \mu\text{m}$, although advances in camera sensors are pushing this wavelength longer. In contrast, the upper illumination wavelength of SS-OCT can reach $1.5\ \mu\text{m}$. Consequently, the selection of two categories is closely dependent on the particular application.

This chapter reviewed an application of the SD-OCT in imaging the nano-motion of the organ of Corti. The SD-OCT system presented high detection sensitivity. The motion is mapped corresponding to the particular location within the organ of Corti. In addition, this chapter reviewed the application of the SS-OCT in imaging and quantifying microbubbles in water. The technique presented an enhanced detection depth. The approach to overcome the jitter noise and the approach to calibrate the chipped interferogram are demonstrated in the work. However, due to the lack of suitable phase unwrap algorithm, the obtained results suffer from 2π ambiguity.

Chapter 3

Gold nanoparticles and their detection

3.1 Introduction

Colloidal gold nanoparticles have been utilized for centuries by artists because of the vibrant colours produced by their interaction with visible light [33]. During the last 20 years, gold nanoparticles have been extensively used in biomedical and diagnostic arenas [34],[35]. For instance, in precise drug delivery, they can be used to optimize and improve the distribution of drugs in diseased organs, tissues and cells [34]. In cancer research, gold nanoparticles can be used to target tumour and as imaging contrast agents in surface enhanced Raman spectroscopy *in vivo* [35]. In cancer treatment, they are being investigated as photothermal cancer therapy agents for *in vivo* applications since they can destroy cancer cells that cannot be surgically removed, including aggressive cancer cells that are resistant to radiation and chemotherapy [35]. These applications are based on the fact that gold nanoparticles exhibit useful optical properties which can be tuned to absorb and scatter light across the visible and near-IR region [33].

Considering the tunable optical properties of gold nanoparticles and the significance of gold nanoparticles in biomedical applications, the development of suitable techniques to detect the presence and image the distribution of gold nanoparticles in biological tissue is a priority.

This chapter reviews the optical properties of gold nanoparticles and their applications in biomedicine. Two reported techniques in detecting and imaging gold nanoparticles in different media are studied. The limitations of these techniques are discussed, which motivated the author to develop more effective techniques to detect and image gold nanoparticles in complex media.

3.2 Optical properties of gold nanoparticles

Gold nanoparticles distinguish themselves from other nanoparticles such as polymeric nanoparticles and semiconductor quantum dots by their unique surface plasmon resonance (SPR) properties. SPR effects, manifested under certain conditions, consist in the interaction of a fraction of the light energy incident on the gold

nanoparticle with delocalized electrons in the metal. The photon energy is absorbed by the metal, and surface plasmons on the metallic surface can be excited, thereby transforming a photon into a surface plasmon [36]. Consequently, the SPR, resulting from the interaction between the photon and the metal enhances a series of radiative and non-radiative properties of gold nanoparticles [37]. In the non-radiative process, gold nanoparticles convert the absorbed light into heat quickly, which is known as the photothermal property being widely used in the photothermal therapy. In the radiative process, gold nanoparticles absorb the photon energy and then emit photons in the form of scattered light either at the same frequency as the incident light or at a shifted frequency. This property makes gold nanoparticles contrast agents in cancer imaging.

Due to the SPR, the optical absorption and scattering properties of gold are 5-6 orders of magnitude stronger than most absorbing organic dye and fluorescent molecules [37][38]. Thus, a fine tuning of the optical properties of gold nanoparticles can be actualized by a precise control of the SPR excitation wavelength band. This band is heavily determined by the parameters of particles' shape, size and architecture [39]-[44].

Gold nanoparticles with designed nanostructures have a tailored SPR wavelength band [45][46]. As the earliest developed gold nanostructure, gold nano-spheres exhibit limited absorption of light in the transmission window for biological entities (650 – 900 nm) [33],[39]. The limited choice of peak absorption wavelengths restricts the depth at which gold nano-spheres can be employed as imaging and photothermal agents in biomedical applications [33]. In contrast, other gold nanostructures are of particular interest due to their tunable peak absorption SPR wavelength. For instance, by varying the aspect ratio, the SPR wavelength of gold nanorods (GNRs) can be tuned from 600 nm to 1400 nm to cover the visible and NIR regions, which greatly enhances the depth employability of GNRs in biomedical applications [40]. Similarly, by varying the ratio of dielectric core radius to gold shell thickness, the SPR wavelength of gold nanoshells (GNSHs) can be tuned from 800 nm to 2200 nm [47][48]. Compared with GNSHs (hundreds of nanometres in size), GNRs (tens of nanometres) have more advantages for *in-vivo* molecular imaging. Because GNRs are smaller in size, they are more suitable to be used in thin blood vessels. Also, compared with GNSHs, GNRs find wider use in photothermal therapeutics since they have a higher photothermal conversion efficiency than GNSHs in the NIR region [39][42][43].

3.3 Biomedical applications of gold nanoparticles

3.3.1 Drug delivery

Gold nanoparticles have seen a dramatic increase in use in the last 20 years in disease treatment, not just by providing precise control of heating to target tissue but also for their revolutionary use in drug delivery. Since they have the ability to take up and hold proteins on their surface, gold nanoparticles are suitable agents for the delivery of drugs to cellular destinations [34][35]. They are biocompatible and can be functionalized by conjugating with a wide range of biomolecular structures from genes to stem cells[34],[35].

Gold nanoparticles functionalized with specific biomolecules can effectively destroy cancer cells or bacteria [34],[35]. As shown in Fig. 3.1, antileukemic and antibacterial drug molecules can be carried by the GNPs which are small in size and exhibit a large surface area to volume ratio.

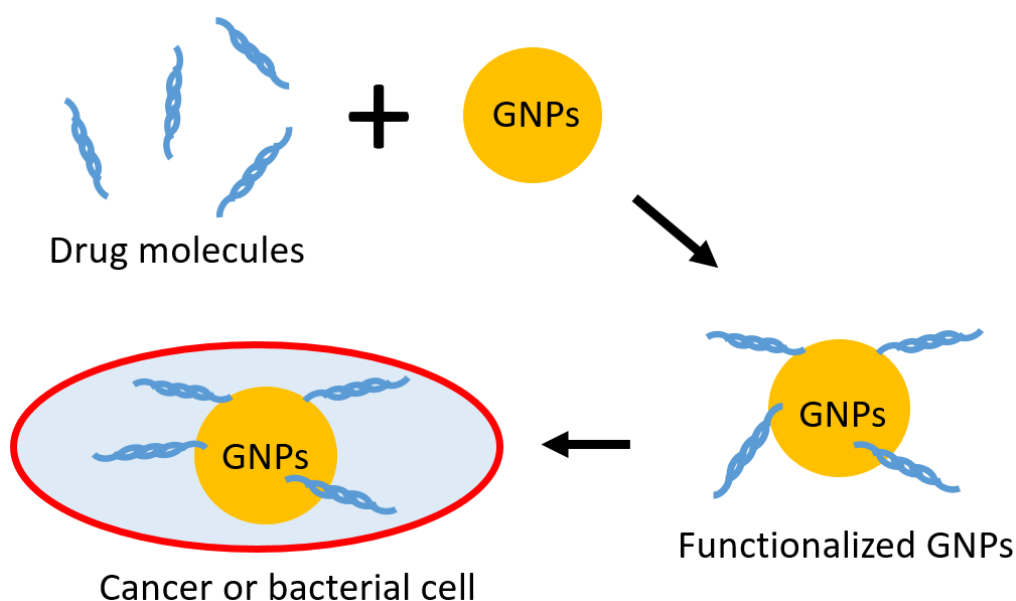


Fig. 3.1. Functionalized GNPs for drug delivery.

Some functionalized gold nanoparticles are able to target specific cells with high loading efficiency [34],[49],[50]. Due to the interaction between gold nanoparticles and cell surface lipids, gold nanoparticles coated with suitable drugs can cross cellular membranes and enter into the targeted cells. For instance, GNPs covalently attached to low molecular weight chitosan have been used to design high efficiency vectors for

vaccine delivery [51]. Similar techniques have been used for high efficiency gene delivery [49],[50].

3.3.2 Cancer diagnostic agents

The use of nanoparticles as agents to enhance the contrast in imaging cancer cells has been gaining popularity in recent years [34]. The functionalization of gold nanoparticles to fluorescent dyes allows them to target cells for the purpose of diagnostic imaging [52]. As shown in Fig. 3.2, they can be functionalized with fluorophores to target specific cancer cells for imaging tumours [51],[52]. Moreover, gold nanoparticles coated with polyethylene glycol (PEG) have been used to target human breast carcinoma cells for imaging [57].

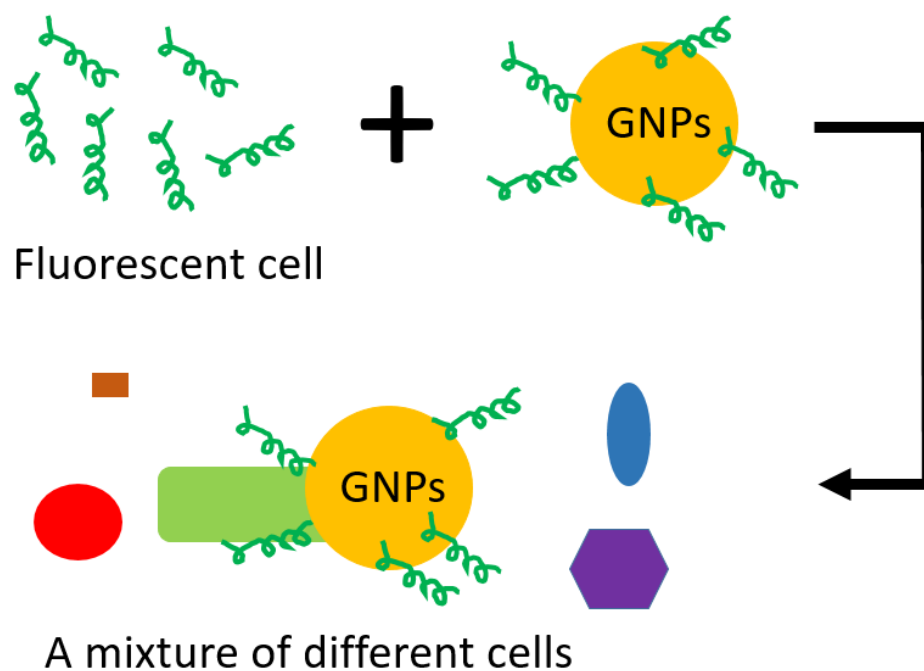


Fig. 3.2. Gold nanoparticles functionalized with specific peptides can be used as imaging agents to target specific cells within a mixture of cells.

3.3.3 Cancer treatment

The purpose of functionalising gold nanoparticles is to make them selectively target and accumulate at higher concentrations inside cancerous cells than inside normal cells [45]. Specially designed gold nanoparticles with unique optical properties show promise in the photothermal treatment of cancers [45][46][49]. These gold nanoparticles are designed to have a high absorption rate at a particular wavelength in the near infrared (NIR) range due to a deep penetration depth of the light in the biological tissue.

The photothermal treatment can be implemented in a few steps. Firstly, the functionalized gold nanoparticles are injected into the tumour site. After a time interval of usually a few hours, gold nanoparticles migrate to the tumour sites and the photothermal treatment can be performed by irradiating the tumour site with NIR laser beams with carefully selected wavelengths (usually SPR wavelength) and power parameters. Gold nanoparticles subsequently absorb the photon energy and convert it into heat which destroys cancers.

In recent years, photothermal treatments have been refined and have seen an increase in adoption due to the development of novel nanostructures of gold nanoparticles. Such nanostructures include gold nanoshells (GNSHs), gold nanorods (GNRs), gold nanowires and gold nanocubes. For instance, gold nanoshells (GNSHs) have been reported to be useful in photothermal cancer treatment using ultra-low power near infrared light [46],[53].

3.4 Photothermal property and TPL emission of GNRs

As discussed in section 3.2, in the NIR SPR wavelength band, GNRs are of more interest than other gold nanostructures. When GNRs are irradiated by SPR light, several processes may happen. For instance, as a radiative process, GNRs emit strong two-photon luminescence (TPL) when they are exposed to a Ti:Sa laser beam [41][45][54]. This feature makes GNRs suitable agents in the TPL based imaging technology [40]. Moreover, if the density of GNRs is low, the individual GNR can be trapped and manipulated by a continuous-wave (CW) laser beam or a femtosecond laser beam with the SPR wavelength [42]. This technique is known as the optical trapping of individual GNRs. The optical trapping property makes GNRs excellent candidates for *in-vivo* micromanipulation, such as the optical tweezer manipulation [43],[44]. In contrast, if the density of the GNRs irradiated by the SPR light is high, the photothermal trapping of GNRs takes place [40]. The optical trapping is more applicable to micron-sized dielectric particles. Both the optical trapping and the photothermal trapping are applicable to gold nanoparticles due to the high absorptivity of gold nanoparticles to SPR wavelength. The two trapping phenomena are schematically explained in Fig. 3.3.

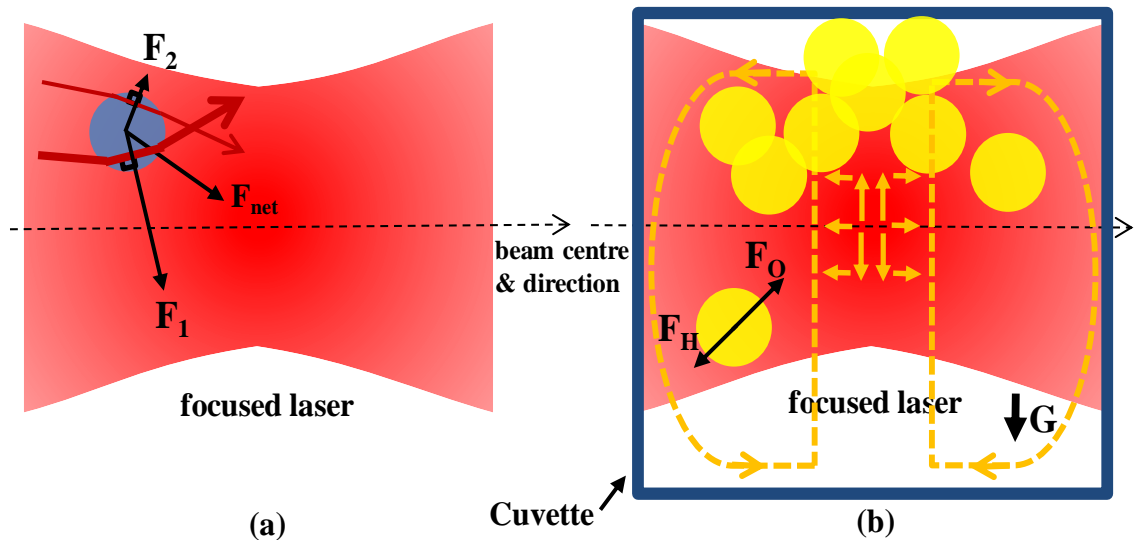


Fig. 3.3. (a): Optical trapping of a single dielectric particle, the radiation pressure force and the gravitational force are ignored as they are too small compared with the optical trapping force. (F_1): the force on the particle by the ray (thicker red arrow) closer to the centre of the focused laser beam. (F_2): the force on the particle by ray (thinner red arrow) away from the centre of the focused laser beam. (F_{net}): the net force on the particle, which returns the particle to the beam focus. (b): Photothermal trapping of a large number of gold nanoparticles in the liquid solution in a cuvette (blue box), the radiation pressure force is ignored, but the gravitational force (G) is considered in the convection flow. (F_O): Optical trapping force accumulating gold nano-particles. (F_H): Thermophoretic force repelling gold nano-particles from the beam focus (heating point). The direction of the convective flow is labelled by the yellow arrows.

In the case where the density of the particles closed to the laser focal point is low, the optical trapping force can be explained using ray optics. As shown in Fig. 3.3.(a), two rays of light emitted from the laser are refracted as they enter and exit the particle. Since the refraction direction of the existing ray is different from its origination direction, the momentum of the ray changes. Due to conservation of momentum, there should be an equal and opposite momentum change on the particle. Hence, each ray refracted by the particle generates a force to the particle, and the direction of the force is opposite to the direction of momentum change of the ray. As the laser operates with a Gaussian beam profile intensity, and the laser beam is focused by an objective lens, the beam intensity is stronger in beam centre than that at the beam edge. As a result, as seen in Fig. 3.3.(a), the force (F_1) on the particle side closer to the beam focus is larger than the force (F_2) on the particle side away from the beam centre, and the net force (F_{net}) on the particle tends to trap the particle into the centre.

Particles also migrate when the laser is slightly or not focused, where particles move away from the light source due to the momentum transfer from absorbed and

scattered light rather than the refracted light. This force is referred to as a radiation pressure force which can be ignored if the laser beam is tightly focused [97]. The gravitational force is also ignored in the demonstration since it is too small compared with the optical trapping force.

In the case where the gold nanoparticles are subjected to the focused SPR light, the photothermal trapping will happen in addition to the optical trapping, especially when the density of gold nanoparticles is high. As seen in Fig. 3.3.(b), each individual gold nanoparticle experience an optical trapping force (F_O) pulling it to the beam focus [107]. The photothermal trapping of GNRs is due to the high absorption rate of GNRs to the SPR light [55],[56]. Specifically, when GNRs are irradiated by the SPR light, 96% of absorbed photons are converted into heat via non-radiative electron relaxation [41]. As seen in Fig. 3.3.(b), the generated heat would generate a temperature gradient which creates a convective flow of the solution inside the cuvette and a thermophoretic force (F_H in Fig. 3.3.b) to each gold nanoparticle. The thermophoretic force repels gold nanoparticles along temperature gradients from the beam focus (heating point) [98], whereas the convective flow accumulates gold nanoparticles to the beam focus [40]. The net result of two opposite phenomena is the accumulation of gold nanoparticles since the convection flow overcomes. This process explains the photothermal trapping of gold nanoparticles [40]. The direction (yellow arrow) of the convective flow in Fig. 3.3.(b) takes the gravitational force (G) into consideration. As shown, the heating focus generates pressures to all directions, but the solution away from the bottom surface of the cuvette is easier to be pushed away since the solution there is not as dense as that close to the bottom surface due to the gravitational force (G). When the aggregated temperature reaches the melting point of gold, gold nanoparticles would melt and stick together [40]. The accumulation would happen on a colder surface [40],[98], i.e. the cuvette inner surface close to the beam focus in Fig. 3.3.(b).

Compared with the optical trapping of an individual GNR, the photothermal trapping of a large number of GNRs provides a different approach to manipulate and navigate GNRs [58]. In order to study and to monitor the photothermal trapping process and to image the aggregated GNRs, a technique that relies on detecting the TPL signal has been reported [40] and will be discussed in section 3.5.1.

3.5 Review of techniques in detecting and imaging gold nanoparticles

Different techniques have been reported for the detection and imaging of gold nanoparticles [34],[60],[61]. Inductively coupled plasma mass spectrometry (ICP-MS) is a technique for the quantitative determination of gold nanoparticles with different sizes [60]. However, this technique is not field-deployable, and the system setup is sophisticated [60],[61]. In contrast, X-ray fluorescence (XRF) systems are portable, but the technique is not sufficiently sensitive enough to detect and image gold nanoparticles in biological tissue [34],[61]

This section reviews two other techniques used to detect GNRs and GNSHs respectively. The first technique detects the TPL signal to produce images of aggregated GNRs that are accumulated by the photothermal trapping force induced by the Ti:Sa beam; the other technique employs a swept-source based phase sensitive OCT system to detect the photothermal response of GNSHs. The limitation of each technique is discussed in the respective section.

3.5.1 Photothermal trapping and TPL imaging of GNRs

When GNRs are present at a particular location in sufficiently high concentration and are exposed to the SPR light, two phenomena take place. A) GNRs produce TPL signal, and hence GNRs can be used as imaging agent in *in-vivo* and *in-vitro* imaging [62]. B) since 96% of the absorbed photon energy is converted into heat, the temperature gradient created photothermal trapping force field has the effect of creating the accumulation of surrounding GNRs.

By detecting the TPL signal to study the photothermal trapping process, Chen et. al. developed a technique to study the photothermal trapping process of GNRs [40].

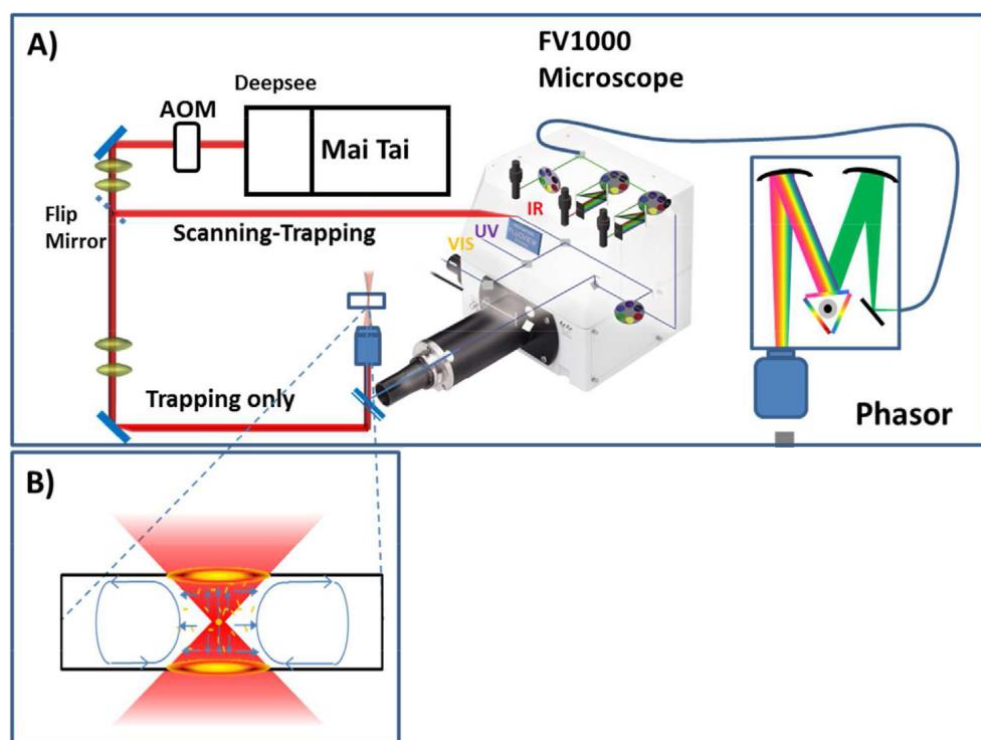


Fig. 3.4. Schematic of the photothermal trapping and imaging system developed by Chen et. al. (A): Setup of the system. (B): Proposed photothermal trapping by local heating and convective flow. Ti:Sa laser (Mai Tai). Group velocity dispersion compensation unit (Deepsee). Acousto-optic modulator (AOM). (Reproduced from Chen et al. [40] by permission of the IOP Science)

The system built by Chen et. al. is demonstrated in Fig. 3.4.A. As seen, a Ti:Sa laser (Mai Tai) beam, the output power of which is controlled by an acoustic optical modulator (AOM), is directed into a confocal microscope system (FV1000) implemented with a group velocity dispersion compensation unit. The generated TPL signal is detected by an internal photomultiplier in the microscope to generate intensity images.

The photothermal trapping scheme is illustrated in Fig. 3.4.B. An 80 μm deep cuvette is filled with the GNR solution with a concentration of 5.7×10^{11} / ml. These GNRs have an axial diameter of 10 nm, a length of 44 nm and the SPR wavelength of 840 nm. The converted heat creates a heat spot near the laser focus, and the generated temperature gradient results in a convective flow that brings nearby GNRs to the beam focus. If the density of GNRs is high, more and more heat can be generated to accumulate and aggregate GNRs. The accumulation will in return enhance the convective flow, resulting in a snowball effect. Then, a positive feedback loop is established, and the area of aggregated GNRs extends.

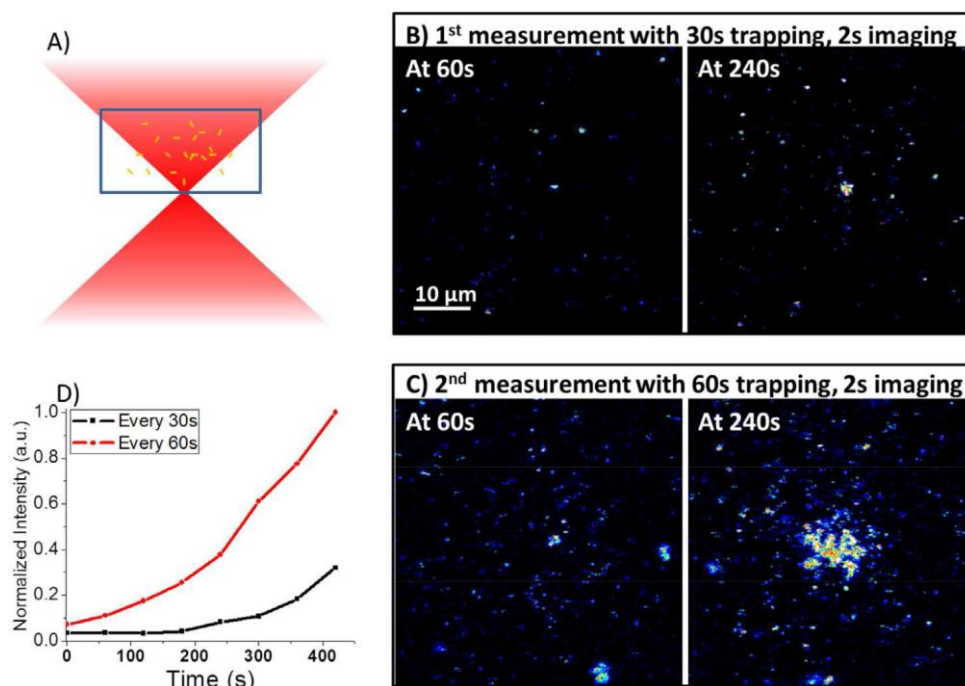


Fig. 3.5. Demonstrating that if the density of GNRs is high, the photothermal trapping of GNRs happens. (A): the Ti:Sa laser beam is focused at the bottom surface of the cuvette. (B): First measurement scheme: 30 seconds trapping followed by 2 seconds scanning/imaging. (C): Second measurement scheme: 60 seconds trapping followed by 2 seconds scanning/imaging. (D): Average TPL intensity curves of two schemes. (Reproduced from Chen et al. [40] by permission of the IOP Science)

In order to image the photothermal trapping process, Chen et. al. detected the generated TPL signal. They employed the Ti:Sa beam as both the photothermal trapping beam and the TPL signal exciting beam. As illustrated in Fig. 3.5.A, the Ti:Sa beam (average power: 0.5 mW) is focused on the bottom surface of the cuvette.

In order to prove that when the density of GNRs is high, the photothermal trapping of GNRs happens in addition to the optical trapping of GNRs. Chen et. al. carried out two measurement schemes. In the first measurement scheme, in the first step, the Ti:Sa laser was parked at a certain lateral position on the sample for 30 seconds to perform the photothermal trapping. In the second step, the beam was scanned over the parking area to excite the TPL signal which was subsequently detected by the photomultiplier in the microscope to produce 2D TPL intensity images. The scanning/imaging process took 2 seconds. These two steps were repeated in turn for 8 times. The 2nd and the 8th of the obtained 8 images are presented in Fig. 3.4.5. As seen, the degree of accumulation of GNRs that results from 240 seconds of trapping is larger than that generated from 60 seconds of trapping. However, the images in Fig. 3.5.B do not indicate that the accumulated GNRs came from the photothermal trapping. That is because the accumulation effect might come from the optical trapping.

In the second measurement scheme, a new cuvette filled with the same GNR solution was used. This time the trapping time was increased from 30 s to 60 s, but the scanning/imaging time was kept at 2 s. The two trapping-imaging steps were repeated in turn for 8 times. The 1st and the 4th of obtained 8 images are presented in Fig. 3.5.C. Logically, if the optical trapping is the only force leading to the accumulation effect, the diameter of the GNR cluster obtained in the second measurement scheme should be exactly double that obtained in the first measurement scheme. However, the diameter of the GNR cluster (240 s) in Fig. 3.5.C is obviously more than 2 times larger than the one (240 s) in Fig. 3.5.B.

The only plausible reason to explain the large GNR cluster in Fig. 3.5.C is that the accumulated heat creates a strong convective flow of the GNR solution, which brings additional surrounding GNRs to the Ti:Sa beam focus. Consequently, the extra trapped GNRs are contributed by the photothermal trapping, which agrees with the demonstration in Fig. 3.3.(b) and Fig. 3.4.B.

To quantify the photothermal trapping process, Chen et. al. plotted the measured average intensity of TPL signal over time, as presented in Fig. 3.5.D. As seen, the TPL intensity obtained from the second measurement scheme is more than twice that from the first measurement scheme.

As demonstrated in section 3.4 and Fig. 3.3.(b), the thermophoretic force (F_H in Fig. 3.3.b) repels particles from the beam focus, whilst the convection brings particles to the beam focus. In given conditions, these two effects provide a mechanism to manipulate particles. For instance, in the published work [98], by positioning the beam focus at certain locations relative to the studied sample, DNA was trapped into ring patterns on a cold surface.

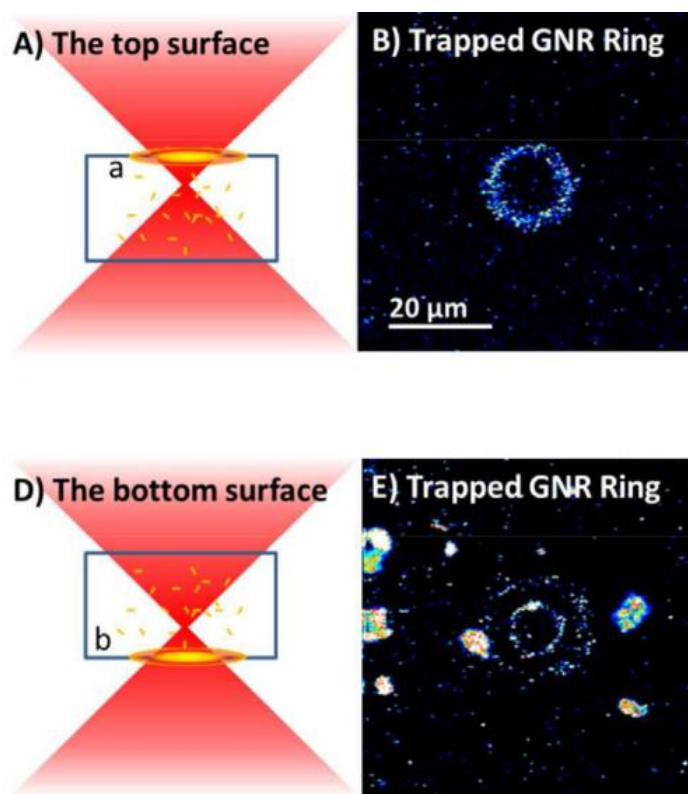


Fig. 3.6. Photothermal trapping and patterning of GNRs on the top and bottom surfaces of the cuvette. (A): The Ti:Sa beam focus is 10 μm below the top surface of the cuvette. (B): TPL image of the top surface of the cuvette. A ring pattern is formed on the top surface of the cuvette. (C): Spectral phasor analysis. (D): The Ti:Sa beam focus is 10 μm above the bottom surface of the cuvette. (E): TPL image of the bottom surface of the cuvette. A ring pattern is formed on the bottom surface of the cuvette (80 μm deep). (F): Spectral phasor analysis. (Reproduced from Chen et al. [40] by permission of the IOP Science)

Chen et. al. used the photothermal trapping of GNRs to manipulate and pattern them on the top and bottom surfaces of the cuvette. As demonstrated in Fig. 3.6.A and Fig. 3.6.D, the Ti:Sa beam focus was placed either closer to the top surface or to the bottom surface of the cuvette. At these two positions, they managed to create ring patterns of GNRs on the surface, as shown in Fig. 3.6.B and Fig. 3.6.E. The ring is formed at the interface between the laser beam and the glass cuvette. The temperature difference between the cuvette and the solution makes GNRs stick on the glass surface closer to the beam focus [98]. On GNRs within the ring, the trapping force from the convection flow and the repelling force from the thermophoresis reach balance. These two images indicate that the photothermal trapping can be used to manipulate and navigate GNRs.

In summary, the high photothermal conversion efficiency of GNRs exposed to SPR wavelengths allows an effective conversion of absorbed photon energy into heat, which

in turn leads to the photothermal trapping effect. The average Ti:Sa power capable of inducing the photothermal trapping could be as low as 0.5 mW. The Ti:Sa beam excited TPL signal can be used to image and monitor the photothermal process of GNRs.

However, all measurements conducted by this TPL technique were with GNRs diffused in clear media (water). The photothermal trapping of GNRs in complex media such as scattering media or biological sample is unknown. Since GNRs are seeing a wide use in biomedical applications, their behaviour in tissue is worth investigating. Unfortunately, the TPL detection is not sufficiently sensitive enough if GNRs are diffused in complex media.

One alternative solution to the challenge of imaging and detecting the photothermal behaviour of GNRs in media with more complex scattering and absorption parameters is to use phase sensitive OCT. Since most photon energy absorbed by GNRs is converted into heat, the generated local temperature gradient would create a local refractive index variation and local vibration of the part containing GNRs. The refractive index variation and local vibration is equivalent to the local OPD variation which can be detected by a phase sensitive OCT system, and the obtained result could be used to study the photothermal trapping of GNRs in complex media.

3.5.2 Photothermal detection of GNSHs using phase sensitive SS-OCT

Instead of detecting the TPL signal, Adler et. al. employed a swept source based phase sensitive OCT system to detect the local OPD variation induced by the photothermal response of GNSHs to the Ti:Sa beam [63]. They introduced a photothermal modulation of GNSHs by chopping the Ti:Sa laser beam at a certain frequency. The modulated Ti:Sa beam induced a small-scale localized temperature oscillation at the chopping/modulation frequency. Then, the temperature oscillation resulted in an OPD variation which was measured by the phase sensitive SS-OCT [63].

Compared with the TPL detection, where the generated TPL signal is weak, the technique of phase sensitive OCT has a few advantages. Firstly, the employed phase sensitive OCT system exhibits a nanometre-scale displacement sensitivity to detect the OPD variation. Secondly, SS-OCT has the ability to perform depth-resolved measurement, which means that the detection can be made at different axial layers of interest in the sample without axially moving the sample or the beam focus as the TPL detection did.

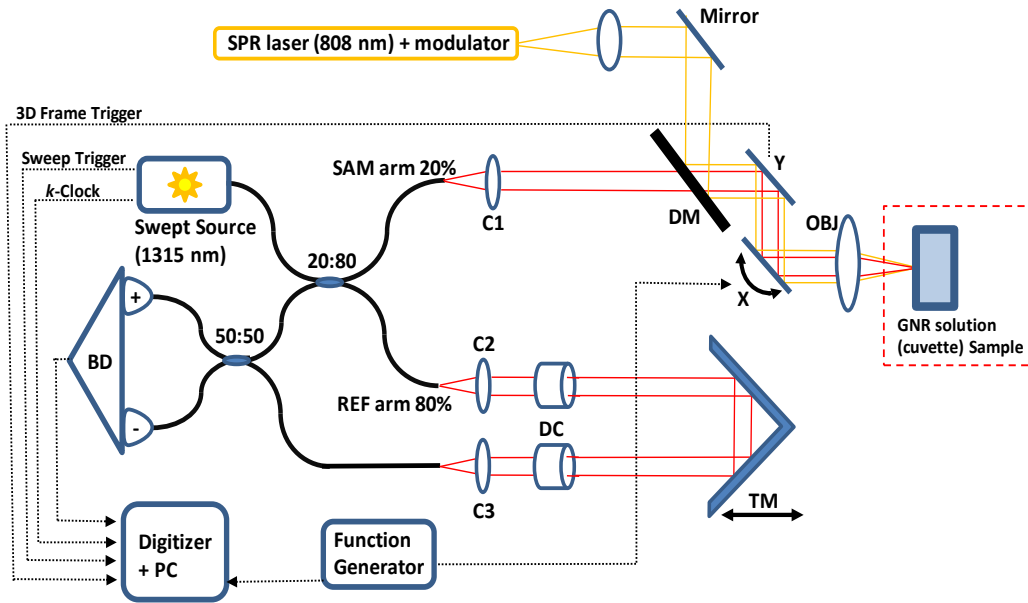


Fig. 3.7. Swept-source based phase sensitive OCT system with photothermal modulation devices. OCT swept source (FDML) operates at a centre wavelength of 1315 nm and a sweep rate of 240 kHz. Collimating lenses (C1, C2, C3). Objective lens (OBJ). Dichroic mirror (DM). Galvanometer mirrors (X, Y). Balanced photodiode (BD). Sample under investigation: a glass cuvette filled with the GNSH solution.

The phase sensitive SS-OCT system for photothermal detection of GNSHs is demonstrated in Fig. 3.7. Given by the reference [63], the GNSH solution has a concentration of 10^{10} /mL. Each GNSH has a core diameter of 120 nm, a shell thickness of 16 nm and a SPR wavelength of 780 nm. The GNSH solution is held in a glass cuvette, where the first glass/liquid interface provides the reference phase. The signal phase is measured on the liquid/glass interface. The reference phase measured from the front inner surface of the cuvette is always subtracted from the measured phase to remove the noise contributed by the air flow in free space. A fibre coupled 808 nm laser beam is coaxially combined with the OCT beam (centred at 1315 nm) by a dichroic mirror. The 808 nm laser is modulated by a digital pulse generator which is synchronized to the beginning of each wavelength sweep of the swept source. A pair of galvo-scanners are used to scan the combined beam over the cuvette.

To prove that the GNSHs can generate the photothermal response to the 808 nm beam, Adler et. al. modulated the 808 nm beam and performed phase measurements on two cuvettes separately filled with the pure deionized (DI) water and the GNSH solution. According to the published results [63], when the sample is DI water, the phase traces are featureless regardless of whether the laser is activated or not. In contrast, using the GNSH solution as the sample, strong phase response is observed only when the

modulated 808 nm laser beam is activated, and the photothermal response of the GNSH solution shows the same modulation frequency as the 808 nm beam.

The result indicates that the absorption of DI water to the 808 nm beam is not sufficient enough to cause localized heating. In contrast, the photothermal response of GNSHs to the modulated 808 nm beam creates a localized temperature variation that induces a localized OPD variation in the sample. In essence, the phase sensitive SS-OCT system is detecting the OPD variation. The phase noise of the system was measured to be 2.2 mrad, corresponding to a displacement sensitivity of 0.15 nm of the phase sensitive SS-OCT system.

A set of measurements were performed at different modulation frequencies (1 kHz, 15 kHz and 60 kHz) of the 808 nm beam. The results indicate that if the modulation frequency of the 808 nm beam increases, the GNSH sample has less time to dissipate heat, and the photothermal response of the sample becomes complex.

In order to enhance the measurement sensitivity, Alder et. al. performed Fourier transforms (FFT) to output traces. Performing FFT on the output phase gives the frequency of the OPD variation. When the modulation frequency of the 808 nm beam increases, the output phase behaviour is getting harder to distinguish. In this case, the amplitude of the FFT peak at corresponding frequency provides an enhanced measure to quantify the photothermal response of GNSHs.

As discussed in section 3.4.1, the TPL imaging approach investigates the photothermal trapping process of gold nanoparticles by detecting the weak TPL signal. In comparison, the phase sensitive SS-OCT technique detects the photothermal response of gold nanoparticles by measuring the OPD variation. Since 96% of the absorbed photon energy by gold nanoparticles is converted into heat, measuring the OPD variation caused by thermal expansion is more efficient than detecting the TPL signal linked to a fraction of the remaining 4% of the absorbed energy. Consequently, the phase sensitive SS-OCT technique is superior to the TPL imaging approach in terms of the measurement sensitivity. However, the phase sensitive SS-OCT in [63] was not employed to generate images of the aggregated gold nanoparticles as the TPL imaging approach did.

3.6 Discussion and conclusion

Besides gold nanoparticles, other nanoparticles are of interests in biomedicine. Superparamagnetic iron oxide nanoparticles (SPIONs) are currently used for magnetic sensing, targeted drug delivery, hyperthermia treatment and magnetic resonance imaging [101]. Since SPIONs are not intrinsically fluorescent and lack optical contrast, classical optical microscopy methods are not suitable to detect and image them especially in tissue sample. In the work Bogart et al. [102], photothermal microscopy is used to image SPIONs in cells. Photothermal microscopy employs, similar to the photothermal OCT technique discussed in section 3.5.2, a modulated heating/pumping beam to modulate the photothermal response of SPIONs. The generated photothermal response creates a local refractive index variation which is then detected by another probing beam and lock-in detection. Like phase sensitive OCT, the photothermal microscopy detects the interferometric phase variation. The results in Bogart et al. [102] indicate that by using photothermal microscopy, the photothermal imaging presents a better contrast than the fluorescence imaging of cells containing SPIONs.

Compared with phase sensitive OCT, photothermal microscopy is not able to perform depth resolved imaging. In addition, the specimen studied in photothermal microscopy have to be cut into thin slices, whilst the specimen in OCT does not need to be sliced since OCT detects the back scattered light. In photothermal microscopy, one raster scanning made by a pair of galvo-scanners generates a microscopy (lateral cross-section) image of the detected sample. In contrast, one raster scanning in OCT generates a 3D image of the detected sample, from which the lateral cross-section images at particular depths of interests can be sliced. The 3D imaging of OCT will be demonstrated in Chapter 4 and Chapter 5.

Photothermal heterodyne imaging is another technique used to image non-fluorescent nanoparticles [105]. Different types of soft matter systems, including polystyrene beads, thin polymer films, and *Escherichia coli* bacterial cells, present sensitivity of the photothermal heterodyne technique [106]. Like photothermal microscopy, photothermal heterodyne employs a modulated heating/pumping light to modulate the photothermal response of studied nanoparticles. Unlike the photothermal microscopy and phase sensitive OCT that detects the interferometric phase variation, photothermal heterodyne detects the optical frequency or wavelength shift of the probing beam without using interference. Since the wavelength shift has the same

modulation frequency as the modulated heating beam, the lock-in detection is used in the technique. Compared with the other two techniques, the sensitivity of photothermal heterodyne lies two orders of magnitude above them, which allows it for the detection of individual gold nanoparticles [106]. However, unlike phase sensitive OCT, photothermal heterodyne is not capable of axial cross-section (tomography) imaging due to its limited detection depth.

This chapter provides a brief description of gold nanoparticles, including their optical properties and their applications in biomedicine. The optical and photothermal trapping schemes applied to gold nanoparticles are discussed.

This chapter discusses two techniques that were reported to study the photothermal effects of gold nanoparticles: the first technique detects the TPL signal to image the aggregated gold nanoparticles resulting from the photothermal trapping; the other technique employs a phase sensitive SS-OCT system to measure the photothermal response of gold nanoparticles. Each technique has its own advantages and disadvantages. The TPL approach is able to image the gold nanoparticle cluster caused by the photothermal trapping, but using a photon counter detector to detect the weak TPL signal could not guarantee a robust signal to noise ratio (SNR). Furthermore, despite being an important factor, the temperature variation during the process was ignored in the TPL technique. In comparison, the detection of phase sensitive SS-OCT technique is more efficient as discussed in 3.5.2. In addition, the phase sensitive OCT technique provides measurement sensitivities of around 0.1 nm and superior SNR with the help of the FFT analysis. However, the reported phase sensitive SS-OCT technique performs measurements only in the A-scan mode, without generating the 2D image of gold nanoparticles. Another drawback of the phase sensitive SS-OCT technique is that the photothermal trapping phenomenon of gold nanoparticles was disregarded. All measurements presented in two reports were made on gold nanoparticles diffused in clear media, with neither of the two techniques used to perform detection of gold nanoparticles in scattering media or biological tissue.

Although phase sensitive OCT has great potential, a swept source based phase sensitive OCT system might not be the optimal choice to generate *en-face* phase images to study the photothermal trapping of gold nanoparticles in complex media. This is because SS-OCT systems typically require the implementation of additional devices to stabilize the output phase. In contrast, the spectrometer based OCT has a nanometre-

scale measurement sensitivity, and no extra device is needed in the setup to stabilize the output phase. Hence, the author of this thesis developed a spectrometer based phase sensitive OCT system to perform the photothermal detection and imaging of gold nanoparticles in biological tissue.

Chapter 4

Spectrometer based phase-sensitive OCT and its application in dynamic photothermal detection and imaging of GNRs in clear media and biological tissue

4.1 Introduction

The theoretical and experimental studies of photothermal trapping of micro particles have been explained earlier [64][65][66]. However, until recently not much attention was given to the photothermal trapping of GNRs [40][65]. As discussed in section 3.4, it is becoming increasingly important to develop suitable methods for imaging GNRs and measuring their unique optical properties. In the published work [40], the aggregated GNRs resulting from photothermal trapping are imaged by detecting the two-photon luminescence (TPL) signal. However, the detection of the weak TPL signal was demonstrated only on GNRs diffused in clear media, not in biological tissue or other scattering media.

OCT has the capability to detect OPD variations of any particular layers of interest at depths of several mm in biological tissue. Because 96% of the photon energy absorbed by GNRs is converted into heat via non-radiative electron relaxation [40], using OCT to perform photothermal detection of GNRs in biological tissue should be an approach with higher efficiency and sensitivity than TPL detection if background fluorescence exists. In addition, The TPL detection might be disturbed if a background fluorescence exists in the studied specimen. As discussed in section 3.5.2, a swept source based phase sensitive OCT system with high measurement sensitivity and detection depth has been employed to image GNRs in water. However, complexity was added to the setup in order to mitigate the effects of swept source jitter noise.

In order to investigate and image the photothermal trapping of GNRs in biological tissue, a more efficient detection technology than both the TPL and the SS-OCT is desirable. The technique should have simple setup, acceptable detection depth, high measurement sensitivity, and the ability to produce 2D images of GNRs. To meet these requirements, a quantitative spectrometer based phase sensitive OCT system was developed by the author in the Applied Optics Group at the University of Kent. In this system, an OCT beam was directed in such a way as to coaxially overlap with a Ti:Sa laser beam providing photothermal excitation, with the goal of investigating and imaging photothermal trapping of GNRs in clear and biological media.

The principle of the phase measurement in phase sensitive OCT is discussed in the beginning of this chapter. Several experiments will be demonstrated in this chapter, as follows:

- The phase sensitive SD-OCT system was calibrated through dynamic phase measurements of piezo motions with known driving parameters.
- We measured and compared the displacement sensitivities of the system at different camera exposure time settings in two SD-OCT configurations: the configuration with a distinct reference path and a sample path; and the other configuration employing a common sample/reference path.
- The minimum Ti:Sa power capable of inducing a detectable photothermal response of GNRs was measured to be 0.5 mW. This value agrees with the latest reported minimum Ti:Sa power for the photothermal trapping of GNRs.
- The SD-OCT system was used to generate *en-face* phase images of aggregated GNRs resulting from the photothermal trapping. The imaging contrast was enhanced by displaying the difference between successive *en-face* phase images while the Ti:Sa beam was modulated.
- The photothermal trapping of GNRs in biological tissue showed a greater complexity than in the clear media.

The study discusses the application of phase sensitive SD-OCT in imaging the photothermal trapping of GNRs.

4.2 Measuring micro vibration using phase sensitive OCT

Employing phase sensitive OCT to measure micrometre scale OPD fluctuations has been discussed and mathematically evaluated in earlier studies [63][67][68][69]. In frequency domain OCT, the interferogram, containing the information of one reflective layer of the detected sample, obtained in frequency domain is expressed as:

$$I(k) = 2|E_R E_S| \cos(k2z + \varphi) \quad (4.1)$$

where $k = 2\pi/\lambda$ is the wavenumber, φ is the random system noise added to phase, and $2z$ is the OPD between reference path and the sample path if OPD = 0 is placed at the top of the sample. A complex Fourier transform of $I(k)$ gives the interferogram $I(z)$ in time domain:

$$I(z) = FT[I(k)] = A(z) \exp[i\Phi(z)] \quad (4.2)$$

where the magnitude $A(z)$ serves to reconstruct conventional OCT images, and $\Phi(z)$ provides the phase information at the optical depth z in the sample. Both $A(z)$ and $\Phi(z)$ contain depth resolved structural sample information, and both $A(z)$ and $\Phi(z)$ vary with the OPD in the axial direction. The difference is that the amplitude $A(z)$ cannot be used to measure any OPD variation smaller than the axial resolution of the OCT system, whereas the phase $\Phi(z)$ can be used to measure the OPD variation smaller than the axial resolution. According to Eq. (4.1), the relation between $\Phi(z)$ and the OPD variation over time $z(t)$ can be expressed as:

$$\Phi(z, t) = 2 \times \frac{2\pi}{\lambda} \times n \cdot z(t) + \varphi \quad (4.3)$$

where φ is the random noise, n is the refractive index of the media, and the factor of 2 comes from the double path of the beam in the OCT sample arm. If the OPD variation is a periodic movement, for instance a sinusoidal vibration with vibrating magnitude A and frequency f_0 , Eq. (4.3) becomes:

$$\Phi(z, t) = 2 \times \frac{2\pi}{\lambda} \times n \cdot A \cdot \sin(2\pi f_0 t) + \varphi \quad (4.4)$$

According to Eq. (4.4), $\Phi(z, t)$ behaves in a sinusoidal manner that has the same frequency f_0 with the sinusoidal vibration. By measuring the amplitude of the $\Phi(z, t)$ trace, the vibration amplitude A of the source can be obtained.

In practice, the $\Phi(z, t)$ trace can be generated using a phase sensitive OCT system, and the sinusoidal vibrating source could be a piezo actuator driven by sinusoidal voltages. However, as seen in Eq. (4.4), this method suffers from the random phase noise φ . To overcome φ , another method generating the trace of phase differential $\Delta\Phi(z, t)$ can be applied.

By calculating the phase difference $\Delta\Phi(z, t)$ between two successive $\Phi(z, t)$ values that are obtained between a time interval Δt , the noise term φ in Eq. (4.3) can be cancelled:

$$\Delta\Phi(z, t) = \frac{8\pi^2}{\lambda} \times n \cdot A \cdot f_0 \cdot \cos(2\pi f_0 t) \cdot \Delta t \quad (4.5)$$

According to Eq. (4.5), by measuring the amplitude of the $\Delta\Phi(z, t)$ trace, the vibration magnitude A of the sinusoidal vibration can be obtained. This method is immune to the phase noise term φ in Eq. (4.4) if only the frequency of φ is high. However, the method becomes limited in sensitivity when the amplitude of the $\Delta\Phi(z, t)$ trace is as low as its noise floor [68]. To overcome this limitation, Fourier analysis could be applied to the $\Delta\Phi(z, t)$ trace to separate the signal from the noise. Specifically, performing a FFT on Eq. (4.5) gives a FFT peak at the pre-known frequency f_0 of the vibration. By measuring the amplitude of the FFT peak, the vibration amplitude A of the vibrating source can be obtained:

$$\text{FFT}[\Delta\Phi(z, t)] = p(z, f) = \frac{4\pi^2}{\lambda} \cdot A \cdot f_0 \cdot \Delta t \xrightarrow{\text{yields}} A = \frac{|p(f_0)| \cdot \lambda}{4\pi^2 \cdot f_0 \cdot \Delta t} \quad (4.6)$$

where $|p(f_0)|$ is the amplitude of the FFT peak, and f is the vibration frequency variable.

As discussed above, to work out the displacement amplitude of micro vibrations, three different methods can be used by using the same phase sensitive OCT system. Each method generates one of the output traces: $\Phi(z, t)$, $\Delta\Phi(z, t)$ and $\text{FFT}[\Delta\Phi(z, t)]$. By measuring the magnitude of each trace, Eq. (4.4), Eq. (4.5) or Eq. (4.6) can be used to calculate the displacement amplitude of the vibrating source. As will be demonstrated

in section 4.4.2, we compared the experimental results obtained from each of the three methods to the piezo actuator datasheet to evaluate and compare the effectiveness of these three methods.

4.3 System configuration

The schematic of the phase sensitive SD-OCT system built by the author is presented in Fig. 4.1. The OCT source is a superluminescent diode (Amonics, ALS-1050-S, 13 mW, 35 nm bandwidth centred at 1050 nm). The output light travels through a fibre isolator and subsequently a 2×2 fibre-optic Michelson interferometer composed of a 50:50 fibre coupler (Thorlabs, TW1064R5A2A). Using collimating lenses (Thorlabs, F220APC-1064), 2.4 mm diameter beams are formed in both arms. In the sample arm of the interferometer, after a dichroic mirror, the OCT beam is coaxially combined with a Ti:Sa laser (Coherent, Mira Seed, 3 mW output power, 80 MHz repetition rate, 2 mm diameter, 150 fs pulse duration, 25 nm bandwidth centred at 800 nm) beam used as the photothermal excitation source. The superposed beams are incident on a pair of galvanometer mirrors (Thorlabs, GVS302) and subsequently an objective (Thorlabs, LSM02-BB, focal length = 18 mm) producing a focused spot size of 3.1 μm on the sample. The Ti:Sa beam is modulated by an optical chopper wheel. In the reference arm of the interferometer, a glass block is used to compensate the dispersion created by the objective in the sample arm. Light beams returning from both arms interfere at a commercial spectrometer (BaySpec, OCTS-10001050-1100) consisting of a high speed line scan CMOS camera (Goodrich SUI, SU1024-LDH, maximum line rate: 47000 kHz, digital output rate: 14-bit). The camera has 1024 pixels with the pixel size of 25×500 μm and a spectral range of 900 nm, resulting in a spectral resolution of 0.88 nm at the centre wavelength of 1050 nm. The output signal from the camera is then digitized by a camera link image acquisition card (National Instruments, PCIe-1430) installed in a computer.

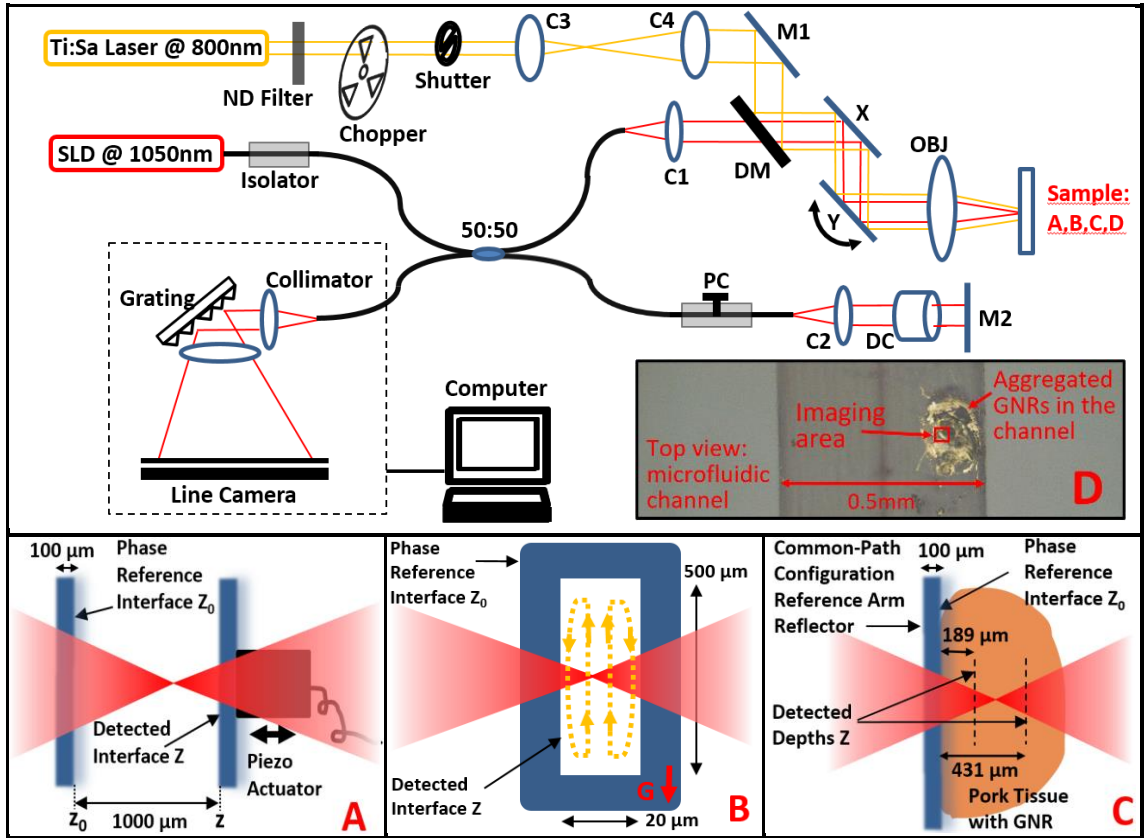


Fig. 4.1. Schematic layout of phase sensitive SD-OCT with photothermal detection capability. Superluminescent diode (SLD), neutral density filter (ND Filter), collimating lenses (C1,C2), fibre coupler (50:50), achromatic doublets (C3,C4), dichroic mirror (DM), scanning mirrors (X,Y), objective lens (OBJ), dispersion compensating block (DC), mirrors (M1,M2), polarization controller (PC). The sample is replaced by inserts (A), (B) and (C). Insert (D): 10 \times microscopy view of aggregated GNRs resulted from photothermal trapping in a microfluidic channel. In (A), the front surface of the first coverslip was used as the reference mirror/reflector if the common-path OCT setup was employed. (B) was used only in the separate sample/reference path OCT setup. In (B), the arrows show direction of the convective flow of the GNR solution inside the cuvette. The direction of these arrows considers the gravitational force (labelled as G) and the position of the Ti:Sa beam focus. In (C), the front surface of the coverslip was used as the reference mirror/reflector if the common-path OCT setup was employed.

During our measurements, since the light falling on the pixels located towards the two edges of the camera sensor array exhibited no interferometric feature, 674 out of 1024 elements in the middle of the camera sensor array were actually enabled. A B-spline interpolation algorithm was devised to rescale and resample the chirped interferogram (the chirp effect will be discussed in detail in Chapter 5 and Chapter 6). Thus, the calibrated interferogram had 674 data points evenly distributed in k -space. The calibrated interferogram then underwent a complex FFT, obtaining a depth-resolved 337-pixel A-scan intensity profile and a depth-resolved 337-pixel A-scan phase profile. In conventional OCT, the A-scan intensity profile was used to build the

B-scan image of the studied object. The A-scan phase profile was used only in phase measurements.

This SD-OCT system was evaluated to have an axial resolution of $17\ \mu\text{m}$ and an imaging depth of $z_{range} = 1.44\ \text{mm}$ in air (where the sensitivity decays by 6 dB from $z = 0$). This evaluation was performed by taking A-scan measurements using a mirror in the sample arm. The full width at half maximum (FWHM) of the A-scan peak of the mirror surface was used to arrive at a value for the axial resolution of the system for each type of sample (see later discussion in 4.4.9; for example, using a refractive index value of $n = 1.38$ for the biological tissue we used, the axial resolution and imaging depth in such tissue become respectively $12\ \mu\text{m}$ and $1.01\ \text{mm}$).

The absolute phase value $\varphi(z, t)$ at the depth of interest z in the sample was retrieved in two steps. Firstly, in the A-scan intensity profile, we identified the pixel order corresponding to the interested depth z . Then, we extracted the phase value $\varphi(z, t)$ of the same pixel order in the A-scan phase profile.

When an OCT system is used to perform phase measurements, the setup that configured with a separate reference arm and a separate sample arm is subject to random phase noise created by mechanical or thermal fluctuations in each independent arm [70]. In comparison, the OCT setup configured with a common sample/reference path experiences less mechanical or thermal fluctuations. In our SD-OCT system, both configurations can be applied. As shown in Fig. 4.1, the common path configuration is realised by blocking the beam in the reference arm, and placing a $100\ \mu\text{m}$ thick microscope coverslip in front of the sample being imaged/measured. The front (air/glass) surface of the first (left) coverslip shown in Fig. 4.1.A and Fig. 4.2 serves as the reference mirror in the common sample/reference path configuration for the series of measurements described in 4.4.1-4.4.5. Likewise, the front surface of the coverslip that is attached to the tissue sample, shown in Fig. 4.1.C, serves as the reference mirror in the common sample/reference path configuration for the series of measurements described in 4.4.9-4.4.10.

Considering the need to mitigate against phase noise, the common path configuration was always the preferred option. However, due to the geometry of the samples tested, the independent reference arm configuration had to be employed for some measurements. The choice of the system configuration will be clarified in each section.

Using either the common path configuration or the independent reference arm configuration, since phase values of all points along the same axial line are obtained in the same A-scan measurement over 2 ms, all phase data experience the same noise. This is because random fluctuations happen on a much longer timescale than 2 ms. Consequently, the phase noise can be removed by subtracting a reference phase from the signal phase. As demonstrated in Fig. 4.1.A, the reference phase $\varphi(z_0, t)$ is measured on the back surface (at z_0) of the first coverslip, and the signal phase $\varphi(z, t)$ is measured on the front surface (at z) of the coverslip mounted on the piezo actuator. Likewise, as demonstrated in Fig. 4.1.C, the reference phase $\varphi(z_0, t)$ is measured on the back surface (at z_0) of the coverslip, and the detected phase $\varphi(z, t)$ is measured at different axial locations in the tissue sample. The dynamic difference $\Phi(z, t)$ between $\varphi(z, t)$ and $\varphi(z_0, t)$ can be calculated as:

$$\Phi(z, t) = \varphi(z, t) - \varphi(z_0, t) \quad (4.7)$$

In our measurements, $\Phi(z, t)$ was obtained by calculating the cross-power term $Y_{zz_0}(t)$ between the complex A-scan profiles obtained from the reference interface z_0 and the interferogram obtained from the detected interface z , as demonstrated in Fig. 4.1.A. Then, $\Phi(z, t)$ can be calculated as:

$$Y_{zz_0}(t) = Y_z(t) \cdot \overline{Y_{z_0}(t)} = AA_0 e^{i(\varphi(z,t) - \varphi(z_0,t))} = AA_0 e^{i(\Phi(z,t))} \quad (4.8)$$

where $Y_z(t)$ and $Y_{z_0}(t)$ are complex A-scan values obtained from interfaces z and z_0 . In our measurements, a reference surface was always employed to provide the reference phase $\varphi(z_0, t)$ to eliminate the phase noise on the output signal, as demonstrated in Fig. 4.1.B and Fig. 4.1.C. In the rest of the thesis, the expression “detected phase signal” refers to $\Phi(z, t)$ instead of $\varphi(z, t)$. The LabVIEW implementation calculating $\Phi(z, t)$ is presented in Fig. A.1.

4.4 Methodology and Results

The methodology and corresponding results are presented across several sections below.

To start with, the operating performance of the phase sensitive SD-OCT system was tested in controlled conditions, using a piezo actuated coverslip to provide small

amounts of movement in the sample arm. This is done without the need to operate the Ti:Sa laser in Fig. 4.1 since there is no photothermal effect. The procedures of characterizing the performance are demonstrated in sections 4.4.1 to 4.4.5, which provide a comprehensive analysis of the system performance.

In section 4.4.1, the procedures of generating three different output traces of $\Phi(z, t)$, $\Delta\Phi(z, t)$ and $\text{FFT}[\Delta\Phi(z, t)]$ are demonstrated.

In section 4.4.2, based on the measurements of these three output traces, the recovered displacement amplitude is compared with the data sheet of the piezo actuator, effectively performing a calibration of the phase measurements carried out with the SD-OCT system.

In section 4.4.3, the displacement sensitivity of the OCT system is characterized in two setup configurations: the common path configuration and the independent reference arm configuration.

In section 4.4.4, with the system working in the common path configuration, the degradation of displacement sensitivity to defocus is characterized.

In section 4.4.5, the FFT analysis is carried out on the output phase to improve the displacement sensitivity of the system.

From section 4.4.6 to section 4.4.9, the Ti:Sa laser in Fig. 4.1 is enabled, and the phase sensitive OCT system is used for the photothermal detection and imaging of GNRs in DI water and in the bio-tissue sample. Section 4.4.6 characterizes the photothermal response of GNRs to the modulation frequency of the Ti:Sa laser beam. Section 4.4.7 characterizes the photothermal response of GNRs to the output power of the Ti:Sa laser beam.

After the measurements demonstrated in section 4.4.7, aggregated GNRs resulting from the photothermal trapping by the Ti:Sa beam was observed. The procedure of photothermal imaging of the aggregated GNRs in the DI water is demonstrated in section 4.4.8. The procedure of photothermal imaging of GNRs in the bio-tissue sample is demonstrated in section 4.4.9.

4.4.1 Output traces

To work out the displacement amplitude A of a target subjected to periodic vibrations, either of the three methods discussed in section 4.2 can be applied. These

methods can generate output traces of the phase $\Phi(z, t)$, the phase differential $\Delta\Phi(z, t)$ and the Fourier transform $\text{FFT}[\Delta\Phi(z, t)]$ respectively. By measuring the magnitudes of each of these traces, the values can be substituted into Eq. (4.4), Eq. (4.5) and Eq. (4.6) respectively to calculate the displacement amplitude A of the vibrating source.

All measurements in this section were performed in the setup employing the common path configuration, by blocking the path of the beam propagating in the separate reference arm shown in Fig. 4.1 and utilising instead the reflection provided by the front surface of the coverslip in front of the vibrating sample in the object arm. As shown in Fig. 4.1.A or Fig. 4.2, the vibrating target employed here is a 100 μm thick glass coverslip mounted on a piezo actuator (Thorlabs, PA4FEW). When driven by pre-set sinusoidal voltages, the piezo actuator undergoes periodic vibrations with known frequencies and amplitudes. Another stationary coverslip is placed 1000 μm in front of the actuated one. The axial positions of these coverslips were adjusted such that the OCT beam is placed in the middle of the two coverslips. This separation between two coverslips was chosen to prevent air vibration.

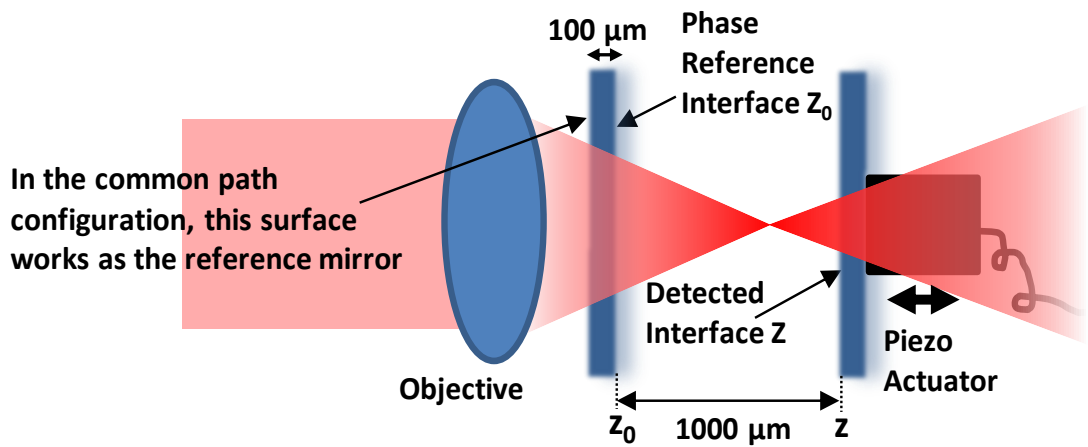


Fig. 4.2. Zoomed image of Fig. 4.1.A. The front surface of the stationary glass coverslip works as the reference mirror when the system is working in the common path configuration. The reference phase $\varphi(z_0, t)$ was measured on the interface at z_0 , and the signal phase $\varphi(z, t)$ was measured on the front surface of the actuated coverslip.

As seen in Fig. 4.2, the front surface of the stationary coverslip serves as the reference mirror for the common sample/reference path configuration. The back surface (at z_0) of the stationary coverslip provides the reference phase $\varphi(z_0, t)$, and the phase $\varphi(z, t)$ containing the vibration information is measured on the front surface (at z) of

the actuated coverslip. The output phase $\Phi(z, t)$ is calculated according to Eq. (4.7) and Eq. (4.8).

4.4.1.(a) Output trace of phase $\Phi(z, t)$

To begin with, phase measurements were performed on the front surface of the actuated coverslip at depth z (Fig. 4.2). The piezo actuator was driven by sinusoidal voltages first with a fixed frequency (10 Hz) and different amplitudes (1 V, 2 V, 3 V, 4 V), then with a fixed amplitude (4 V) and different frequencies (5 Hz, 10 Hz, 15 Hz, 20 Hz). The dynamic traces of $\Phi(z, t)$ obtained from two groups of driving parameters are presented in Fig. 4.3 and Fig. 4.4 respectively. During the measurement, a random phase drift (presented as φ in Eq. (4.4)) added a varying DC component to $\Phi(z, t)$. For ease of comparison, the $\Phi(z, t)$ traces in Fig. 4.3 and Fig. 4.4 were moved laterally and vertically to overlap with each other to allow for easier visual comparisons of frequency and amplitude.

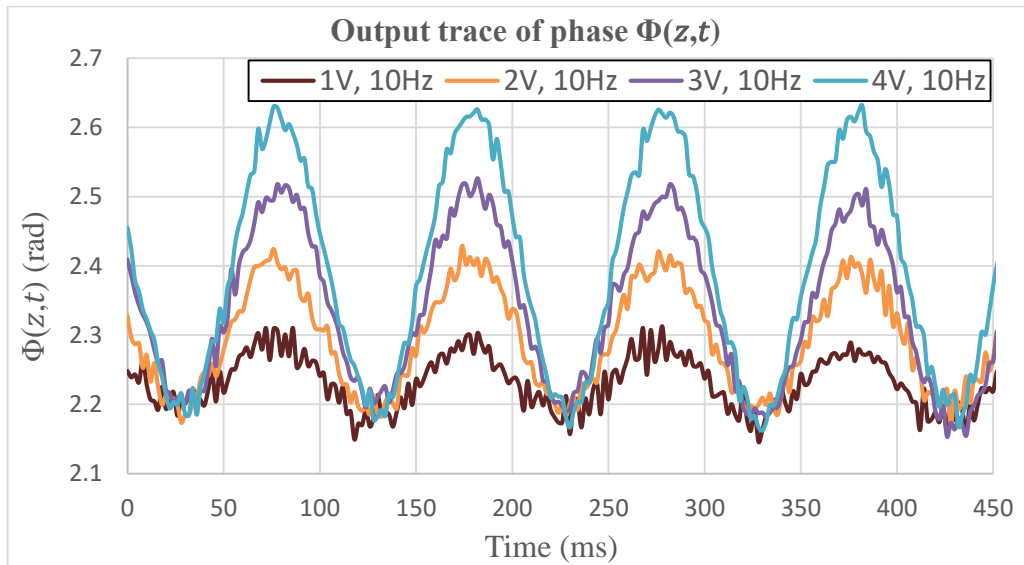


Fig. 4.3. Output trace of $\Phi(z, t)$. Measurements were made with the piezo actuator driven by sinusoidal voltages with fixed frequency (10 Hz) and different amplitudes (1 V, 2 V, 3 V, 4 V). Traces were moved laterally and vertically to overlap with each other for easier visual comparison.

As seen in Fig. 4.3, the output traces of $\Phi(z, t)$ have the same modulation frequency as the driving frequency (10 Hz) of the actuator. As expected, since the amplitudes of driving voltages are different, these output $\Phi(z, t)$ traces have different amplitudes. In contrast, as seen in Fig. 4.4, the obtained $\Phi(z, t)$ traces have roughly the same amplitude but their modulation frequencies are those of the driving actuator. It can

be concluded that all obtained $\Phi(z, t)$ traces in Fig. 4.3 and Fig. 4.4 agree with Eq. (4.4) where the modulation frequency of $\Phi(z, t)$ varies with the vibration frequency f_0 of the vibrating source, and the variation amplitude of $\Phi(z, t)$ varies with the vibration amplitude A of the vibrating source. To meet the purpose of obtaining the actual amplitude of the vibrating coverslip, firstly, we sent more sets of driving parameters to the actuator and measured the amplitudes of the generated $\Phi(z, t)$ traces. Then, we took the measured amplitude values into Eq. (4.4) to calculate the vibration amplitude A of the coverslip. The results are compared with the data sheet of the actuator, as will be demonstrated in section 4.4.2.

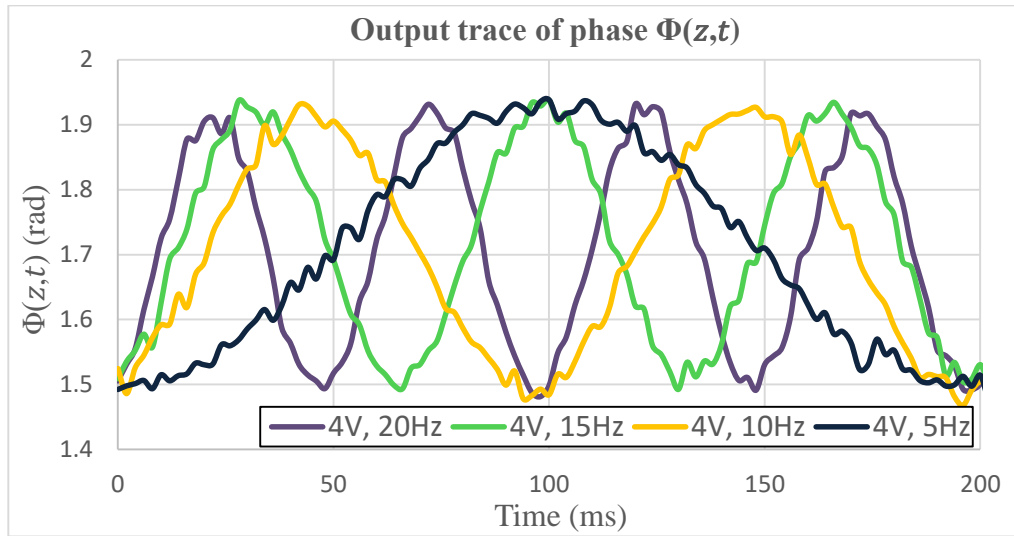


Fig. 4.4. Output trace of phase $\Phi(z, t)$. Measurements were made with the piezo actuator driven by sinusoidal voltages with a fixed amplitude (4 V) and different frequencies (5 Hz, 10 Hz, 15 Hz, 20 Hz). Traces were moved laterally and vertically to overlap with each other for easier visual comparison.

When the trace $\Phi(z, t)$ was measured over a time period of a few seconds, the phase noise term φ in Eq. (4.4) took random values. The net result was that φ caused the $\Phi(z, t)$ signal to drift in an unwanted fashion, which created inconvenience for data interpretation. The problem was solved by generating the output trace of the phase differential $\Delta\Phi(z, t)$.

4.4.1.(b) Output trace of phase differential $\Delta\Phi(z, t)$

As the second method, we employed the same system setup but made changes to the LabVIEW programme so that it dynamically output the trace of the phase differential $\Delta\Phi(z, t)$. In practice, $\Delta\Phi(z, t)$ is the difference between successive phase values $\Phi(z, t + \Delta t)$ and $\Phi(z, t)$ which were generated from successive A-scans with a

time interval of $\Delta t = 2$ ms. The value of Δt is determined by the A-scan rate (500 Hz) of the OCT system. During the measurement, the actuator was driven by sinusoidal voltages first with a fixed amplitude (4 V) and different frequencies (10 Hz, 25 Hz), then with a fixed frequency (5 Hz) and different amplitudes (14 V, 28 V, 42.5 V). The obtained $\Delta\Phi(z, t)$ traces from two groups of driving parameters are presented in Fig. 4.5 and Fig. 4.6 respectively.

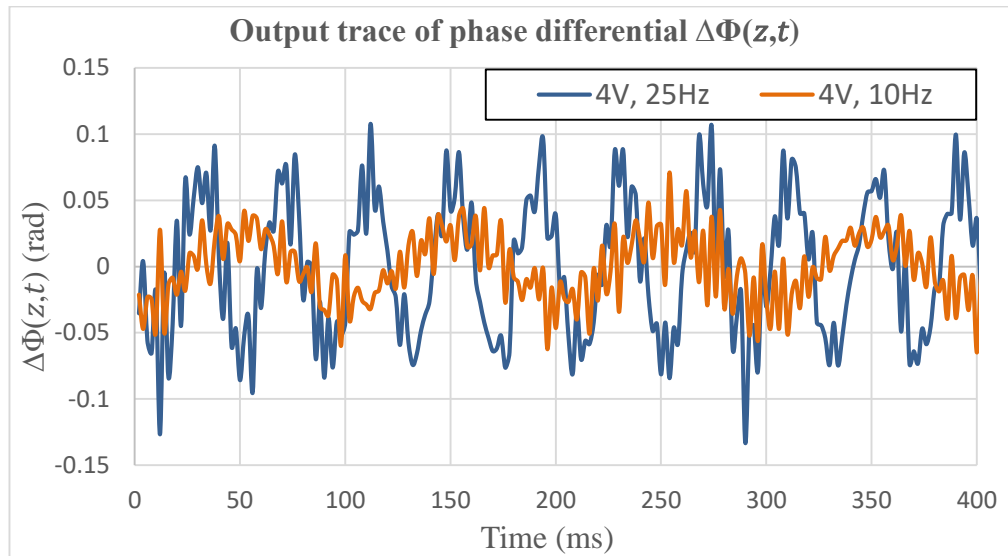


Fig. 4.5. Output trace of phase differential $\Phi(z, t)$. Measurements were made with the piezo actuator driven by sinusoidal voltages with a fixed amplitude (4 V) and different frequencies (10 Hz, 25 Hz). Traces were moved laterally to overlap with each other for easier visual comparison.

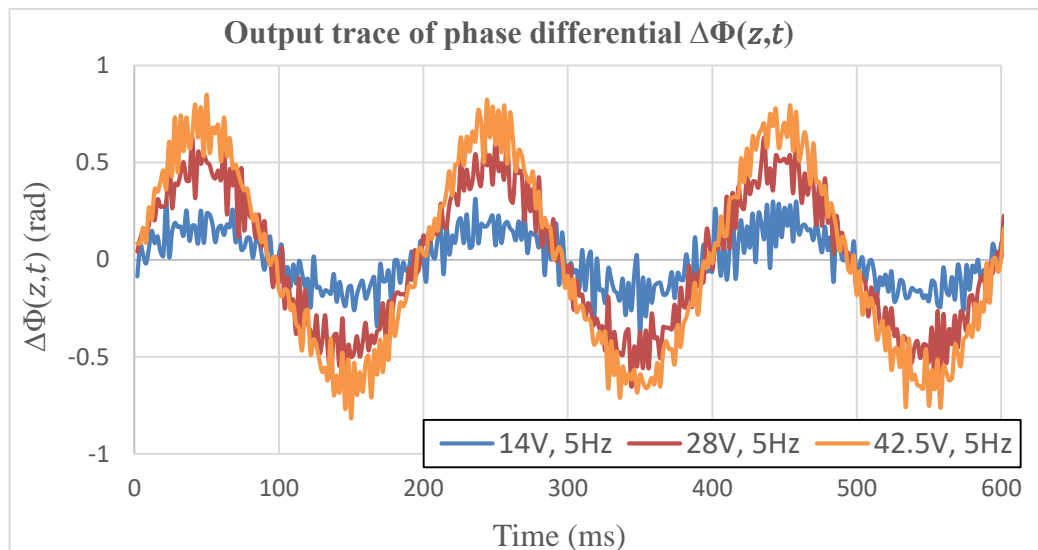


Fig. 4.6. Output trace of phase differential $\Phi(z, t)$. Measurements were made with the piezo actuator driven by sinusoidal voltages with a fixed frequency (5 Hz) and different amplitudes (14 V, 28 V, 42.5 V). Traces were moved laterally to overlap with each other for easier visual comparison.

For ease of comparison, the obtained $\Delta\Phi(z, t)$ traces were moved laterally to overlap with each other, as presented in Fig. 4.5 and Fig. 4.6. As seen from figures, since the random phase fluctuation (φ in Eq. (4.4)) is removed by the differentiation operation (from Eq. (4.4) to Eq. (4.5)), the obtained $\Delta\Phi(z, t)$ traces vary around 0 rad only, with no DC added.

Unlike the $\Phi(z, t)$ traces in Fig. 4.4, where the amplitude of $\Phi(z, t)$ trace is independent of the vibration frequency of the actuator, the amplitudes of the $\Delta\Phi(z, t)$ traces in Fig. 4.5 vary with the vibration frequency of the actuator. As expected, this result agrees with Eq. (4.5), where the vibrating frequency f_0 is a factor multiplying the cosine term and modifies the amplitude of $\Delta\Phi(z, t)$.

As seen in Fig. 4.6, with the vibration frequency of the actuator fixed but the vibration amplitude changed, the modulation frequencies of $\Delta\Phi(z, t)$ traces are equal to the vibration frequency of the actuator, whilst the amplitudes of $\Delta\Phi(z, t)$ traces vary with the vibration amplitudes of the actuator. Once again, as expected, this result agrees with Eq. (4.5), where the vibration amplitude A is only a factor of the modulation amplitude of $\Delta\Phi(z, t)$ and has no effect on the modulation frequency of $\Delta\Phi(z, t)$.

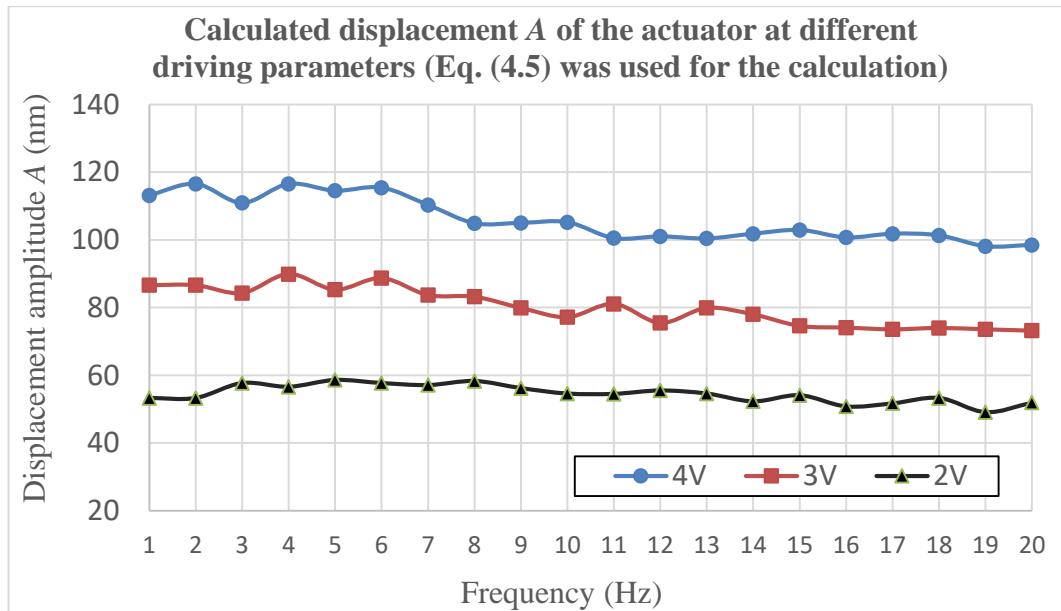


Fig. 4.7. Calculated displacement amplitudes A of the actuator driven by different parameters. The calculation is based on output traces of $\Delta\Phi(z, t)$. Eq. (4.5) was used to calculate the displacement amplitude A . The actuator was driven by sinusoidal voltages with different amplitudes (2 V, 3 V, 4 V) and different frequencies (1 Hz to 20 Hz, with 1 Hz interval).

Another test of the phase measurement performance of the SD-OCT system was performed by driving the actuator with sinusoidal voltages with different amplitudes (2 V, 3 V, 4 V) and frequencies (from 1 Hz to 20 Hz, at 1 Hz intervals). For each driving voltage, we measured the amplitude of the generated $\Delta\Phi(z, t)$ trace and used Eq. (4.5) to calculate the displacement amplitude A of the actuator. In the calculation, we assigned 0.002 s to Δt due to the A-scan rate (500 Hz) of the system. Calculated values of A are presented in Fig. 4.7. As seen, from 1 Hz to 20 Hz, the vibration amplitude of the actuator is more determined by the amplitude of the driving voltage and has less dependence on the driving frequency, as would be expected at low driving frequencies.

In summary, the results in section 4.4.1.(a) and section 4.4.1.(b) prove that the behaviour of $\Phi(z, t)$ and $\Delta\Phi(z, t)$ measured by our system is consistent with equations Eq. (4.4) and Eq. (4.5). Consequently, it can be concluded that the phase sensitive SD-OCT system behaves in an expected manner in measuring the nanometre scale vibration of the piezo actuator although the absolute values of our measurements are not yet calibrated against the manufacturer's datasheet.

4.4.1.(c) Output trace of $FFT[\Delta\Phi(z, t)]$

A third approach to recover phase with the same system setup employed a LabVIEW programme that dynamically output the trace of $FFT[\Delta\Phi(z, t)]$. While the system was running, the Fourier transform was performed on the last 1024 $\Delta\Phi(z, t)$ values stored in the acquisition buffer. A number of $FFT[\Delta\Phi(z, t)]$ traces are presented in Fig. 4.8, with the piezo actuator driven by sinusoidal voltages with a fixed frequency (5 Hz) and different amplitudes (from 10 V to 55 V, with 5 V interval).

In summary, by testing output traces of $\Phi(z, t)$, $\Delta\Phi(z, t)$ and $FFT[\Delta\Phi(z, t)]$ respectively, it can be concluded that the three methods introduced in section 4.2 are independent to each other for measuring the displacement amplitude of the actuator. In order to evaluate and compare these three methods, the values of A obtained from each method were compared with the data sheet (displacement against driving voltage) of the piezo actuator, as demonstrated in the following section.

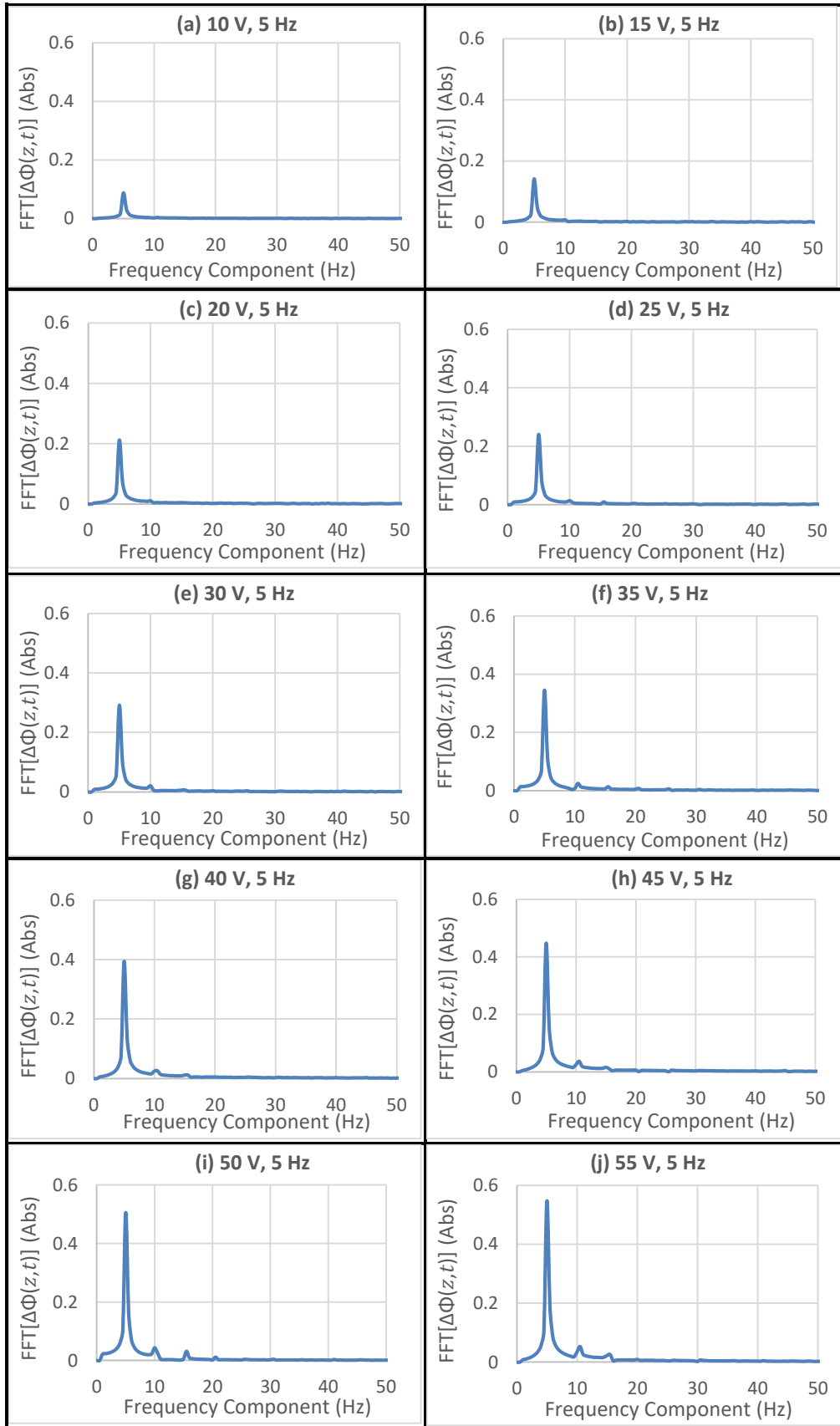


Fig. 4.8. Output traces of $\text{FFT}[\Delta\Phi(z,t)]$, obtained by performing the Fourier transform on the latest 1024 $\Delta\Phi(z,t)$ data. The piezo actuator was driven by sinusoidal voltages with a fixed frequency (5 Hz) and different amplitudes (10 V – 55 V, with 5 V interval).

4.4.2 Calibration

Measurements were made on the piezo actuator driven by sinusoidal voltages with a 5 Hz frequency and several different voltage values. The acquired data allowed retrieval of the absolute vibration amplitude in three different ways demonstrated in section 4.4.1, generating output traces of $\Phi(z, t)$, $\Delta\Phi(z, t)$ and $\text{FFT}[\Delta\Phi(z, t)]$. Eq. (4.4), Eq. (4.5) and Eq. (4.6) were used respectively to calculate the displacement amplitudes A of the actuator. The obtained results of A from all three methods are plotted against the driving voltage of the actuator, as presented in Fig. 4.9. In order to evaluate and compare the precisions of these methods and to calibrate the phase sensitive SD-OCT system, the “displacement to driving voltage” data sheet of the piezo actuator is also plotted in Fig. 4.9.

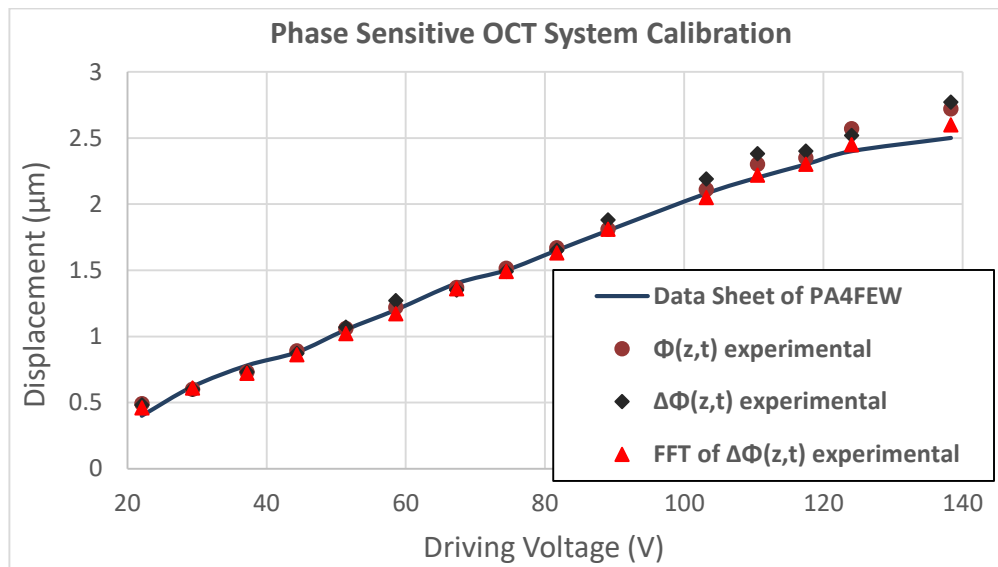


Fig. 4.9. System calibration. Measured amplitudes of traces of $\Phi(z, t)$, $\Delta\Phi(z, t)$ and $|p(f_0)|$ were taken into Eq. (4.4), Eq. (4.5) and Eq. (4.6) respectively to calculate the displacement amplitudes A of the actuator. Obtained results (coloured dots) of A are compared with the data sheet (blue line) of the actuator (PA4FEW, Thorlabs).

As seen in Fig. 4.9, the displacement amplitudes A obtained from each of the three methods match well to the data sheet of the actuator. The greatest discrepancy is 2.5 μm and is found at the highest driving voltage. As mentioned in section 4.3, when our SD-OCT system is operated in the conventional manner that outputs only the amplitude signal rather than amplitude and phase signals, the axial resolution of the system is 17- μm in air. Thus, it is not easy to evaluate the performance of the conventional OCT system if it is used to measure vibration amplitudes smaller than 17 μm . Nevertheless, it

is noticeable in Fig. 4.9 that the displacement range of the actuator is 0 μm to 3 μm , and its displacement is measurable by using the phase sensitive SD-OCT system.

Given by the coloured dots in Fig. 4.9, compared with the other two methods, the method generating the $\text{FFT}[\Delta\Phi(z, t)]$ output trace results in a better agreement with the data sheet (blue line) of the actuator from 90 V to 140 V. This is due to the inherently averaging nature of the Fourier transform treatment. Because of its better measurement precision, we employed the Fourier transform method to characterize the displacement sensitivity of the phase sensitive SD-OCT system, as will be demonstrated in the following section.

4.4.3 Characterization of displacement sensitivity

The smallest distinguishable phase fluctuation about an averaged DC value is a measure of the phase sensitivity σ_ϕ of a phase sensitive OCT system [71][72], and the phase sensitivity σ_ϕ then determines the axial displacement sensitivity σ_z according to Eq. (4.3). In this study, we employed two commonly used methods to characterise the displacement sensitivity of the SD-OCT system.

The first method is based on the perspective of the system noise level, where the fundamental limitation on the phase sensitivity arises from the signal-to-noise ratio (SNR) in the measurement procedure [73][74]. Under the assumption that the SNR of the measured OCT signal intensity satisfies $\text{SNR} \gg 1$, and the phase sensitivity σ_ϕ is given by $\sigma_\phi = \frac{1}{\sqrt{\text{SNR}}}$, according to Eq. (4.3), the displacement sensitivity σ_z can be expressed as [73][74][75]:

$$\sigma_z = \frac{\lambda_0 \sigma_\phi}{4\pi n} = \frac{\lambda_0}{4\pi n \sqrt{\text{SNR}}} \quad (4.9)$$

where $\lambda_0=1060$ nm is the centre wavelength of the OCT light source, $n = 1$ is the refractive index of air, and σ_z is the displacement sensitivity of the system.

In our measurements, two factors affected the level of SNR and thus the displacement sensitivity σ_z of the system. The first factor was the system configuration. It is known that an interferometer configured with an independent reference arm has a different system noise level from the common sample/reference path configured setup [73][74][75]. The second factor was the setting of the spectrometer camera exposure time. For the camera, the exposure time to the light determines the sensitivity of

exposed sensor pixels. Specifically, extending the exposure time results in an improvement in the pixel sensitivity but a reduced data acquisition speed and thus the operating speed of the OCT system. Consequently, it is necessary to find the trade-off between the camera exposure time and the system operating speed.

A Goodrich SUI camera was used in the system setup in Fig. 4.1. It provided 40 different pre-settings, each of which had a fixed combination of camera exposure time and pixel sensitivity, optimised in pairs. We selected 8 from the 40 pre-set pairs. For each of these 8 choices the SNR was measured in the two different interferometer configurations, the common path configuration and the independent reference arm configuration. The SNR was evaluated as the ratio of the A-scan peak of the second surface (at z_0 in Fig. 1.A or Fig. 4.2) of the stationary interface to its noise floor in the A-scan profile. The values of the SNR measured from each configuration and from each camera exposure time were substituted into Eq. (4.9) to calculate the displacement sensitivity σ_z of the system. The values of σ_z obtained in this way are compared in Fig. 4.10.(b) and Fig. 4.10.(c).

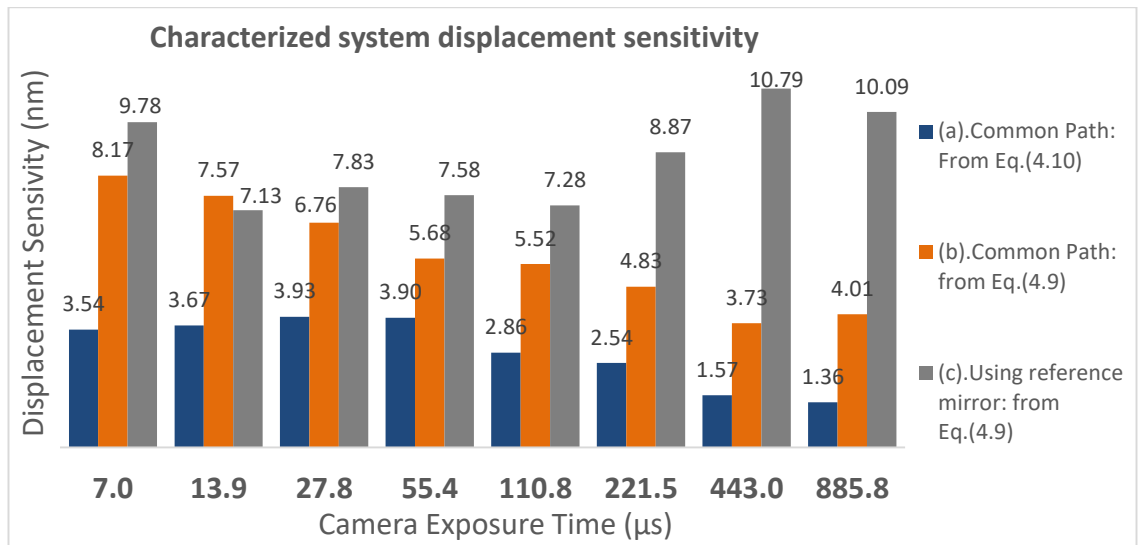


Fig. 4.10. Characterized displacement sensitivity of the phase sensitive SD-OCT system. (a): obtained in the common path configuration, calculated using Eq. (4.10). (b): obtained in the common path configuration, calculated using Eq. (4.9). (c): obtained in the independent reference arm configuration, calculated using Eq. (4.9).

The second method we employed to characterise the displacement sensitivity σ_z of the system was based on the perspective of the stability of the output phase measured on a stationary sample. It has been reported that the phase fluctuations contributed by interferometric instabilities increase the phase noise floor and thus degrades the phase

and displacement sensitivity [71][72]. In our measurements, the output phase stability was characterized by its statistical standard deviation φ_{SD} , and then the displacement sensitivity σ'_z , according to Eq. (4.3), can be calculated and expressed as [71][72]:

$$\sigma'_z = \frac{\lambda_0 \varphi_{SD}}{4\pi n} \quad (4.10)$$

where φ_{SD} is the standard deviation of 1024 successive phase $\Phi(z, t)$ values. To work out σ'_z in Eq. (10), we performed A-scan measurements continuously (at the rate of 500 Hz) at a fixed lateral location on the stationary coverslip interface (the one at z_0 in Fig. 4.1.A or Fig. 4.2), and then calculated the standard deviation of 1024 successive output phase $\Phi(z, t)$ values. Measurements were performed in the common path configuration for each of the 8 selected camera exposure settings. Results are presented in Fig. 4.10.(a).

Comparing Fig. 4.10.(b) and Fig. 4.10.(c), it can be concluded that the displacement sensitivity of the common path configured system is always better than that of the independent reference arm configured system. Based on this conclusion, in our measurements, we always chose the common path configuration if the geometry of the studied sample permitted. The independent reference arm configuration was used only when the thickness of the studied sample did not fit the common path configuration.

As seen in Fig. 4.10.(a), when the common path configuration is employed, the method based on the output stability perspective and Eq. (4.10) result in a displacement sensitivity value of 1.57 nm (at the camera exposure time setting of 443 μ s) and 1.36 nm (at the camera exposure setting of 886 μ s). The conclusion is that in the common path configured system, the camera exposure time settings of 443 μ s and 886 μ s provide the best (and similar) displacement sensitivities. The same conclusion can also be drawn from the method based on the SNR perspective and Eq. (4.9), as seen in Fig. 4.10.(b) at 443 μ s and 886 μ s. When the sensitivities are roughly similar, a faster data acquisition speed is always preferred. Consequently, we chose the camera exposure time setting of 443 μ s when only A-scan measurements were performed.

Comparing Fig. 4.10.(a) and Fig. 4.10.(b), though both in the common path configuration, the two methods based on different perspectives give different characterized results of the system's displacement sensitivity. The accuracy of each

method will be examined separately by performing the Fourier analysis to the output phase, as demonstrated in section 4.4.4 below.

4.4.4 Improved displacement sensitivity

To experimentally evaluate two methods introduced in section 4.4.3 in characterizing the displacement sensitivity of the phase sensitive SD-OCT, we performed phase measurements on actual micro vibrations by driving the piezo actuator with 100 Hz sinusoidal voltages with several different amplitudes. All measurements were performed in the common path configuration, with the camera exposure time set at 443 μm . Results are presented in Fig. 4.11.

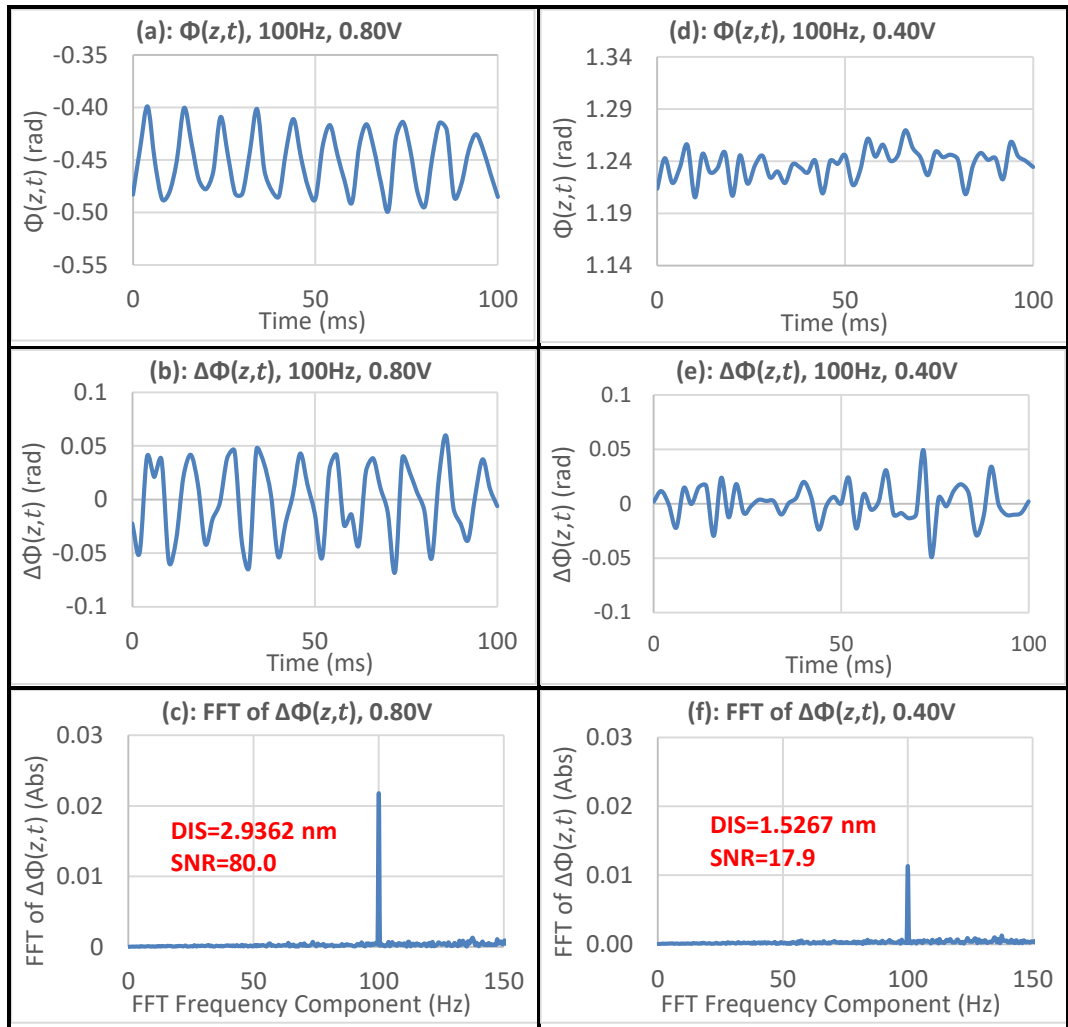


Fig. 4.11. Output traces of $\Phi(z,t)$, $\Delta\Phi(z,t)$ and $\text{FFT}[\Delta\Phi(z,t)]$. (a), (b) and (c): obtained with the actuator driven by a 0.8 V sinusoidal signal at 100 Hz. (d), (e) and (f): obtained with the actuator driven by a 0.4 V sinusoidal signal at 100 Hz. DIS: displacement sensitivity. SNR: signal to noise ratio.

Fig. 4.11.(a), (b) and (c) are output traces of $\Phi(z, t)$, $\Delta\Phi(z, t)$ and $\text{FFT}[\Delta\Phi(z, t)]$ respectively, with a 0.8 V sinusoidal driving voltage sent to the actuator. Fig. 4.11.(d), (e) and (f) were obtained with a 0.4 V sinusoidal driving voltage. As seen in Fig. 4.11.(a) and (b), when the sinusoidal driving voltage is 0.8 V, both the $\Phi(z, t)$ trace and the $\Delta\Phi(z, t)$ trace exhibit clear sinusoidal patterns, and the modulation frequencies of these traces agree with the driving frequency (100 Hz) of the actuator. In Fig. 4.11.(c), we used the amplitude $|p(f_0)|$ of the FFT peak at 100 Hz and Eq. (4.6) to calculate the vibration amplitude A of the actuator, obtaining 2.94 nm which is less than the characterized value of 3.73 nm (as seen in Fig. 4.10.(b) at 443 μs). Consequently, the method based on the SNR perspective and Eq. (4.9) is too conservative.

As seen in Fig. 4.11.(d) and (e), when the sinusoidal driving voltage of the actuator is 0.4 V, neither the $\Phi(z, t)$ trace nor the $\Delta\Phi(z, t)$ trace exhibits a sinusoidal pattern. In Fig. 4.11.(f), we measured the amplitude $|p(f_0)|$ of the FFT peak at 100 Hz and used Eq. (4.6) to calculate the vibration amplitude A of the actuator, obtaining 1.53 nm which is comparable with the characterized value of 1.57 nm (as seen in Fig. 4.10.(a) at 443 μs). Consequently, the method based on the output phase stability perspective and Eq. (4.10) is more accurate than the SNR perspective. Moreover, as seen in Fig. 4.11.(d), (e) and (f), when the actual displacement of the actuator is too small to be detected by the output traces of $\Phi(z, t)$ and $\Delta\Phi(z, t)$, the output trace of $\text{FFT}[\Delta\Phi(z, t)]$ can be used to improve the displacement sensitivity of the system.

In order to identify the minimum displacement sensitivity of the system, we decreased the driving voltage of the actuator and generated the output trace of $\text{FFT}[\Delta\Phi(z, t)]$. Selected $\text{FFT}[\Delta\Phi(z, t)]$ traces are presented in Fig. 4.12. In each individual graph in Fig. 4.12, we measured the amplitude $|p(f_0)|$ of the FFT peak at 100 Hz and substituted it into Eq. (4.6) to calculate the displacement amplitude A of the actuator. As seen from Fig. 4.12.(A-D), the displacement sensitivity of the system is improved to values in the sub-nanometre scale. As seen in Fig. 4.12.(D), the minimum detectable displacement is as small as 0.17 nm with a SNR of 2.1. Taking measurements in the absence of piezo motion, the SNR is calculated as the numerical ratio of the height of the FFT peak at 100 Hz to its noise floor.

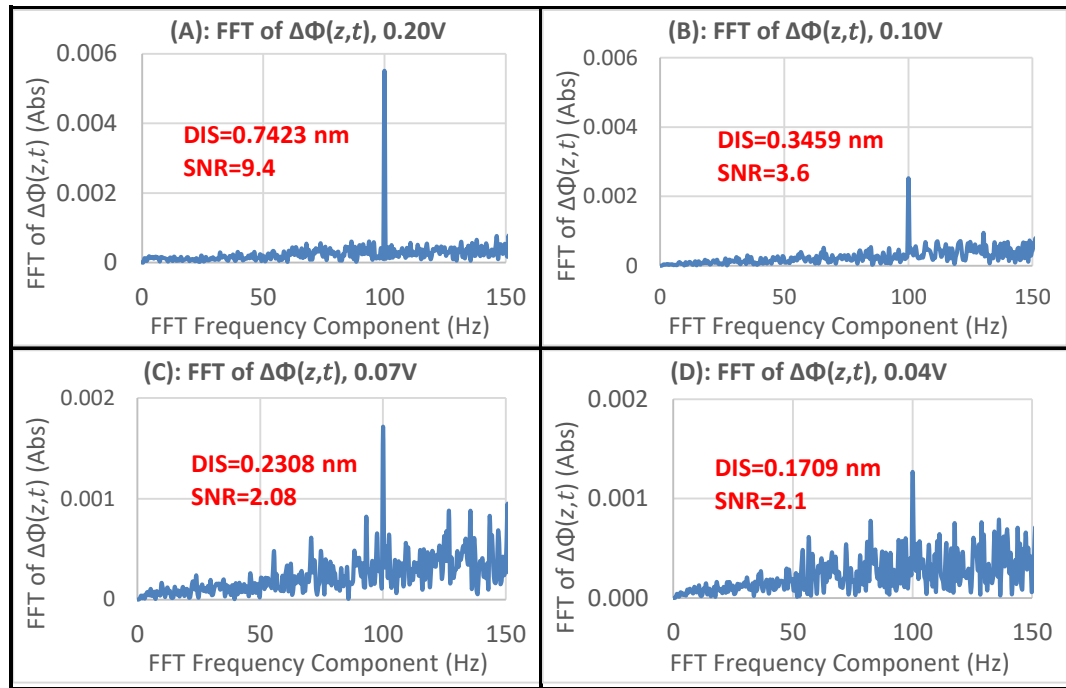


Fig. 4.12. Output traces of $\text{FFT}[\Delta\Phi(z,t)]$. (A), (B), (C) and (D): obtained with the actuator driven by 100 Hz sinusoidal signal voltages at 0.2 V, 0.1 V, 0.07 V and 0.04 V respectively. DIS: displacement sensitivity. SNR: signal to noise ratio.

All measurements described in sections 4.4.3 to 4.4.4 were taken on the sample schematically demonstrated in Fig. 4.1.A or Fig. 4.2, in which the focus point of the beam is placed between the two coverslips, but closer to the actuated coverslip. A configuration like this always results in an optimized displacement sensitivity since the phase signal was measured on the actuated coverslip that was placed close to the beam focus. In practice, the measured sample has a thickness of the order of a multiple of the depth of focus, and the region far from the beam focus could not benefit from the optimized displacement sensitivity though in the common path configuration. Thus, characterizing the degradation of the displacement sensitivity to defocus has a high practical value.

4.4.5 Degradation of displacement sensitivity to defocus

The measurement of sensitivity degradation to probe beam defocus within the sample plays an important role in phase microscopy [76]. In our common path configured SD-OCT system (Fig. 4.1), we characterized the sensitivity degradation to defocus by measuring the displacement sensitivity with the detected surface of the coverslip (Fig. 4.2) mounted on the actuator placed at different axial positions. Results are presented in Fig. 4.13.

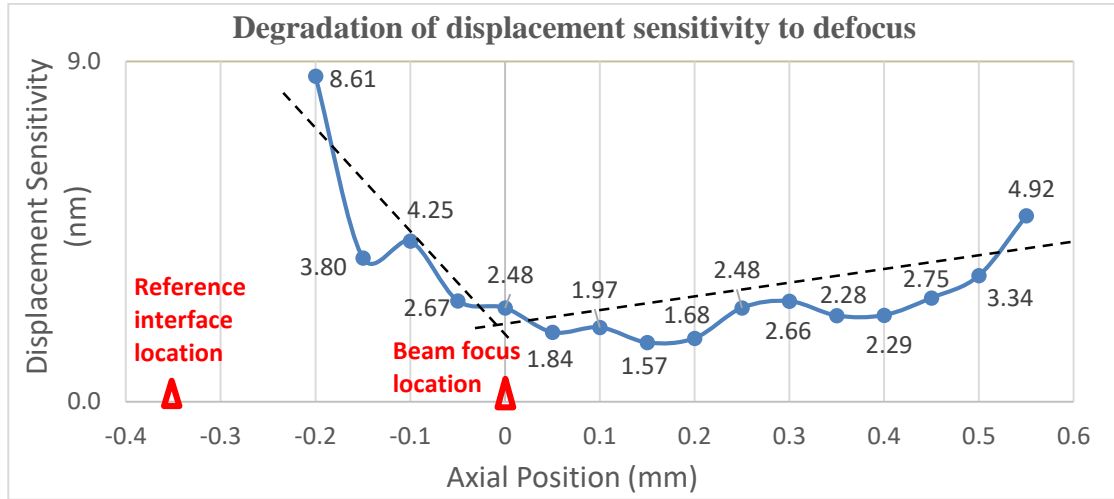


Fig. 4.13. Characterized displacement sensitivity degradation to the defocus. The reference interface located at z_0 in Fig. 4.1.A or Fig. 4.2, is fixed at -0.35 mm on the “Axial Position” axis. The beam focus position is fixed at 0 mm. The position of the detected interface located at z in Fig. 4.1.A or Fig. 4.2 was axially moved away from the reference interface.

In Fig. 4.13, the “Axial Position” serves as the position coordinate in the axial direction. The stationary reference interface located at z_0 in Fig. 4.1.A or Fig. 4.2 is fixed at -0.35 mm on the coordinate axis. This surface provides the reference phase $\varphi(z_0, t)$. The tightest beam focus is associated with a nominal depth of 0 mm on the coordinate axis in this representation. The coverslip mounted on the actuator was placed at different axial positions (in steps of 0.05 mm from -0.2 mm to 0.55 mm on the coordinate axis). At each axial position, the phase $\varphi(z, t)$ was measured. The output phase value obtained at each axial location was taken into Eq. (4.10) to calculate displacement sensitivity σ'_z . The front surface of the stationary coverslip served as the reference mirror/reflector of the common path configuration.

As seen in Fig. 4.13, when the detected interface is placed 0.15 mm to the right of the beam focus, a best displacement sensitivity of 1.57 nm is obtained. Also, given by two fitting lines on both sides of the beam focus, the region to the right of the beam focus has a displacement sensitivity degradation of 1.72 nm/mm, whereas the region to the left of it has a value of 30.65 nm/mm. Thus, it can be concluded that the degradation is clearly a consequence of the properties of the focusing optics being used. In addition, in consideration of the blue curve in Fig. 4.13, in the following experiments that were performed on the photothermal detection and imaging of GNRs, the detected sample containing GNRs was placed within the axial range -0.05 mm to 0.45 mm where the displacement sensitivity performance is sufficiently good.

4.4.6 Photothermal response of GNRs to Ti:Sa modulation frequency

In sections 4.4.1 - 4.4.5, we measured and quantified the operating parameters of the phase sensitive SD-OCT system. We have calibrated the output phase, characterized the displacement sensitivity of two system configurations, optimized the displacement sensitivity using the Fourier analysis, and measured the displacement sensitivity degradation in the imaging depth. From this section to section 4.4.8, we demonstrate how this OCT system was employed for the photothermal detection and imaging of GNRs in clear media and in biological tissue. Depending on the unique feature of each individual experiment, in order to make the OCT system work with the optimized measurement sensitivity performance, we selected suitable system configuration and camera exposure time settings for each measurement.

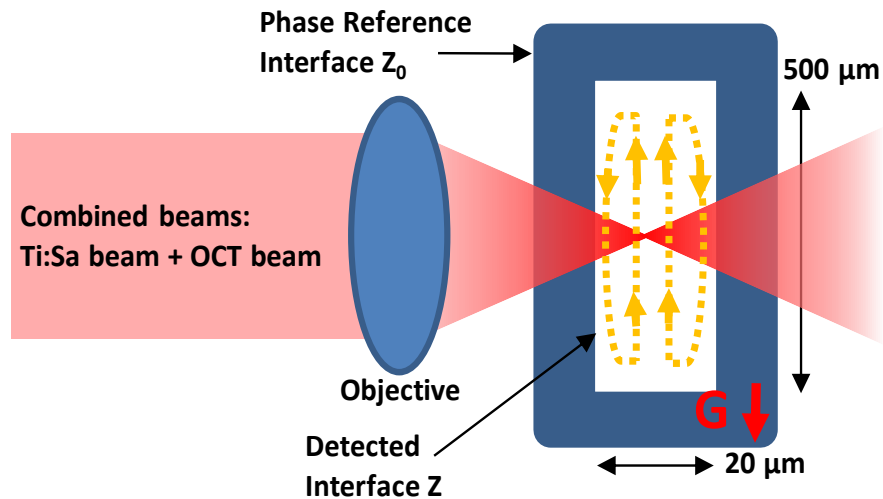


Fig. 4.14. Zoomed image of Fig. 4.1.B. A glass made microfluidic channel ($500 \mu\text{m} \times 20 \mu\text{m}$) filled with GNR solution. The focus of the combined beam is placed in the middle of the channel. The reference phase $\varphi(z_0, t)$ was measured on the front surface (at z_0) of the glass channel. The detected phase $\varphi(z, t)$ was measured on the glass/solution interface (at z). The arrows show direction of the convective flow of the GNR solution inside the cuvette. The direction of these arrows considers the gravitational force (labelled as G) and the position of the Ti:Sa beam focus inside the cuvette.

This section demonstrates the photothermal response of GNRs to the modulation frequency of the Ti:Sa beam with a fixed output power. To excite the photothermal response of GNRs, the Ti:Sa laser in Fig. 4.1 is enabled, with its output beam modulated on-off by a square wave through the use of a chopper wheel. A glass made microfluidic channel filled with the GNR solution (Nanopartz Inc., 1014 particles/mL, peak absorption wavelength 800 nm) is placed on the right side of the objective, as

demonstrated in Fig. 4.1.B or Fig. 4.14. The reference phase $\varphi(z_0, t)$ was measured on the air/glass interface (at z_0) of the microfluidic channel, and the signal phase $\varphi(z, t)$ was measured in the region of the glass/solution interface (at z) in the channel. The output phase $\Phi(z, t)$ was calculated according to Eq. (4.7) and Eq. (4.8).

As discussed in section 4.4.3, and shown in Fig. 4.10, the independent reference arm configuration proves to offer inferior displacement sensitivity compared with the common path configuration. In the experiment discussed in this section, we tried both configurations on this microfluidic channel sample. Since the thickness of the glass material (between z_0 and z) is larger than the imaging depth of the OCT system, the beam focus that provides the best displacement sensitivity performance could not be placed in the middle of the channel when the common path configuration was used. Thus, in order to place the beam focus in the middle of the channel (as seen in Fig. 4.14), we chose the independent reference/sample arm configuration.

During the measurement process, we fixed the average Ti:Sa power at 119.4 mW on the sample and varied the modulation frequency of the chopper from 0 Hz to 250 Hz. With both galvo-scanners (Fig. 4.1) disabled, we performed only A-scan detections with a fixed system operating rate of 500 Hz. The output traces of $\Delta\Phi(z, t)$ and $\text{FFT}[\Delta\Phi(z, t)]$ were generated. As discussed in section 4.4.3, when the OCT system works in the A-scan mode, the camera exposure time setting of 443 μs balances the measurement sensitivity and the system operating rate. Thus, we set the camera exposure time at 443 μs . According to Fig. 4.10, in the separate reference arm configuration, and with the camera set at 443 μs , the system is capable of a displacement sensitivity of 10.79 nm.

For comparison purposes, the measurements carried out on the GNR solution sample were also performed on another microfluidic channel with the same geometry but filled with pure DI water. Selected output traces of $\Delta\Phi(z, t)$ and the $\text{FFT}[\Delta\Phi(z, t)]$ from both the GNR solution sample the DI water sample are presented in Fig. 4.15.

Since the chopper wheel provides a square wave on-off modulation and the beam profile is Gaussian, the overall modulation of the Ti:Sa beam is a quasi-square wave. At lower frequencies in particular, when measurements were made on the GNRs solution sample exposed to the modulated Ti:Sa beam, the output traces of $\Delta\Phi(z, t)$ resemble, as expected, differentials of square waves, as seen in Fig. 4.15.(a-c). The frequencies of traces in Fig. 4.15.(a-c) agree with corresponding modulation frequencies of the Ti:Sa

beam. Fig. 4.15.(d) shows the output trace of $\Delta\Phi(z,t)$ obtained from the DI water sample, which appears generally featureless, indicating the lack of the photothermal response when the GNRs are absent.

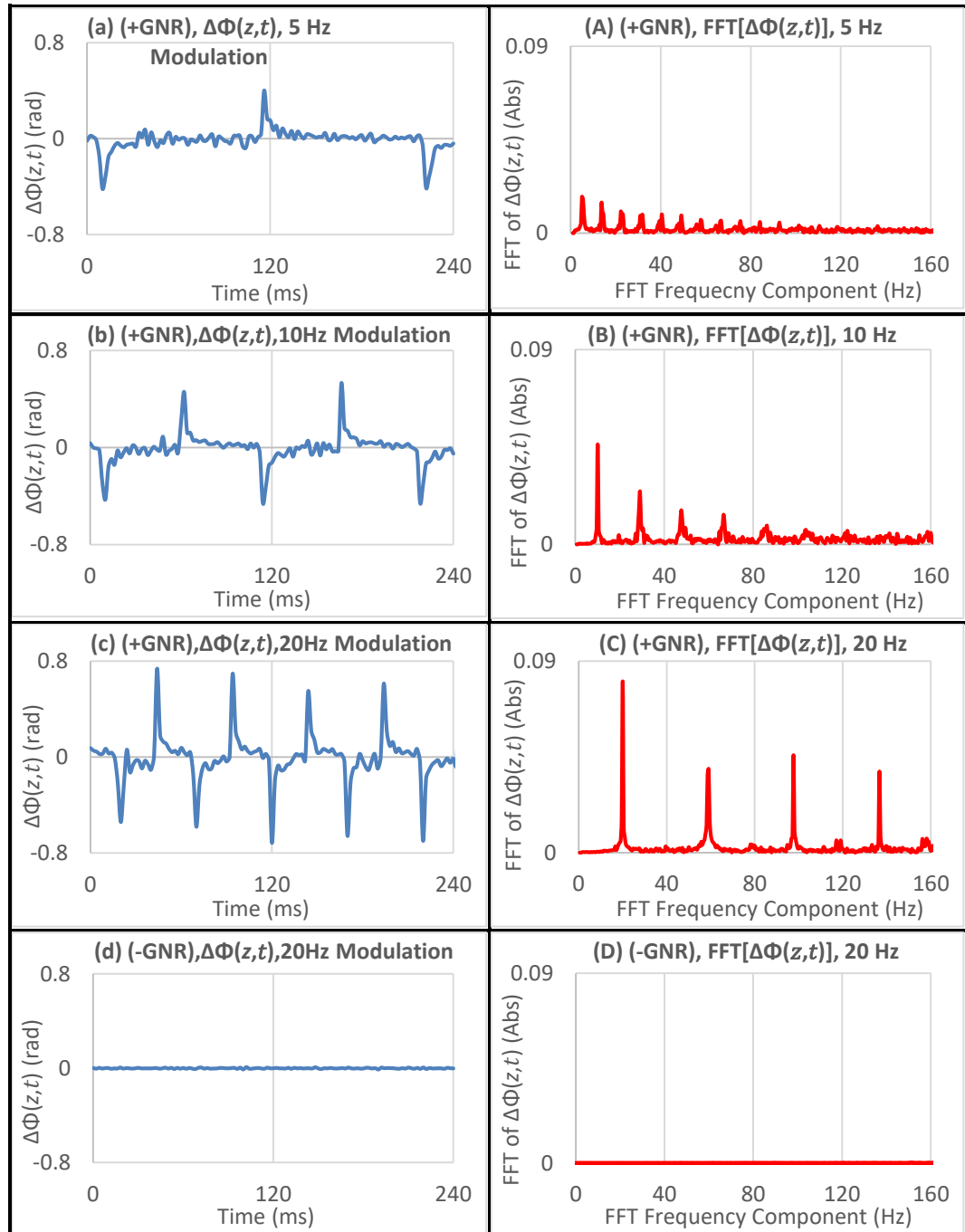


Fig. 4.15. (a), (b) and (c): output traces of $\Delta\Phi(z,t)$ (blue), obtained from the GNR solution sample with Ti:Sa modulation frequencies of 5 Hz, 10 Hz and 20 Hz respectively. (d): output trace of $\Delta\Phi(z,t)$, obtained from the DI water sample with a Ti:Sa modulation frequency of 20 Hz. (A), (B) and (C): output traces of $\text{FFT}[\Delta\Phi(z,t)]$ (red), obtained from the GNRs solution sample with Ti:Sa modulation frequencies of 5 Hz, 10 Hz and 20 Hz respectively. (D): output trace of $\text{FFT}[\Delta\Phi(z,t)]$, obtained from the DI water sample with a Ti:Sa modulation frequency of 20 Hz.

In order to generate the output trace of $\text{FFT}[\Delta\Phi(z, t)]$, the Fourier transform was performed on the latest 1024 dynamic $\Delta\Phi(z, t)$ data. Fig. 4.15.(A-C) show the FFT of Fig. 4.15.(a-c) at corresponding Ti:Sa modulation frequencies. For each $\text{FFT}[\Delta\Phi(z, t)]$ trace, the frequency component with the highest FFT peak corresponds to the modulation frequency of the Ti:Sa beam. Fig. 4.15.(D) was obtained from the DI water sample. Once again, this featureless trace indicates the lack of photothermal response when the GNRs are absent. It can be concluded from Fig. 4.15 that GNRs exhibit photothermal response to the Ti:Sa laser beam, and this feature of GNRs can be used to detect their existence in the detected sample.

As seen from Fig. 4.15.(A-C), if the modulation frequency is different, the height of the FFT peak at the modulation frequency is different, which indicates a varied magnitude of the photothermal response of GNRs to the Ti:Sa beam. Thus, it is necessary to measure and characterize the photothermal response of GNRs to the modulation frequency of the Ti:Sa beam. To this end, we fixed the average Ti:Sa power at 119.4 mW on the sample and varied the modulation frequency of the chopper wheel from 0 Hz to 250 Hz. From each obtained output trace of $\text{FFT}[\Delta\Phi(z, t)]$, we measured the height of the FFT peak at the corresponding frequency. Values obtained are plotted against the corresponding Ti:Sa modulation frequency in Fig. 4.16. In practice, the highest Ti:Sa modulation frequency (250 Hz) was determined by and was equal to half of the A-scan operating rate (500 Hz) of the SD-OCT system.

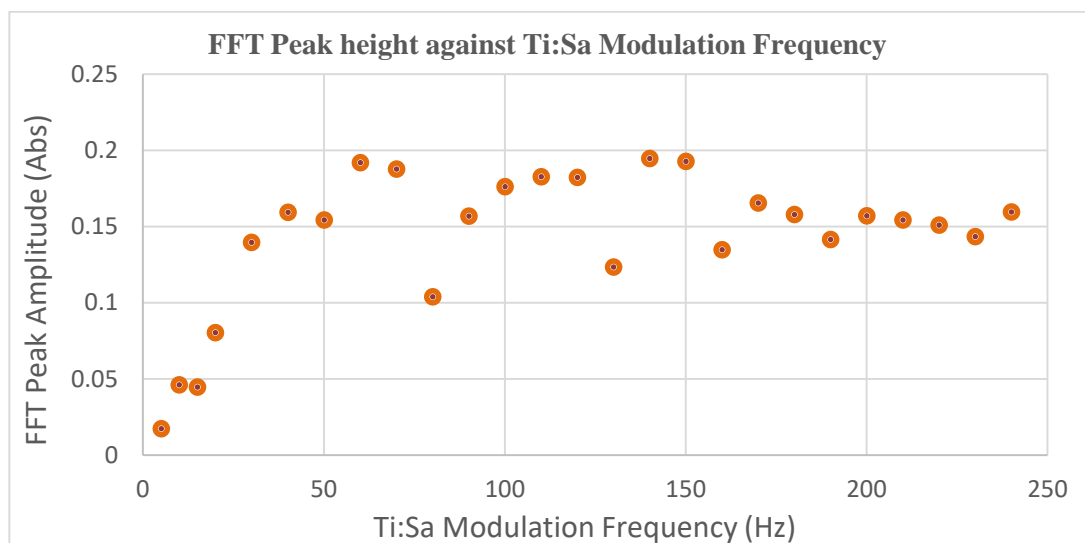


Fig. 4.16. Height of the FFT peak at different Ti:Sa modulation frequencies (0 Hz - 250 Hz). The average Ti:Sa power on the GNRs solution sample was fixed at 119.4 mW for all measurement.

As seen in Fig. 4.16, the local aggregation of GNRs in solution exhibits a superior photothermal response in the range 60 Hz - 250 Hz compared to the range 5 Hz - 60 Hz. Thus, in order to have a maximum photothermal effect, we chose 220 Hz as the Ti:Sa modulation frequency in the following experiment measuring the photothermal response of GNRs to the Ti:Sa beam power.

4.4.7 Photothermal response of GNRs to Ti:Sa power

In order to characterize the photothermal response of GNRs to the Ti:Sa beam power and to identify the minimum Ti:Sa power capable of triggering a detectable photothermal response of GNRs, we fixed the modulation frequency of the chopper wheel (Fig. 4.1) at 220 Hz and varied the output power of the Ti:Sa laser.

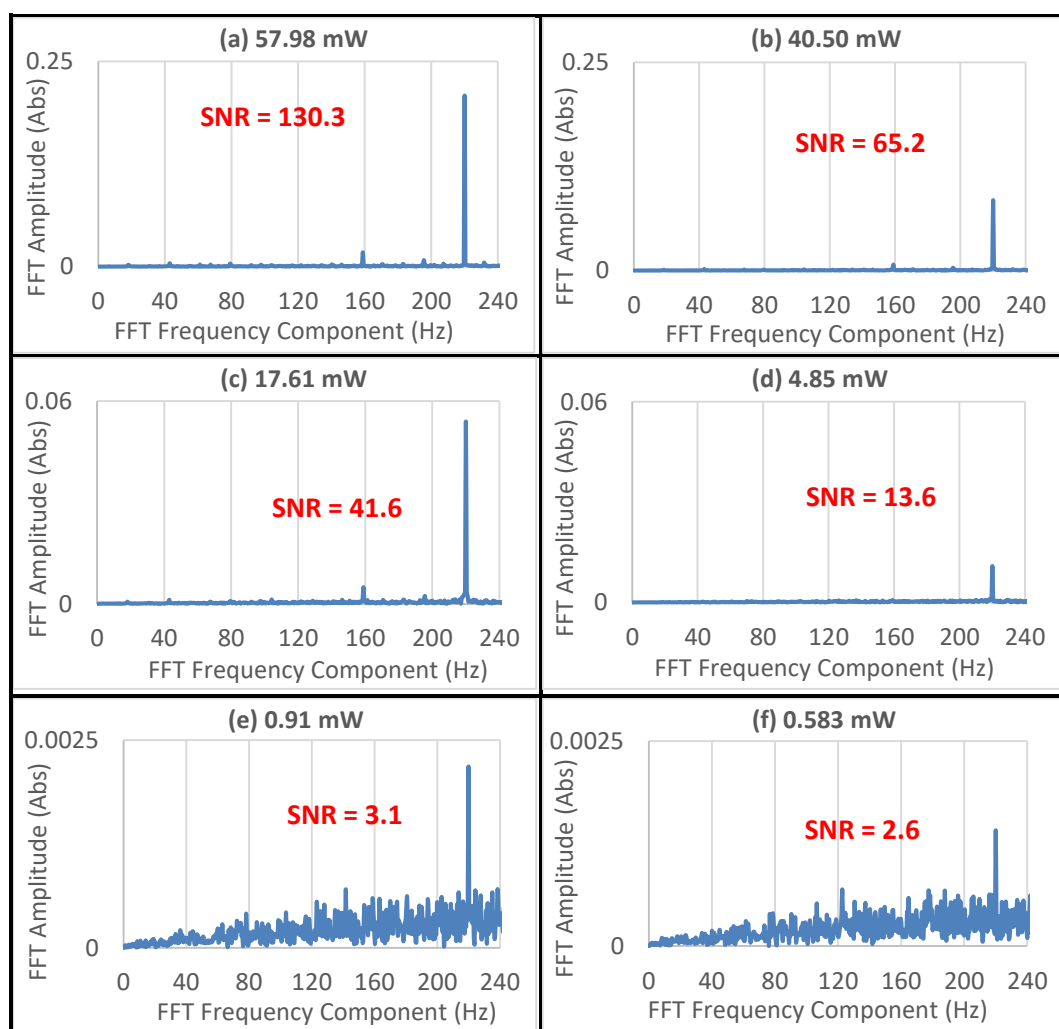


Fig. 4.17. Output traces of $\text{FFT}[\Delta\Phi(z, t)]$. Traces were obtained from different Ti:Sa beam power on the GNR solution sample. Ti:Sa modulation frequency: 220 Hz. SNR: signal to noise ratio, evaluated as the numerical ratio of the peak/amplitude of the FFT peak at 220 Hz to its noise baseline.

In the experiment, the initial Ti:Sa power on the GNR solution sample was initially set at 119.4 mW, then the power was increasingly attenuated by a ND filter (Fig. 4.1). At each individual Ti:Sa power level, output traces of $\text{FFT}[\Delta\Phi(z, t)]$ were generated. Selected $\text{FFT}[\Delta\Phi(z, t)]$ traces at different Ti:Sa power values are presented in Fig. 4.17. As seen in each individual graph, a FFT peak exists at the Ti:Sa modulation frequency (220 Hz) regardless of the Ti:Sa power. The larger the attenuation of the Ti:Sa power, the smaller the signal to noise ratio (SNR) of the FFT peak at 220 Hz. Fig. 4.17.(f) indicates that the minimum Ti:Sa power capable of inducing a detectable photothermal response of GNRs is 0.583 mW. This value is in line with the latest reported minimum Ti:Sa power (0.5 mW) capable of photothermal trapping GNRs [40].

In order to characterize the photothermal response of GNRs to the Ti:Sa power, we ignored differences in noise floor levels between individual graphs in Fig. 4.17, and the height/amplitude of the FFT peak at 220 Hz in each graph was measured. The values of the FFT peaks obtained in this way are plotted against the corresponding Ti:Sa power in Fig. 4.18.

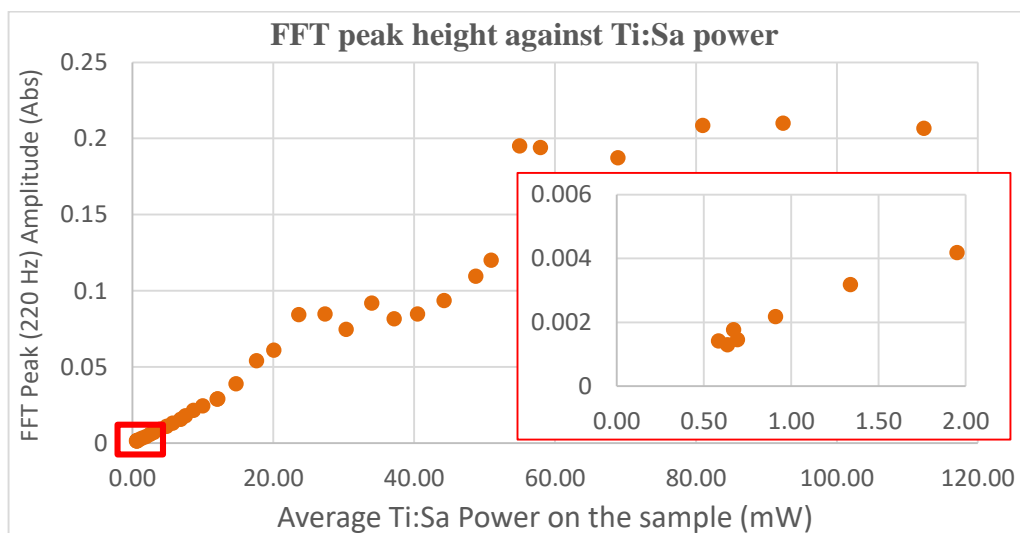


Fig. 4.18. Height/amplitude of the FFT peak at 220 Hz against the Ti:Sa power on the GNRs sample. Insert: zoom into the graph for Ti:Sa power less than 2 mW.

As seen in Fig. 4.18, below the Ti:Sa power of 60 mW, a decrease in the Ti:Sa power results in a decrease of the photothermal response of GNRs. Above the Ti:Sa power of 60 mW, the saturation of the photothermal response of GNRs takes place. As seen in the insert in Fig. 4.18, below the Ti:Sa power of 1 mW, the photothermal response of GNRs is still detectable. At such a low power incident on the GNRs, the Ti:Sa induced photothermal response of GNRs can be still detected by the phase

sensitive SD-OCT system. It is worth pointing out that this minimum power level was achieved when the SD-OCT was not working with the best displacement sensitivity performance. A better sensitivity would have been achieved if the common path configuration had been employed.

4.4.8 Photothermal imaging of GNRs in clear media

After the experiments demonstrated in section 4.7, an aggregation of GNRs resulting from the photothermal trapping was observed, as shown in Fig. 4.1.D or Fig. 4.19. The aggregation of GNRs comes from self-assisted photothermal trapping of GNRs under the excitation of the light beam with SPR wavelength [40]. As discussed in chapter 3, the two-photon luminescence (TPL) detection has been reported to image the photothermal trapping process of GNRs [40]. However, the TPL detection suffers if background fluorescence exists. As an alternative method to TPL, we employed the phase sensitive SD-OCT system to perform photothermal imaging of aggregated GNRs. *En-face* phase images of aggregated GNRs were produced. The experimental process is introduced in this section.

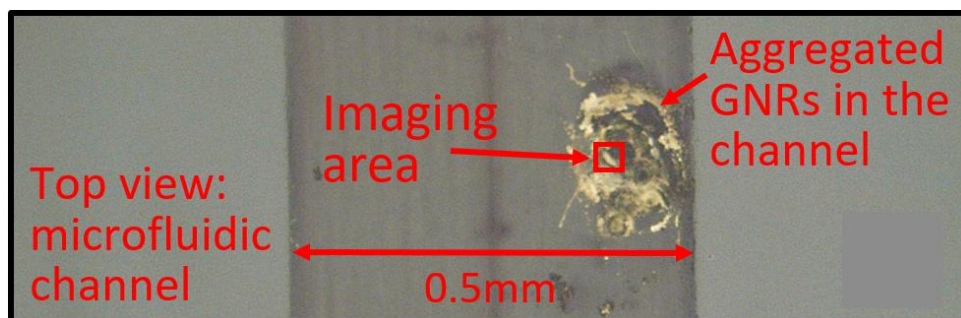


Fig. 4.19. Transmitted light microscopy (20 \times) image of the aggregated GNRs in the microfluidic channel. The aggregation results from the photothermal trapping of GNRs. The width of the channel: 0.5 mm. *En-face* OCT images were produced on an imaging area of 60 μm \times 60 μm on the aggregated GNRs.

The experiment was conducted in the independent reference arm configuration. Since a 3D volume of data had to be collected before slicing out the *en-face* image, a high data acquisition speed was required. Thus, we set the camera exposure time at 27.8- μs to guarantee an adequate data acquisition speed. According to Fig. 4.10, the configuration and the camera setting determined a displacement sensitivity of 7.83 nm.

The phase value $\Phi(z, t)$ used to construct *en-face* images were obtained in the same way as described in section 4.4.6. The two galvo-scanners in Fig. 4.1 were

enabled to provide a raster scanning. Coaxially combined OCT and Ti:Sa beams were scanned over an area of $60 \times 60 \mu\text{m}$ over the aggregated GNRs in the channel (Fig. 4.19). The slow galvo-scanner executed a sawtooth movement, determining a 3D frame rate of 2 frames/s. The fast galvo-scanner executed a triangle movement, performing a line scan rate of 90 cycles/s (11.1 ms/line), equivalent with the beam integrating each pixel for $65 \mu\text{s}$ if the *en-face* image is composed of $170 \text{ pixels} \times 170 \text{ pixels}$. A LabVIEW programme was designed to assemble all collected A-scans into a 3D data array. From the 3D data array, at the end of each 2D scanning frame, an *en-face* image ($170 \times 170 \text{ pixel}$, $0.35 \mu\text{m}/\text{pixel}$) displaying phase matrix with elements $\Phi_t(x_m, y_n)$ was sliced out at the glass/solution interface. Due to the lack of suitable phase unwrapping algorithm, the value of $\Phi_t(x_m, y_n)$ is confined between $-\pi$ and $+\pi$:

$$-\pi \leq \Phi_t(x_m, y_n) \leq \pi \quad (4.11)$$

where t indicates that the *en-face* image is produced at a certain time t , and x_m, y_n are the image lateral coordinates. After a 2D scanning frame interval of $\Delta t = 0.5 \text{ s}$, another 3D data array containing the volume information of the same scanning area is acquired. Then, from the new 3D array, a new phase matrix $\Phi_{t+\Delta t}(x_m, y_n)$ at the glass/solution interface was sliced out. In order to highlight the difference between these two successive *en-face* phase matrices: $\Phi_t(x_m, y_n)$ and $\Phi_{t+\Delta t}(x_m, y_n)$, we used the LabVIEW programme to calculate and display the difference between these two *en-face* phase matrices, as presented by $\delta\Phi(x_m, y_n)$:

$$\delta\Phi(x_m, y_n) = \Phi_{t+\Delta t}(x_m, y_n) - \Phi_t(x_m, y_n) \quad (4.12)$$

where $-2\pi \leq \delta\Phi(x_m, y_n) \leq 2\pi$. As can be predicated, if there is no difference between $\Phi_{t+\Delta t}(x_m, y_n)$ and $\Phi_t(x_m, y_n)$, the produced *en-face* image should be completely black. The LabVIEW implementation is presented in Fig. A.2.

When the shutter in Fig. 4.1 was closed, GNRs presented no photothermal response, and a black *en-face* image shown in Fig. 4.20.(A,a) was obtained. Ideally, this image should be completely black since the difference between successive acquired *en-face* phase matrices is zero. In practice, differences could still be created by the movement error of galvo-scanners, especially when the OCT beam scanning over the sharp borders between GNR areas and voids. In Fig. 4.20.(A,a), these borders are shown as thin contours.

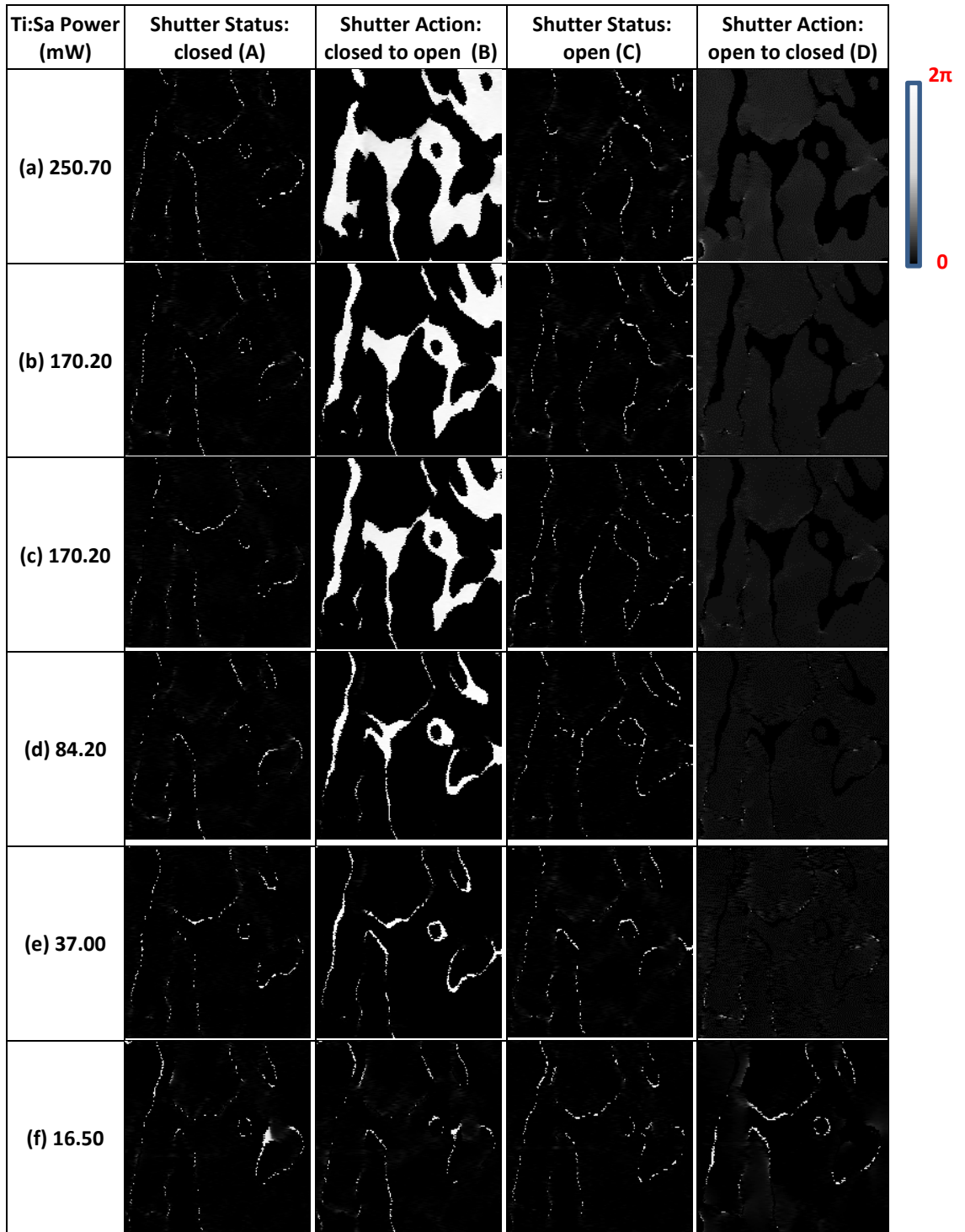


Fig. 4.20. *En-face* phase images of the aggregated GNRs (in the red block in Fig. 4.19) in the microfluidic channel. Images were obtained by mapping $\delta\Phi(x_m, y_n)$ in Eq. (4.12) into grayscale values. Taking the status of the shutter “from closed to open, then from open to closed” as a cycle, experiments were conducted in series of cycles with attenuated Ti:Sa power on the GNRs.

When the shutter in Fig. 4.1 was switched from closed to open, the Ti:Sa beam excited the photothermal response of GNRs. In this case, differences arose between successively acquired *en-face* phase matrices. These differences are showing in the

image produced by the SD-OCT system, as presented in Fig. 4.20.(B,a). The bright area in the image indicates the presence of GNRs. Consequently, the aggregated GNRs resulting from the photothermal trapping can be imaged by performing photothermal imaging using the phase sensitive SD-OCT system.

Leaving the shutter in the open status, the image in Fig. 4.20.(C,a) generated straight after the one in Fig. 4.20.(B,a) is mostly black. This is an expected result because when the shutter gate was left open, the GNRs were in equilibrium (steady-state) and continuing to generate the same photothermal response to the uninterrupted Ti:Sa beam as before. Therefore, no difference is expected between successively acquired *en-face* phase matrices. Once again, the white thin contours Fig. 4.20.(C,a) came from the movement errors of galvo-scanners.

When the shutter was switched from open to closed, the photothermal response of GNRs was switched off, and the *en-face* image in Fig. 4.20.(D,a) was obtained. Comparing Fig. 4.20.(D,a) and Fig. 4.20.(B,a), the black region in Fig. 4.20.(D,a) is bright in Fig. 4.20.(B,a), and the bright region in Fig. 4.20.(D,a) is black in Fig. 4.20.(B,a). This brightness inversion is due to an inverted order (on=>off and off=>on) of photothermal responses of GNRs to the Ti:Sa beam.

Taking the shutter “from closed to open, then from open to closed” as a cycle, experiments were conducted in series of cycles with the power of the Ti:Sa output power attenuated to several different levels. As seen in Fig. 4.20.(B) rows (a–f), the lower the Ti:Sa power, the smaller the areas of bright sectors. As seen in Fig. 4.20 row (f), when the Ti:Sa power is as low as 16.5 mW, the difference between images in this cycle could be barely seen, indicating that the minimum Ti:Sa power could be used for the photothermal imaging of GNRs should be higher than 16.5 mW. Images in Fig. 4.20 row (b) and Fig. 4.20 row (c) are acquired intentionally with the same Ti:Sa power of 170.2 mW. The similarity between corresponding images in Fig. 4.20 row (b) and Fig. 4.20 row (c) indicates that the experiment is highly repeatable.

As seen in Fig. 4.20 column (D), the contrast of these images is low when the shutter was switched from open to closed. This is because when $\delta\Phi(x_m, y_n)$ in Eq. (4.12) was mapped into grayscale values, all values between -2π and 0 were forced to 0 without being actually scaled to intermediate grey levels. The drawback of the low contrast is that the region covered by GNRs could not be identified easily when the shutter was switched from open to closed. In order to make images in Fig. 4.20 column

(B) and Fig. 4.20 column (D) have equivalent contrasts to highlight the photothermal response induced variation, a constant π was added to both sides of Eq. (4.12), resulting in $-\pi \leq [\pi + \delta\Phi(x_m, y_n)] \leq 3\pi$. Then, the matrix of $[\pi + \delta\Phi(x_m, y_n)]$ was mapped into grayscale values to produce *en-face* images, as presented in Fig. 4.21.

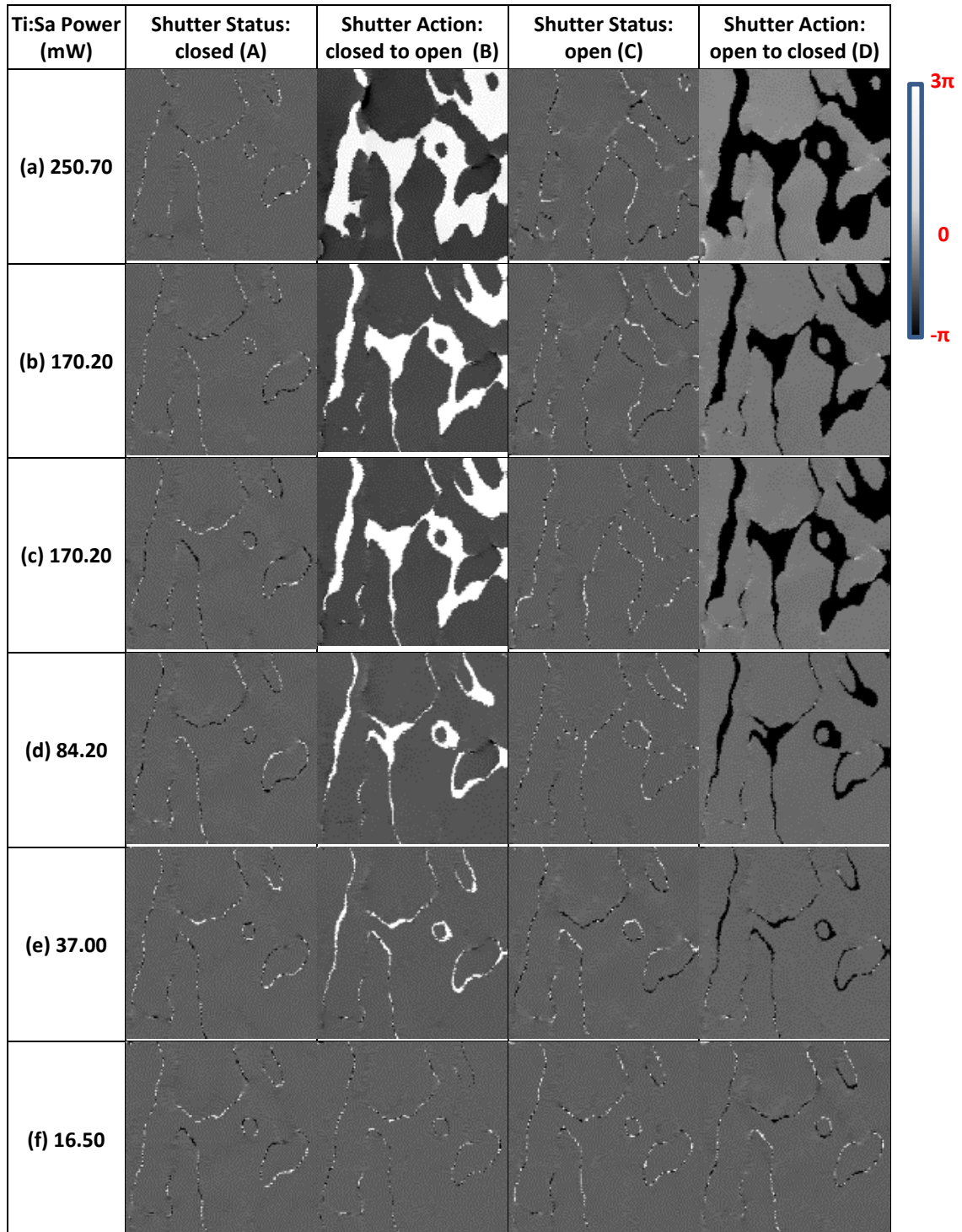


Fig. 4.21. *En-face* images of aggregated GNRs (shown in the red block in Fig. 4.19) in the microfluidic channel. Images were obtained by mapping $[\pi + \delta\Phi(x_m, y_n)]$ to grayscale levels. Taking the status of the shutter “from closed to open, then from open to closed” as a cycle, experiments were conducted in series of cycles with different Ti:Sa power levels incident on the GNRs.

As seen in Fig. 4.21 column (D), images have high contrast when the shutter was switched from open to closed, which is good for distinguishing regions with and without GNRs in the sample. Comparing images in Fig. 4.20 and Fig. 4.21, they show identical patterns though different algorithms were used to treat the phase data. Consequently, adding a constant π to $\delta\Phi(x_m, y_n)$ in Eq. (4.12) improved the image contrast without degrading the experiment result.

In this section, we demonstrated how to use the phase sensitive SD-OCT system to generate *en-face* images to display the photothermal response of aggregated GNRs. It can be concluded that by detecting the photothermal effects of GNRs, phase sensitive SD-OCT can be used to image the distribution of GNRs in clear media. The drawback of the technique is that the output phase $\Phi_t(x_m, y_n)$ was restricted between $-\pi$ and π , in which case any phase value larger than π was forced to π . Thus, the value of $\delta\Phi(x_m, y_n)$ used to construct *en-face* images were restricted between -2π and 2π , according to Eq. (4.12). This phase wrapping resulted in a simplex grayscale distribution in images in Fig. 4.20 column (B) and Fig. 4.20 column (D) since most of phase values used in constructing images were concentrated on either 0 or 2π . The net result of this drawback is that the phase sensitive OCT was not able to provide the thickness information of the aggregated GNRs, which is directly related to the strength of photothermal trapping of GNRs by the Ti:Sa beam.

4.4.9 Photothermal detection of GNRs in biological tissue

Compared with freely diffused GNRs in DI water, GNRs in biological tissue have more complex surroundings. In order to perform photothermal detection of GNRs in biological tissue, we duplicated the procedures demonstrated in sections 4.4.6 and 4.4.7 on a piece of pork tissue injected with the GNR solution.

The pork tissue sample used in the measurement is schematically demonstrated in Fig. 4.1.C and Fig. 4.22. As seen, a piece of tissue is mounted on a 100 μm glass coverslip. The GNR solution used in previous sections was injected into the tissue 5 minutes before measurements.

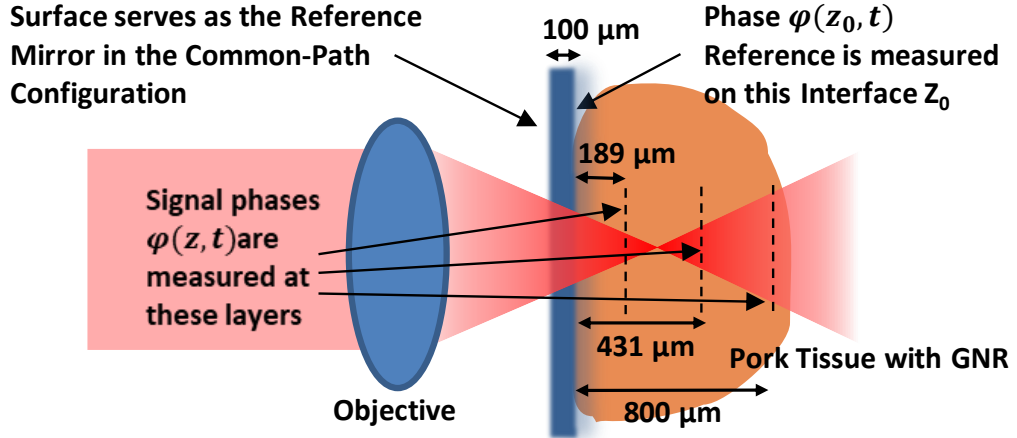


Fig. 4.22. Pork tissue injected with GNR solution. The front surface of the 100 μm thick coverslip serves as the reference arm mirror/reflector for the common path configuration of the system. The beam focus is placed in the tissue. The reference phase $\varphi(z_0, t)$ was measured on the back surface (z_0) of the coverslip, and the detected phase $\varphi(z, t)$ was measured at the multiple depths of 189 μm , 431 μm and 800 μm in the tissue.

Unlike the thick microfluidic channel used in sections 4.4.6 – 4.4.8, the coverslip used here is only 100 μm thick. Thus, the beam focus could still be placed inside the tissue sample even using the common path configuration which provides a better measurement sensitivity than the independent reference arm configuration, as proved in section 4.4.3. Because measurements in this section only involved A-scan detections, we set the camera exposure time at 443 μs . According to Fig. 4.10, the combination of the camera setting and the system configuration determined a displacement sensitivity of 1.57 nm which was also the best displacement sensitivity of the system without using the FFT analysis to the output phase.

As seen in Fig. 4.22, the front surface of the coverslip served as the reference arm mirror for the common path configuration. The reference phase $\varphi(z_0, t)$ was measured on the glass/tissue interface, and the detected phase $\varphi(z, t)$ was measured inside the tissue. The phase $\Phi(z, t)$ used to produce the output trace was calculated from Eq. (4.7) and Eq. (4.8).

The Ti:Sa beam (Fig. 4.1) was modulated at 120 Hz by the chopper wheel. Coaxially combined Ti:Sa and OCT beams are targeted on a single lateral position on the sample (Fig. 4.1.C or Fig. 4.22), with the pair of galvo-scanners disabled. In order to have the optimal measurement sensitivity, as discussed in sections 4.4.6 and 4.4.7, the

output trace of $\text{FFT}[\Delta\Phi(z, t)]$ was produced for the photothermal detection of GNRs in the tissue sample.

In order to locate GNRs in the tissue, we kept changing the detecting depth within the axial range of 200 microns to 1 mm in the tissue sample. In the meanwhile, we monitored the $\text{FFT}[\Delta\Phi(z, t)]$ trace. When we reached the depth of 800 μm below the glass/tissue interface (Fig. 4.22), a FFT peak appeared at 120 Hz on the “Frequency Component Axis”, as shown in Fig. 4.23.(a), indicating that GNRs existed at that depth. As mentioned in section 4.3, the imaging range of this SD-OCT system is 1000 μm in tissue. Thus, the depth of 800 μm is closed to the imaging limit of the system. Selected $\text{FFT}[\Delta\Phi(z, t)]$ traces are presented in Fig. 4.23, and they were obtained every 5 seconds in a measurement sequence lasting 30 seconds.

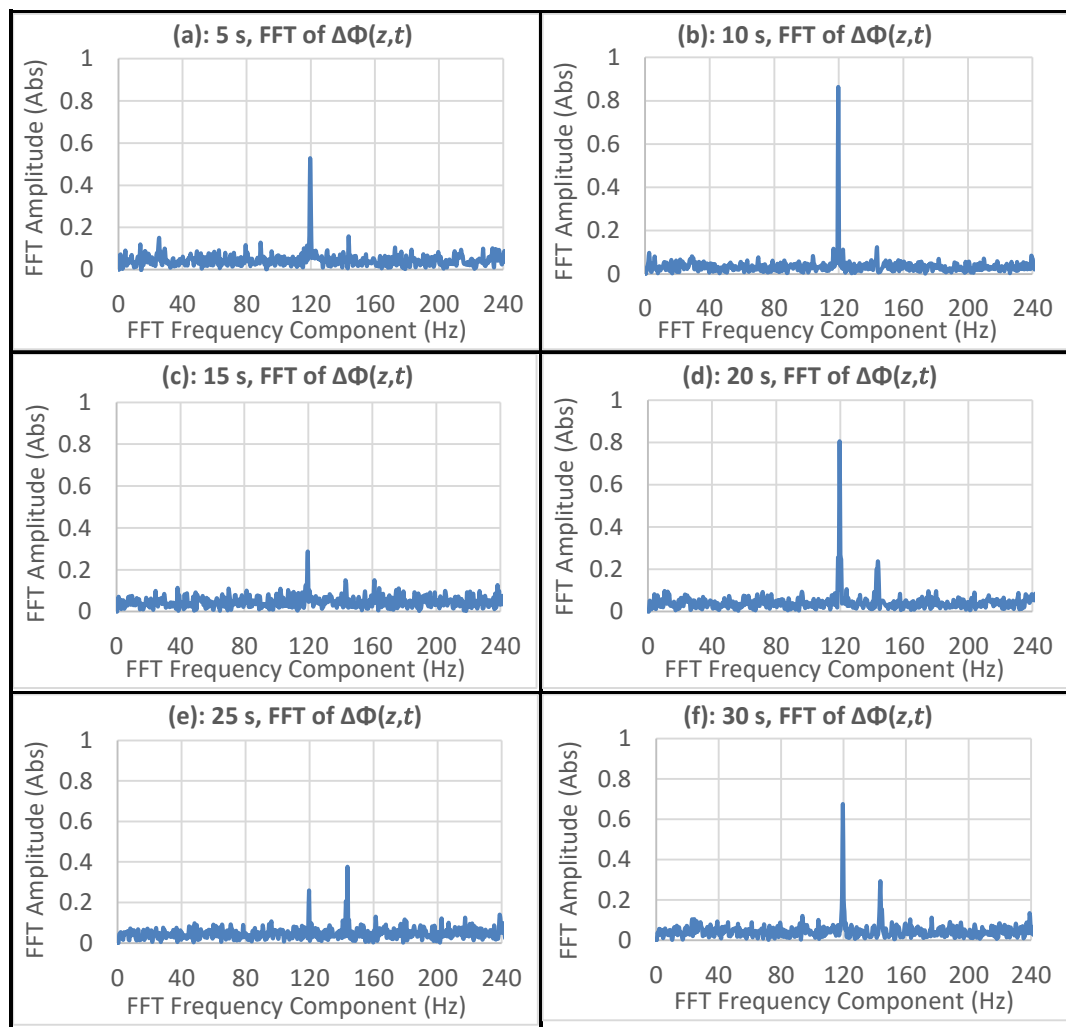


Fig. 4.23. Output trace of $\text{FFT}[\Delta\Phi(z, t)]$, measured at the depth of 800 μm in the tissue sample. (a)-(f) were obtained every 5 seconds in a measurement lasting 30 seconds. The Ti:Sa beam in Fig. 4.1 was modulated at 120 Hz by the chopper wheel.

Unlike the stable FFT peaks obtained in sections 4.4.6 and 4.4.7 where GNRs were diffused in DI water, the height of the FFT peak measured from the tissue sample fluctuated with time. The fluctuation of the FFT peak at the modulation frequency of the Ti:Sa beam indicates that when GNRs are in tissue, the movement of GNRs introduced by photothermal trapping is affected and obstructed by the tissue structure. Thus, the concepts used to explain the photothermal trapping of GNRs in clear media in the reference [40] may not fully explain the photothermal trapping of GNRs in biological tissue.

4.4.10 Photothermal imaging of GNRs in biological tissue

In section 4.4.8, we demonstrated how to produce *en-face* phase images for photothermal imaging GNRs diffused in DI water. We duplicated the procedure in section 4.4.8 and generated photothermal images of GNRs in biological tissue. The parameters of the system used here, including the 2D scanning frame rate and the camera exposure setting, are same as described in section 4.4.8, except that we chose the common path configuration rather than the independent sample/reference arm configuration. According to Fig. 4.10, the camera exposure setting of 27.8 μm in the common path configured system determines a displacement sensitivity of 3.93 nm of the system.

In order to generate *en-face* phase images of GNRs in the tissue sample, we had to identify the layer containing GNRs. To this end, we duplicated the procedure demonstrated in section 4.4.9. As demonstrated in Fig. 4.22, we found GNRs in depths of 189 μm and 431 μm respectively. Then, by using the shutter (Fig. 4.1) to control the Ti:Sa beam, we generated *en-face* images to display the distribution of GNRs located at these two layers. Results are presented in Fig. 4.24, in which the images came from mapping the phase difference $\delta\Phi(x_m, y_n)$ in Eq. (4.12) into grayscale values, without the constant π being added to $\delta\Phi(x_m, y_n)$.

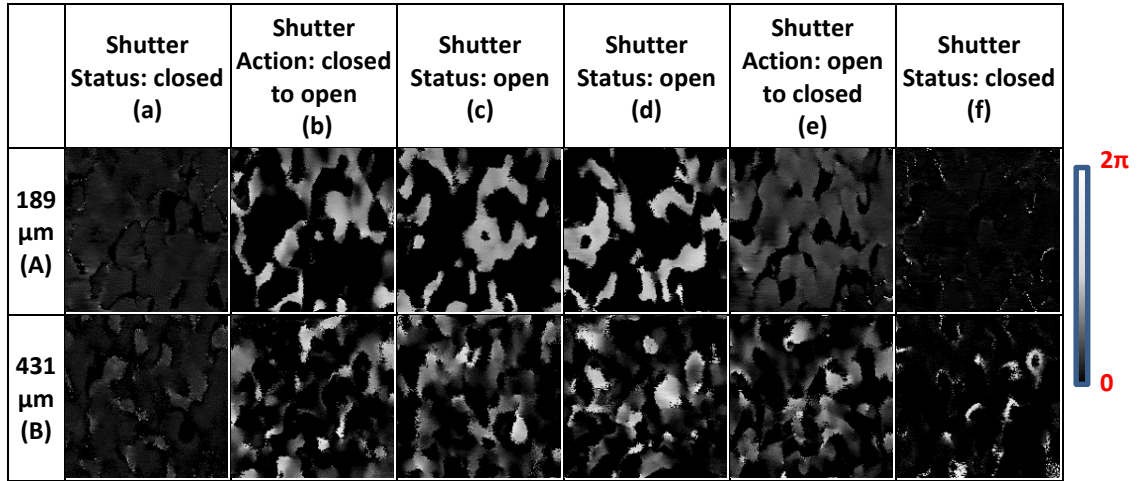


Fig. 4.24. *En-face* images of photothermal trapped GNRs in the pork tissue sample. Images were obtained by mapping $\delta\Phi(x_m, y_n)$ in Eq. (4.12) into grayscale. Images display two different layers containing GNRs inside the tissue sample. For each layer, 4 images were recorded when the shutter gate (Fig. 4.1) was staying in the open status. Columns (b)-(e) were obtained every 2 seconds after the shutter was opened.

As seen in in Fig. 4.24 column (a), images show mostly dark when the shutter gate (Fig. 4.1) is closed. When the shutter was switched from closed to open, the obtained images (Fig. 4.24 column (b)) have patterns of bright shades. Analogous to Fig. 4.20 column (B), these patterns show regions covered by GNRs in respective layers. This result indicates that the phase sensitive SD-OCT can be used for photothermal imaging GNRs at different layers inside the biological tissue.

Images in Fig. 4.24 columns (b)-(e) were obtained every 2 seconds after the shutter was opened. Unlike the images in Fig. 4.20 column (C) that are mostly black, these images have varying patterns. It can be concluded from the varying patterns that the photothermal trapping induced movements of GNRs in tissue were obstructed by the tissue structure. Moreover, some changes in tissue morphology may take place as the generated heat varied the local temperature of the tissue.

When the shutter was switched moved from open to closed, the obtained images in Fig. 4.24 column (e) are analogous to Fig. 4.20 column (C), displaying an inversed photothermal response order (off= \Rightarrow on) of GNRs.

Analogous to Fig. 4.20 column (D), images in Fig. 4.24 column (f) are mostly black while the shutter is left in the closed status. The black images indicate that no photothermal response is detected while the Ti:Sa beam is blocked.

4.5 Discussion and Conclusion

In this chapter, we discussed the theoretical basis for using phase sensitive interferometer to measure micro displacement. The setup of our custom phase sensitive SD-OCT is described. Its working parameters in the conventional OCT function mode (non-phase-sensitive) were given, and the procedure of measurement is omitted here. We demonstrated the whole procedure to quantify the performance of this phase sensitive SD-OCT system, including how to calibrate the system, how the displacement sensitivity was characterized in two separate system configurations, and how the displacement sensitivity was degraded to defocus in the common path configuration. We also evaluated the fundamental and hardware limits of the system. Then, we applied the system to the photothermal detection and photothermal imaging of GNRs in both the ID water solution and the biological tissue sample. As a summary of this chapter, key results are discussed, and main conclusions are listed as following.

In section 4.4.1, we demonstrated how to generate output traces of $\Phi(z, t)$, $\Delta\Phi(z, t)$, and $\text{FFT}[\Delta\Phi(z, t)]$ according to the theory discussed in section 4.2. We generated and tested each of these three output traces by performing phase measurements on a piezo actuated microscope coverslip. The resulting measurements agree with the relevant theory and mathematical equations: Eq. (4.4), Eq. (4.5), and Eq. (4.6).

In section 4.4.2, we demonstrated how the system was calibrated. We compared the result of the vibrating amplitude obtained from three different output traces with the datasheet of the piezo actuator. Results obtained from measurements of three output traces agree well with the datasheet. Nevertheless, we found that the result from the $\text{FFT}[\Delta\Phi(z, t)]$ trace has a better agreement with the datasheet compared with the other two traces. We speculate the superiority of the $\text{FFT}[\Delta\Phi(z, t)]$ method to the inherently averaging nature of the Fourier transform treatment.

In section 4.4.3, we employed two widely used mathematical models to characterize the displacement sensitivity of the OCT system in two configurations: the common path configuration and the independent reference arm configuration. In the each configuration, the displacement sensitivity was also characterized under different camera exposure time settings. As a result, we summarized the characterized displacement sensitivity of the system in different configurations and camera settings in a bar chart (Fig. 4.10). As shown in that chart, two mathematical models give different

but comparable results, indicating that the displacement sensitivity of the OCT system is in the nanometre scale, and the common path configuration has a better displacement sensitivity than the separate reference arm configuration. This is an expected result since a separate reference arm makes the output phase susceptible to mechanical or thermal fluctuations in both arms. In addition, we notice that a longer camera exposure time improves the displacement sensitivity of the system but it also slows down the A-scan acquisition speed. In our measurements, the camera exposure setting of 443 μs and the A-scan detection rate of 500 Hz results in an acceptable trade-off between the displacement sensitivity and the data acquisition speed when the system works in the A-scan operating mode with both galvo-scanners disabled.

In section 4.4.4, firstly, we took phase measurements on real nanometre scale displacements. By comparing the result of the vibrating amplitude obtained from measurements with the result characterized from two mathematical models, we find that the model based on the output phase stability perspective is more accurate than the other model. Secondly, we compared the measurement sensitivity of three output traces: $\Phi(z, t)$, $\Delta\Phi(z, t)$, and $\text{FFT}[\Delta\Phi(z, t)]$. The conclusion is that by applying FFT on the output trace of $\Delta\Phi(z, t)$, the displacement sensitivity of the system can be improved to the sub-nanometre scale (0.17 nm).

In section 4.4.5, we set the camera exposure time at 443 μs , made the system work in the common path configuration, and used the superior mathematical model to characterize the displacement sensitivity degradation to the defocus. By doing this, we find an axial region of the objective, which exhibits the best measurement sensitivity performance. Given by this result, we obtained the idea of where to place the detected sample to benefit from the best displacement sensitivity of the OCT system.

By conducting the work described in above sections, we gained information on how to set appropriate operating parameters to make the phase sensitive SD-OCT system work in the optimized condition to perform the photothermal detection and imaging of GNRs in clear and biological media.

In section 4.4.6, we coaxially combined a Ti:Sa laser beam with the OCT beam to excite the photothermal response of GNRs. We measured the photothermal response of GNRs to the modulation frequency of the Ti:Sa beam. It is concluded that by detecting the photothermal effect, the phase sensitive SD-OCT system is able to detect the

existence of GNRs in clear medium. Moreover, the GNR solution exhibits a superior photothermal response in the range 60 Hz - 250 Hz compared to the range 5 Hz - 60 Hz.

In section 4.4.7, based on the results obtained from section 4.4.6, we fixed the Ti:Sa modulation frequency at 220 Hz and measured the photothermal response of GNRs to the output power the Ti:Sa beam. It is concluded that the minimum Ti:Sa power capable of inducing a detectable photothermal response of GNRs is 0.583 mW. This value is in line with the latest reported minimum Ti:Sa power (0.5 mW) capable of photothermal trapping GNRs [40] in the DI water, where the TPL detection was employed. Consequently, to investigate the photothermal trapping of GNRs, the phase sensitive SD-OCT should exceed the TPL detection if the SD-OCT system would have employed the common path configuration.

In section 4.4.8, given that measuring 3D volume data requires a fast data acquisition speed, we chose a faster camera exposure time setting to enhance the A-scan rate at an expense of decreased displacement sensitivity. Then, we generated *en-face* phase images as grayscale x-y maps, displaying photothermal response induced changes. The on/off state of Ti:Sa excitation of GNRs was controlled by enabling and disabling the propagation of the Ti:Sa beam to the GNR solution sample. When comparing the phase values before and after the Ti:Sa excitation, lateral positions covered by aggregated GNRs are represented as white, whereas positions with no GNRs are represented as black in the *en-face* images. The achieved greatest contrast in these *en-face* phase images proved that the phase sensitive SD-OCT method is superior to the TPL detection [40] in imaging the photothermal trapping of GNRs.

In the 3D mode, all phase values were wrapped between $-\pi$ and π . Consequently, the thickness of the aggregated GNRs, which is linked to the strength of photothermal trapping, cannot be efficiently quantified by the SD-OCT technology with no phase unwrapping function. Nevertheless, SD-OCT has a significant potential of doing this by employing common path configuration to improve the sensitivity, and by employing a suitable phase unwrapping algorithm on the retrieved phase.

In section 4.4.9, we injected the GNR solution into a piece of pork tissue and employed the photothermal detection technique to locate GNRs inside the tissue sample. Because the common path configuration was employed, the detection and imaging were conducted in an enhanced displacement sensitivity. The depth of 800 μm , where GNRs were located by the phase sensitive SD-OCT, is close to the maximum imaging depth of

the OCT system (1000 μm in tissue). Thus, the SD-OCT technology could be able to locate GNRs deeper in the tissue if a higher resolution spectrometer had been employed. The fluctuation of the FFT peak indicates that the photothermal trapping of GNRs in tissue is obstructed by the tissue structure in a complex manner.

In section 4.4.10, we generated *en-face* phase images to display changes induced by the photothermal response of GNRs in the tissue sample. Unlike the photothermal imaging of GNRs in DI water, because the common path configuration was used in this section, the system had an improved displacement sensitivity which resulted in a large number of phase values in the middle of $-\pi$ and π to build the images.

When the shutter gate stayed in an open status, the produced *en-face* images during a time period had varying patterns. This result agrees with the fluctuation of the height of the FFT peak in section 4.4.9. The fluctuation of the FFT signal and the varying pattern in the *en-face* images indicate that the photothermal trapping induced migration of GNRs in biological tissue is influenced by the random nature of the tissue structure, and the photothermal trapping of GNRs in tissue has a greater complexity than in DI water.

In summary, the experimental results presented in this chapter indicate that the spectrometer based phase sensitive OCT is suitable for photothermal detection and imaging of GNRs in both clear and biological media. However, the detection and imaging depth of the SD-OCT system was limited to 1 mm in tissue, which stimulated our interests to develop a swept source based phase sensitive OCT system that exhibits a deeper imaging range, as will be demonstrated in the following chapter.

Chapter 5

Swept source based phase-sensitive OCT system and its application in dynamic photothermal detection and imaging of GNRs in clear and scattering media

5.1 Introduction

FD-OCT can be implemented in two ways: spectral-domain OCT (SD-OCT) employing a broadband light source and a spectrometer; or swept-source OCT (SS-OCT) employing a swept laser source and a photodetector [77][78]. The SD-OCT system built by the author for the purpose of carrying out phase sensitive measurements has been discussed in Chapter 4. As mentioned, it has a limited imaging depth up to 1 mm in highly scattering tissue, whereas the penetration depth of SS-OCT can reach a few millimetres [21][79]. Our SD-OCT has a controllable A-scan acquisition rate of 500 Hz to a few kHz, whereas SS-OCT has reported A-scan acquisition rate up to 370 kHz [21]. Our SD-OCT has an excellent sub-nanometre scale displacement sensitivity, whereas reported SS-OCT systems have worse displacement sensitivities in the nanometre scale [21][80]. Although the measurement sensitivity of SS-OCT is not as good as SD-OCT, in terms of the advanced data acquisition speed and the enhanced imaging depth, phase sensitive SS-OCT is another option for the photothermal detection and imaging of gold nanoparticles [63].

Phase sensitive SS-OCT has been reported for the photothermal detection of gold nanoshells (GNSHs) in clear media [63]. Analogous to phase sensitive SD-OCT, phase sensitive SS-OCT completed the task by detecting the OPD variation caused by the photothermal response of GNSHs. Though the measurement of SS-OCT presented excellent SNR at high operating speed, the measurement was only made on GNSHs diffused in clear media. In addition, the reported work [63] did not generate images to investigate the distribution of GNSHs in the sample.

We developed a swept source based phase sensitive SS-OCT system and employed it to perform the photothermal detection and imaging of GNRs in clear and scattering media. Real time *en-face* images are produced to display the distribution of GNRs in clear and scattering media. The methodology and corresponding experimental results are presented in 5.3. The noise levels of the output phase from this SS-OCT system and the SD-OCT system demonstrated in Chapter 4 are compared in this Chapter.

5.2 System configuration

Fig. 5.1 presents the configuration of the phase sensitive SS-OCT system implemented with photothermal modulation devices. The OCT swept source (AXSUN Technology, 1060) has a spectral sweep rate of 100 kHz, a duty cycle of 46%, and a spectral full-width at half maximum (FWHM) of 100 nm centred at 1060 nm. As seen in Fig. 5.1, the swept source beam is coupled into a fibre based Michelson interferometer with three collimators at the fibre outputs. A fraction of 80% of the optical power is guided into the reference arm, and the remaining 20% is guided to the sample arm in a 2.4 mm wide beam. In the sample arm, a Ti:Sa laser beam (centred at 800nm, pulse duration of 150fs, 80 MHz) is coaxially combined with the OCT beam using a dichroic mirror. The combined beams hit a pair of galvo-scanners (THORLABS, GVS302) and subsequently an objective/scan lens (THORLABS, LSM02-BB, $f=18$ mm) that produces a focused spot size of 3.1 μm . An optical shutter gate is used to enable or disable the Ti:Sa beam to the SS-OCT system. The Ti:Sa beam is also modulated from 10 Hz to 60 Hz by an optical chopper wheel. In the reference arm, the beam propagates through two glass dispersion compensation blocks (THORLABS, LSM02DC), so that the dispersion in the reference arm matches the dispersion created by the objective in the sample arm.

OCT beams returned from both arms interfere at the output of the interferometer. The interference signal is detected by a balanced photodetector (THORLABS, PDB430C DC to 350 MHz bandwidth) capable of removing the DC component in the signal and generating an electrical time-varying AC interference signal. These fringes are then acquired by a 12 bit waveform digitizer (AlazarTech, ATS9350, 500 MS/s sampling rate) installed in a PC. The digitizer has a trigger input port and a k -clock input port. The trigger input is connected to the trigger output on the swept laser. This connection enables the synchronization between the spectral sweep of the laser and the A-scan acquisition of the digitizer since the swept laser produces a trigger spike at the

start of each spectral sweep [80]. The k -clock input port on the digitizer is connected to the k -clock output on the swept laser. This connection allows the digitizer to perform uniform data sampling in k -space while digitizing the interference signals. In reality, the k -clock on the swept laser is nonlinear in the time domain but uniform in k -space. Thus, if the k -clock connection is made between the swept source and the digitizer, no extra data resampling or data post-processing is required [21][81].

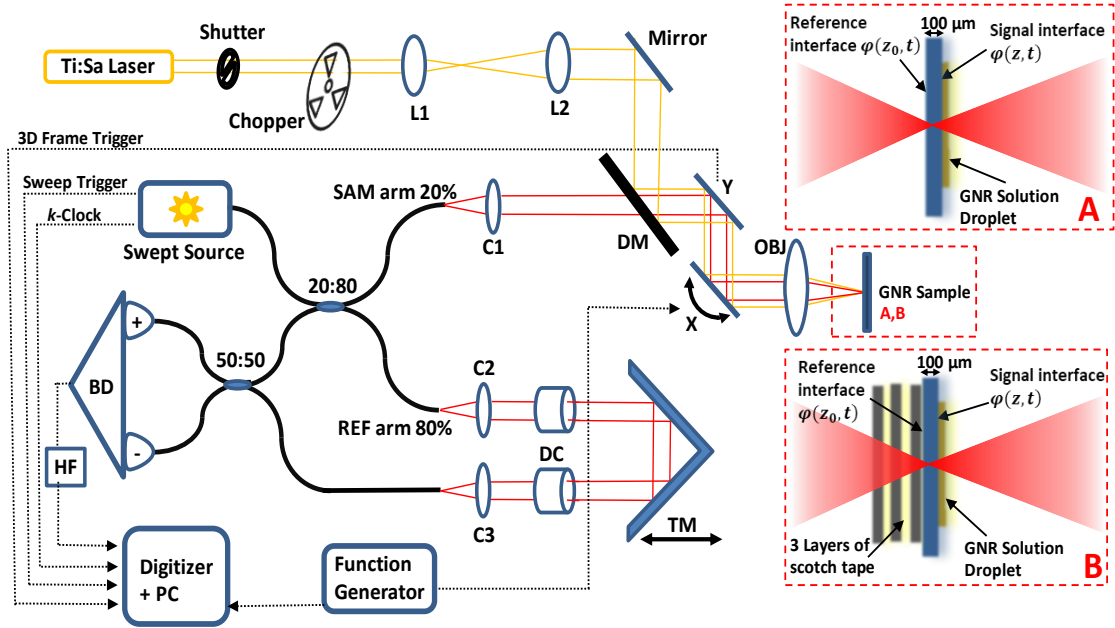


Fig. 5.1. Schematic of the phase sensitive SS-OCT system implanted with photothermal modulation devices. Collimators (C1-C3). Galvo-scanners (X,Y). Objective lens (OBJ). Dispersion compensation blocks (DC). Balanced photodetector (BD). High pass filter (HF). Computer (PC). Translating mirror (TM). Doublet lens (L1, L2). Dichroic mirror (DM). Insert (A): sample used for the photothermal detection and imaging of GNRs in clear media. Insert (B): sample used for photothermal imaging of GNRs in scattering media.

In the setup, a high pass electrical filter (THORLABS, EF515, >10 MHz pass band) was inserted between the balanced photodetector and the digitizer. The filter further removed low frequency components introduced by the residual light reflected from the reference arm, which helped to enhance the image contrast. Moreover, it removed the residual low frequency signal from the detector, which was reported to be created by the imperfect common mode rejection of the balanced photodetector [63].

The digitized interference fringes were processed by our custom-designed LabVIEW programme, generating an interferogram consisting of 1024 points evenly distributed in the k -space. After that, the LabVIEW programme performed a complex FFT on the interferogram to retrieve a 512-pixel A-scan profile containing the depth-

resolved amplitude and phase information of the detected sample. The amplitude was mapped to the grayscale to produce an A-scan column of pixels. By actuating the faster galvo-scanner (in Fig. 5.1) to scan the OCT beam in the lateral direction over the sample, a B-scan image was constructed. By actuating both galvo-scanners to make a raster scanning over the sample, a 3D volume of data could be collected and constructed. By slicing the data at a particular layer of the 3D volume data, an *en-face* image at the depth of interest in the sample was generated. The SS-OCT system has a measured axial resolution of $\delta z = 14 \mu\text{m}$ (FWHM). This value was maintained constant throughout a measured imaging range of $z = 3.5 \text{ mm}$ in air.

5.3 Methodology and Results

The methods used to evaluate the working performance and to characterize the noise level of the output phase are analogous to the methods described in Chapter 4. We employed the SS-OCT system to make phase measurements on micrometre scale vibrations generated by an actuated coverslip. During the measurements, the Ti:Sa laser in the system setup (Fig. 5.1) was disabled.

Sections 5.3.1, 5.3.2 and 5.3.3 demonstrate how devices in the SS-OCT system are synchronized in operating modes of A-scan, B-Scan and *en-face* respectively. The phase measurement performance of each mode is evaluated in the corresponding section.

The system noise level of the SD-OCT and the SS-OCT are compared in section 5.3.4.

The photothermal detection and imaging of GNRs in clear media are demonstrated in section 5.3.5 and section 5.3.6 respectively. The photothermal imaging of GNRs in scattering media is demonstrated in section 5.3.7.

5.3.1 Phase measurement in A-scan

5.3.1.(a) Synchronization

For a SS-OCT system, it is critical to synchronize the swept laser, galvo-scanners and digitizer. As seen in Fig. 5.1, the swept laser exports a trigger at the beginning of each spectral sweep. Receiving this trigger, the digitizer records 1024 data points to generate an A-scan interferogram. Since the sweep rate of the employed swept source is 100 kHz, the determined A-scan detection rate is 100 kHz, which corresponds to $10 \mu\text{s}$

for each A-scan. The 10 μs is the total time for each spectral sweep cycle of the laser, consisting of 5 μs forward spectral sweep and another 5 μs backward spectral sweep.

In our approach, only the interferogram generated in the forward sweep was recorded, leaving out the one generated in the backward sweep. Thus, the digitizer was required to record data only in the first 5 μs , leaving the remaining 5 μs waiting for the next sweep trigger from the swept laser. To this end, the sampling rate of the digitizer was set to be 250 MS/s such that it took 4.1 μs to record the 1024 samples, which accounted for roughly 4/5 of the 5 μs . Thus, the spectral sweep of the laser and the data acquisition of the digitizer started simultaneously, and then they kept progressing together until the data acquisition stopped 0.9 μs before the spectral sweep turning around. A synchronization like this allows the data acquisition to fully use the sweep spectrum of the laser, resulting in optimized imaging range of the SS-OCT system. Next, the interferogram produced in the first 5 μs was buffered into the PC memory for processing.

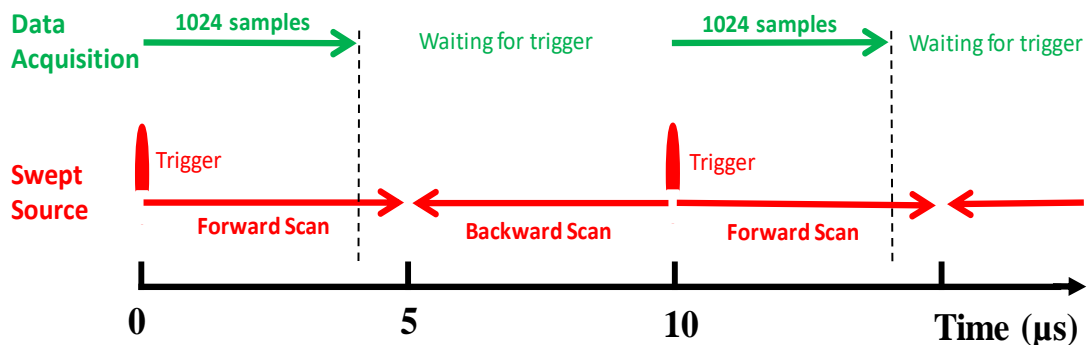


Fig. 5.2. The synchronization between the swept source and the data acquisition in the A-scan operating mode. The data acquisition waits for the trigger from the swept source.

Receiving the interferogram, in the remaining 5 μs , our LabVIEW programme was designed to perform a complex FFT on the interferogram, resulting in two separate A-scan profiles, one containing amplitude values as a function of depth z and the other one containing phase values as a function of depth z . The LabVIEW implementation is presented in Fig. A.3. In this 5 μs , the digitizer was waiting for the next trigger from the swept source. The synchronization is schematically demonstrated in Fig. 5.2.

In summary, when the system is operating in the A-scan operation mode, each A-scan lasts 10 μs (equivalent to an operation rate of 100 kHz), with 5 μs acquiring data and another 5 μs processing data.

5.3.1.(b) Measurement

In order to test the phase measurement performance of the SS-OCT system, we performed A-scan phase measurements on a 100 μm thick microscope coverslip mounted on a piezo actuator (THORLABS, PA4FEW).

In order to eliminate the phase noise, the method used in Chapter 4 was duplicated here. As seen in Fig. 5.3, a stationary coverslip is placed at z_0 in front of the actuated one at z . The reference phase $\varphi(z_0, t)$ was measured on the interface z_0 , and the detected phase $\varphi(z, t)$ was measured on the interface z . Eq. (4.7) and Eq. (4.8) were used to calculate their difference $\Phi(z, t)$ as the output phase.

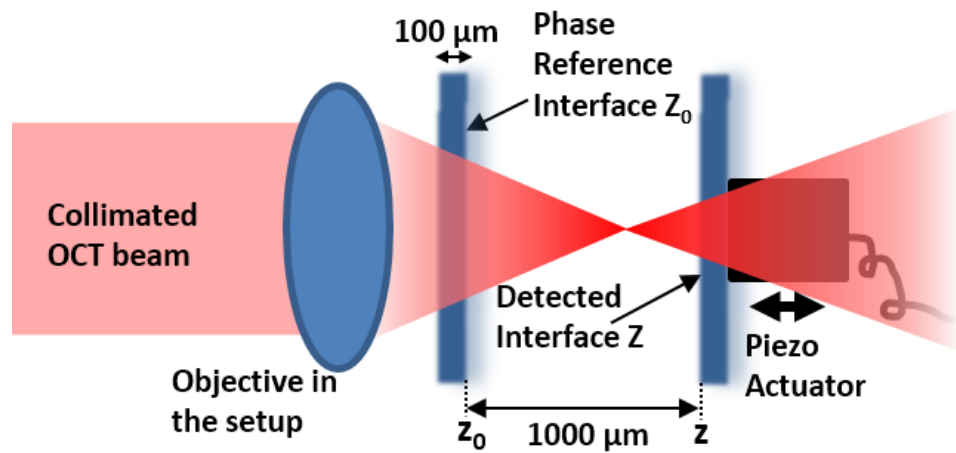


Fig. 5.3. A stationary coverslip is placed at z_0 in front of the actuated one located at z . The reference phase $\varphi(z_0, t)$ was measured on the interface at z_0 , and the detected phase $\varphi(z, t)$ was measured on the front surface of the actuated coverslip.

The common path configuration was employed to perform measurements. The following two steps were used to retrieve the phase signal at the detected layer in the sample. Firstly, an A-scan amplitude profile (Fig. 5.4) was generated and monitored. As seen in Fig. 5.4, in this A-scan amplitude profile, the pixel orders of two peaks corresponding to the z_0 interface and the z interface are identified by a LabVIEW routine which is presented in Fig. A.4. The first peak (with the pixel order of 27th) in Fig. 5.4 corresponds to the back surface of the left coverslip in Fig. 5.3. The second peak (with the pixel order of 305th) in Fig. 5.4 corresponds to the front surface of the actuated coverslip in Fig. 5.3. Since the front surface of the left coverslip in Fig. 5.3 was used as the reference mirror for the common path configuration, it has no corresponding peak in the A-scan profile. Secondly, we set the LabVIEW programme to output the phase value $\varphi(z, t)$ and the phase difference $\Phi(z, t) = \varphi(z, t) - \varphi(z_0, t)$. $\varphi(z, t)$ was

retrieved from the 305th pixel in the A-scan phase profile, and $\varphi(z_0, t)$ was retrieved from the 27th pixel in the A-scan phase profile. In Fig. 5.4, the output trace of $\varphi(z, t)$ is indicated as white, and the output trace of $\Phi(z, t)$ is indicated as red.

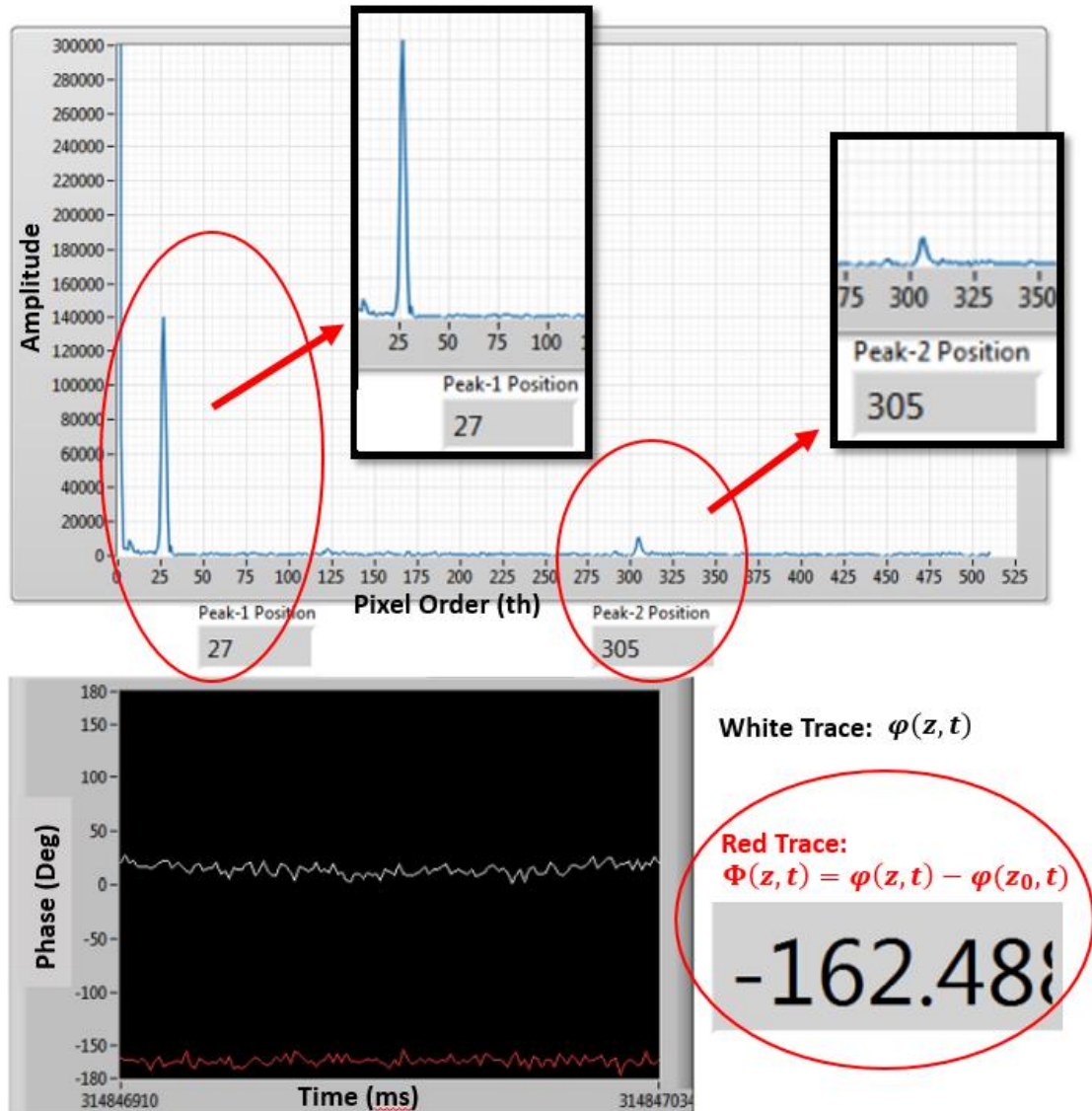


Fig. 5.4. Retrieving $\varphi(z, t)$ and $\Phi(z, t)$. In the A-scan (Amplitude against Pixel Order) profile, the LabVIEW programme identifies the pixel orders of the reference interface (at z_0 in Fig. 5.3) and the detected interface (at z in Fig. 5.3). Then, the LabVIEW programme outputs the phase value $\varphi(z, t)$ as the white trace and the phase difference $\Phi(z, t)$ as the red trace.

To test the phase measurement performance of the SS-OCT system, the piezo actuator (Fig. 5.1) was driven by sinusoidal voltages with a fixed frequency (1 Hz) and different amplitudes (1 V, 2 V, 3 V, 4 V). As indicated by the results presented in Chapter 4, at these driving parameters, the actual movement of the actuated coverslip

cannot be detected by the amplitude signal in the A-scan but can be detected by the phase signal $\Phi(z, t)$.

The obtained dynamic output traces of $\Phi(z, t)$ are presented in Fig. 5.5. As seen, they are sinusoidal in shape with the same modulation frequency as the vibrating frequency of the actuator. As expected, these sinusoidal traces present different amplitudes in accordance with the corresponding driving voltages of the actuator. These facts coincide with Eq. (4.4) and the concept of the phase-resolved measurements discussed in section 4.2. However, unlike the $\Phi(z, t)$ traces (in section 4.4.1) generated using the SD-OCT system, traces in Fig. 5.5.(a), (b) and (c) here have spikes on them. The number of the spikes on these traces are different, and the distribution of them appears random. However, the trace in Fig. 5.5.(d) is free of spikes, indicating that they are not always present. Thus, these spikes are the net result of the unpredictable and intermittent jitter noise from the swept OCT source.

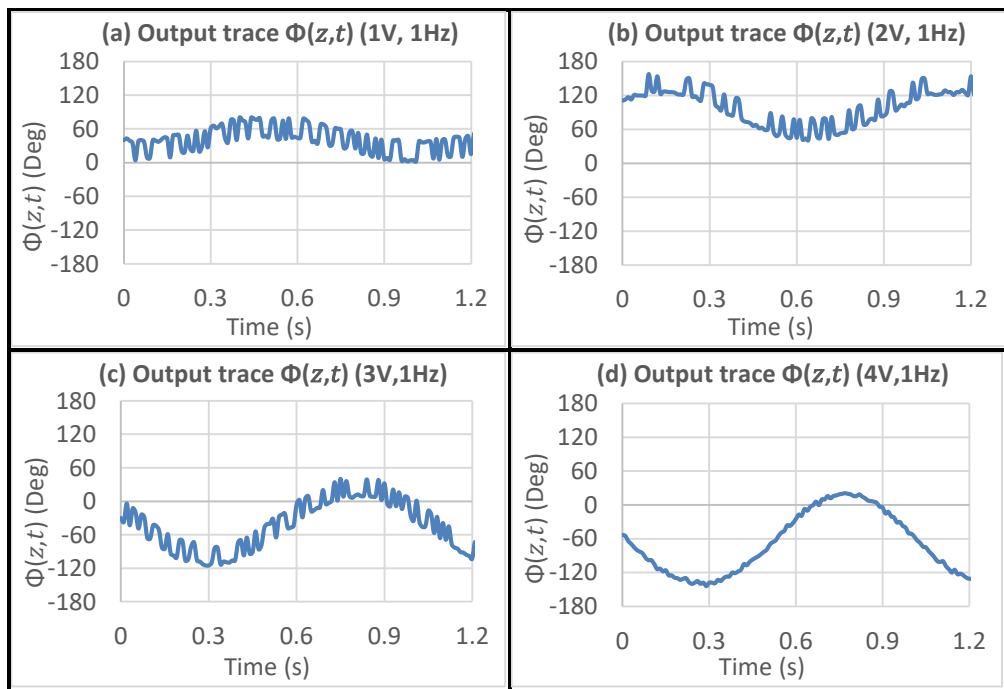


Fig. 5.5. Output traces of $\Phi(z, t)$. The piezo actuator was driven by sinusoidal voltages with a fixed frequency (1 Hz) and different amplitudes (1 V, 2 V, 3 V, 4 V).

Then, the piezo actuator was driven by sinusoidal voltages with a fixed amplitude (3 V) but different frequencies (5 Hz, 10 Hz, 15 Hz, 20 Hz). As presented in Fig. 5.6, the output traces of $\Phi(z, t)$ obtained under different driving parameters were shifted on purpose to overlap in the centre for the ease of comparison.

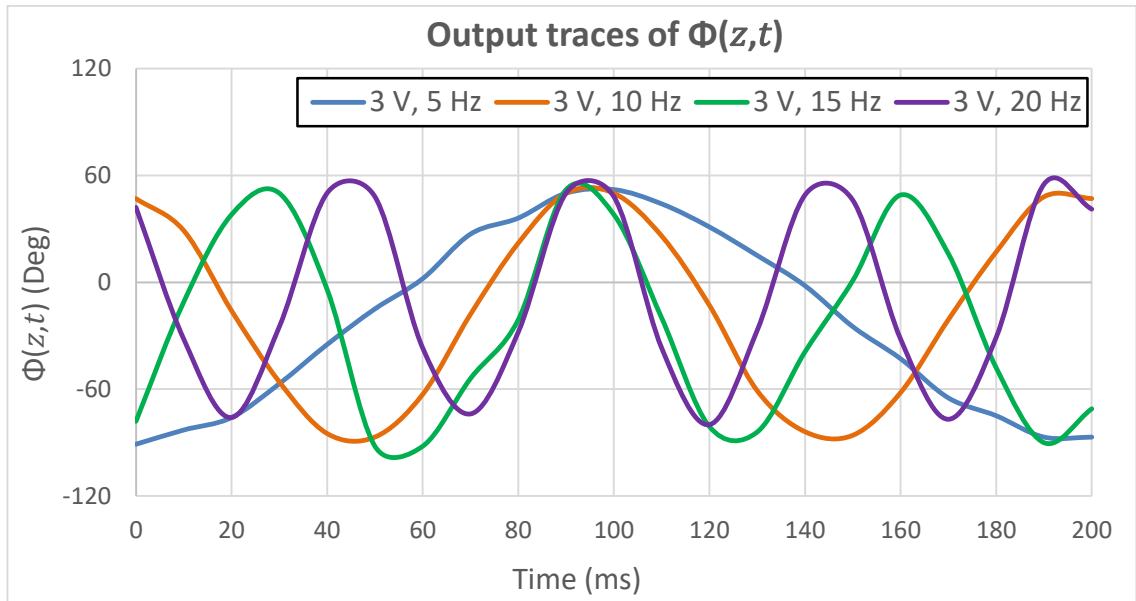


Fig. 5.6. Output traces of $\Phi(z, t)$. The piezo actuator was driven by sinusoidal voltages with the same amplitude (3 V) but different frequencies (5 Hz, 10 Hz, 15 Hz, 20 Hz).

As seen, all $\Phi(z, t)$ traces have roughly the same amplitude but different periods which broadly correspond to the driving frequency of the actuator in each case. Nevertheless, compared with the traces in Fig. 5.5, the $\Phi(z, t)$ traces in Fig. 5.6 are clean and free of spikes. Consequently, the effect on the output phase from the jitter noise is clearly unpredictable and irregular. The noise affected the first 3 measurements in Fig. 5.5.

Thirdly, we performed phase measurements on the actuated coverslip in the absence of a piezo driving signal. Ideally, as can be expected, the dynamic $\Phi(z, t)$ trace should be a straight line since the detected object was at rest. However, an output line with irregularly distributed spikes was obtained, as presented in Fig. 5.7. Once again, this behaviour supports our reasoning that the spikes present on output traces of $\Phi(z, t)$ are due to the random and unpredictable swept source jitter noise.

Output trace of $\Phi(z, t)$

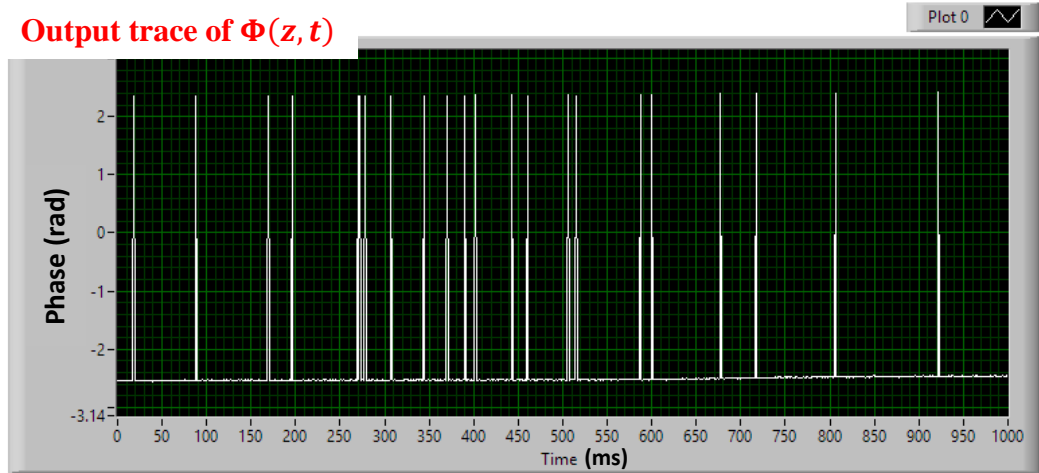


Fig. 5.7. Output trace of $\Phi(z, t)$. The measurement was made with no piezo driving signal.

To conclude, traces presented in Fig. 5.5 and Fig. 5.6 are in agreement with Eq. (4.4) where the modulation frequency of the $\Phi(z, t)$ output trace is equal to the frequency f_0 of the sinusoidal vibration, and the modulation amplitude of $\Phi(z, t)$ is proportional to the vibration amplitude A of the actuator. Consequently, our custom-built SS-OCT system is capable of performing quantitative phase measurements on micrometre scale vibrations when the jitter noise from the swept laser isn't causing spikes to the output trace. The unstable output phase and clearly degraded SNR indicate that the phase sensitive SS-OCT is less suitable to measure micrometre OPD variations compared with the phase sensitive SD-OCT in Chapter 4.

5.3.2 Phase measurement in B-scan

5.3.2.(a) Synchronization

In contrast with A-scan detection in which the beam is fixed at a lateral position on the sample, in the B-scan mode, the beam is scanning back and forth along a line. As demonstrated in Fig. 5.1, in order to produce a raster scanning for 3D imaging, two function generators are connected to a pair of galvo-scanners, one making a faster scanning of the beam and the other one making a slower scanning of the beam. To generate B-scan images, the slower galvo-scanner was disabled, and the faster galvo-scanner executed a triangle movement to scan the OCT beam at a rate of 100 Hz, i.e. 10 ms for each round trip scan. The 10 ms round trip includes 5 ms forward scanning and 5 ms backward scanning (triangular driving waveform).

In order to synchronize the galvo scanning and the B-scan acquisition, the function generator was also connected to the digitizer. The function generator sent a series of TTL pulses at the rate of 100 Hz (same as the scanning rate of the faster scanner) to the digitizer. Each TTL pulse served as a trigger for the digitizer to mark the first A-scan in each B-scan image. The B-scan imaging rate was determined by the scanning rate, which was 100 Hz.

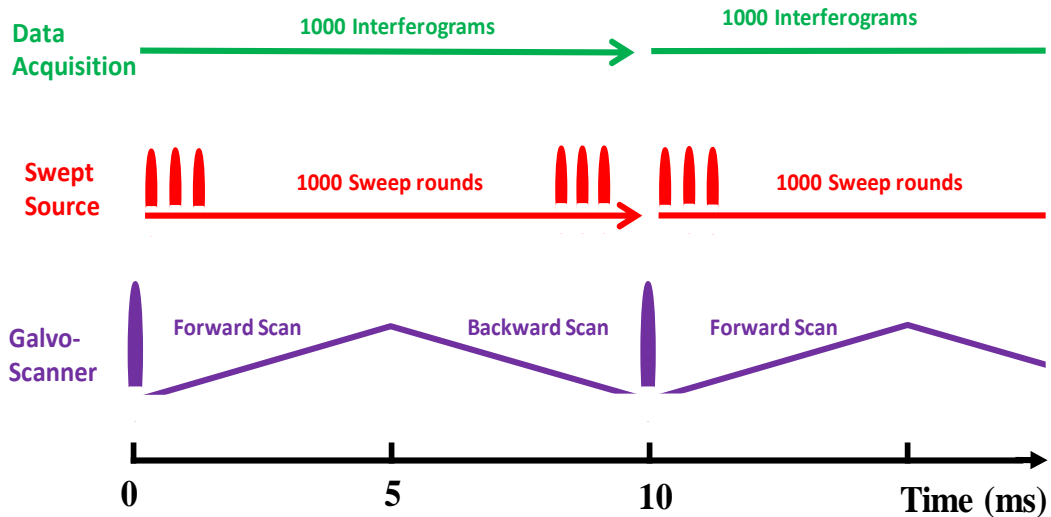


Fig. 5.8. The synchronization between the galvo-scanner, the swept source and the data acquisition in the B-scan operating mode. The swept source waits for the trigger from the galvo-scanner, and the data acquisition waits for the trigger from the swept source.

Because the sweeping rate of the laser is 100 kHz, 500 interferograms can be generated by the digitizer in the 5 ms forward scanning of the galvo-scanner, and another 500 interferograms in the 5 ms backward scanning. Thus, two sets of interferograms were acquired along the same line over the static sample. The digitizer was set to buffer 1000 interferograms (A-scans) after receiving a TTL trigger from the function generator, which determined a B-scan image size of 1000 A-scans. Our designed LabVIEW programme performed complex FFT on these 1000 interferograms, producing a B-scan image composed of 1000 A-scans. Each A-scan contained both amplitude and phase information of the detected sample at the corresponding scanning position. The synchronization is schematically demonstrated in Fig. 5.8. Each B-scan image is composed of two mirror images which show the same information along the scanned line.

To conclude, in the B-scan imaging mode, the SS-OCT beam was displaced laterally at a rate of 100 Hz after receiving a TTL trigger from the function generator.

After receiving the same trigger, the digitizer started to buffer 1000 interferograms at the rate of 100 kHz which was determined by the sweeping rate of the laser. 10 ms later, when the scanner completed the round trip, the FFT was performed to the buffered 1000 interferograms, generating a B-scan image with 1000 A-scans. By retrieving phase values from these 1000 A-scans, a B-scan phase trace was obtained.

5.3.2.(b) Measurement

Phase measurements in B-scan mode have been reported to quantify diameters of microbubbles in clear and scattering media [26]. In B-scan mode, the movement of the beam may add uncertainty or noise onto the retrieved phase. Thus, it is necessary to investigate the influence given by the beam movement and the scanning angle to the output phase.

The measurement was made on the sample demonstrated in Fig. 5.3, with both coverslips in fixed positions. 1000 A-scans were acquired in each scanning round trip. The scanner was driven by triangle voltages with a fixed frequency of 100 Hz and different amplitudes (100 mV, 150 mV) respectively. Results are presented in Fig. 5.9 and Fig. 5.10. In both figures, the red trace is the B-scan output trace of $\Phi(z, t)$, and the white trace is the B-scan output trace of $\varphi(z, t)$.

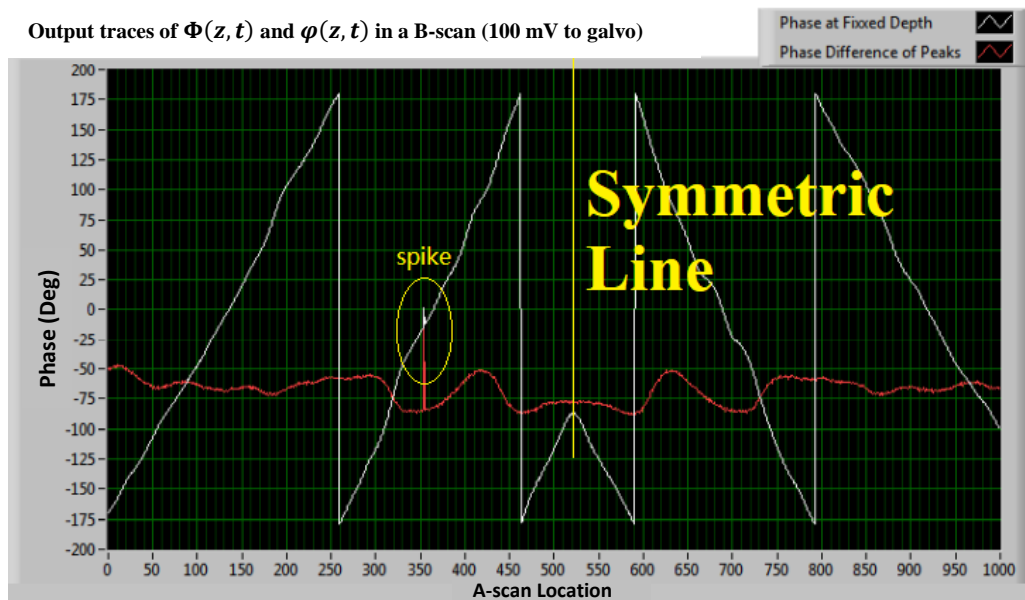


Fig. 5.9. Output traces of $\Phi(z, t)$ (red) and $\varphi(z, t)$ (white) from a B-scan scanning, figure showing output phase value against the A-scan location in a B-scan consisting of 1000 A-scans. Driving voltage amplitude of the galvo-scanner: 100 mV.

As seen in Fig. 5.9, with 100 mV voltage to the scanner, the B-scan output trace of $\Phi(z, t)$ (red) experiences an odd spike but otherwise varies smoothly over $35^\circ - 40^\circ$ of phase, whereas the $\varphi(z, t)$ trace (white) changes much more substantially and is wrapped between -180° and 180° . The variation of the $\varphi(z, t)$ trace is due to the extra added OPD created by the lateral beam scanning. The different behaviour of two traces confirms the importance of employing the reference interface (at z_0 in Fig. 5.2) to provide the reference phase $\varphi(z_0, t)$. Specifically, given the very limited extent of the lateral scan (100 mV corresponds to $60 \mu\text{m}$ scanning length on the sample), any two points, regardless of depth, within the same A-scan share the same additional OPD created by the lateral scanning. Hence, by subtracting $\varphi(z_0, t)$ from $\varphi(z, t)$, the influence given by the lateral scanning can be cancelled.

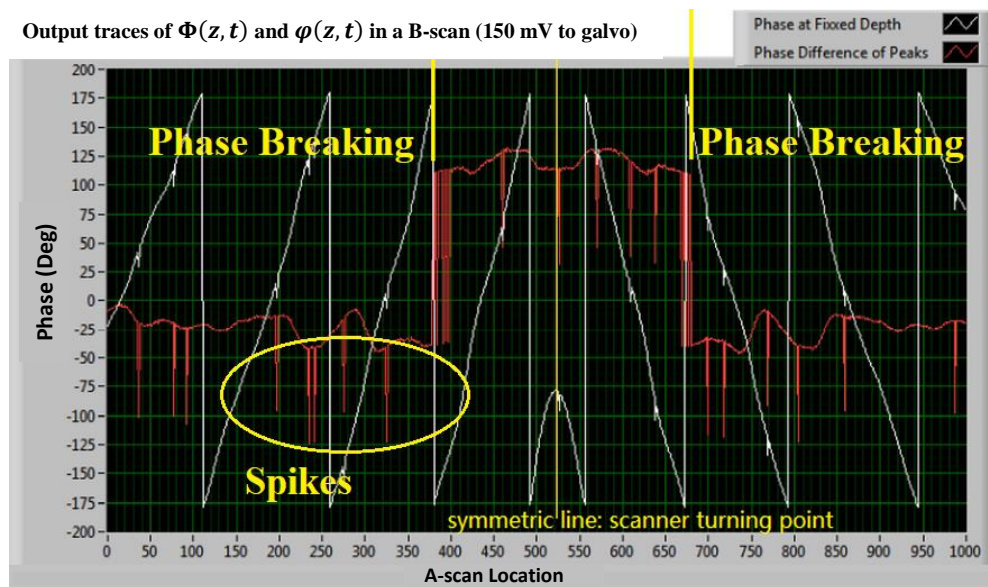


Fig. 5.10. Output traces of $\Phi(z, t)$ (red) and $\varphi(z, t)$ (white) in a B-scan, figure showing output phase value against the A-scan position in a B-scan file. Driving voltage of the galvo-scanner: 150 mV.

Driving the scanner with a 150 mV voltage results in lateral scanning over a greater field. As seen in Fig. 5.10, the output trace of $\Phi(z, t)$ (red) is discontinuous and has breakpoints at the A-scan positions with orders of 380 and 680. This indicates that when the scanning angle is larger than a certain value, the additional OPD created by the lateral beam scanning could not be cancelled by simply subtracting the reference phase $\varphi(z_0, t)$ from $\varphi(z, t)$. In this case, the phase measurement in B-scan is invalid due to a lack of continuity in the output trace. Thus, the scanning angle should be limited within a range, beyond which the lateral scanning induced OPD would render the output phase

discontinuous. For this reason, we limited the scanner driving voltage to 100 mV for all measurements described in following sections.

Since the beam was scanned forth and back over the same line on the sample, the symmetrical pattern of all traces in Fig. 5.6 and Fig. 5.7 indicates that the phase measurement in B-scan was highly repeatable. Still, due to the sweep jitter, unwanted and irregularly distributed spikes appear occasionally on these output traces.

5.3.3 Phase map generation & en-face phase image generation

5.3.3.(a) Synchronization

To generate phase maps and *en-face* phase images, a 3D volume of data of the detected sample has to be constructed beforehand. To this end, as shown in Fig. 5.1, both the X and Y galvo-scanners were employed to provide a 2D raster scanning. The faster galvo-scanner (X) executed a triangle movement to scan the OCT beam at a rate of 250 Hz, equivalent to 2 ms forward scanning and 2 ms backward scanning. In each of the two 2 ms, 200 interferograms were recorded for constructing a B-scan image. The slower galvo-scanner (Y), providing the scanning in another dimension, executed a sawtooth movement at a rate of 1.25 Hz, with 800 ms ramping upward and then sharply dropping back.

To synchronize the two galvo-scanners with the 3D data acquisition, a trigger signal was sent from the Y scanner to the digitizer when the Y scanner was ready to ramp upward. In the following 800 ms, the X scanner carried out 200 round trips, and the digitizer recorded 400 interferograms in each round trip of the X scanner. During this 800 ms interval, the digitizer was set to buffer a total of $200 \times 400 = 80,000$ interferograms into the memory.

When the 2D scanning was completed, a data-processing utility within our custom-built LabVIEW programme arranged these 80,000 interferograms into a 200×400 array. Each element in this array is an interferogram consisting of 1024 data points. Thus, the constructed 3D data set has a volume size of $200 \times 400 \times 1024$ pixels. After the FFT is performed to each A-scan array, the obtained 3D data set, which will be used to produce the 3D image, has a volume size of $200 \times 400 \times 512$ pixels. Because the faster galvo-scanner scanned each line twice, forward and backward, the 3D data set had a mirror term. We left out the mirror term and made a $200 \times 200 \times 512$ array which was mapped to the grayscale to produce a 3D image of the detected sample. The phase maps and *en-*

face phase images demonstrated in the following sections were sliced from generated 3D images.

5.3.3.(b) Phase map & en-face phase image generation

Phase sensitive Bessel beam interferometry has been reported to characterize the curvature of a liquid mirror [103] [104]. Because of its high sensitivity, the technology was also used to measure the precession angle of the liquid mirror [103]. Both the curvature and precession angle of the liquid mirror are measured from a phase map generated from the coherent interference between a reference Bessel beam and another coherent beam reflected by the liquid mirror. The phase map is actually an interference pattern showing as concentric annuli, as shown in Fig. 5.11. However, although the technology provided high sensitivity, since the employed beam was in the CW mode, this technology was not able to perform depth resolved imaging. In contrast, preserving the high sensitivity, our home-built phase sensitive SS-OCT has the advantage of making depth resolved detection and imaging.

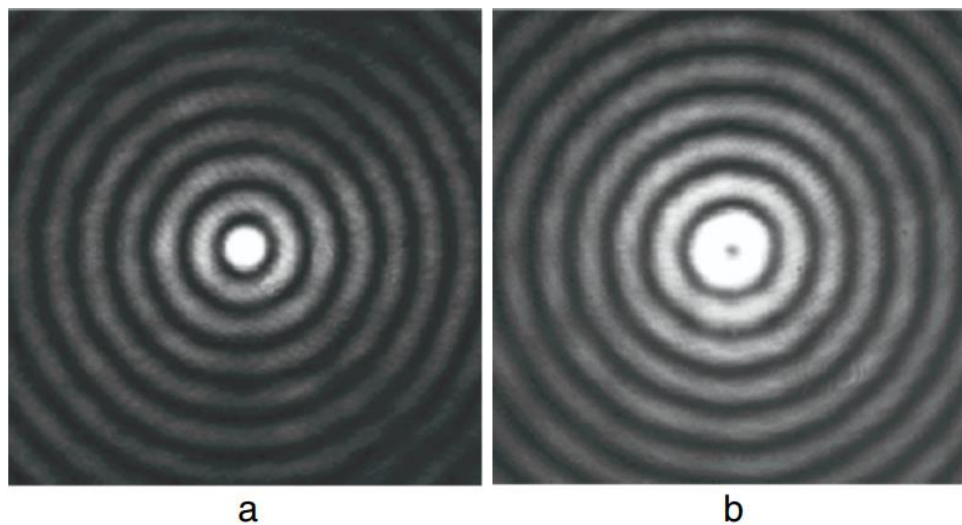


Fig. 5.11. Phase maps generated from the coherent interference between a reference Bessel beam and another coherent beam passing through the crystal. (Reproduced from Belyi et al. from [104] by permission of the Journal of Optics).

The sample used by us was a 100 μm thick coverslip with a GNR solution droplet on the surface. As shown in Fig. 5.12.A, the reference (clean) surface of the coverslip is facing to the objective. A top view of the GNR solution droplet is shown in Fig. 5.12.B. Following the procedure described in section 5.3.3.(a), the SS-OCT system was employed to produce 3D images of the coverslip. Both galvo-scanners were driven by 100 mV voltages, producing a 2D scanning area of 60 μm \times 60 μm in the red square in

Fig. 5.12.B. The following steps were performed to generate phase maps and *en-face* phase images.

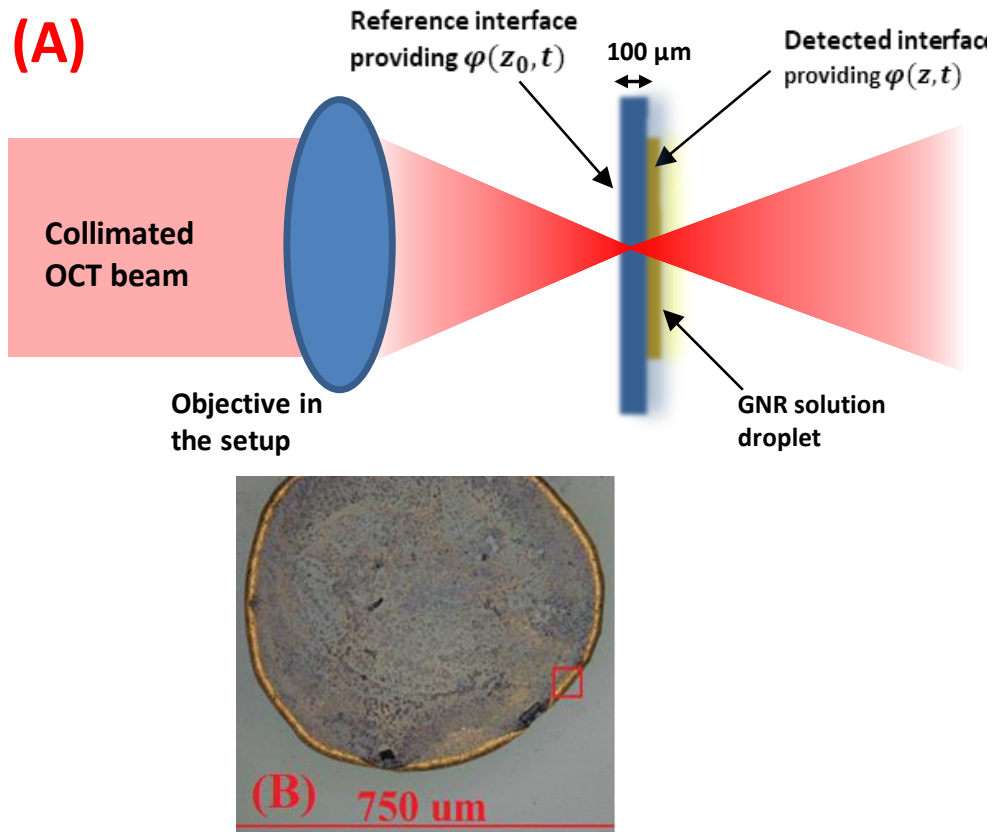


Fig. 5.12. (A): The GNR solution droplet sample used in phase map generation. The clean surface of the coverslip is facing to the objective. (B): 10 \times microscopy image of the GNR solution droplet. Red square in (B): the scanning area.

Firstly, the amplitude value $A(z_0, t)$ retrieved from the coverslip front surface was used to build an *en-face* OCT image, presented in Fig. 5.13.A. The phase value $\varphi(z_0, t)$ retrieved from the front surface was used to build the phase map, presented in Fig. 5.13.a. As seen, the phase map of the front surface appears as concentric rings which are due to the lateral scanning induced OPD in the scanning direction. This pattern agrees with the phase maps in Fig. 5.11 from the reported work [79].

Secondly, the amplitude value $A(z, t)$ and the phase value $\varphi(z, t)$ retrieved from the back surface of the coverslip were used to generate the *en-face* OCT image and the phase map of the back surface covered by the GNR solution droplet, as presented in Fig. 5.13.B and Fig. 5.13.b respectively. In the *en-face* OCT image (Fig. 5.13.B), features of the edge of the droplet are visible. As seen in the phase map in Fig. 5.13.b, especially along the edge of the droplet, phase values are discontinuities. In contrast, in the central

region of droplet, the existence of GNRs plays a part in disturbing the regularity of the phase map but not as much and not in such an obvious way as in the edge region. The bare glass region on the coverslip where no GNRs are present shows a smooth and regular phase variation.

Thirdly, to generate an *en-face* phase image, the phase map (Fig. 5.13.a) of the front surface was treated as the reference, which was then subtracted from the phase map (Fig. 5.13.b) of the back surface. The obtained image is presented in Fig. 5.13.c.

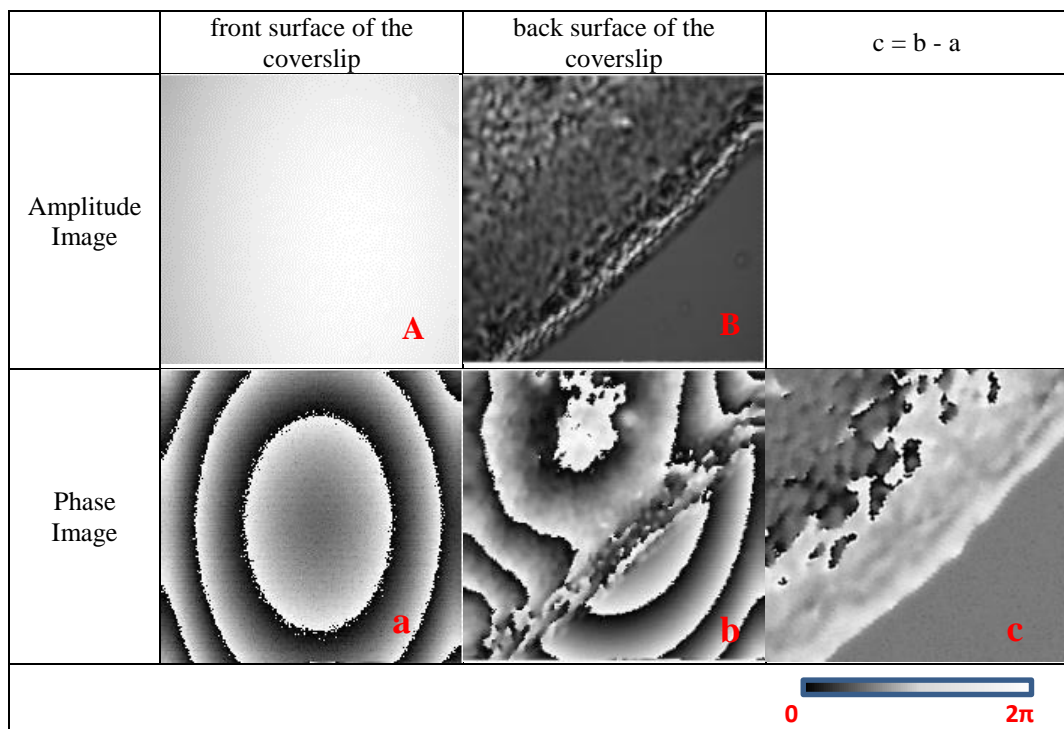


Fig. 5.13. (A) and (B): *En-face* OCT images of the front surface and the back surface of the coverslip in Fig. 5.12. (a) and (b): phase maps of the front surface and the back surface of the same coverslip. (c): *en-face* phase image obtained by subtracting (a) from (b). Image size: $60 \times 60 \mu\text{m}$.

Comparing the *en-face* phase image in Fig. 5.13.c and the *en-face* OCT image in Fig. 5.13.B, the *en-face* phase image loses most of the details that are visible in the *en-face* OCT image. This is because the phase value retrieved from the SS-OCT system was wrapped between 0 and 2π , and any phase value larger than 2π was forced to the value of 2π . In the future study, to solve the 2π ambiguity and generate *en-face* phase images showing detailed features of the detected sample, a suitable phase unwrap algorithm is required.

Employing a reference surface in *en-face* phase image generation agrees with what we did in previous sections. By subtracting the reference phase map from the phase map

of the interested depth, the concentric ring pattern is removed in the generated *en-face* phase image, leaving only the phase distribution of the subject at the layer of interest in the studied sample.

Compared with the Bessel beam interferometry [21][79], using phase sensitive SS-OCT to generate phase maps has the advantage that the detection is not limited to the surface of the sample. Phase maps can be generated at any particular layer within an imaging range in the sample. The imaging range is determined by the performance of the employed SS-OCT. Depth resolved *en-face* phase imaging will be performed in following sections to perform photothermal imaging of GNRs.

5.3.4 System noise of SD-OCT and SS-OCT

Given by the spikes on the output traces in Fig. 5.5, Fig. 5.7, Fig. 5.9 and Fig. 5.10, the built SS-OCT system suffered from the jitter of the swept source when the system was operating in the phase measurement mode. In contrast, this is not an issue in the SD-OCT system demonstrated in Chapter 4. In order to quantify the system noise level of the SS-OCT system with respect to the SD-OCT system, we performed a direct comparison of the output stability between the SD-OCT system and the SS-OCT system.

The configuration of the SD-OCT is illustrated in Fig. 4.1, and the configuration of the SS-OCT is illustrated in Fig. 5.1. To make the comparison fair, the used data were taken from the independent reference arm configuration for both systems, and the measurements were made on the same actuated coverslip sample (Fig. 4.2 and Fig. 5.3). The Ti:Sa lasers and the pairs of galvo-scanners in two systems were disabled. The A-scan rates of both systems were set to 500 Hz.

Assuming the mechanical or thermal fluctuations between two coverslips in either Fig. 4.2 or Fig. 5.3 can be ignored, the noise contributed by the fluctuations outside two coverslips can be removed by subtracting $\varphi(z_0, t)$ from $\varphi(z, t)$. Thereby, the motion of the actuated coverslip was the only factor contributing to the output trace of $\Phi(z, t)$ for both OCT systems. In this case, any noise disturbing the output phase $\Phi(z, t)$ is due to the system noise for both OCT systems, including the jitter noise and the electronic noise.

The system noise determines the minimum detectable phase variation of an OCT system. To compare the minimum detectable phases of both systems, phase measurements were performed with the piezo actuator disabled in both systems. Output

traces of $\Phi(z, t)$ obtained in a testing period of 10 seconds from both system are presented in Fig. 5.14.

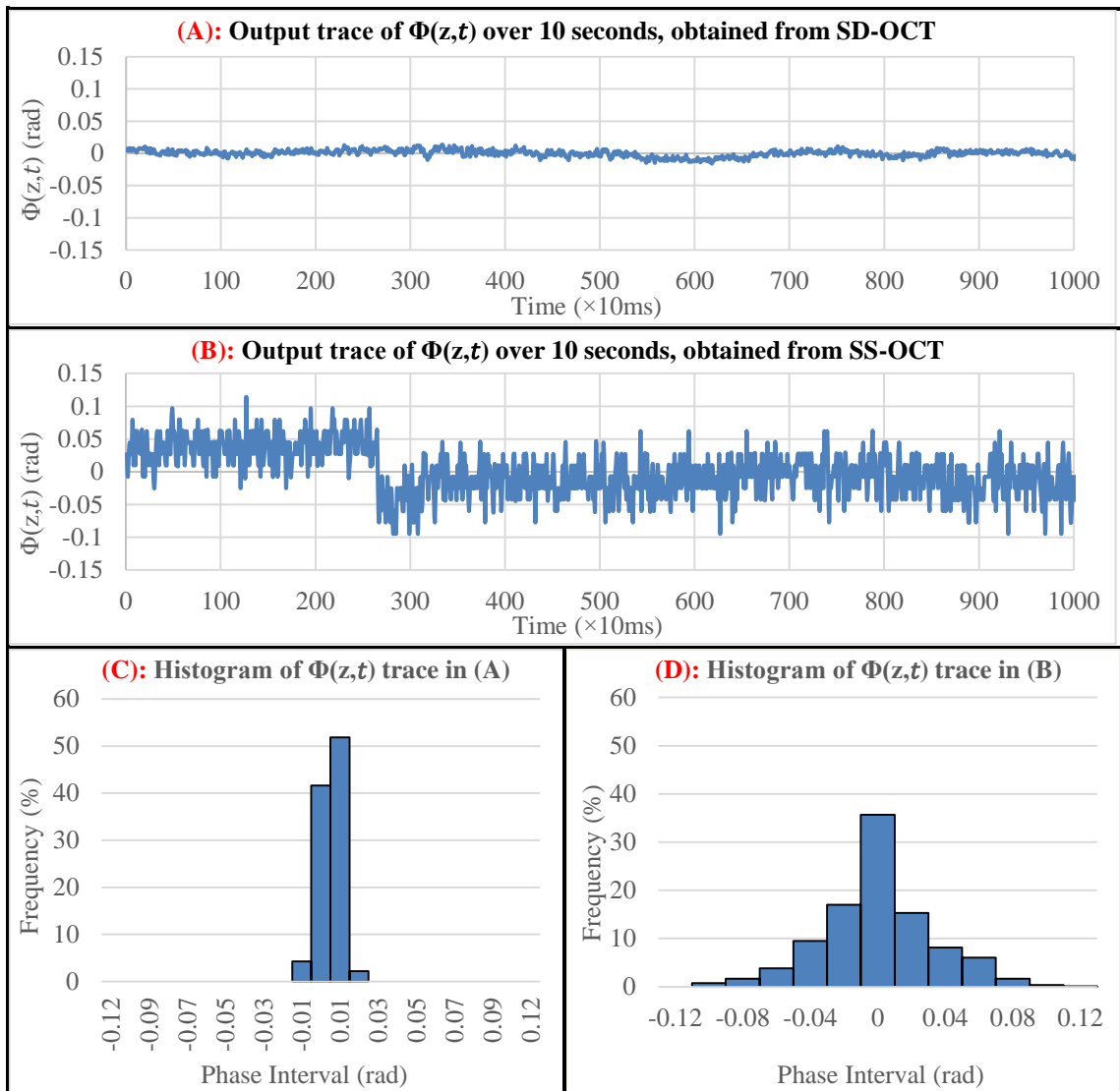


Fig. 5.14. (A): Dynamic output trace of $\Phi(z, t)$ obtained from the SD-OCT system. (B): Dynamic output trace of $\Phi(z, t)$ obtained from the SS-OCT system. (C): histogram of the $\Phi(z, t)$ trace in (A). (D): histogram of the $\Phi(z, t)$ trace in (B).

Ideally, the fluctuation in $\Phi(z, t)$ should always be 0 radian since there was no relative motion between two coverslips when the piezo actuator was disabled. In practice, this would not happen due to air currents in the 1 mm gap between the surfaces and also due to the inevitable electronic noise. Comparing Fig. 5.14.A and Fig. 5.14.B, the uncertainty of the output phase from the SD-OCT system is significantly lower than that from the SS-OCT system. The noticeable phase jump in Fig. 5.14.B is characteristic of SS-OCT measurements due to the jitter in the swept source. The jitter is attributed to the relative phase inconsistency between successive spectral sweeps of the swept source.

To quantify noise levels of two OCT systems, the $\Phi(z, t)$ traces in Fig. 5.14.A and Fig. 5.14.B were grouped in histograms respectively presented in Fig. 5.14.C and Fig. 5.14.D. The full widths at half maximum (FWHMs) of two graphs indicate that the output phase uncertainty of the SD-OCT system is 3 times better than that of the SS-OCT system.

With the piezo actuator activated, extra measurements were performed on the vibrating actuated coverslip. For both OCT systems, the piezo actuator was driven by a 4 V sinusoidal voltage at 1 Hz. Traces of $\Phi(z, t)$ obtained over 1 second from the two systems are presented in Fig. 5.15.

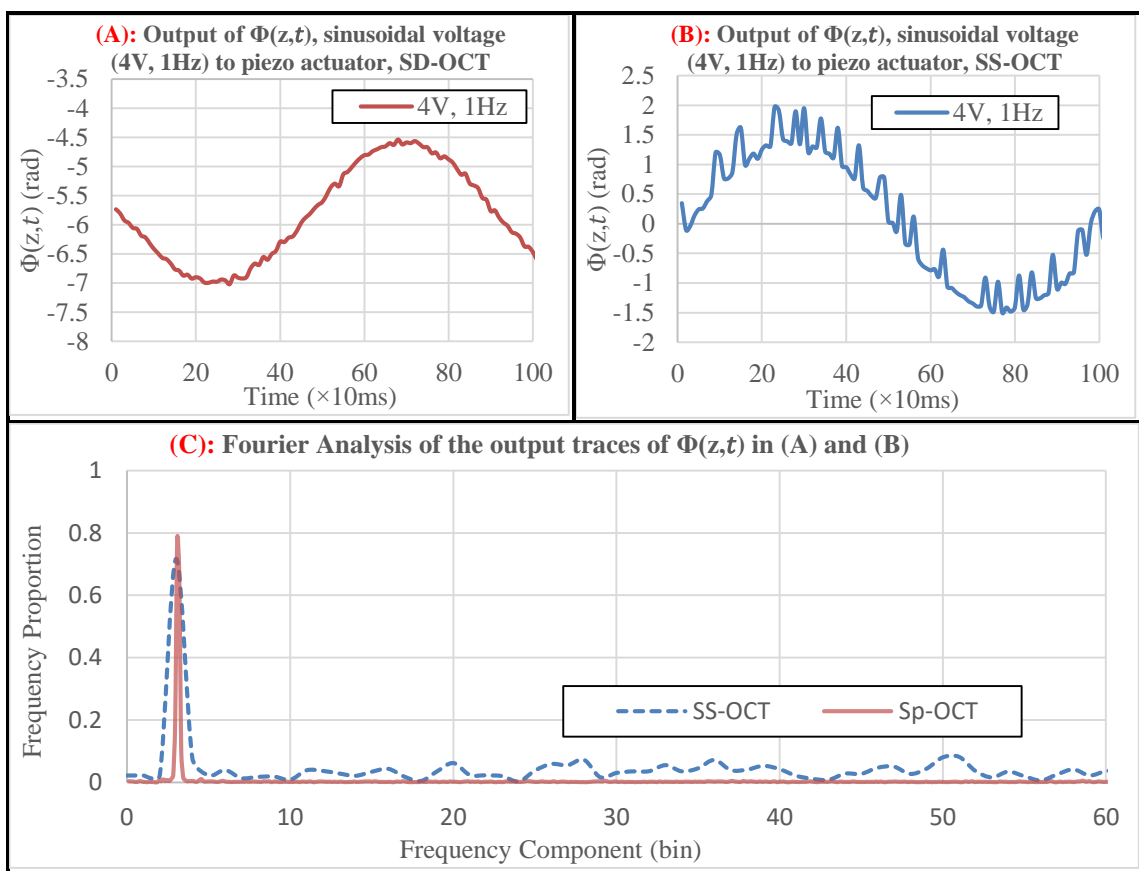


Fig. 5.15. (A): dynamic output trace of $\Phi(z, t)$ obtained from the SD-OCT system. (B): dynamic output trace of $\Phi(z, t)$ obtained from the SS-OCT system. In both systems, the piezo actuator was driven by a 4 V sinusoidal voltage at 1 Hz. (C): Fourier analysis performed on the traces of $\Phi(z, t)$ in (A) and (B). Their peak widths are in a numerical ratio of 3:1.

As seen in Fig. 5.15.A and Fig. 5.15.B, $\Phi(z, t)$ traces obtained from two systems present sinusoidal patterns with the same frequency as the driving voltage sent to the actuator. Comparing Fig. 5.15.A and Fig. 5.15.B, the $\Phi(z, t)$ trace from the SD-OCT system is clean, whereas the $\Phi(z, t)$ trace from the SS-OCT system contains several

random spikes. Even though most spikes can be removed by filtering treatments, their existence indicates that the phase sensitive SS-OCT is noisier in nature than the phase sensitive SD-OCT.

To analyse the spectral components of two traces in Fig. 5.15.A and Fig. 5.15.B, the Fourier transform was performed on both traces and the results are presented in Fig. 5.15.C. As seen, the frequency component of the $\Phi(z, t)$ trace (solid red line) from the SD-OCT system is more concentrated at the vibrating frequency than that (wave blue line) from the SS-OCT system. Comparing the full widths at half maximum (FWHMs) of two FFT peaks, the uncertainty caused by the system noise in the SD-OCT system is 3 times smaller than that in the SS-OCT system.

Although the built SS-OCT system may not achieve the potential of the SD-OCT system to perform a full quantitative phase measurement, its potential in qualitative phase measurements is still of interest considering its superiority in the imaging depth range discussed in section 5.1, especially for the photothermal detection and imaging of gold nanoparticles.

5.3.5 Photothermal detection of GNRs in clear media

In order to apply the SS-OCT system to perform photothermal detection of GNRs, the Ti:Sa laser in the setup (Fig. 5.1) was enabled, the output power of which was 230-mW. The Ti:Sa beam is on/off modulated by a chopper wheel to induce a modulation of the photothermal response of GNRs. Both galvo-scanners in the setup were disabled such that combined OCT and Ti:Sa beams were hitting on a single lateral location on the sample. The sample used here was the one schematically demonstrated in Fig. 5.12. The independent reference arm configuration was employed. As seen, the front surface of the coverslip provided the reference phase $\varphi(z_0, t)$, and the detected phase $\varphi(z, t)$ was measured on the back surface partially covered by the GNR solution droplet. Their difference $\Phi(z, t)$ was calculated using Eq. (4.7) and Eq. (4.8). Measurements were performed on two selected locations on the surface: one location had GNRs; the other location had no GNR. Output traces of both $\varphi(z, t)$ and $\Phi(z, t)$ were generated, and obtained results under different experimental conditions are presented in Fig. 5.16.

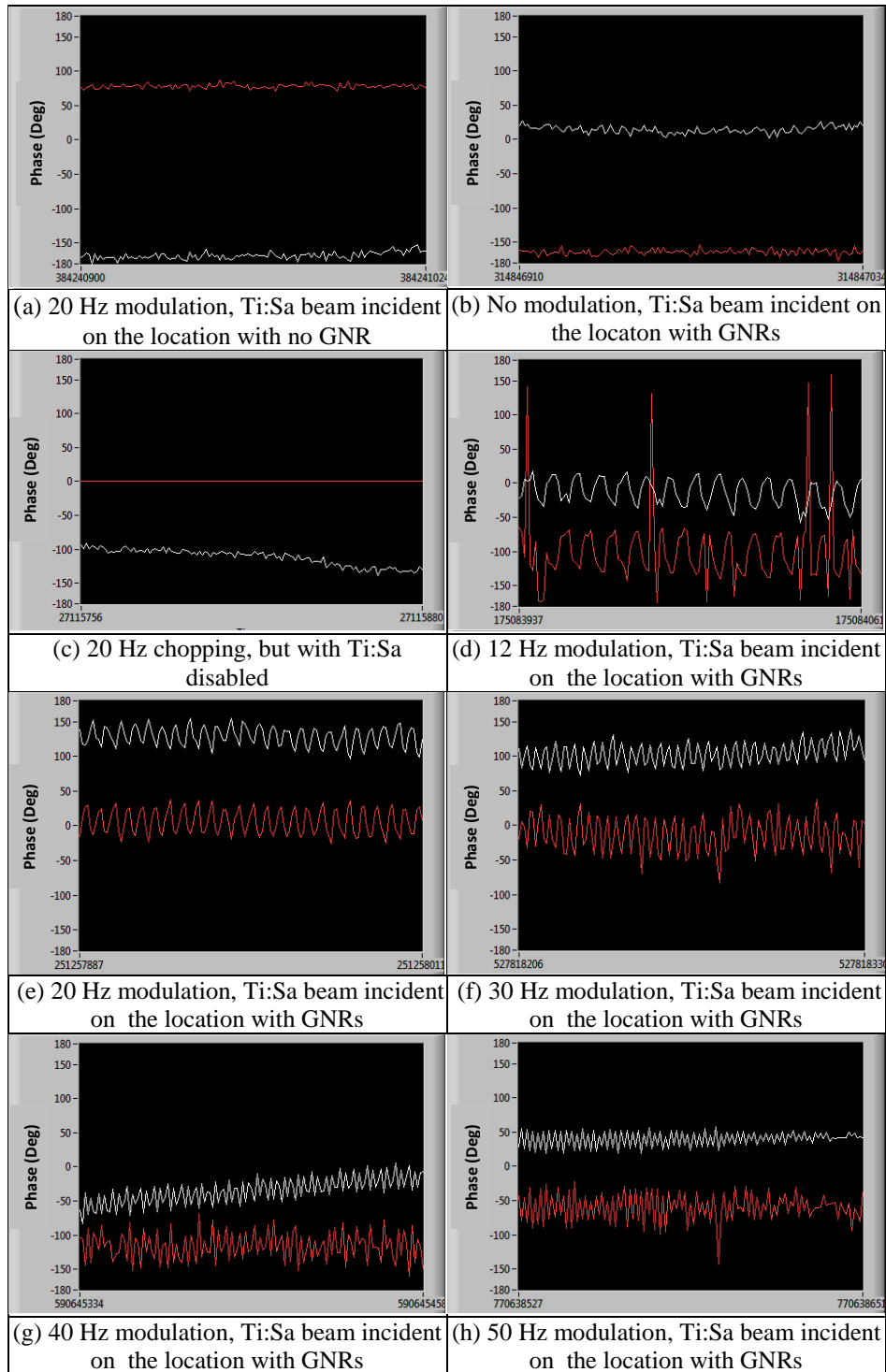


Fig. 5.16. Photothermal detection of GNRs in clear media, figures showing output phase as a function of time. White trace: output traces of $\varphi(z, t)$; Red trace: output traces of $\Phi(z, t)$. Measurements were performed in controlled conditions over the same duration of 1.2 s.

The white traces in Fig. 5.13 are outputs of $\varphi(z, t)$ over time, and the red traces are outputs of $\Phi(z, t)$ over time. Fig. 5.13.a was obtained with the Ti:Sa beam on the location with no GNR. Fig. 5.13.b was obtained from a GNR region on which the Ti:Sa beam was incident but not modulated. Fig. 5.13.c was obtained when the Ti:Sa laser

was disabled with no output beam, but the chopper wheel was in operation. Fig. 5.13.d to Fig. 5.13.h were obtained when the Ti:Sa beam was incident on a GNR region, and it was modulated at selected frequencies (12 Hz, 20 Hz, 30 Hz, 40 Hz, and 50 Hz), with a 50% duty cycle.

The featureless traces in Fig. 5.13.a indicate that when the GNR is absent, the local temperature change induced OPD variation is not significant enough to be detected by the SS-OCT system. Fig. 5.13.b indicates that great contrast cannot be observed without modulating the Ti:Sa beam. The straight red trace in Fig. 5.13.c indicates that the utilisation of the reference surface and the reference phase $\varphi(z_0, t)$ can remove the noise created by the air flow or mechanical motion in the setup. Each trace in Fig. 5.13.d to Fig. 5.13.h presents the same modulation frequency as each corresponding modulation frequency of the Ti:Sa beam, indicating that the phase sensitive SS-OCT system is able to detect the photothermal response of GNRs. However, as seen in Fig. 5.13.d to Fig. 5.13.h, as the Ti:Sa modulation frequency is increased, the modulation of the generated output trace becomes less visible. Once again, the spikes on the red trace in Fig. 5.13.d indicate that the swept source generates the unexpected and unpredictable jitter which cannot be removed by employing the reference surface and the reference phase $\varphi(z_0, t)$.

To conclude, as well as the phase sensitive SD-OCT system demonstrated in Chapter 4, the phase sensitive SS-OCT system is also capable of performing photothermal detection of GNRs. However, from the output phase stability point of view, the SS-OCT system is less suitable to perform quantitative measurements due to the jitter in the swept source.

5.3.6 Photothermal imaging of GNRs in clear media

Employing the SS-OCT system, we generated *en-face* phase images to identify the distribution of GNRs on the coverslip. The coverslip sample used here is the one demonstrated in Fig. 5.12, in which an area of $60 \mu\text{m} \times 60 \mu\text{m}$ was scanned over the edge of the GNR solution droplet. The *en-face* phase imaging process has been demonstrated in section 5.3.3. The optical shutter gate in the setup (Fig. 5.1) was used to enable and disable the Ti:Sa beam to the sample. *En-face* phase images obtained from 2 sets of replicated measurements are presented in Fig. 5.17.

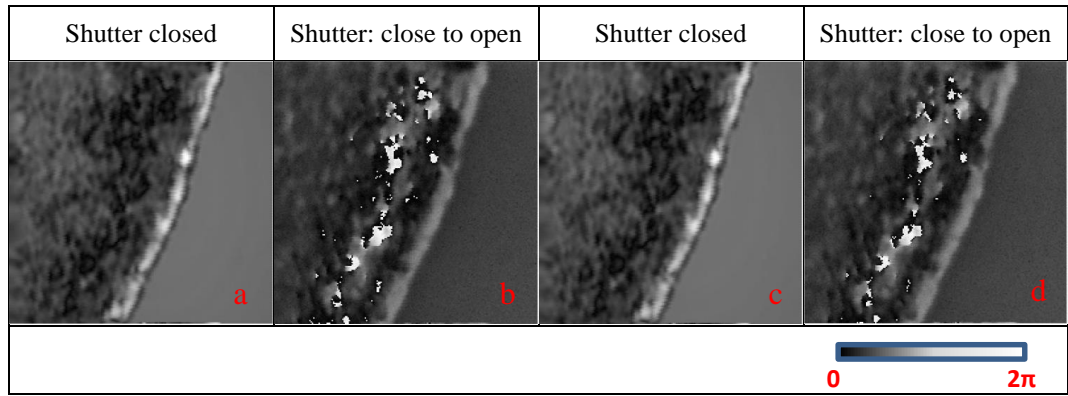


Fig. 5.17. Photothermal imaging of GNRs in clear media. The photothermal response of GNRs is displayed in the *en-face* phase image. (a) and (c) were obtained when the Ti:Sa beam to the sample was blocked. (b) and (d) were obtained when the Ti:Sa beam reached the sample. Images were obtained from 2 sets of replicated measurements. Image size: 60×60 μm.

As seen in Fig. 5.17.a and Fig. 5.17.c, when the shutter was closed, the Ti:Sa beam to the sample was blocked, and the *en-face* phase image only showed the outline of the droplet. As seen in Fig. 5.17.b and Fig. 5.17.d, when the shutter was switched from closed to open, the region with high density of GNRs created a strong photothermal response which was then recorded in the *en-face* phase image.

As seen in Fig. 5.17, *en-face* phase images show different features when the GNR sample is modulated by the Ti:Sa beam, indicating that the phase sensitive SS-OCT system can be used for photothermal imaging of GNRs in clear media. In order to improve the contrast and to highlight the different features induced by the photothermal response, the LabVIEW programme was designed to subtract successively generated *en-face* phase images and then display the resulting difference. Images obtained from 6 sets of replicated measurements are presented in Fig. 5.18.

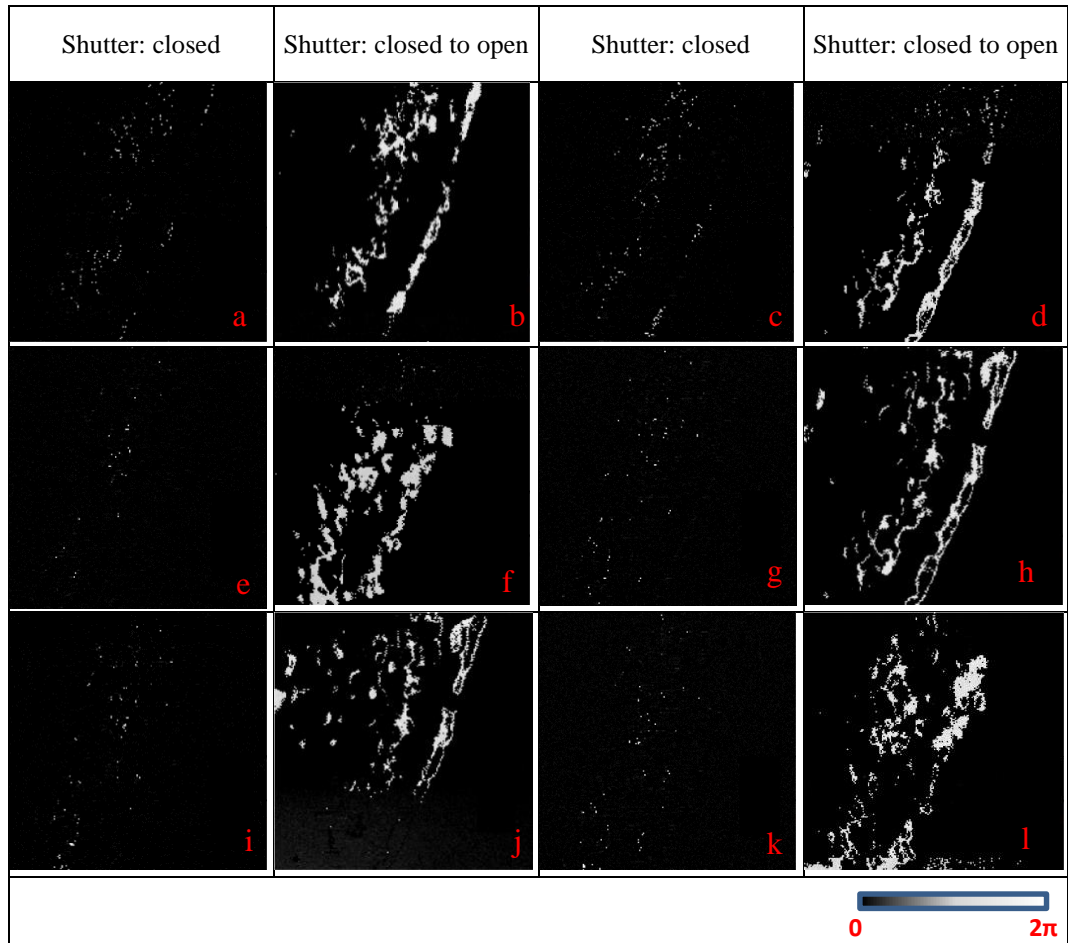


Fig. 5.18. Photothermal imaging of GNRs in clear media, images displaying the difference between successively generated *en-face* phase images. Images show 6 consecutive measurements over the same position on the sample. Besides the reason from the jitter in the swept source, the lack of reproducibility (as seen in b, d, f, h, j, l) is also due to the heating beam altering the structure of the sample as the Ti:Sa beam might melt GNRs each time the shutter in the system setup (in Fig. 5.1) was switched from closed to open. Ti:Sa beam power: 160 mW. Image size: 60×60 μm.

As seen in Fig. 5.18.(a), (c), (e), (g), (i) and (k), when the Ti:Sa beam to the sample was blocked, the difference between successive *en-face* phase images is zero, resulting in mostly black images. These images are not completely black due to the scanning error of the galvo-scanners. As seen in Fig. 5.18.(b), (d), (f), (h), (j) and (l), when the shutter was switched to open to enable the Ti:Sa beam propagation to the GNR sample, images with optimized contrast were obtained. The locations covered by GNRs are shown as bright features in these images.

Consequently, by displaying the difference (Fig. 5.18) between successively generated *en-face* phase images, GNR regions are identified more obviously than displaying the *en-face* phase images (Fig. 5.17). However, images Fig. 5.18.(b), (d), (f), (h), (j) and (l) have different patterns. Once again, the bad measurement reproducibility

of the technique is attributed to the jitter in the swept source. Furthermore, the lack of reproducibility might be due to the altering of the structure of the GNR sample, given by the heating from the Ti:Sa beam each time the shutter (in Fig. 5.1) was switched from closed to open. However, this factor should be less considered than the jitter noise in the swept source since the measurements performed by the spectrometer based phase sensitive OCT system (Chapter 4) show good reproducibility, as seen in Fig. 4.20 and Fig. 4.21. The Ti:Sa beam power used in this section is 160 mW which is comparable to the power (170 mW) used to test the measurement reproducibility of the spectrometer based OCT system, as seen in Fig. 4.20 row (b) and row (c) and in Fig. 4.21 row (b) and row (c).

To conclude, the repeatability of using the SS-OCT system for photothermal imaging of GNRs is not as good as that of the SD-OCT system demonstrated in Chapter 4. However, due to the advantage offered by SS-OCT in terms of imaging depth, it may be a valuable option to perform photothermal imaging of GNRs in scattering media particularly if source jitter is not an issue.

5.3.7 Photothermal imaging of GNRs in scattering media

To benefit from the imaging depth superiority of the SS-OCT system, we employed it for photothermal imaging of GNRs behind scatterers. As shown in Fig. 5.1.B or Fig. 5.19, three layers of scotch tapes were stuck on the front surface of the coverslip to simulate scatterers. As seen, the combined Ti:Sa and OCT beams pass through the scatters, hit the tape/glass interface that providing the reference phase $\varphi(z_0, t)$, and then hits the glass/GNRs interface that providing the detected phase $\varphi(z, t)$. Two galvo-scanners made a 2D scanning area of $60 \mu\text{m} \times 60 \mu\text{m}$ over the edge of the GNR solution droplet.

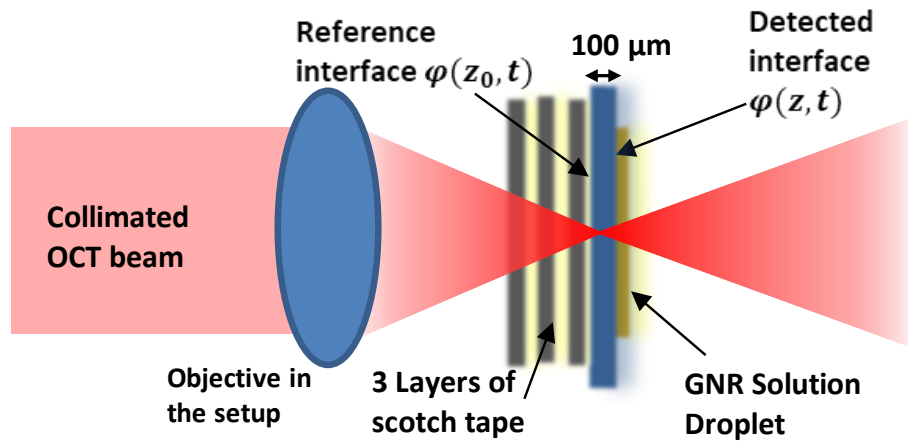


Fig. 5.19. Configuration of the sample used for photothermal imaging of GNRs in scattering media. 3 layers of scotch tape are stuck on the front surface of the coverslip to simulate scatters. The reference phase $\varphi(z_0, t)$ was measured on the tape/glass interface, and the detected phase $\varphi(z, t)$ was measured on the back surface covered by GNRs.

Following the technique demonstrated in section 5.3.6, we displayed the difference between successively generated *en-face* phase images. 6 sets of successive measurements are presented in Fig. 5.20.

As commented in section 5.3.6, the predominantly black images in Fig. 5.20.(a), (c), (e), (g), (i) and (k) indicate that no difference exists between successive *en-face* phase images when the excitation Ti:Sa beam to the sample was blocked. Each time the shutter was switched from closed to open, GNRs generated photothermal responds to the Ti:Sa beam. In the second and fourth column of Fig. 5.20, the patterns observed in the lighter shades of grey indicate the presence of GNRs and their distribution. It can be concluded that the SS-OCT system is capable of performing photothermal imaging of GNRs behind scatterers. Still, images in Fig. 5.20.(b), (d), (f), (h), (j) and (l) have different patterns. Since they are 6 times of successive measurements, the lack of reproducibility in Fig. 5.20 agrees with that in Fig. 5.18. Once again, the fact is due to the jitter in the swept source.

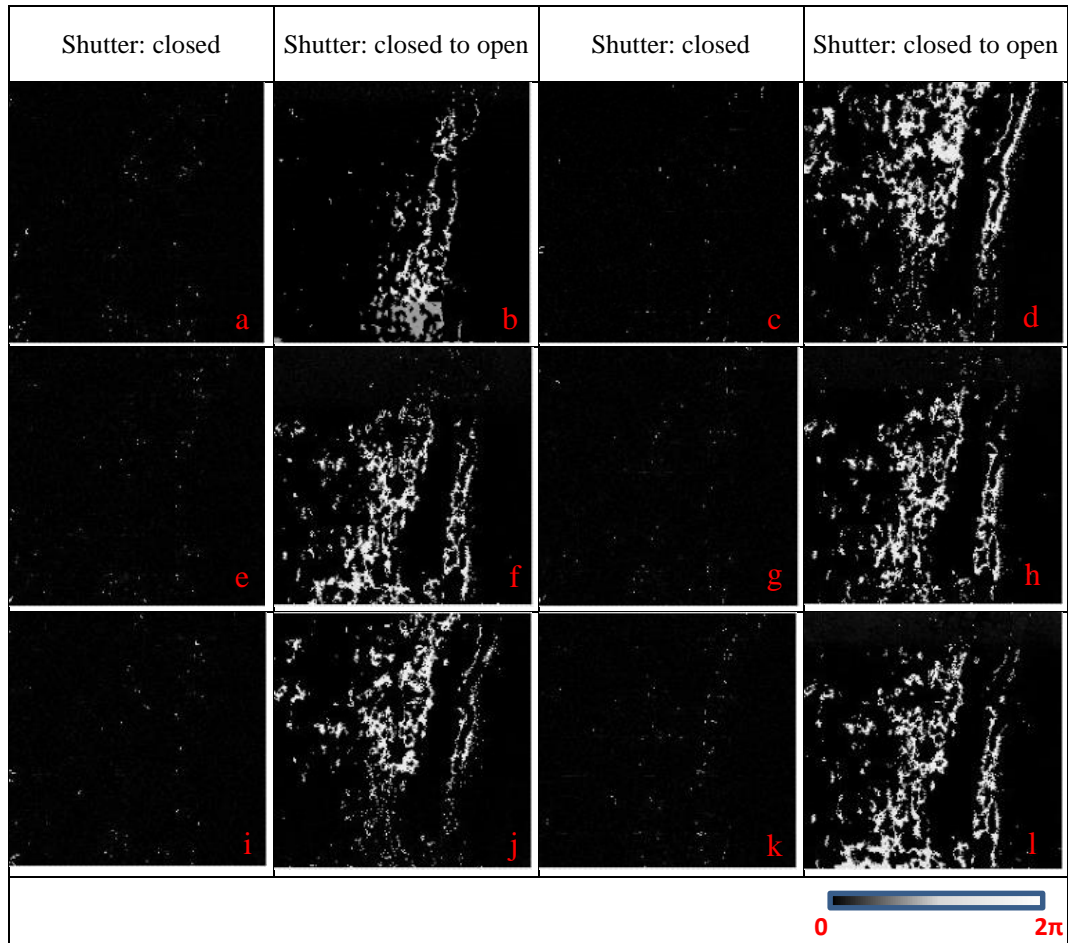


Fig. 5.20. Photothermal imaging of GNRs in scattering media. Images displaying the difference between successively generated *en-face* phase images. Images were obtained from 6 consecutive measurements over the same position on the sample. Besides the reason from the jitter in the swept source, the lack of reproducibility (as seen in b, d, f, h, j, l) is also due to the heating beam altering the structure of the sample as the Ti:Sa beam might melt GNRs each time the shutter in the system setup (in Fig. 5.1) was switched from closed to open. Measured Ti:Sa beam power: 50 mW. Image size: 60×60 μm.

5.4 Discussion and Conclusion

This chapter presents a phase sensitive SS-OCT system built by the author, which is capable of performing photothermal detection and imaging of GNRs in scattering media. The use of the swept source results in the capability to perform coherence imaging deeper (3.3 mm) into the sample. However, its working performance can be acceptable only if the output phase is less noisy.

The methods used on the SS-OCT system to briefly test its phase measurement performance are similar to those used on the SD-OCT system described in Chapter 4. Nevertheless, the experiments and contents presented in this chapter are not a replication of those in Chapter 4. Specifically, sections 5.3.1, 5.3.2 and 5.3.3

demonstrate the synchronization procedures in the A-scan mode, B-scan mode, phase map generation and *en-face* phase imaging. These procedures are not covered in Chapter 4.

The phase maps shown in Figure 5.13 are intrinsically the intersection of the sample surface with the wavefront (surface of equal phase) of the OCT beam. Analogous to the wavefront of the Gaussian beam, the wavefront of the OCT beam can be treated as a quasi-flat surface before it passes through an objective lens. Lateral scanning of the beam produces a series of curved surfaces of equal phase, as has been described in [82]. The concentric rings in the phase map in Fig 5.13 are the intersection of the curved phase surfaces with the detected sample surface. In our case, the first surface met with the curved phase surfaces was the flat front surface of a coverslip in Fig. 5.12. Thus, the generated phase map was concentric annulus with a centre, as seen in Fig. 5.13.a. The second surface met with the curved phase surfaces was the rough back surface of the coverslip. Then, the regular concentric annulus phase map was disturbed by the GNRs on the surface, as seen in Fig. 5.13.b. By subtracting these two phase maps, the *en-face* phase image in Fig 5.13.c was obtained. This operation removed the concentric annulus pattern and thus left only the phase features of the interested surface. This operation has the same principle of deducting a reference phase $\varphi(z_0, t)$ from the detected phase $\varphi(z, t)$ in order to produce the output phase $\Phi(z, t)$, which was also done on A-scan measurements elsewhere in the project.

In section 5.3.6, the *en-face* phase images generated in this way proved to be able to quantify at multiple spatial locations the photothermal response of GNRs modulated by the Ti:Sa beam. The technology provided an approach to study the distribution of GNRs in clear media. However, the contrast in the *en-face* phase image was not optimized. As seen in Fig. 5.17.b and Fig. 5.17.d, the photothermal response of GNRs and the features of the sample are mixed together in the *en-face* phase images. As an improvement, the image contrast was enhanced by displaying the difference between successively generated *en-face* phase images. By doing this, the features of the sample were removed in the new *en-face* image, and therefore only the photothermal response of GNRs was recorded. This technique was also used to optimize the photothermal imaging of GNRs in scattering media, as demonstrated in section 5.3.7.

The noise levels on the output traces of the SS-OCT and the SD-OCT are compared in section 5.3.4. The SS-OCT exhibits a worse output phase stability than the

SD-OCT. Hence, the SS-OCT is not suitable for performing quantitative phase measurements but can be used for qualitative phase measurements. The unstable output phase was mainly caused by the jitter in the swept source. Belonging to the system noise of the SS-OCT, the jitter takes effects only in phase measurements because it is an expression of an uncertain relative phase relation between successive spectral sweeps in the swept source.

To overcome the jitter noise, instead of connecting the sweep trigger on the swept source to the digitizer, a fibre Bragg grating has been reported to select a particular wavelength in the sweep range. The selected wavelength is treated as the start of each spectral sweep. When the sweep goes across the selected wavelength, a trigger is released to start the data acquisition [83]. By doing this, the data acquisition does not start off until the sweep goes across the selected wavelength in each sweep cycle. This approach guarantees that the sweep-to-sweep always starts at the same wavelength and thus the sweep jitter is eliminated. On the other hand, as a side effect, since the actually used spectral range becomes shorter, the system employing the fibre Bragg grating suffers a loss in the imaging depth range. Consequently, a suitable solution to solve the jitter noise in SS-OCT is certainly worth efforts in future study.

Chapter 6

Phase sensitive Master/Slave optical coherence tomography

6.1 Introduction

As has been discussed in Chapter 2, due to its increased imaging depth, improved operating speed and sensitivity advantage, Fourier domain OCT has replaced time domain OCT to become the preferred approach for applications requiring speed and sensitivity. Fourier domain OCT encodes the axial depth of a detected scatterer into the modulation density of the channelled spectrum at the detector output. Along the probing beam, the depths information of all scatterers in the detected sample are encoded simultaneously in the interferogram which is the sum of all channelled spectra from all accessible scatterers. To decode the interferogram, a Fourier Transform (FFT) operation to the interferogram results in an axial reflectivity profile (A-scan profile) representing the reflectivity properties of a succession of scattering points in depth along the probing beam in the detected sample.

Both the SD-OCT system described in Chapter 4 and the SS-OCT system described in Chapter 5 employ this FFT operation, and both of them suffer from a few common disadvantages. The first common disadvantage comes from the penalty of having to carry out the extra signal processing associated with the digitization / calibration process of the interferogram before the FFT is applied. This is because the interferogram is chirped in frequency in both systems. Specifically, in SD-OCT, since the interferogram is recorded by a line camera incorporated in the spectrometer, the chirp results from a non-linear distribution of the optical frequency component of the interferogram to the linear pixel array of the camera. In SS-OCT, since the interferogram is recorded by a photodetector, the chirp is due to the mismatch between non-linear wavenumber $k(t)$ sweeping and the constant speed data acquisition. An FFT performed on a chirped interferogram returns a worsening axial resolution than an FFT performed on a linearised interferogram.

Various approaches have been reported to redistribute the chirped interferogram to make it evenly distributed in k -space. In SS-OCT, the swept source is equipped with a supplementary frequency clock (k -clock) which outputs pulses evenly distributed in optical frequency (k -space) [63]. By connecting the k -clock to the data acquisition device, a synchronization between the frequency sweep and the data acquisition can be achieved. In SD-OCT, a specifically designed prism can be placed after the diffraction grating to linearize the spectral dispersion of the spectrometer in wavenumber [84]. Moreover, direct electronic linearization of the interferogram has been realised by controlling the data transfer clock of the camera [85]. In addition, sophisticated algorithms have been designed to calibrate the nonlinearly distributed interferogram over the linear array of sensor pixels in the camera [88][89]. In both types of OCT system, software programmes requiring significant computational resources have been designed to resample the interferogram along the optical frequency axis [86][87][88][89].

The second common disadvantage of both OCT systems is that neither SS-OCT nor SD-OCT is able to generate *en-face* images in real time since the procedure is time consuming for a number of reasons. Firstly, the calibration or linearization of the interferogram takes time. Secondly, as discussed in Chapter 4 and Chapter 5, both techniques have to collect a 3D volume of data before slicing out the *en-face* image, which is also time consuming.

Another common disadvantage of both systems is due to an unbalanced optical dispersion in two arms of the interferometer. The unbalanced dispersion adds irregularity to the interferogram. Compared with the chirp, the influence given by the unbalanced dispersion is relatively easier to solve. Several solutions have been reported to compensate the dispersion, including using matched lengths of glass [90], spectral delay line [91] and fibre Bragg gratings [92].

In 2013, Podoleanu and Bradu introduced a new class of spectral domain interferometry technique named as Master–Slave Interferometry (MSI) and applied it to OCT imaging [93]. In MSI, there are two interferometers working in parallel, a slave interferometer and a master interferometer. The detected signal is collected in the slave interferometer, and the OPD values are determined in the master interferometer [93].

An OCT system employing the MSI technique is known as Master–Slave OCT (MS-OCT). In 3D OCT, MS-OCT opens novel possibilities for parallel sensing and for

parallel signal processing. As a new approach to spectral domain OCT, MS-OCT does not rely on FFT. This feature allows MS-OCT to eliminate the process of interferogram linearization and calibration with a low setup cost. Moreover, MS-OCT has an increased speed of *en-face* imaging. A disadvantage of MS-OCT is that before the sample is being imaged in the slave interferometer, hundreds of masks need to be recorded in the master interferometer. The procedure of recording masks takes time and adds complexity. Moreover, MS-OCT is not able to perform phase resolved measurements [94].

In 2016, Rivet et. al upgraded Master-Slave Interferometry to Complex Master-Slave Interferometry (CMSI) [94]. In CMSI, a procedure was developed to infer hundreds of masks from a reduced number (3-6) of masks that are obtained from actual measurements. This led to a substantial decrease in the time needed to record masks. Due to the increased operating speed, CMSI was then applied to OCT. Although an OCT employing CMSI was shown to be theoretically able to perform phase resolved measurements, no experimental work was carried out to prove this assertion.

To test the phase measurement function of CMSI, we applied the CMSI technique into the SS-OCT system demonstrated in Chapter 5 and referred to the new system as CMS-OCT. In this chapter, the principles of MSI and CMSI are discussed, followed by the demonstration of our experimental methods to perform phase resolved measurements using the CMS-OCT system. As the result, phase maps and *en-face* phase images generated from the CMS-OCT and the SS-OCT are compared.

6.2 Principles of MSI

As illustrated in Fig. 6.1.(a), the MSI technique employs a configuration of two interferometers: a slave interferometer (SI) and a master interferometer (MI). Both MI and SI operate in the same spectral domain interferometry configuration. The configuration could be either a spectrometer based interferometer or a swept source based interferometer.

The master interferometer (MI) and slave interferometer (SI) in Fig. 6.1.(a) use a shared light source (OS) and respective data acquisition blocks: master acquisition block (MAB) and slave acquisition block (SAB). The detected object (O) is placed in the slave interferometer (SI).

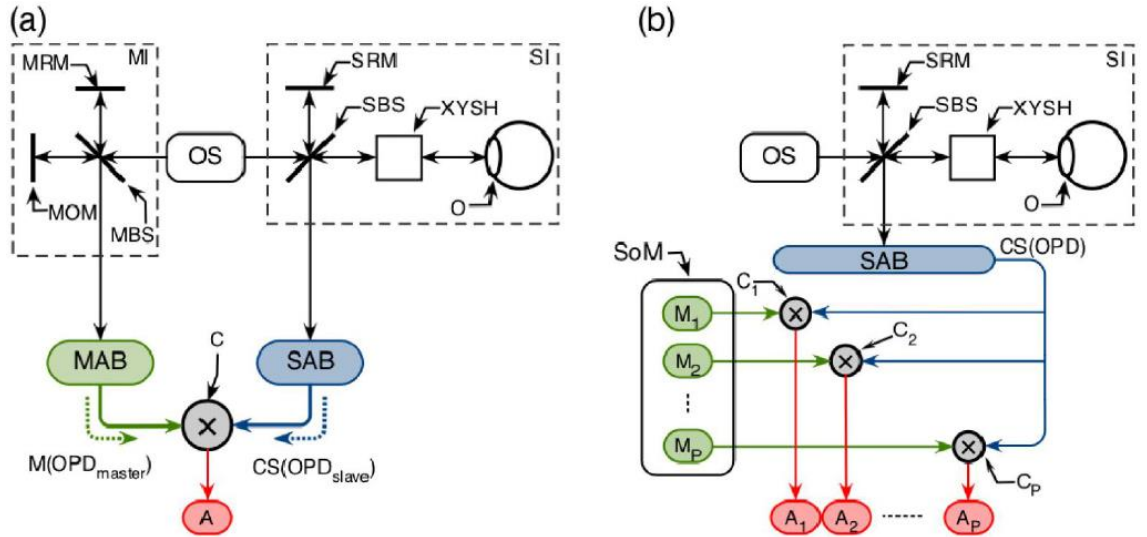


Fig. 6.1. Operating principle of MSI. (a): Implementation of the MSI using two interferometers: a master interferometer (MI) and a slave interferometer (SI). Optical source (OS). Master beam splitter (MBS). Slave beam splitter (SBS). Master reference mirror (MRM). Slave reference mirror (SRM). Detected object (O). Master object mirror (MOM). 2D scanning mirrors (XYSH). Master acquisition block (MAB). Slave acquisition block (SAB). Comparison block (C). (b): Parallel implementation of MSI, where the MI in (a) is replaced by a storage bank of a number of P masks (SoM). Masks (M_1, M_2, \dots, M_P) generated in the master interferometer. Comparison blocks (C_1, C_2, \dots, C_P). Amplitudes (A_1, A_2, \dots, A_P) of sampled points from respective depths z_1, z_2, \dots, z_P in the sample.

In the master interferometer (MI), a series of interferograms are generated while the master reference mirror was moved step by step in the axial direction. These interferograms generated in the MI are named as masks. Thus, at each step, the mask recorded ($M(OPD_{master})$) corresponds to a certain optical path difference (OPD_{master}) between the master reference mirror (MRM) and the master object mirror (MSM). In the slave interferometer (SI), only one interferogram ($CS(OPD_{slave})$) is generated, containing the totality of the axial information of the detected object (O).

Unlike the spectral domain interferometry that performs FFT to the interferogram measured from the object O to obtain the A-scan profile, the master/slave interferometry (MSI) uses a comparison block, presented as (C) in Fig. 6.1.(a), to compare the interferogram obtained in the slave interferometer (SI) with each individual mask obtained in the master interferometer (MI). Thus, the number of comparisons is determined by the number of masks obtained in the MI. Mathematically, the comparison is implemented by a correlation operation $Corr(OPD)$:

$$Corr(OPD) = CS(OPD_{slave}) \otimes M(OPD_{master}) \quad (6.1)$$

and the correlation is evaluated over the whole optical spectrum of the light source:

$$A(\text{OPD}) = \sum_{k_S} \text{Corr}(\text{OPD}) \quad (6.2)$$

where k_S is the wavenumber variable. For each comparison, the value of $A(\text{OPD})$ in Eq. (6.2) is used to quantify the reflectivity property of a scatterer at the depth of $\text{OPD}_{\text{slave}} = \text{OPD}_{\text{master}}$ in the object. Thus, a larger value of $\text{Corr}(\text{OPD})$ indicates a higher similarity of the compared interferogram and mask and thus a higher reflectivity property of the scatterer at the depth of $\text{OPD}_{\text{slave}} = \text{OPD}_{\text{master}}$ in the object.

In principle, the MI and the SI are operating at the same time. When the master reference mirror (MRM) is moving step by step, a series of masks are being recorded, and the correlation operations are being conducted. During this process, the positions of the master object mirror (MOM) in the MI, the object (O) and slave reference mirror (SRM) in the SI are fixed. After the master reference mirror (MRM) completes a full range of axial scanning, a 1-D array of $A(\text{OPD})$ (Eq. (6.2)) is produced, and the number of elements in the array is equal to the number of the masks. Analogous to the A-scan profile obtained from the FFT operation in SS-OCT and SD-OCT, this $A(\text{OPD})$ array is in fact the A-scan profile of the studied object O. In order to generate B-scan images, one of the two galvo-scanners in Fig. 6.1.(a) can be used to scan the beam in the slave interferometer (SI). In order to generate *en-face* images, both galvo-scanners need to be used.

However, in order to complete an A-scan in MSI, although the slave reference mirror (SRM) in the slave interferometer (SI) is fixed, the master reference mirror (MRM) in the master interferometer (MI) is axially stepped to a number of successive depth locations. The operating process of an OCT system employing MSI may therefore appear very similar to that of a time-domain OCT system, which is time consuming. In order to reach an operating speed as fast as that of frequency domain OCT, a simplified setup is employed.

As seen in Fig. 6.1.(b), in the simplified setup, only one interferometer is implemented. In the first step, this interferometer is used as the master interferometer (MI), in which object O in Fig. 6.1.(b) is replaced by a mirror, and the two galvo-scanners (XYSH) are kept at rest. A series of masks M_1, M_2, \dots, M_P are recorded by stepping the reference mirror. These masks are subsequently stored in the memory of a computer, resulting in a storage of masks (SoM). To guarantee a reasonable axial

resolution, the number P of these masks should be larger than the value obtained by dividing the imaging range of the OCT system with its axial resolution:

$$P \geq \frac{\text{axial imaging range}}{\text{resolution}} \quad (6.3)$$

In the next step, the sample object is positioned back in the interferometer in Fig. 6.1.b, and the reference mirror (SRM) is held at rest. Then, the interferometer is used as the slave interferometer (SI), and an interferogram is measured from the sample object.

The obtained interferogram in the SI is then compared with each of the previously saved masks in MI through a number of P operations (C_1, C_2, \dots, C_P) which are conducted in parallel. Each comparison operation (C) obtains a correlation amplitude $A(\text{OPD})$ (Eq. (6.2)), and all obtained correlation amplitudes (A_1, A_2, \dots, A_P) are constructed to a 1-D array presenting the A-scan profile of the sample object. In this step, all optical components in the setup in Fig. 6.1.(b) are held rest. Thus, by employing the simplified setup and the parallel processing, the OCT system employing MSI offers the same advantage of high-speed acquisition as FD-OCT.

As discussed in Chapter 4 and Chapter 5, FD-OCT performs a FFT operation to each individual interferogram to obtain an A-scan profile. Before the FFT operation, the linearization process has to be performed on the interferogram to correct the chirp. In contrast, MSI-OCT obtains the A-scan profile by performing a number of P correlation operations which are conducted in parallel. MSI-OCT eliminates the interferogram linearization process. The performance of a MSI-OCT system was compared to that of an SS-OCT system and found to be similar in axial resolution and detection sensitivity [93].

Compared with SS-OCT, another advantage of MSI-OCT is the speed of *en-face* imaging. As discussed in section 5.3.3, in SS-OCT, the process of *en-face* imaging involves processes of interferogram linearization, FFT operation and 3D data reconstruction. Only after these steps can the *en-face* image of the layer of interest be sliced from the 3D volume of data. In contrast, in MSI-OCT, the mask from the depth of interest can be selected out from the number of P previously stored masks in the MI. Then, in the SI, all interferogram obtained from the 2D scanning of the beam at different lateral locations are compared with the selected mask. The correlation amplitude obtained in this way forms an *en-face* image of the depth of interest in the

sample. The MSI-OCT was shown to be 8 times faster than the SS-OCT in performing *en-face* imaging [93].

Although the MSI technology have above discussed advantages, it presents the following shortcomings:

(1) A large number of masks need to be experimentally recorded in the MI, and the process is time consuming.

(2) Unlike the FD-OCT, the MSI-OCT is not able to perform phase measurements due to an uncertain relative phase relation between successive masks obtained from the MI.

Nevertheless, both drawbacks have been addressed by Rivet et. al. who developed a novel model to record the MI masks [94].

6.3 Principles of CMSI

To address the MSI shortcomings above, an improved technique, Complex Master-Slave Interferometry (CMSI) was developed [94]. Unlike the MSI, CMSI does not record all MI masks directly but uses a LabVIEW procedure to infer a large number of masks from a reduced number (3-5) of actually recorded masks [94]. Since the masks produced are complex values, the CMSI was predicted to be able to perform phase measurements.

In CMSI, Rivet et. al. mathematically modelled the chirp effects by introducing two functions $g(\nu)$ and $h(\nu)$ into the MI mask (interferogram) function $M(\nu, z)$ and the SI sample (interferogram) function $I(\nu)$. $g(\nu)$ represents the effect from the non-uniform distribution of the optical frequency ν along the interferogram, and $h(\nu)$ represents the effect given by the unbalanced dispersion in two interferometer arms [94]. Both $g(\nu)$ and $h(\nu)$ are functions of the optical frequency ν .

In the mathematical model involving $g(\nu)$ and $h(\nu)$, for each optical frequency component ν , the complex interferogram $I(\nu)$ is obtained from the slave interferometer (SI) and contains the sample information, which can be written as:

$$I(v) = \int r(\rho)A(g(v))\exp[i(\frac{2\pi}{c}g(v)2\rho + h(v))]d\rho \quad (6.4)$$

where $r(\rho)$ is the complex reflectivity of the sample and varies with the depth variable ρ ($\rho = 0$ corresponds to $OPD = 0$ in the interferometer), c is the speed of light, and $A(g(v))$ represents the amplitude of the interferogram. In conventional spectral domain OCT, a FFT applied to the integral on the right hand side of Eq. (6.4) over the optical frequency v is used to calculate the A-scan profile of the detected sample. In contrast, in MSI and CMSI, Eq. (6.4) is compared with the mask $M(v, z)$ obtained in the master interferometer (MI). For each optical frequency component v , the complex $M(v, z)$ measured and stored in the MI can be expressed as:

$$M(v, z) = A(g(v))\exp[i(\frac{2\pi}{c}g(v)2z + h(v))] \quad (6.5)$$

where z represents the axial position of the master reference mirror (in Fig. 6.1), where the corresponding $M(v, z)$ is measured. Thus, according to Eq. (6.1) and Eq. (6.2), the correlation amplitude $MSI(z)$ between Eq. (6.4) and Eq. (6.5) is calculated as:

$$MSI(z) = \int M(v, z)'I(v)dv \quad (6.6)$$

where $M(v, z)'$ is the complex conjugate of $M(v, z)$. Substituting Eq. (6.4) and Eq. (6.5) into Eq. (6.6), $MSI(z)$ is expressed by:

$$MSI(z) = \iint r(\rho)|A(g(v))|^2 \exp[-i(\frac{2\pi}{c}g(v) \times 2(z - \rho))]d\rho dv \quad (6.7)$$

As discussed in 6.2, because the master interferometer (MI) and the slave interferometer (SI) are sharing the same interferometer, the same amount of unbalanced system dispersion $h(v)$ is presenting in both MI and SI, and thus the effect from $h(v)$ is totally eliminated in the $MSI(z)$ in Eq. (6.7) which is then only influenced by the non-uniform v distribution function $g(v)$.

The principle of CMSI is to work out the $g(v)$ function and the $h(v)$ function. Both $g(v)$ and $h(v)$ are used to infer a large number of interferogram masks which are stored in the MI and used for the subsequent correlation operation. To workout $g(v)$ and $h(v)$, the argument of Eq. (6.5) is extracted, generating the phase $\phi^{\text{exp}}(v, z)$ being used to generate $g(v)$ and $h(v)$:

$$\phi^{\text{exp}}(v, z) = \frac{2\pi}{c} g(v)2z + h(v) + \varphi_{\text{rand}}(z) \quad (6.8)$$

where $\varphi_{\text{rand}}(z)$ is the random phase noise. A partial derivative of Eq. (6.8) in respect to v removes the phase noise $\varphi_{\text{rand}}(z)$, leading to:

$$\frac{\partial}{\partial v} \phi^{\text{exp}}(v, z) = \frac{4\pi g'(v)}{c} z + h'(v) \quad (6.9)$$

where $g'(v)$ and $h'(v)$ are derivatives of $g(v)$ and $h(v)$. A linear regression according to z works out the slope $\frac{4\pi g'(v)}{c}$ and the intercept $h'(v)$ in Eq. (6.9). To this end, at least two phase terms of $\phi^{\text{exp}}(v, z)$ need to be known. To obtain two $\phi^{\text{exp}}(v, z)$, at least two masks $M(v, z)$ are necessary to be recorded at two different axial locations in the MI. Then, an indefinite integration can be used to calculate $g(v)$ and $h(v)$.

When $g(v)$ and $h(v)$ are known, the complex mask function $M(v, z)$ in Eq. (6.5) can be used to infer a large number of masks. Each inferred mask corresponds to the interferogram at a certain depth location z . Substituting $A(g(v))$ from Eq. (6.5) into Eq. (6.7), the correlation amplitude $MSI(z)$ at a certain depth z can be obtained, which contains the reflectivity property of the scatterer at that depth. Assembling all $MSI(z)$ from all depth, an A-scan profile of the sample is obtained. The number of pixels in the A-scan profile is equal to the number of inferred masks. For instance, if number of inferred masks is $N = 1000$, and the imaging depth is 3 mm, the number of pixels in the A-scan profile will be 1000, and the actual distance Δz between successive pixels in the A-scan profile will be $\Delta z = \frac{3 \text{ mm}}{1000} = 3 \mu\text{m}$.

In summary, CMSI uses two functions $g(v)$ and $h(v)$ to quantify the chirp effects given by the nonlinear interferogram and the unbalanced dispersion respectively. $g(v)$ and $h(v)$ are calculated by actually recording only 2-5 masks in the master interferometer. Then, these two functions obtained are used to infer hundreds of masks that are stored in the computer memory. These stored masks will be compared with the interferogram obtained from the detected sample in the slave interferometer (SI). Consequently, in contrast to the MSI which requires hundreds of masks to be actually measured and recorded, the CMSI requires only 2-5 masks to be actually measured, with the rest to be inferred by the LabVIEW programme. This approach dramatically increases the operating speed of CMSI. Moreover, since the returned masks from the master interferometer (MI) in CMSI are complex, the interferometric phase in CMSI

should be retrievable. Nevertheless, the phase measurement function of CMSI remained unproven.

6.4 System configuration

In order to check if an OCT system employing the CMSI technique is indeed able to perform phase measurements, the author implement the CMSI technique into the SS-OCT setup demonstrated in Chapter 5. The new system is referred as Complex Master Slave OCT (CMS-OCT). It shares the same setup with the SS-OCT system described in section 5.2.

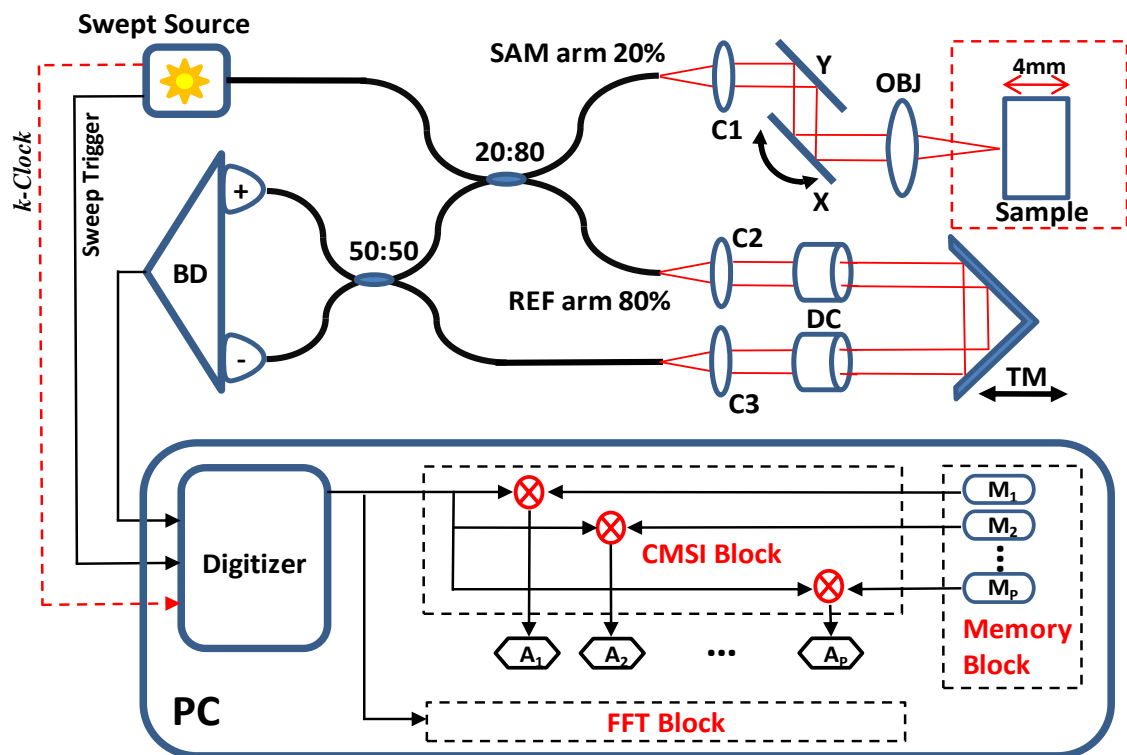


Fig.6.2. Schematic of phase sensitive CMS-OCT system. The digitizer is installed in the computer to acquire interference signals. The acquired data are manipulated by two different modes: the SS-OCT mode and the CMS-OCT mode. These two manipulation modes are operated by two separate LabVIEW programmes installed in the computer. In the SS-OCT mode, the FFT Block performs FFT on the interferogram, resulting in the A-scan profile. In the CMS-OCT mode, the CMSI Block performs correlation operations between the interferogram obtained from the slave interferometer (SI) and the number of P masks (interferograms) obtained from the master interferometer (MI). The k -Clock from the swept source is enabled in the SS-OCT mode and disabled in the CMS-OCT mode. Collimators (C1-C3). Galvo scanners (X,Y). Objective lens (OBJ). Piezo actuator (PA). Dispersion compensation blocks (DC). Balanced photodetector (BD). Computer (PC). Transmission mirror (TM). Sample: 4 mm thick microscope glass slide.

The configuration of the CMS-OCT system is illustrated in Fig. 6.2. As seen, the system can feasibly operate in two modes: (i) the SS-OCT mode; and (ii) the CMS-OCT mode. In the SS-OCT mode, the system works along the lines demonstrated in Chapter 5, where the connection (red dash-line in Fig. 6.2) between the swept source k -clock and the digitizer is enabled to remove the chirp effect from the nonlinear spectra sweeping. The A-scan profile of the detected sample is the result of an FFT operation performed in the FFT block (in Fig. 6.2). In the CMS-OCT mode on the other hand, as the system is immune from the chirp effect, the k -clock connection is not required. The A-scan profile comes from the correlation operation performed in the CMSI block (in Fig. 6.2).

At any moment in time only one of the two operating modes can be used to take measurements and images. The two operating modes shared the same system setup, but a separate LabVIEW programme was realised for each mode. The switch between the two modes is quick and convenient, which was done by switching between the two LabVIEW programmes and did not involve changes in the physical hardware. We compared the results obtained from the CMS-OCT operating mode with those obtained from the SS-OCT operating mode in order to evaluate the phase measurement performance of the CMS-OCT.

6.5 Methodology and Results

6.5.1 *En-face* OCT image and phase map generation in CMS-OCT

The processes of *en-face* OCT imaging and phase map generation in the SS-OCT mode have been demonstrated in section 5.3.3. This section describes the processes leading to the *en-face* OCT imaging and phase map generation in the CMS-OCT mode. The sample employed was a 4 mm thick microscope glass slide.

The following steps were conducted to generate *en-face* OCT images and phase maps of the front surface of the glass slide sample.

Firstly, we replaced the glass slide in Fig. 6.2 by a mirror and made the interferometer work as the master interferometer (MI). Three masks were actually recorded by placing the mirror at axial positions of 0.5 mm, 1.0 mm and 1.5 mm, with $OPD = 0$ as the origin (0 mm). These 3 masks were used to calculate functions $g(v)$ and $h(v)$ which were then used to infer 200 masks over the imaging depth range of 2 mm, based on the principle discussed in section 6.3. These 200 inferred masks were then stored in the memory of the computer in Fig. 6.2.

Secondly, the glass slide sample was placed in the object arm and made the interferometer work as the slave interferometer (SI). Then, the interferogram containing the reflectivity information of the sample was recorded.

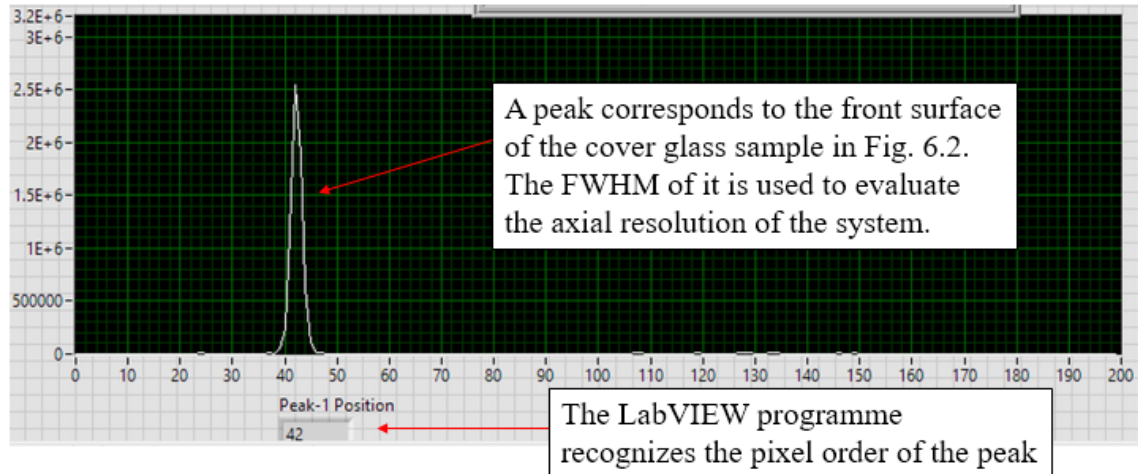


Fig. 6.3. A-scan profile of the cover glass sample, obtained with the system working in the CMS-OCT operating mode. Since 200 masks (interferograms) were inferred over an imaging depth of 2 mm, the A-scan profile is composed of 200 pixels. The peak located at pixel order 42 corresponds to the front surface of the glass slide sample. Since the imaging depth of the system is 2 mm, the back surface of the 4 mm cover glass is not visible in the A-scan profile. The FWHM of the peak is used to evaluate the axial resolution of the CMS-OCT system as 25 μm .

Thirdly, the interferogram obtained in the SI was correlated with each of the stored 200 masks that were previously inferred in the MI. The results of 200 correlation operations were assembled, resulting in a 1-D complex array. Then, the amplitude values of the 200 elements in the 1-D array was retrieved by the LabVIEW sub-VI, resulting in an A-scan amplitude profile composed of 200 pixels, as presented in Fig. 6.3. The LabVIEW implementation is presented in Fig. A.5.

Since the A-scan profile is a measure of the reflectivity properties of the glass slide along the probing beam, the peak in Fig. 6.3 corresponds to the front surface of the glass slide. Since the imaging depth of CMS-OCT was set to 2 mm (although it can be extended to 3.3 mm if necessary), the back surface of the 4 mm slide is not visible in the A-scan profile in Fig. 6.3.

Fourthly, in the A-scan amplitude profile, the designed LabVIEW programme identified the pixel order of the peak as 42nd, as shown in Fig. 6.3.

Lastly, to produce the *en-face* OCT image, the 42nd mask stored in the computer memory was picked out. Two galvo-scanners were enabled to scan the OCT beam over

an area of $60 \mu\text{m} \times 60 \mu\text{m}$ on the sample. 28,900 A-scan interferograms were recorded from 170×170 lateral locations uniformly distributed within the area of $60 \mu\text{m} \times 60 \mu\text{m}$. Then, each interferogram was correlated with the 42nd mask selected from the computer memory, resulting in a 170×170 2-D complex array. The phase values were retrieved from these complex values by a LabVIEW sub-VI, and were subsequently mapped to grayscale elements to produce a phase map composed of 170×170 pixels, as presented in Fig. 6.4.(b). Separately, the amplitude values were retrieved from the 170×170 2-D complex array and were mapped to grayscale values to produce an *en-face* OCT image, as presented in Fig. 6.4.(B). The LabVIEW implementation used to retrieve the phase value is presented in Fig. A.6.

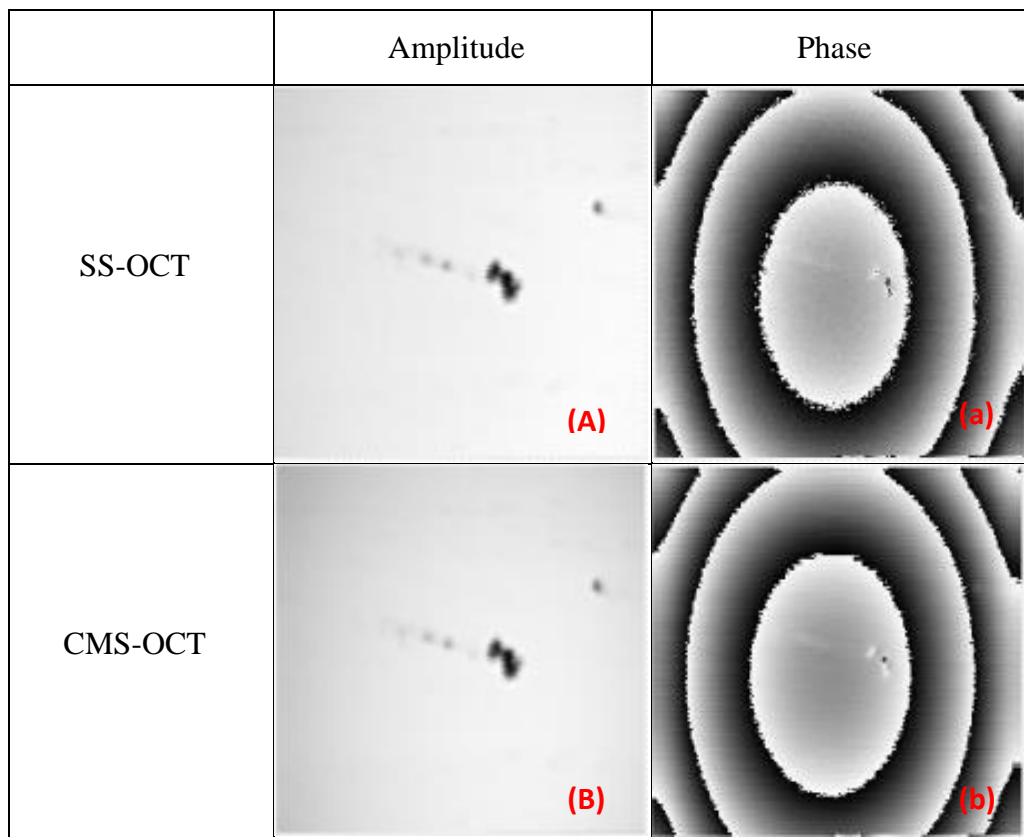


Fig. 6.4. (A) and (B): *En-face* OCT images of the glass slide front surface. (a) and (b): phase maps of the glass slide front surface. (A) and (a) were obtained in the SS-OCT mode. (B) and (b) were obtained in the CMS-OCT mode. In (A) and (B), the dust specks on the glass surface are clearly visible as dark features and their full depth extent is showing. In (a) and (b), the phase continuity of local region in the phase map is also disrupted by the dust specks. Image size: $60 \mu\text{m} \times 60 \mu\text{m}$.

To make a comparison, the *en-face* OCT image and the phase map of the front surface of the glass slide were generated in the SS-OCT operating mode, as presented in Fig. 6.4.(A) and Fig. 6.4.(a) respectively. The methodology has been demonstrated in

section 5.3.3.(b) and Fig. 5.13. As seen in Fig. 6.4.(A) and Fig. 6.4.(B), the dust specks on the glass surface are clearly visible in two *en-face* OCT images generated from both SS-OCT and CMS-OCT modes. The similarity between Fig. 6.4.(A) and Fig. 6.4.(B) indicates that the SS-OCT and the CMS-OCT have the same performance in generating *en-face* OCT images.

Given by Fig. 6.4.(a) and Fig. 6.4.(b), well defined concentric rings are presented in both phase maps produced respectively from the SS-OCT mode and the CMS-OCT mode. As seen, the dust features on the glass surface disrupt the relative phase relations in the local region in each phase map. The tiny difference between the two phase maps is that the one generated in the SS-OCT mode (Fig. 6.4.(a)) is smoother, whereas the one generated in the CMS-OCT (Fig. 6.4.(b)) looks more grainy. The similarity between Fig. 6.4.(a) and Fig. 6.4.(b) indicates that, in a very similar way to phase sensitive SS-OCT, CMS-OCT is also capable of performing phase resolved measurements. Consequently, for the first time, the predicted phase measurement function of the CMS-OCT is experimentally proven.

As discussed in section 5.3.3, in the SS-OCT mode, a 3D volume of data had to be collected before the *en-face* OCT image or the phase map was extracted. In contrast, in the CMS-OCT mode, only one mask corresponding to the layer of interest in the sample was selected from the 200 stored masks to produce *en-face* OCT images or phase maps.

The FWHM of the peak in Fig. 6.3 was used to evaluate the axial resolution of the CMS-OCT system. Thus, the axial resolution was evaluated as $\frac{2 \text{ mm}}{200} \times 2.5 = 25 \text{ } \mu\text{m}$, where 2.5 is the pixel width at half maximum of the peak. Compared with the axial resolution of 21 μm when the system was working in the SS-OCT mode, the resolution in the CMS-OCT mode is slightly worse although still within experimental error.

6.5.2 Phase measurements in CMS-OCT and SS-OCT

In order to further test the reliability and repeatability of phase measurements in CMS-OCT, additional sets of measurements were performed and phase maps obtained from CMS-OCT were compared with those obtained from SS-OCT.

As seen in Fig. 6.5, the sample used here was a piece of microscope coverslip with a GNR solution droplet on the surface. The droplet is slightly elongated along the horizontal axis, with a diameter varying from 700 μm to 750 μm . Phase maps were produced from two selected regions indicated by red squares in Fig. 6.5. One region covers the edge of the droplet; another region is selected within the droplet boundary. These two selected regions have the same area of 60 $\mu\text{m} \times 60 \mu\text{m}$. Obtained *en-face* OCT images and phase maps obtained from two operating modes are presented in Fig. 6.6 and Fig. 6.7.

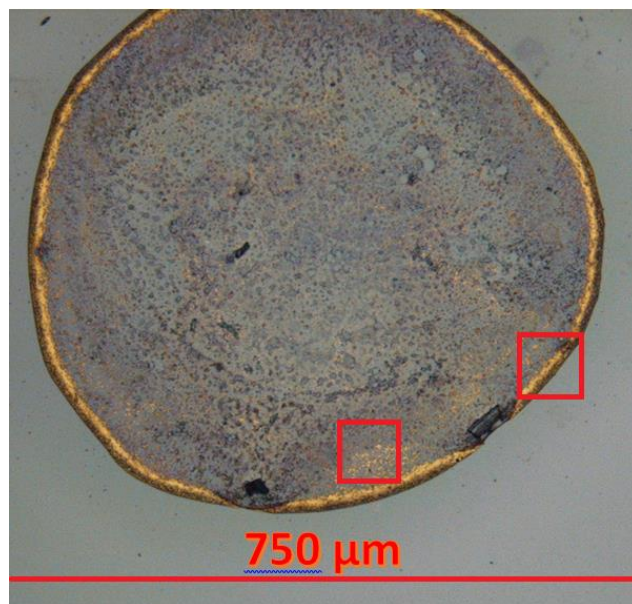


Fig.6.5. 10 \times microscopy image of the GNR solution droplet on the coverslip surface. The diameter of the droplet varies from 700 μm to 750 μm . *En-face* images were made over two red square regions, each of which has an area of 60 $\mu\text{m} \times 60 \mu\text{m}$.

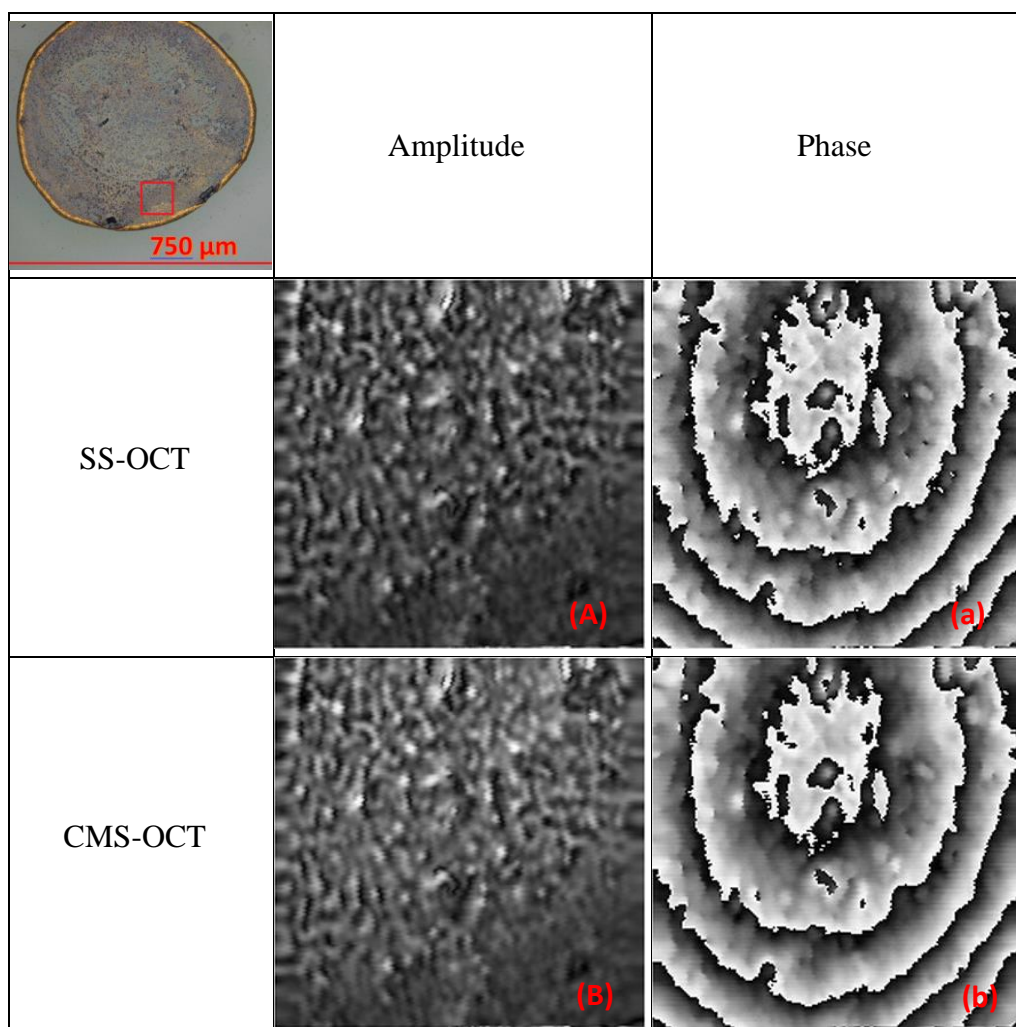


Fig. 6.6. (A) and (B): *En-face* OCT images of the region identified by the red square in the GNR solution droplet. (a) and (b): phase maps of the red square region in the GNR solution droplet. (A) and (a) were obtained in the SS-OCT mode. (B) and (b) were obtained in the CMS-OCT mode. Image size: $60\ \mu\text{m} \times 60\ \mu\text{m}$.

As seen in Fig. 6.6.(A) and Fig. 6.6.(B), the *en-face* OCT images show the features of GNR aggregation in the droplet. The images obtained from both SS-OCT and the CMS-OCT are nearly same except that the brightness of the CMS-OCT image is of a slightly higher level, which could be adjusted in the LabVIEW software. The images in Fig. 6.6.(a) and Fig. 6.6.(b) show a series of ring patterns indicating the presence of phase gradients. Unlike the smooth ring patterns in Fig. 6.4.(a) and Fig. 6.4.(b), these phase maps are significantly affected by the rough and irregular distribution of GNRs in the droplet. However, the phase map (Fig. 6.6.(b)) obtained from the CMS-OCT mode appear almost identical to the one (Fig. 6.6.(a)) obtained from the SS-OCT mode.

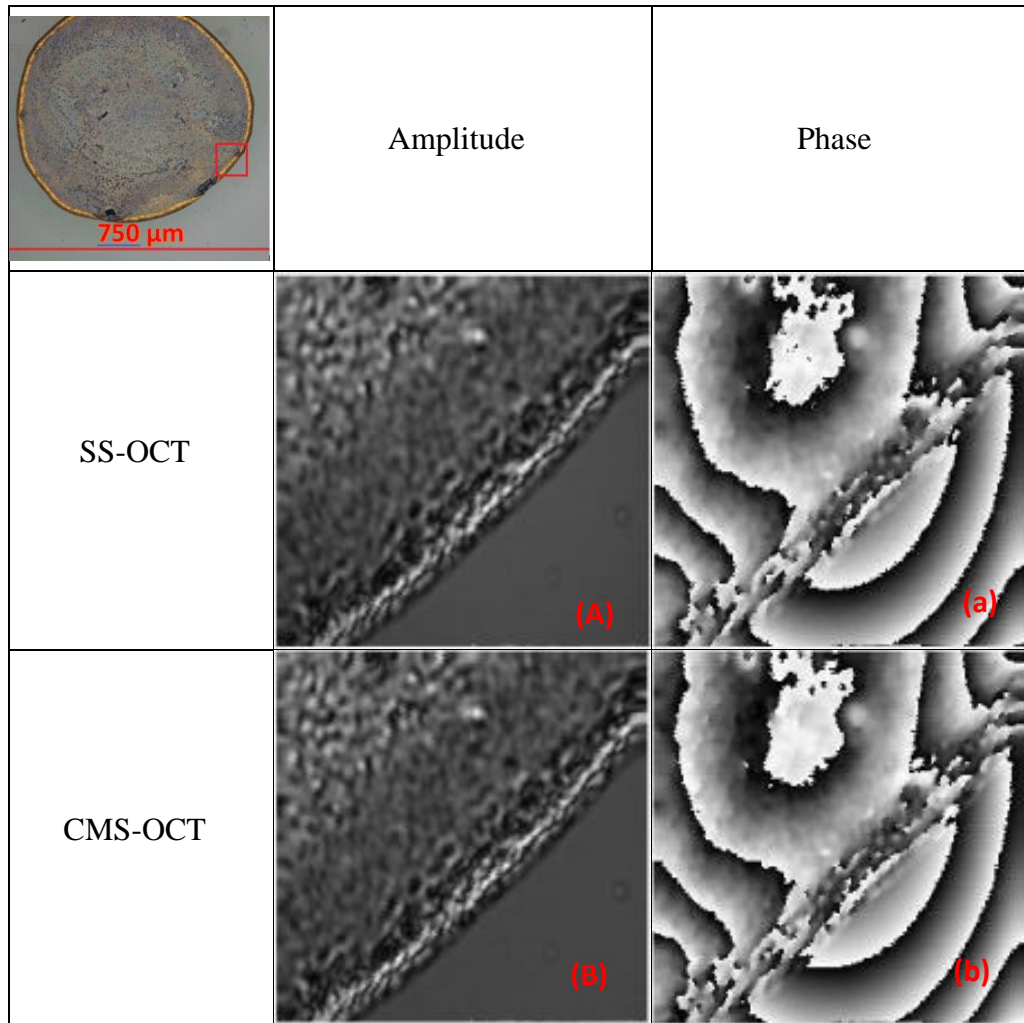


Fig. 6.7. (A) and (B): *En-face* OCT images of the red square region on edge of the GNR solution droplet. (a) and (b): phase maps of the red square region on edge of the GNR solution droplet. (A) and (a) were obtained from the SS-OCT mode. (B) and (b) were obtained from the CMS-OCT mode. Image size: $60\ \mu\text{m} \times 60\ \mu\text{m}$.

As can be seen in Fig. 6.7.(A) and Fig. 6.7.(B), the *en-face* OCT images clearly show the edge of the GNR solution droplet. In both operating modes, the well-defined ring patterns on the glass surface outside the droplet boundary are continuous in the phase maps (Fig. 6.7.(a) and Fig. 6.7.(b)). In contrast, the rings inside the droplet have a rather different and irregular appearance, due to the roughness of the droplet surface. Once again, the map obtained from the CMS-OCT mode (Fig. 6.7.(b)) matches closely to that obtained from SS-OCT mode (Fig. 6.7.(a)).

In summary, phase maps presented in Fig. 6.6 and Fig. 6.7 indicate that CMS-OCT has the same performance as SS-OCT in producing phase maps of the detected sample.

6.6 Discussion and conclusion

In this chapter, we studied the operating principles of both MSI and CMSI. MSI is a new approach to the spectral domain OCT, which does not need k -clock or extra software programme to eliminate the chirp in interferograms. MSI presents several advantages compared to SD-OCT and SS-OCT. The process of interferogram resampling and the FFT operation, which are necessary in SD-OCT and SS-OCT, are replaced by the correlation operation in MSI. Since the correlation operation can be performed in parallel, MSI shortens the data processing time. Moreover, spectral domain OCT is unable to perform real time *en-face* imaging due to time consuming data processing, whereas MSI provides direct access to the *en-face* imaging of the depth of interest in the sample. Furthermore, MSI-OCT is immune to non-calibrated interferogram, whereas the non-calibrated spectrum requires addressing in SS-OCT and SD-OCT [93].

Nevertheless, MSI presents some shortcomings. As a time consuming process, hundreds of masks (interferograms) need to be manually measured in the master interferometer (MI). In addition, since the relative phase relation between each mask obtained in the MI is discarded during the recording process, MSI is not able to perform phase measurements.

These particular disadvantages of MSI are addressed by CMSI. CMSI does not directly measure hundreds of masks but infers a large number of masks from a reduced number (typically 2-5) of masks that need to be actually recorded in the master interferometer (MI). The procedure involves using the measured 2-5 masks to calculate two functions: the $g(v)$ function expressing the chirp in the interferogram; and the $h(v)$ function expressing the unbalanced dispersion in the setup. These two functions are then used to infer hundreds of masks that can be stored in the computer for the later correlation operation. Because the inferred masks in CMSI have certain relative phase relations, CMSI was predicted to be able to perform phase measurements.

Before the study presented in this chapter, no experiment had been conducted to prove the capability of CMS-OCT to recover phase information from the detected sample. We applied the CMSI technique to the existing SS-OCT setup and wrote specific LabVIEW codes to perform phase measurements. The resulting OCT setup was able to operate in both SS-OCT mode and CMS-OCT mode. In the CMS-OCT mode, the k -clock from the swept source was disabled, and the digitizer installed in the

computer used its internal clock. Since the k -clock function implemented in the swept source is costly, CMS-OCT has a lower setup cost than SS-OCT.

We observed that the amplitude-derived axial resolution of the CMS-OCT is comparable with that of SS-OCT. By generating phase maps in both operating modes and comparing the obtained results, it is concluded that CMS-OCT has virtually identical phase measurement performance to SS-OCT.

Chapter 7

Conclusions

7.1 Summary

The projects presented in this thesis are focused on the use of phase sensitive OCT to perform photothermal detection and imaging of gold nanoparticles in clear media and in vitro tissue and scattering media. Three different OCT systems were specifically developed to carry out the task. Research tools, including specialised LabVIEW codes, were developed by the author to enable the production of *en-face* images to characterise the distribution of gold nanoparticles at multiple depth layers within scattering media and biological tissue samples, which is also the overall aim of the thesis. By demonstrating the capability to identify and locate aggregated gold nanoparticles with lateral resolution of 5 μm and depth displacement sensitivity of 0.17 nm, this goal has been successfully met.

The theory presented in the first two chapters provides context to the principles of phase measurements in monochromatic interferometry and in OCT. A brief review of applications of the phase measurement was given in each chapter. Chapter 3 provides an introduction of gold nanoparticles, including their unique optical properties and their applications in biomedicine. Several different techniques to detect their existence and/or location were reviewed, and the limits of each technique was discussed.

Chapter 4 introduces the experimental work of developing a spectrometer based phase sensitive OCT system to perform photothermal detection and imaging of GNRs in the tissue sample. To calibrate the system, phase measurements were initially made on vibrations with amplitudes on the micrometre scale. The process to characterise the operating parameters of the system was fully detailed. The system was used to measure the strengths of photothermal response of GNRs to both the modulation frequency and the power of the excitation Ti:Sa beam. The photothermal detection was used to identify the axial location of GNRs injected in the tissue sample. High contrast *en-face* phase images were acquired to show the distribution of GNRs in the allocated layers in the sample.

Chapter 5 is a presentation of the experimental work to develop a swept source based phase sensitive OCT system to perform photothermal detection and imaging of GNRs in scattering media. With the capabilities of the SD-OCT system for photothermal detection and imaging of GNRs well demonstrated in Chapter 4, this part of the overall project was aimed at increasing the depth of the photothermal detection and imaging by employing a SS-OCT system. The performance of the system was evaluated by taking phase measurements of micro vibrations. In terms of phase measurements, the output of the SS-OCT system is very similar to that of the SD-OCT system demonstrated in Chapter 4, except for the high system noise level. The system noise level of the SS-OCT was characterized to be 4 times higher than that of the SD-OCT (in Chapter 4). In this chapter, particular attention was paid to the synchronization of devices with the system operating in the A-scan mode, B-scan mode and *en-face* imaging mode. The system was used to perform photothermal detection and imaging of GNRs in the clear media and the scattering media. The process of generating *en-face* phase images was fully detailed. In particular, high contrast images of GNRs in highly scattering media were obtained by mapping the difference between successful *en-face* phase images into grayscale.

Chapter 6 is an exploration into phase sensitive Complex Master/Slave OCT. The theories and principles of Master/Slave interferometry and Complex Master/Slave interferometry were introduced. A CMS-OCT employing the CMSI technique was developed. The system was feasible of both the CMS-OCT operating mode and the SS-OCT operating mode. Phase measurements were performed in both operating modes. The phase maps generated from two operating modes were compared to test the phase measurement function of the CMS-OCT. For the first time, the capability of the Complex Master/Slave interferometry to perform phase measurements is demonstrated experimentally.

7.2 Achievements

Across all the works presented in this thesis there have been a number of significant accomplishments. By performing phase measurements, the SD-OCT system was demonstrated to be capable of achieving a displacement sensitivity of at least 1.57-nm for measuring vibrations and movements. Nevertheless, if sample vibration can be induced at known frequencies, Fourier analysis could be used to improve the displacement sensitivity of the SD-OCT system up to 0.17 nm.

The methodology demonstrated in Chapter 4 provided the full step-by-step process of calibrating and characterizing the operating performance of a phase sensitive OCT system. These methods could be treated as a valid reference to be duplicated by other researchers working on phase sensitive OCT to test and optimize their systems.

Employing the phase sensitive SD-OCT, we were able to locate GNRs at multiple layers in the tissue sample.

By displaying the difference between successive *en-face* phase images, the photothermal imaging of GNRs achieved an enhanced contrast. This method does not add extra cost to the system. Also, this method remains the operating speed of the OCT system, and it does not rely on sophisticated and time consuming image processing algorithms.

Very little work has been reported to date on the photothermal trapping of GNRs. During the photothermal detection measurements, we observed the aggregation of GNRs resulted from photothermal trapping. The phase sensitive SD-OCT system was employed to image the GNRs in bulk. The *en-face* photothermal images obtained have an enhanced contrast compared with those obtained with the previously reported TPL technique in imaging the photothermal trapping of GNRs. The good contrast benefitted from the high photothermal conversion efficiency of GNRs. The result indicates that phase sensitive OCT has a great potential in replacing the TPL technique to study the photothermal trapping of gold nanoparticles.

Although it is widely accepted that extra devices have to be implemented into the SS-OCT system to stabilize the output phase, no work has been conducted to compare the system noise levels of the phase sensitive SS-OCT system and the phase sensitive SD-OCT system. We conducted the comparison by taking phase measurements on the same sample in both OCT systems. The results presented in section 5.3.4 were adapted from a SPIE Proceedings publication [95].

For the first time, the phase sensitive capability of CMSI was demonstrated in experiments. By employing CMS-OCT to produce *en-face* phase images directly at a particular layer of interest in the sample, there was no need to acquire the 3D volume data of the studied sample prior to slicing the *en-face* image. Consequently, a phase sensitive CMS-OCT operates faster at producing *en-face* phase images compared with the phase sensitive SS-OCT and the phase sensitive SD-OCT.

7.3 Evaluation

A number of aspects hindered the progress of this research, with the 2π phase ambiguity being the chief among them. For both the SD-OCT system (Chapter 4) and the SS-OCT system (Chapter 5), the produced output phase values were wrapped between 0 and 2π , in which any phase value larger than 2π was forced to 2π in the output. In the A-scan operating mode, this problem was easily solved by putting a “phase unwrap” sub-VI before the output port in the LabVIEW programme. This sub-VI completed the task by monitoring a string of output values to avoid random phase jumps resulting from phase wrapping. However, in the *en-face* imaging mode, since the relative phase relation between successively produced 3D volumes of data is uncertain, we did not successfully develop a suitable algorithm to solve the phase wrap.

We found that the phase sensitive OCT system employing the common object/reference path configuration exhibits the best displacement sensitivity performance. However, not all measurements were performed in this configuration. For those measurements using the glass microfluidic channel as the sample, since the glass layer is too thick, the axial position of interest would go beyond the detection range of the OCT system if the common path configuration had been applied. Although the separate reference arm configuration with a worse displacement sensitivity performance was employed for those measurements, the results obtained in all measurements were still successful, which indicates the potential of phase sensitive OCT in photothermal detection and imaging of gold nanoparticles.

Although phase sensitive OCT proved to be superior to the TPL technique in imaging the distribution of aggregated gold nanoparticles resulting from the photothermal trapping, due to the lack of a suitable phase unwrap algorithm, neither SD-OCT nor SS-OCT was capable of quantifying the degree of the aggregation which was directly related to the degree of the photothermal trapping.

The greatest disappointment of this research was that the CMS-OCT was not used for the photothermal detection and imaging of gold nanoparticles. Since the CMS-OCT developed by the author was swept source based, the output phase still suffered from the jitter in the swept laser. If the spectrometer based OCT system had been modified to a CMS-OCT system, the output phase would be free of spikes and jumps. If this was the case, the CMS-OCT could be faster in producing *en-face* images to show the distribution of gold nanoparticles in complex media.

7.4 Future work

The primary objective for any future work would be to use phase sensitive OCT to quantify the strength of the photothermal trapping of gold nanoparticles. This can be achieved by developing a suitable phase unwrapping algorithm to manipulate the output phase. Then, the thickness of the aggregated gold nanoparticles will be shown as varied grey levels in the *en-face* image. Furthermore, employing the phase unwrapping algorithm, the *en-face* imaging area would be enlarged since the phase discontinuity created by the scanning induced lateral OPD can be solved.

Extra components can be used in the SS-OCT setup to stabilize the output phase, allowing quantitative phase measurements to be performed deep in the tissue sample by using a less noisy phase sensitive SS-OCT system.

A spectrometer based CMS-OCT system should be applied for the photothermal detection and imaging of gold nanoparticles.

There is continuing work in the industry for OCT systems on increasing performance parameters of swept sources linewidth. Because GNRs are highly reflective, it is possible to obtain a signal from depths greater than 5 mm, which are well within the capabilities of today's swept laser sources [96]. Potential exists therefore to develop more knowledge about a variety of interconnected aspects such as propagation of the excitation beam in tissue, local heating effects determined by confocality, minimum excitation power required from different depths, relaxation time required for heat dissipation.

References

- [1] F. Zernike, "How I discovered phase contrast," *Science* **121**(3141), 345-349 (1995).
- [2] Nikon, "Introduction to phase contrast microscopy," <https://www.microscopyu.com/techniques/phase-contrast/introduction-to-phase-contrast-microscopy>
- [3] K.A. Nugent, D. Paganin, and T.E. Gureyev, "A phase odyssey," *Phys. Today* **54**(8), 27 (2001).
- [4] M. A. Choma, A. Ellerbee, J. A. Izatt, W. Drexler, and J. G. Fujimoto, *Optical Coherence Tomography Technology and Application* (Springer, 2015), Chap. 40.
- [5] J. Farinas and A.S. Verkman, "Cell volume and plasma membrane osmotic water permeability in epithelial cell layers measured by interferometry," *Biophys. J.* **71**(6), 3511-3522 (1996).
- [6] T. Ikeda, G. Popescu, P.R. Dasari, and M.S. Feld, "Hilbert phase microscopy for investigating fast dynamics in transparent systems," *Opt. Lett.* **30**(10), 1165-1167 (2005).
- [7] G. Popescu, T. Ikeda, C.A. Best, K. Badizadegan, R.R. Dasari, and M.S. Feld, "Erythrocyte structure and dynamics quantified by Hilbert phase microscopy," *J. Biomed. Opt.* **10**(6), 060503 (2005).
- [8] P. Deen, M. Verdijk, N. Knoers, B. Wieringa, L. Monnens, CH van Os, and BA van Oost, "Requirement of human renal water channel aquaporin-2 for vasopressin-dependent concentration of urine," *Science* **264**(5155), 92-95 (1994).
- [9] A. S. Verkman, "Optical methods to measure membrane transport processes," *J. Membr. Biol.* **184**(2), 99-110 (1995).
- [10] M. Echevarria and A. S. Verkman, "Optical measurement of osmotic water transport in cultured cells: evaluation of the role of glucose transporters," *J. Gen. Physiol.* **99**(4), 573-589 (1992).
- [11] V. A. Andreev and K. V. Indukaev, "Phase modulation microscope MIM-2.1 for measurements of surface microrelief. General principles of design and operation," *J. Russian Laser Res.* **26**(5), 380-393 (2005).
- [12] V. A. Andreev, K. V. Indukaev, O. K. Ioselev, A. I. Legkii, G. L. Lazarev, and D. A. Orlov, "Phase modulation microscope MIM-2.1 for measurements of surface microrelief. Results of Measurements," *J. Russian Laser Res.* **26**(5), 394-401 (2005).
- [13] A. R. Brazhe, N. A. Brazhe, N. N. Rodionova, A. I. Yusipovich, P. S. Ignatyev, G. V. Maksimov, E. Mosekilde, and O.V. Sosnovtseva, "Non-invasive study of nerve fibres using laser interference microscopy," *Phil. Trans. R. Soc. A* **366**(1880), 3463-3481 (2008).
- [14] J. Fischbarg, J. Li, K. Kuang, M. Echevarria, and P. Iserovich, "Determination of volume and water permeability of plated cells from measurements of light scattering," *Am. J. Physiol.* **265**(5), C1412-C1423 (1993).
- [15] S. Muallem, R. Zhang, P. A. Loessberg, and R. A. Star, "Simultaneous recording of cell volume changes intracellular pH or Ca²⁺ concentration in single osteosarcoma cells UMR-106-01," *J. Biol. Chem.* **267**(25), 17658-17664 (1992).

- [16] J. Farinas, V. Simenak, and A. S. Verkman, "Cell volume measured in adherent cells by total internal reflection microfluorimetry: application to permeability in cells transfected with water channel homologs," *Biophys. J.* **68**(4), 1613-1620 (1995).
- [17] A. F. Fercher, K. Mengedoht, and W. Werner, "Eye-length measurement by interferometry with partially coherent light," *Pot. Lett.* **13**(3), 186-188 (1988).
- [18] D. Huang, E. A. Swanson, Ch. P. Lin, J. S. Schuman, W. G. Stinson, W. Chang, M. R. Hee, T. Flotte, K. Gregory, C. A. Puliafito, and J. G. Fujimoto, "Optical coherence tomography," *Science* **254**(5035), 1178-1181 (1991).
- [19] M. L. Gabriele, G. Wollstein, H. Ishikawa, L. Kagemann, J. Xu, L. S. folio, and J. S. Schuman, "Optical coherence tomography: history, current status, and laboratory work," *Invest Ophthalmol Vis Sci.* **52**(5), 2425-2436 (2011).
- [20] Y. Zhang, B. Cense, J. Rha, R. S. Jonnal, W. Gao, R. J. Zawadzki, J. S. Werner, S. Jones, S. Olivier, and D. T. Miller, "High-speed volumetric imaging of cone photoreceptors with adaptive optics spectral-domain optical coherence tomography," *Opt. Express* **14**(10), 4380-4394 (2006).
- [21] R. Huber, D. C. Adler, and J. G. Fujimoto, "Buffered Fourier domain mode locking: unidirectional swept laser sources for optical coherence tomography imaging at 370,000 lines/s" *Opt. Lett.* **31**(20), 2975-2977 (2006).
- [22] M.V. Sarunic, S. Weinberg, and J. A. Izatt, "Full-field swept-source phase microscopy," *Opt. Lett.* **31**(10), 1462-1464 (2006).
- [23] M. A. Choma, A. K. Ellerbee, S. Yazdanfar, and J. A. Izatt, "Doppler flow imaging of cytoplasmic streaming using spectral domain phase microscopy," *J. Biomed. Opt.* **11**(2), 024014 (2006).
- [24] C. Joo, T. Akkin, Ki H. Kim, and J. E. de Boer, "Spectral-domain optical coherence phase and multiphoton microscopy," *Opt. Lett.* **32**(6), 623-625 (2007).
- [25] R. K. Wang, and A. L. Nuttall, "Phase sensitive optical coherence tomography imaging of the tissue motion within the organ of Corti at a subnanometer scale a preliminary study," *J. Biomed Opt.* **15**(5), 056005 (2010).
- [26] R. K. Manapuram, V. G. R. Manne, and K. V. Larin, "Phase-sensitive swept source optical coherence tomography for imaging and quantifying of microbubbles in clear and scattering media," *Journal of Applied Physics* **105**(10), 102040 (2009).
- [27] M. R. Hee, B. E. Bouma, and G. J. Tearney, *Handbook of Optical Coherence Tomography* (Marcel Dekker, 2002), Chap. 2.
- [28] Y. Chen, C. P. Liang, Y. Liu, A. H. Fischer, A. V. Parwani, and L. Pantanowitz, "Review of advanced imaging techniques," *J Pathol Inform*, **3**(22), (2012).
- [29] T. S. Neuman, "Arterial gas embolism and decompressions sickness," *News Physiol. Sci.* **17**(2), 77-81 (2002).
- [30] R. Brucher, and D. Russell, "Automatic online embolus detection and artefact rejection with the first multifrequency transcranial Doppler," *Stroke* **33**(8), 1969-1974 (2002).

- [31] N. M. Holbrook, E. T. Ahrens, M. J. Burns, and M. A. Zwieniecki, "In vivo observation of cavitation and embolism repair using magnetic resonance imaging," *Plant Physiol.* **126**(1), 27-31 (2001).
- [32] D. M. Barratt, P. G. Harch, and K. V. Meter, "Decompression illness in divers: a review of the literature," *Neurologist* **8**(3), 186-202 (2002).
- [33] Particle Works white paper, "Gold Nanoparticles," <http://www.particle-works.com/product-category/gold-nanoparticles/?gclid=CO-buMKB79ECFcaV7QodvjEI1A>.
- [34] P. M. Tiwari, K. Vig, V. A. Dennis, and Sh. R. Singh, "Functionalized gold nanoparticles and their biomedical applications," *Nanomaterials* **1**(1), 31-63 (2011).
- [35] B. Duncan, C. Kim, and V. M. Rotello, "Gold nanoparticle platforms as drug and biomacromolecule delivery systems," *J. Contr. Release* **148**(1), 122-127 (2010).
- [36] P. Pattnaik, "Surface plasmon resonance Applications in understanding receptor-ligand interaction," *Appl. Biochem. Biotechnol.* **126**(2), 79-92 (2005).
- [37] X. Huang, and M. A. El-Sayed, "Gold nanoparticles: optical properties and implementations in cancer diagnosis and photothermal therapy," *J. of Advanced Research* **1**(1), 13-28 (2010).
- [38] P. K. Jain, K. S. Lee, I. H. El-Sayed, and M. A. El-sayed, "Calculated absorption and scattering properties of gold nanoparticles of different size, shape, and composition: applications in biological imaging and biomedicine" *J. Phys. Chem. B* **110**(14), 7238-48 (2006).
- [39] J. Stone, St. Jackson, and D. Wright, "Biological applications of gold nanorods," *NanoMed. and NanoBio.* **3**(1), 100 (2010).
- [40] H. Chen, E. Gratton, and M. A. Digman, "Self-assisted optothermal trapping of gold nanorods under two-photon excitation," *Methods Appl. Fluoresc.* **4**(3), 035003 (2016).
- [41] L. Tong, Q. Wei, Al. Wei, and J. X. Cheng, "Gold nanorods as contrast agents for biological imaging: optical properties, surface conjugation and photothermal effects," *Photochem Photobiol.* **85**(1), 21 (2010).
- [42] M. Pelton, M. Liu, H. Y. Kim, G. Smith, Ph. Guyot-Sionnest, and N. F. Scherer, "Optical trapping and alignment of single gold nanorods by using plasmon resonances," *Opt. Letters* **31**(13), 2075-2077 (2006).
- [43] F. Hajizadeh, and S. Nader S. Reihani, "Optimized optical trapping of gold nanoparticles," *Opt. Express* **18**(2), 551-559 (2010).
- [44] Ch. S. Unkel, I. Zins, O. Schubert, and C. Sönnichsen, L. B. Oddershede, "Quantitative optical trapping of single gold nanorods," *Nano Lett.* **8**(9), 2998-3003 (2008).
- [45] T. D. Yang, W. Choi, T. H. Yoon, K. J. Lee, J. S. Lee, J. H. Joo, M. G. Lee, H. S. Yim, K. M. Choi, B. Kim, J. J. Lee, H. Kim, D. Y. Lee, K. Y. Jung, and S. K. Baek, "In vivo photothermal treatment by the peritumoral injection of macrophages loaded with gold nanoshells," *Bio. Opt. Express* **7**(1), 185-193 (2015).

- [46] R. Vankayala, Ch. Ch. Lin, P. Kalluru, Ch. Sh. Chiang, and K. Ch. Hwang, "Gold nanoshells-mediated bimodal photodynamic and photothermal cancer treatment using ultra-low doses of near infra-red light," *Biomaterials* **35**(21), 5527-5538 (2014).
- [47] S. J. Oldenburg, J. B. Jackson, S. L. Westcott, and N. J. Halas, "Infrared extinction properties of gold nanoshells," *Appl. Phys. Lett.* **75**(19), 2897-2899 (1999).
- [48] J. R. Cole, N. A. Mirin, M. W. Knight, G. P. Goodrich, and N. J. Halas, "Photothermal efficiencies of nanoshells and nanorods for clinical therapeutic applications," *J. Phys. Chem. C* **113**(28), 12090–12094 (2009).
- [49] S. M. Noh, W. K. Kim, S. J. Kim, J. M. Kim, K. H. Baek, and Y. K. Oh, "Enhanced cellular delivery and transfection efficiency of plasmid DNA using positively charged biocompatible colloidal gold nanoparticles," *Biochim. Biophys. Acta.* **1770**(5), 747-752 (2007).
- [50] J. S. Lee, J. J. Green, K. T. Love, J. Sunshine, R. Langer, and D. G. Anderson, "poly (β -amino ester) nanoparticles for small interfering RNA delivery," *Nano Lett.* **9**(6), 2402-2406 (2009).
- [51] X. Zhou, X. Zhang, X. Xu, X. Zha, Q. Fu, B. Liu, X. Wang, Y. Chen, Y. Chen, and Y. Shan, "The effect of conjugation to gold nanoparticles on the ability of low molecular weight chitosan to transfer DNA vaccine," *Biomaterials* **29**(1), 111-117 (2008).
- [52] C. Kim, S. S. Agasti, Z. Zhu, L. Isaacs, and V. M. Rotello, "Recognition-mediated activation of therapeutic gold nanoparticles inside living cells," *Nat. Chem.* **2**, 962-966 (2010).
- [53] X. Huang, I. H. El-Sayed, and M. A. El-Sayed, "Applications of Gold Nanorods for Cancer Imaging and Photothermal Therapy," *Methods Mol. Biol.* **624**, 343-357 (2010).
- [54] K. Imura, T. Nagahara, and H. Okamoto "Near-field two-photon-induced photoluminescence from single gold nanorods and imaging of plasmon modes," *J. Phys. Chem. B* **109**(27), 13214–13220 (2005).
- [55] Ch. H. Chou, Ch. D. Chen, and C. R. Ch. Wang, "Highly Efficient, Wavelength-Tunable, Gold Nanoparticle Based Optothermal Nanoconvertors," *J. Phys. Chem. B* **109**(22), 11135-11138 (2005).
- [56] T. Niidome, M. Yamagata, Y. Okamoto, Y. Akiyama, H. Takahashi, T. Kawano, Y. Katayama, and Y. Niidome, "PEG-modified gold nanorods with a stealth character for in vivo applications," *J Control Release* **114**(3), 343-347 (2006).
- [57] A. J. Di Pasqua, R. E. Mishler, Y. L. Ship, J. C. Dabrowiak, and T. Asefa, "Preparation of antibody-conjugated gold nanoparticles," *Matter. Lett.* **63**(21), 1876-1879 (2009).
- [58] Ch. S. Unkel, I. Zins, O. Schubert, C. Sonnichsen, and L. B. Obbershede, "Quantitative optical trapping of single gold nanorods," *Nano Lett.* **8**(9), 2998-3003 (2008).

- [59] M. C. Skala, M. J. Crow, A. Wax, and J. A. Izatt, "Photothermal Optical Coherence Tomography of Epidermal Growth Factor Receptor in Live Cells Using Immunotargeted Gold Nanospheres," *Nano Lett.* **8**(10), 3461-3467 (2008).
- [60] R. Allabashi, W. Stach, A. de la Escosura-Muniz, L. Liste-Calleja, and A. Merkoci, "ICP-MS: a powerful technique for quantitative determination of gold nanoparticles without previous dissolving," *J. Nanopart Res.* **11**(8), 2003-2011 (2009).
- [61] K. Ricketts, C. Guazzoni, A. Castoldi, A. P. Gibson, and G. J. Royle, "An x-ray fluorescence imaging system for gold nanoparticle detection," *Phys. Med. Biol.* **58**, 7841-7855 (2013).
- [62] H. Wang, T. B. Huff, D. A. Zweifel, W. He, P. S. Low, A. Wei, and J. X. Cheng, "In vitro and in vivo two-photon luminescence imaging of single gold nanorods," *Proc. Natl Acad. Sci.* **102**(44), 15752-15756 (2005).
- [63] D. C. Adler, Sh. W. Huang, R. Huber, and J. G. Fujimoto, "Photothermal detection of gold nanoparticles using phase-sensitive optical coherence tomography," *Opt. Express* **16**(7), 4376-4393 (2008).
- [64] D. Braun and A. Libchaber, "Trapping of DNA by Thermophoretic Depletion and Convection," *Phys. Rev. Lett.* **89**(18), 188103 (2002).
- [65] H. Chen, E. Gratton, and M. A. Digman, "Spectral properties and dynamics of gold nanorods revealed by EMCCD-based spectral phasor method," *Microsc. Res. Tech.* **78**(4), 283-293 (2015).
- [66] Y. Liu and A. W. Poon, "Flow-assisted single-beam optothermal manipulation of microparticles," *Optics Express* **18**(17), 18483-18491(2010).
- [67] D. C. Adler, R. Huber, and J. G. Fujimoto, "Phase sensitive optical coherence tomography at up to 370,000 lines per second using buffered Fourier domain mode-locked lasers," *Opt. Letters* **32**(6), 626-628 (2007).
- [68] R. K. Wang, and A. L. Nuttall, "Phase sensitive optical coherence tomography imaging of the tissue motion within the organ of Corti at a subnanometer scale a preliminary study," *J. Biomed Opt.* **15**(5), 056005 (2010).
- [69] R. K. Manapuram, V. G. R. Manne, and K. V. Larin, "Phase-sensitive swept source optical coherence tomography for imaging and quantifying of microbubbles in clear and scattering media," *Journal of Applied Physics* **105**(10), 102040 (2009).
- [70] Z. Yaqoob, W. Choi, S. Oh, N. Lue, Y. Park, Ch. F. Yen, R. R. Dasari, K. Badizadegan, and M. S. Feld, "Improved phase sensitivity in spectral domain phase microscopy using line-field illumination and self phase-referencing," *Opt. Express* **17**(13), 10681-10687 (2009).
- [71] Ch. Joo, T. Akkin, B. Cense, B. H. Park, and J. F. de Boer, "Spectral-domain optical coherence phase microscopy for quantitative phase-contrast imaging," *Opt. Lett.* **30**(16), 2131-2133 (2005).
- [72] B. J. Vakoc, S. H. Yun, J. F. de Boer, G. J. Tearney, and B. E. Bouma, "Phase resolved optical frequency domain imaging," *Opt. Express* **13**(14), 5483-5493 (2005).

- [73] B. H. Park, M. C. Pierce, B. Cense, S. H. Yun, M. Mujat, G. J. Tearney, B. E. Bouma, and J. F. de Boer, "Real-time fiber-based multi-functional spectral-domain optical coherence tomography at 1.3 μm ," *Opt. Express* **13**(11), 3931-3944 (2005).
- [74] B. F. Kennedy, S. H. Koh, R. A. McLaughlin, K. M. Kennedy, P. R. T. Munro, and D. D. Sampson, "Strain estimation in phase-sensitive optical coherence elastography," *Opt. Express* **3**(8), 1865-1879 (2012).
- [75] M. A. Choma, A. K. Ellerbee, S. Yazdanfar, and J. A. Izatt, "Doppler flow imaging of cytoplasmic streaming using spectral domain phase microscopy," *J. Biomed. Opt.* **11**(2), 024014 (2006).
- [76] R. V. Kuranov, A. B. McElroy, N. Kemp, S. Baranov, J. Taber, M. D. Feldman, and Th. E. Milner, "Cell Referenced Swept Source Phase Sensitive Optical Coherence Tomography," *IEEE Photonics Technology Letters* **22**(20), 1524-1526 (2010).
- [77] A. Gh. Podoleanu, "Optical Coherence Tomography," *Journal of Microscopy* **247**(3), 209-299 (2012).
- [78] R. Raghunathan, M. Singh, M. E. Dickinson, and K. V. Larin, "Optical coherence tomography for embryonic imaging: a review," *J. of Biomedical Optics* **21**(5), 050902 (2016).
- [79] Y. Zhang, B. Cense, J. Rha, R. S. Jonnal, W. Gao, R. J. Zawadzki, J. S. Werner, S. Jones, S. Olivier, and D. T. Miller, "High-speed volumetric imaging of cone photoreceptors with adaptive optics spectral-domain optical coherence tomography," *Opt. Express* **14**(10), 4380-4394 (2006).
- [80] M. A. Choma, A. K. Ellerbee, S. Yazdanfar, and J. A. Izatt, "Doppler flow imaging of cytoplasmic streaming using spectral domain phase microscopy," *J. Biomed. Opt.* **11**(2), 024014 (2006).
- [81] M. V. Sarunic, S. Weinberg, and J. A. Izatt, "Full-field swept-source phase microscopy," *Opt. Lett.* **31**(10), 1462-1464 (2006).
- [82] Adrian Gh. Podoleanu, George M. Dobre, and David A. Jackson, "En-face coherence imaging using galvanometer scanner modulation," *Opt. Lett.* **23**(3), 147-149 (1998).
- [83] R. K. Manapuram, V. G. R. Manne, and K. V. Larin, "Development of phase-stabilized swept-source OCT for the ultrasensitive quantification of microbubbles," *Laser Physics* **18**(9), 1080-1086 (2008).
- [84] A. Payne and A. Gh. Podoleanu, "Direct electronic linearization for camera-based spectral domain optical coherence tomography," *Opt. Lett.* **37**(12), 2424-2426 (2012).
- [85] A. Payne and A. Gh. Podoleanu, "Direct electronic linearization for camera-based spectral domain optical coherence tomography," *Opt. Lett.* **37**(12), 2424-2426 (2012).
- [86] Y. Yasuno, V. D. Madjarova, S. Makita, M. Akiba, A. Morosawa, C. Chong, T. Sakai, K.-P. Chan, M. Itoh, and T. Yatagai, "Three-dimensional and high-speed swept-source optical coherence tomography for in vivo investigation of human anterior eye segments," *Opt. Express* **13**(26), 10652-10664 (2005).

- [87] B. Hofer, B. Povazay, B. Hermann, A. Unterhuber, G. Matz, F. Hlawatsch, and W. Drexler, "Signal post processing in frequency domain OCT and OCM using a filter bank approach," Proc. SPIE **6443**, 3001-3006 (2007).
- [88] A. Yang, F. Vanholsbeeck, S. Coen, and J. Schroeder, "Chromatic dispersion compensation of an OCT system with a programmable spectral filter," Proc. SPIE **8091**, 809125 (2011).
- [89] Y. Watanabe, and T. Itagaki, "Real-time display SD-OCT using a linear-in-wavenumber spectrometer and a graphics processing unit," Proc. SPIE **7554**, 75542S (2010).
- [90] M. Wojtkowski, V. Srinivasan, T. Ko, J. Fujimoto, A. Kowalczyk, and J. Duker, "Ultrahigh-resolution, highspeed, Fourier domain optical coherence tomography and methods for dispersion compensation," Opt. Express **12**(11), 2404-2422 (2004).
- [91] C. C. Rosa, John Rogers, and A. Gh. Podoleanu, "Fast scanning transmissive delay line for optical coherence tomography," Opt. Lett. **30**(24), 3263-3265 (2005).
- [92] C. Yang, S. Yazdanfar and J. A. Izatt, "Fast scanning, dispersion-adjustable reference delay for OCT using fibre Bragg gratings," Proc. SPIE **5140**, 53-59 (2003).
- [93] A. Gh. Podoleanu and A. Bradu, "Master-slave interferometry for parallel spectral domain interferometry sensing and versatile 3D optical coherence tomography," Opt. Express **21**(16), 19324-19338 (2013).
- [94] S. Rivet, M. Maria, A. Bradu, Th. Feuchter, L. Leick, and A. Pololeanu, "Complex master slave interferometry," Opt. Express **24**(3), 2885-2905 (2016).
- [95] Y. Hu, and G. Dobre, "Performance comparison of spectrometer based and swept source based phase sensitive optical coherence tomography," Proc. SPIE **10416**, 1041603 (2017).
- [96] Th. Klein, and R. Huber, "High-speed OCT light sources and systems [Invited]," Biomed. Opt. Express **8**(2), 828-859 (2017).
- [97] Wikipedia, "Photophoresis," https://en.wikipedia.org/wiki/Photophoresis#cite_note-2
- [98] D. Braun, A. Libchaber, "Trapping of DNA by thermophoretic depletion and convection," Phys Rev Lett. **89**(18), 188103 (2002).
- [99] Y. Kim, H. Shim, K. Kim, H. Park, J. H. Heo, J. Yoon, Ch. Choi, S. Jang, and Y. Park, "Common-path diffraction optical tomography for investigation of three-dimensional structures and dynamics of biological cells," Opt. Express **22**(9), 10398-10407 (2014).
- [100] A. K. Trull, J. van der Horst, J. G. Bijster, and J. Kalkman, "Transmission optical coherence tomography based measurement of optical material properties," Opt. Express **23**(26), 33550-33563 (2015).
- [101] Q. A. Pankhurst, J. Connolly, S. K. Jones, and J. Dobson, "Applications of magnetic nanoparticles in biomedicine," J. Phys. D **36**, 167-181 (2003).

- [102] L. K. Bogart, A. Taylor, Y. Cesbron, P. Murray, and R. Levy, "Photothermal microscopy of the core of dextran-coated iron oxide nanoparticles during cell uptake," *ACS Nano*. **6**(7), 5961-5971 (2012).
- [103] M. Fortin, M. Piche, and E. F. Borra, "Optical tests with Bessel beam interferometry," *Opt. Express* **12**(24), 5887-5895 (2004).
- [104] V. N. Belyi, N. A. Khilo, S. N. Kurilkina and N. S. Kazak, "Spin-to-orbital angular momentum conversion for Bessel beams propagating along the optical axes of homogeneous uniaxial and biaxial crystals," *J. Opt.* **15**, 044018 (2013).
- [105] S. Berciaud, L. Cognet, G. A. Blab, and B. Lounis, "Photothermal Heterodyne Imaging of Individual Nonfluorescent Nanoclusters and Nanocrystals," *Phys. Rev. Lett.* **93**, 257402 (2004).
- [106] Zh. Li, K. Aleshire, M. Kuno, and G. V. Hartland, "Super-Resolution Far-Field Infrared Imaging by Photothermal Heterodyne Imaging," *J. Phys. Chem. B* **121**(37), 8838-8846 (2017).
- [107] K. Svoboda, and S. M. Block, "Optical tapping of metallic Rayleigh particles," *Opt. Lett.* **19**(13), 930-932 (1994).

Appendix

LabVIEW implementation in OCT systems

This appendix provides a diagrammatic overview of the LabVIEW codes with specific functions discussed throughout the thesis. The caption for each figure gives a brief description of the function for each code.

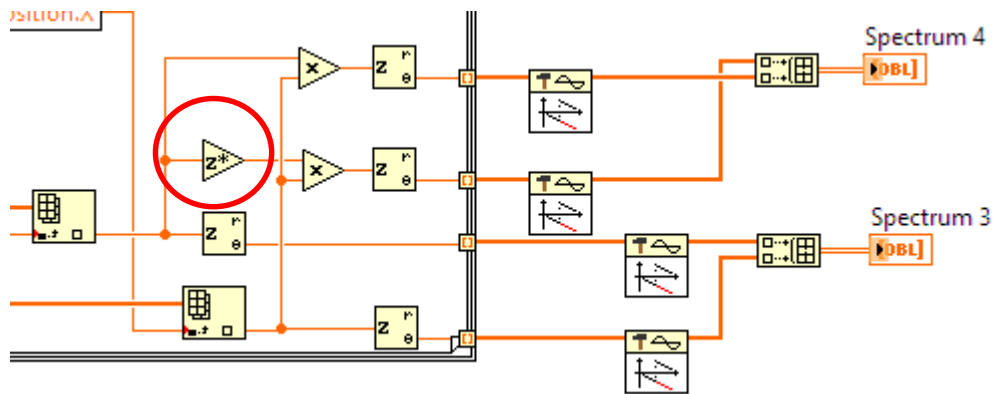


Fig. A.1. Using the conjugate VI (z^* in the red circle) to calculate the output phase:
 $\Phi(z, t) = \varphi(z, t) - \varphi(z_0, t)$.

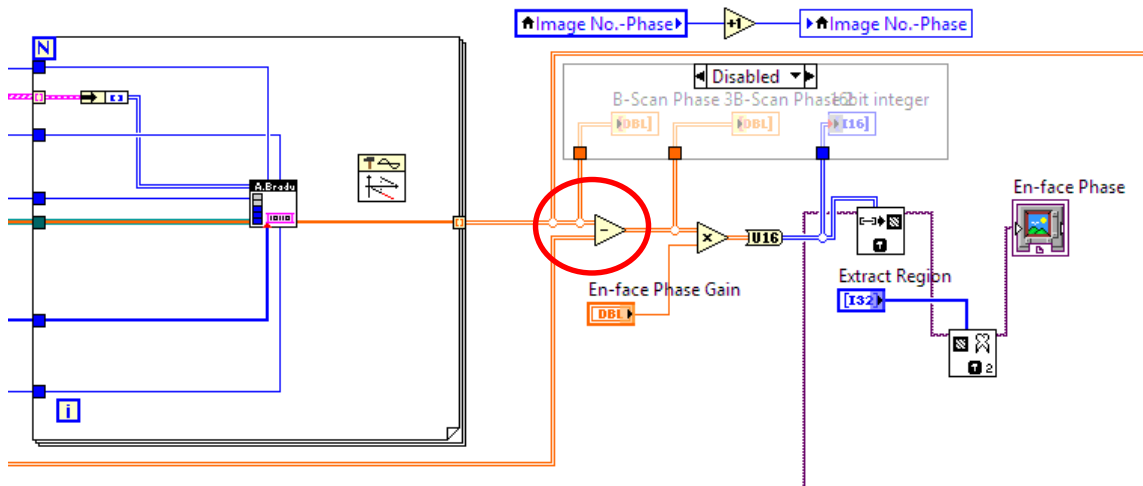


Fig. A.2. Using the subtract VI (“-” in the red circle) to calculate and display the difference between successive *en-face* phase images.

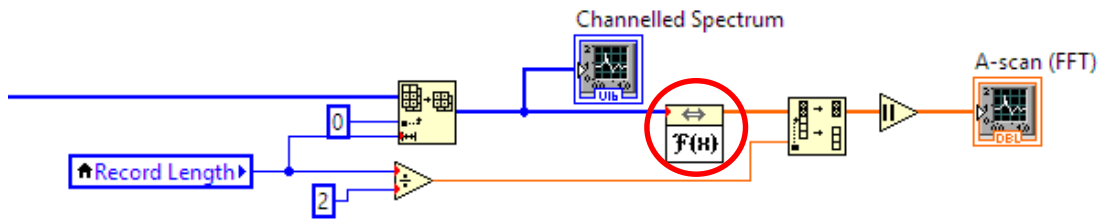


Fig. A.3. Using the FFT VI ($f\{x\}$ in the red circle) to perform FFT operation on the Channelled Spectrum which is then converted to the A-scan profile.

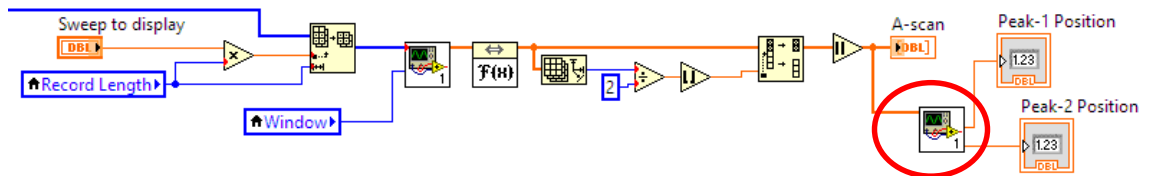


Fig. A.4. Using the “Peak Allocation” VI (in the red circle) to allocate the pixel orders of the two peaks in the A-scan profile.

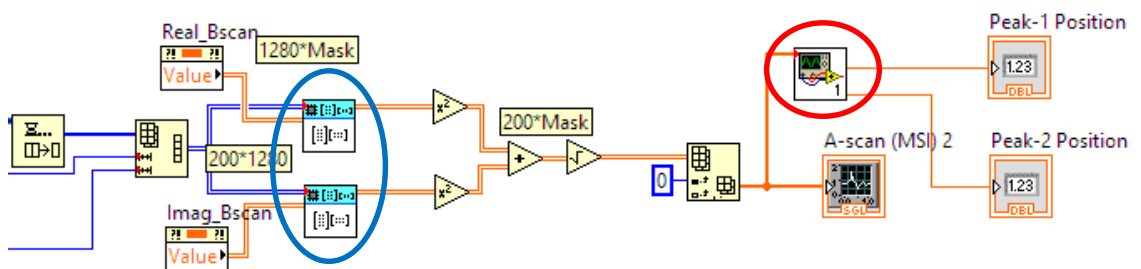


Fig. A.5. Using “correlation” VI (in the blue circle) to produce the A-scan amplitude profile in CMS-OCT. The “Peak Allocation” VI (in the red circle) is used to allocate the pixel orders of the peaks in the A-scan profile.

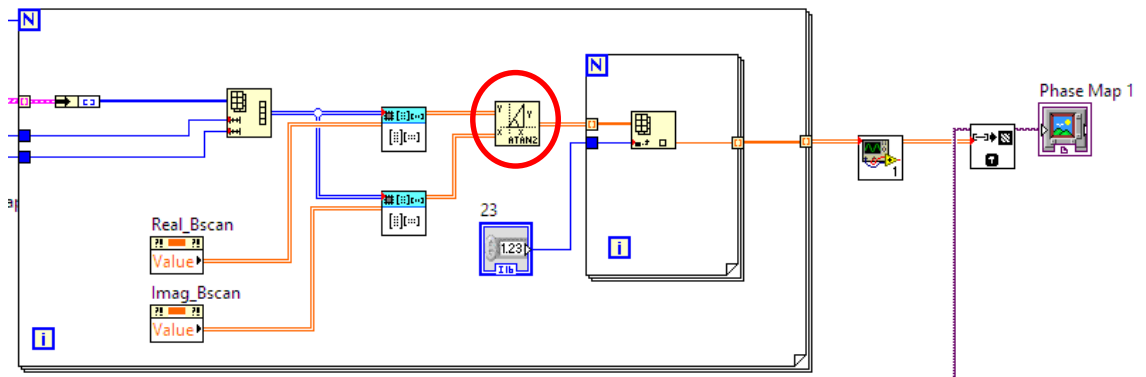


Fig. A.6. Using the CMSI technology, the VI (in the red circle) used to generate the A-scan complex profile produces complex values. Thus, the phase can be retrieved to generate phase maps.